

DISSERTATION

Phase instabilities in strongly correlated *Ce-Pt-Si* materials and superconductivity in novel Ge-based skutterudites $\{Ba, Sr, Th\} Pt_4 Ge_{12}$

ausgeführt zum Zwecke der Erlangung des akademischen
Grades eines Doktors der technischen Wissenschaften
unter der Leitung von

a.o. Univ. Prof. Dr. Ernst Bauer

E138
Institut für Festkörperphysik

eingereicht an der Technischen Universität Wien
Technisch-Naturwissenschaftliche Fakultät
von

Dipl.-Ing. Esmaeil Royanian
Matr.-Nr. 9827083
Friedrich-Engels-Platz 9/6/18
1200 Wien

Wien, im 15.12.2008

Kurzfassung

Die vorliegende Arbeit beschäftigt sich mit kristallographischen und physikalischen Eigenschaften ternärer Verbindungen, und verknüpft strukturelle Eigenschaften mit dem physikalischen Verhalten. Physikalische Eigenschaften und Phasenbeziehungen innerhalb des Systems Ce-Pt-Si wurden mittels verschiedener Meßmethoden untersucht. Verbindungen des Typs Ce-Pt-Si haben interessante elektrische und/oder magnetische Eigenschaften wie z.B. schweres Fermionen Verhalten, Kondo-Gitter Verhalten, unkonventionelle Supraleitung in nicht zentrosymmetrischer Symmetrie, das großes Interesse an physikalischen Eigenschaften von Ce-Pt-Si hervorgerufen hat. Kristallwachstum und Synthese der Verbindungen erfordern vertieftes Wissen über Phasenrelationen sowie Kristallstrukturen. Zu diesem Zweck wurden die Phasenrelationen im ternären System Ce-Pt-Si für den isothermen Schnitt bei 800°C bestimmt.

Die Untersuchung gefüllter Skutterudite hat in den vergangenen Jahren eine Vielzahl von Verbindungen mit einer reichen Mannigfaltigkeit physikalischer Eigenschaften erbracht. MPt₄Ge₁₂, mit M = (Ca, Sr, Ba, Eu), sind die ersten Mitglieder einer neuen Kategorie von Skutteruditen, Raumgruppe Im $\bar{3}$ (Nr. 204), deren Käfigstruktur ausschließlich durch Ge-Atome gebildet wird. Weitere Mitglieder dieser Materialfamilie wurden auch mit M = Th und U hergestellt. Für ThPt₄Ge₁₂ entwickelt sich Supraleitung unter $T_c = 4.75$ K. Für BaPt₄Ge₁₂ und SrPt₄Ge₁₂ wurde unterhalb $T_c = 5.35$ K und 5.10 K Supraleitung bei mittelstarker Elektron-Phonon Wechselwirkung festgestellt. Supraleitung wird den Eigenschaften des Pt-Ge Gerüsts zugeschrieben, in dem Ge-*p* Zustände die elektronische Struktur an der Fermi Energie bestimmen. Auch Ca (zum Teil) und Eu (komplett) stabilisieren diese neuen Skutterudite. Ein maximaler Füllungsgrad von ungefähr 20% Ca ist in Ba_{1-x}Ca_xPt₄Ge₁₂ möglich und führt zu einer Supraleitung unter $T_c = 5.2$ K. Messungen des elektrischen Widerstands zeigen, dass EuPt₄Ge₁₂ sich erst unterhalb von $T_m \approx 1.7$ K magnetisch ordnet. Die physikalische Eigenschaften von UPt₄Ge₁₂ werden von Spinfluktuationen bei niedrigen Temperaturen dominiert; sie verhindern magnetische Ordnung bzw. Supraleitung.

Sowohl Skutterudite {Ca,Sr,Ba,Eu,Th,U}Pt₄Ge₁₂ als auch Clathrate vom Typ I auf Ge-Basis Ba₈T_xGe_y; (T = Cd, Pd, Pt, Zn) sowie Si Clathrat vom Typ II Ba₈Zn_xSi_y und Ba₈Pt_xSi_y sind auch von Interesse für thermoelektrische Anwendungen. Clathratsysteme Ba₈M_xGe_{46-x-y}□_y (M = Pd,Pt,Zn,Cd), in denen M-Atome in die Käfig bildende Struktur eingebaut werden, wurden mittels Kristallchemie, elektrischem und thermischem Transport und Wärmekapazität erforscht. Die Ergebnisse dieser Studie stellten dar, dass die Erhöhung des M-Gehalts die Konzentration von Leerstellen in der Kristallstruktur verringert und das metallische System in Richtung eines Metall-

Isolator Übergangs driftet, wodurch die Ladungsträgerkonzentration dramatisch verringert wird.

Die Struktur von $M_2Pd_{14+x}B_{5-y}$ mit $M = Th, La, Ce, Pr, Nd, Sm, Eu$ und Gd wurde mittels Einkristall Röntgendiffraktionsdaten an $Nd_2Pd_{14}B_5$ und $Th_2Pd_{14}B_5$ (tetragonale Zelle und Raumgruppe $I4_1/AMD$, Nr. 141) bestimmt. Dabei wurde eine nahe strukturelle Verwandtschaft mit $Sc_4Ni_{29}Si_{10}$ festgestellt. Die elektrischen Widerstände von $M_2Pd_{14+x}B_{5-y}$ sind im Allgemeinen durch kleine RRR (Restwiderstandsverhältnis) Werte gekennzeichnet, die auf Defekte der Kristallstruktur zurückzuführen sind. Studien bei niedrigen Temperaturen zeigen, dass langreichweitige magnetische Ordnung in $Gd_2Pd_{14}B_5$ unterhalb 6 K existiert. Die Wärmekapazitätsmessungen weisen darauf hin, dass auch die Verbindungen mit Ce, Nd und Sm unterhalb von 2 K magnetisch geordnet sind, während die Pr-Verbindung als Folge des kristallelektrischen Feldeffekts (CEF) keinen magnetischen Ordnungszustand aufzuweisen scheint, zumindest nicht bis zu 400 mK. Der Gesamtdrehimpuls $J = 4$ des Pr Ions im Rahmen der CEF Effekte der tetragonalen Kristallstruktur von $Pr_2Pd_{14}B_5$ kann einen nicht-magnetischen Grundzustand auf Grund eines Singlett- oder eines nicht magnetischen Dublett-Zustandes einnehmen.

Abstract

The present thesis deals with crystallographic and physical properties of ternary compounds, and connects structural properties with physical behaviour. Physical properties and phase relations within the ternary Ce-Pt-Si system were studied by means of different measuring methods.

Besides the fact that many compounds from the Ce-Pt-Si system have shown interesting electrical and/or magnetic properties such as heavy-fermion behavior, Kondo-lattice behaviour, unconventional superconductivity without an inversion center, provoked large interest in the physical properties of Ce-Pt-Si system. Crystal growth and bulk material syntheses require detailed knowledge of phase relations as well as of crystal structures. Therefor the phase relations were investigated in the ternary system Ce-Pt-Si for the isothermal section at 800°C.

In the past years research in the field of filled skutterudites evidenced a rich diversity of ground state properties as well as the potential for thermoelectric applications. Cage-forming compounds such as zeolithes, fullerenes, clathrates or skutterudites have proven to be not only of scientific but also of significant technological interest. Members of a novel class of materials are essentially composed from $\text{MPt}_4\text{Ge}_{12}$, space group $\text{Im}\bar{3}$, (No. 204), with M=(Ca, Sr, Ba, Eu). Below $T_c = 5.35$ K and 5.10 K for $\text{BaPt}_4\text{Ge}_{12}$ and $\text{SrPt}_4\text{Ge}_{12}$, respectively, electron-phonon coupled superconductivity emerges, ascribed to intrinsic features of the Pt-Ge framework, where Ge-*p* states dominate the electronic structure at the Fermi energy. Further members of this family are M= Th, U, whereby $\text{ThPt}_4\text{Ge}_{12}$ develops superconductivity (SC) below $T_c = 4.75$ K. Electropositive elements Ca (partially) and Eu (completely) stabilize new compounds within the novel class of skutterudites based on a framework solely constituted by Ge-atoms. A maximum filling level of about 20 % of Ca is possible in $\text{Ba}_{1-x}\text{Ca}_x\text{Pt}_4\text{Ge}_{12}$, yielding a superconducting ground state below $T_c = 5.2$ K. Low temperature resistivity studies of $\text{EuPt}_4\text{Ge}_{12}$ evidence magnetic ordering at $T_m \approx 1.7$ K. The physical properties of $\text{UPt}_4\text{Ge}_{12}$ are dominated by spin fluctuations at low temperatures, preventing magnetic order and SC.

The series of skutterudites $\{\text{Ca},\text{Sr},\text{Ba},\text{Eu},\text{Th},\text{U}\}\text{Pt}_4\text{Ge}_{12}$ as well as Ge-based type I clathrates $\text{Ba}_8\text{T}_x\text{Ge}_y$; T = (Cd, Pd, Pt, Zn) and Si-based type II clathrates $\text{Ba}_8\text{Zn}_x\text{Si}_y$ and $\text{Ba}_8\text{Pt}_x\text{Si}_y$ compounds are of particular interest for thermoelectric applications. Ba- and Ge-based clathrate $\text{Ba}_8\text{M}_x\text{Ge}_{46-x-y}\square_y$ (M = Pd, Pt, Zn, Cd), where M-atoms substitute for framework atoms, were investigated by means of crystal chemistry, electrical and thermal transport measurements, and heat capacity. The results of this study showed that an increasing M-content reduces the concentration of vacancies in the crystal structure and drives the metallic system towards the metal-to-insulator tran-

sition, whereby the charge carrier concentration is dramatically reduced.

The structure of $M_2Pd_{14+x}B_{5-y}$ with $M = Th, La, Ce, Pr, Nd, Sm, Eu$ and Gd was determined by means of X-ray single crystal data for $Nd_2Pd_{14}B_5$ and $Th_2Pd_{14}B_5$ (tetragonal unit cell and space group $I4_1/AMD$, No. 141), and was found to be closely related to the structure type of $Sc_4Ni_{29}Si_{10}$. The electrical resistivity of $M_2Pd_{14+x}B_{5-y}$, in general, is characterized by small RRR (residual resistivity ratio) values originated by defects, inherent to the present crystal structure. Studies at low temperatures clearly indicate long range magnetic order in $Gd_2Pd_{14}B_5$ below 6 K. Heat capacity measurements evidence that the compounds based on Ce, Nd and Sm order magnetically below 2 K, while the Pr compound seems not to exhibit a magnetically ordered state, at least down to 400 mK, as a consequence of crystal electric field (CEF) effects. The total angular momentum $J = 4$ of the Pr ion in the context of CEF effects of the tetragonal crystal structure of $Pr_2Pd_{14}B_5$ can create a non-magnetic ground state due to singlet formation or due to the presence of a non-magnetic doublet.

Contents

Introduction	10
1 Theoretical Concepts	15
1.1 Electrical resistivity	15
1.2 Thermal conductivity	16
1.3 Thermopower (Seebeck Coefficient)	19
1.4 Specific heat of solids	21
1.5 Some aspects of the BCS theory	24
1.6 Some concepts of the Ginzburg-Landau Abrikosov-Gor'kov Theory	25
1.7 The thermodynamic critical field H_c	29
1.8 The critical magnetic field H_{c2}	29
2 Experimental	31
2.1 Sample preparation	31
2.1.1 Ce–Pt–Si	31
2.1.2 Clathrate Ba-X-Ge Systems (X=Pd, Cd, Zn)	31
2.1.3 Clathrate I Systems $\text{Ba}_8\{\text{Pd}, \text{Pd}\}_x\text{Si}_{46-x}$	32
2.1.4 $\text{RE}_2\text{Pd}_{14+x}\text{B}_{5-y}$	32
2.2 Physical and chemical investigations	33
2.2.1 Structure analysis	33
2.2.2 Electrical resistivity measurements	33
2.2.3 Thermopower measurements	34
2.2.4 Thermal conductivity measurements	34
2.2.5 Specific heat measurements	35
3 Structural chemistry of ternary Ce–Pt–Si system	36
3.1 Introduction	36
3.2 Binary systems	37
3.3 Ternary systems	38
3.4 Phase relations; the Isothermal Section Ce-Pt-Si at 800°C	39
3.5 Determination of Crystal structures new ternary silicide	42

3.5.1	The crystal structure of τ_{18} -Ce ₅ (Pt _{0.12} Si _{0.88}) ₄ with Sm ₅ Ge ₄ -type	42
3.5.2	The crystal structure of τ_3 - Ce ₂ Pt ₇ Si ₄	43
3.5.3	The crystal structure of τ_{10} - CePtSi ₂	45
3.5.4	Rietveld refinement of Pt ₃ Si	46
3.5.5	Rietveld refinement of τ_{16} - Ce ₃ Pt ₅ Si	46
3.5.6	Rietveld refinement of τ_{17} - Ce ₃ PtSi ₃	47
4	Ge-based skutterudites: {Sr, Ba, Eu, Th, U}Pt₄Ge₁₂; crystal structure and physical properties	50
4.1	{Sr,Ba,Eu,Th,U}Pt ₄ Ge ₁₂ System	50
4.1.1	Crystal structure	50
4.1.2	Lattice dynamics of {Sr, Ba, Eu}Pt ₄ Ge ₁₂	53
4.1.3	Physical Properties; Electrical resistivity	55
4.1.4	Specific heat and phonon density of states	59
4.1.5	Phonon specific heat	62
4.1.6	Superconducting and normal state	65
4.1.7	Magnetic properties	77
4.1.8	Seebeck coefficient	79
4.1.9	Electronic structure	79
4.2	Bulk properties of EuPt ₄ Ge ₁₂	82
4.2.1	Electrical resistivity of EuPt ₄ Ge ₁₂	83
4.2.2	Magnetic properties of EuPt ₄ Ge ₁₂	84
4.2.3	Density of states DOS of EuPt ₄ Ge ₁₂	85
4.2.4	Heat capacity of EuPt ₄ Ge ₁₂	87
5	Clathrate Ba-X-Ge Systems (X=Cd, Pd, Zn)	89
5.1	Ba-Cd-Ge Clathrate System; crystal structure and physical properties	89
5.1.1	Crystal Chemistry of $Ba_8Cd_xGe_{43-5x/8}\square_{3-3x/8}$	89
5.1.2	Physical Properties; Heat Capacity	91
5.1.3	Electrical resistivity	93
5.1.4	Thermal conductivity	95
5.1.5	Thermopower	101
5.2	Ba-Pd-Ge Clathrate System	102
5.2.1	Heat Capacity	102
5.2.2	Electrical resistivity	105
5.2.3	Thermal conductivity	105
5.2.4	Thermopower	108
5.3	Ba-Zn-Ge Clathrate System	110
5.3.1	Heat Capacity	110
5.3.2	Electrical resistivity	111
5.3.3	Thermal conductivity	113

5.3.4	Thermopower	118
5.4	$\text{Ba}_8\{\text{Pd}, \text{Pd}\}_x\text{Si}_{46-x}$ Clathrate I systems; crystal structure and physical properties	119
5.4.1	Crystal chemistry of $\text{Ba}_8\text{Pd}_x\text{Si}_{46-x}$ and $\text{Ba}_8\text{Pt}_x\text{Si}_{46-x}$	119
5.4.2	Physical Properties; Electrical Resistivity	120
5.4.3	Thermal conductivity of $\text{Ba}_8(\text{Pd}, \text{Pt})_x\text{Si}_{46-x}$	122
5.4.4	Thermopower	129
6	Non-centrosymmetric BCS superconductor BaPtSi_3	131
6.1	Introduction	131
6.2	Crystallographic details	131
6.3	Electrical resistivity of BaPt_xSi_y	132
6.4	Low-temperature specific heat and phonon specific heat of BaPt_xSi_y	134
6.5	Determination superconducting and normal state properties .	136
7	Structure and Physical Properties of $M_2\text{Pd}_{14+x}\text{B}_{5-y}$, M= Th, Ce, Pr, Nd, Sm, Eu, Gd	141
7.1	Introduction	141
7.2	Crystal structures of $\{\text{Nd}, \text{Th}\}_2\text{Pd}_{14.9}\text{B}_{4.9}$	141
7.3	Isotypic compounds $M_2\text{Pd}_{14}\text{B}_5$	144
7.4	Electrical resistivity	146
7.5	Magnetoresistance	148
7.6	Specific heat	149
7.7	Magnetic properties	153
Summary		158
A User defined functions		162
A.1	Electrical resistivity	162
A.1.1	Woodard and Cody model	162
A.1.2	parallel resistor model	163
A.1.3	Ferromagnetic case	164
A.1.4	Antiferromagnetic case	164
A.2	Phonon specific heat	165
A.2.1	spin fluctuation systems	166
A.3	Determination of some SC- and Normal-state parameters . . .	167
A.3.1	Determination of the upper critical field of dirty limit type II SC in term WHH model.	169
Bibliography		171
List of Publications		179

Introduction

Since the discovery of superconductivity in CeCu_2Si_2 by Steglich et al. (1980) [1] with high-effective-mass electrons m^* , ($m^* \sim 200m_e$, where m_e is the mass of a free electron), the search for characterization of such *heavy fermion* systems, originating from strong electron-electron correlations, has been a rapidly growing field of study. The heavy fermion (HF) systems [2, 3, 4, 5, 6] known to date include compounds with a variety of ground states, e.g. magnetically ordered compounds such as $\text{Ce}_3\text{Cu}_4\text{Sn}_4$ [7] and $\text{Ce}_2\text{Ni}_3\text{Ge}_5$ [8], superconductivity (CeCu_2Si_2 , UBe_{13} , UPt_3)[9], coexistence of magnetic ordering and superconductivity compounds (UPd_2Al_3 , CeCu_2Si_2)[10], or (CePt_3Si) [11, 12, 13, 14, 15], insulating materials [16, 17] (UPtSn , SmB_6), non-Fermi liquid materials ($\text{U}_2\text{Pt}_2\text{In}$, $\text{CeCu}_{6-x}\text{Ag}_x$)[18, 19]. Besides the fact, that many compounds from the Ce-Pt-Si system have shown interesting electrical and/or magnetic properties such as heavy-fermion behavior in CePtSi [20, 21, 22, 23, 24] and/or Kondo-lattice behaviour in CePtSi_2 [25, 26, 27] and CePt_2Si_2 [28, 29, 30, 31, 32], the recent discovery of CePt_3Si (CePt_3B type) as the first heavy fermion superconductor without a center of symmetry has triggered widespread research activities to search for novel superconducting states in related ternary or quaternary alloy systems [15, 33]. To gain more insight into general physical and chemical properties of such compounds, our studies were extended to the investigation of phase relations in the isothermal section at 800°C which is the subject of the first part of the present work. In fact, these f-electron materials typically have, in comparison to normal metals, enormous electronic specific heat values (100-1500 mJ/mol K²), large values of the low-temperature magnetic susceptibility χ , frequently a maximum in the electrical resistivity at low temperatures, as well as unusual temperature dependencies of the specific heat below about 10 K. In this field, valence instabilities, [6, 34, 35] and the Kondo effect in particular also have received extensive interest [5, 36, 37]. The physical properties of such systems are very different from the behavior of normal metals and compounds, and can be traced back to the presence of semi-filled *f* electron shells and their interaction with conduction electrons. Usually, electrons in fully occupied shells make no contribution to metallic conduction and magnetic properties [38, 39].

In the search for novel, promising thermoelectric materials, skutterudites are prospective candidates for achieving figures of merit above unity. High power factors $S^2\sigma$ and the realistic prospect of a significant reduction of the lattice thermal conductivity have attracted great attention. Due to the fact that the skutterudite structure offers interesting possibilities to change both the electronic and lattice properties, many research groups worldwide now focus their efforts on optimizing these materials.

The name "skutterudite" derives from a naturally occurring mineral, CoAs_3 , first found and mined extensively in a small village in Norway called Skutterud. The crystal structure was firstly identified by Oftedal in 1928 [40]. Already in the mid-1950s researchers in the Soviet Union discovered skutterudites in their search for thermoelectric materials. But binary skutterudites, at that time the only known form, possessed thermal conductivity values too high in order to achieve high figures of merit. In 1977 Jeitschko et al.[41], however, found that the large voids of the CoAs_3 -structure can be filled with atoms of the lanthanoid group. As firstly predicted by Slack et al. in 1994, atoms placed in the voids of these compounds substantially reduce the thermal conductivity by introducing phonon scattering centers [42]. Until then a large number of skutterudites crystallizing in the filled $\text{LaFe}_4\text{P}_{12}$ -structure have been synthesised. Figures of merit, already above unity were found for temperatures around 600°C. Besides their thermoelectric potential, rare earth filled skutterudites exhibit a large variety of interesting ground state properties. Among them are superconductivity, metal-insulator transitions, magnetic order, heavy fermion behaviour or structural phase transitions.

The state of the art on the chemistry and physics of skutterudites has been reviewed by Uher [43] and Nolas [44]. The filled skutterudite structure is named after the first synthesized filled skutterudite, $\text{LaFe}_4\text{P}_{12}$. Compounds crystallizing in this structure are represented by the general formula EpT_4X_{12} , where Ep stands for the electropositive filler element that may be an alkaline earth, a lanthanide or an actinide. Recent investigations showed that even Tl [45] and under special conditions also Y, Hf, Pb, Ge and Sn [46, 47, 48] are able to occupy the $2a$ position of the $\text{LaFe}_4\text{P}_{12}$ -type structure. A high pressure preparation technique allows to prepare even $Ep\text{Fe}_4\text{P}_{12}$ compounds with the heavy lanthanides, $Ep = \text{Gd}, \text{Tb}, \text{Dy}, \text{Ho}, \text{Er}, \text{Tm}, \text{Yb}$ and Lu, as filler elements [49]. A detailed discussion of the role of the filler atoms (Ba, Eu or alkaline earth atoms) in the skutterudite structure is given in chapter 4. The filler atom on the $2a$ site is sixfold coordinated by X -atoms, thereby enclosed in an irregular dodecahedral (12 fold coordinated) cage. Rather large bonding distances between the electropositive filler element and the X -atoms give rise to large thermal, or so called atomic displacement parameters (ADP). It appears that the guest ions "rattle" in their oversized cages, providing soft phonon modes to the total phonon spectrum. The dynamic disorder caused

by the filler elements manifests itself in a strong reduction of the lattice thermal conductivity. In 1999 Sales et al. [50] drew attention to the fact that the ADPs could be used to estimate the lattice thermal conductivity of solids. In the case of skutterudites the authors showed that the room temperature thermal conductivities estimated using isotropic ADPs are in good agreement with experimental data. For recent reviews regarding the superconducting properties of these classes of materials see Ref. [51, 52, 53]. The simple structure, however, acts as a prototype for a large class of compounds including binary as well as ternary and higher order representatives. Building blocks in the framework are 8 tilted octahedra per unit cell enclosing two icosahedral cages. Each of the octahedra is centered by a transition metal atom like Co or its homologues (Rh, Ir). Motivated by the known manifold of interesting physical properties among skutterudites, we searched for ternary and/or higher order compounds exploiting the combination of (i) a high density of d -states of a platinum group metal at the Fermi level with (ii) a rigid framework of rather covalently four-bonded atoms such as Si and/or Ge. Thereby a novel family of Ge based skutterudites, MPt_4Ge_{12} ($M = Sr, Ba, BaCa, Eu, Th, U$) has been identified [54, 55, 56]. It was shown that the superconducting transition in these series (about 5 K) is ascribed to intrinsic features of the Pt-Ge framework, where Ge- p states dominate the electronic structure at the Fermi energy.

As the new class of Ge-based skutterudites was found to extend to 4f-electron systems $\{La, Ce, Pr, Nd\}Pt_4Ge_{12}$ [58], the aim of the present work is a study of the stability and the characterization of bulk properties by means of resistivity, magnetization, specific heat measurements and band structure calculations for $\{Sr, Ba, BaCa, Eu\}Pt_4Ge_{12}$ and actinoid compounds $\{Th, U\}Pt_4Ge_{12}$ [59]. For most compounds in this study, the low temperature behavior is dominated by the appearance of superconductivity around 5 K. While, in general, Th-based systems are in a nonmagnetic 4^+ state, (electronic configuration $5f^06s^2p^2$), thus behaving like simple systems, the ground state of U is dominated by the partial occupation of the $5f$ shell giving rise to long-range magnetic order if Stoner criterion is fulfilled [57]. In the opposite case spin fluctuations may be provoked.

In chapter 5 of this study we focus on novel thermoelectric materials called clathrate. "Clathrate" derives from Latin "clathratus", "furnished by a lattice". Wells et al. [60] defined clathrate materials as inclusion complexes, in which particles of one substance are completely enclosed in cavities formed by the crystal lattice or present in large molecules of another substance, i.e., the crystal takes in foreign molecules during growth, that cannot escape until the crystal is decomposed. Davy [61] first mentioned the formation of clathrates on the basis of crystalline water complexes with inclusion molecules such as Cl_2 - so-called gas hydrates or ice clathrates, since gas molecules are entrapped

in crystalline H₂O. Ice clathrates are thus characterized by a hydrogen-bonded framework similar to that of normal ice, but with a more open structure containing different types of cavities enclosing atoms or molecules. The crystal structure was determined by Stackelberg [62], Clausen [63] and Pauling and Marsh [64]; the formation of two types of clathrates was reported, type I and type II. Now, 9 different clathrate structures are known, type I to IX, which were attempted to be classified by Jeffrey [65], yet, types IV, V, VIII lack any representatives among intermetallics.

In order to raise the efficiency of thermoelectric devices Glen Slack in 1995 proposed the PGEC-concept (Phonon Glass and Electron Crystal) for novel thermoelectric materials, which should combine the properties for good electric conductivity of a crystal with poor thermal conductivity of a glass [66]. This idea was realized in compounds with a rigid structure, responsible for the electrical conductivity and by heavy atoms rattling in large cages, thereby ensuring low thermal conductivity via additional scattering of the phonons [67]. The new approach applies to clathrate phases with an extended three-dimensional framework of germanium or silicon atoms, providing huge voids usually filled by electropositive elements, R = Na, K, Cs, Rb, Sr, Ba, Eu. Taking into account that some *d* and *p* elements are necessary for stabilization of the framework structure as well as for a proper adjustment of the electronic structure, the objects of this investigation are the ternary clathrate phases.

The present work continues systematic investigation of ternary clathrate phases Ba₈M_xGe_{46-x-y}□_y and Ba₆M_xGe_{25-x}, where *p* and *d* elements (M = Pd, Cd, Zn, Pt), are used for stabilization of the framework structure as well as for proper adjustment of the electronic density of states at the Fermi-level. Very limited information is hitherto available on the thermoelectric performance of clathrates stabilized by other transitional metals, such as Pd, Zn or Cd [69, 70].

In general, cage-forming clathrates are expected to be located in a region between metals and insulators where large thermopower values are found ($S \sim 1/n$, where S is the Seebeck coefficient and n the charge carrier density). The principal tasks of these investigations are (*i*) to establish the extensions of single-phase clathrate regions in the ternary system Ba-M-Ge, (*ii*) to elucidate details of the crystal structure of clathrate type I, and (*iii*) to investigate the physical properties of these ternary clathrates.

Another part of this study will focus on ternary silicon-based clathrate phases in combinations with Ba and M = Pd, Pt. Although most (Si, Ge)-based clathrates have been detected by Cordier and Woll [68, 71, 72] hitherto little information is available on the formation and thermoelectric performance of Si-based clathrates Ba₈M_xSi_{46-x-y}□_y (M = Pd, Pt). Therefore the present research work was designed to elucidate formation, crystal structure and physical properties of these materials as well. Theoretical considerations

of thermoelectricity as well as of transport, magnetic and thermodynamic properties of solids are presented within chapter 1. In order to account for the large variety of phenomena expected within these classes of materials, various measurements were carried out; the techniques employed together with aspects of sample preparation are shortly outlined in chapter 2. Each chapter provides a detailed summary of literature already available and structural features of each class of intermetallic compounds investigated in this thesis followed by analyses and interpretation of the experimental results obtained.

Chapter 1

Theoretical Concepts

1.1 Electrical resistivity

The electrical resistivity of metals or intermetallic compounds is determined by the number and mobility of charge carriers. In the Drude model [73], the current density j is expressed as $j = (ne^2\tau/m)E$, where $E = \hbar^2k^2/2m^*$. Hence, the resistivity ρ is expressed as

$$\rho = \frac{m^*}{ne^2\tau}, \quad (1.1)$$

here m^* is the effective electron mass, $|e|$ electron charge, n is the charge density, and τ is the relaxation time for scattering processes. Electrons moving through a metallic conductor are scattered not only by phonons but also by lattice defects, impurity atoms, and other imperfections in an otherwise perfect lattice. These impurities produce a temperature-independent contribution that places an upper limit on the overall electrical conductivity of the metal. In a first approximation both scattering processes can be considered as independent from each other (*Matthiessens's rule*). The resulting relaxation time follows then from

$$\frac{1}{\tau} = \frac{1}{\tau_0} + \frac{1}{\tau_{ph}}. \quad (1.2)$$

τ_0 and τ_{ph} are the respective relaxation times for impurity- and phonon scattering. The relaxation time τ determines the magnitude and temperature dependence of the electrical resistivity. According to *Matthiessen's rule*, it follows

$$\rho(T) = \rho_0 + \rho_{ph}(T). \quad (1.3)$$

ρ_0 is equal to the resistivity of the alloy at the absolute zero temperature and its magnitude is determined by the concentration of lattice defects and other static impurities and errors. ρ_{ph} denotes to the electron-phonon scattering. For the temperature-dependent part of resistivity, further scatter-

ing mechanisms should be considered; one is the electron-electron scattering which always happens between electrons that take part in conduction, and with energies near the Fermi energy, $E_F = (\hbar k_F)^2/2m$ [73, 39, 74]. In terms of scattering theory, the contribution to the total resistivity from the electron-electron scattering is given by $\rho \propto T^2$. But this contribution is often completely overshadowed at elevated temperatures by other scattering mechanisms, like scattering from thermally excited lattice vibrations. Using the linearized Boltzmann equation with the variational method based on the Debye model the *Bloch-Grüneisen* expression [75] obtains for electron-phonon scattering resistivity ρ_{ph}

$$\rho_{ph}(T) = c\theta_D \left(\frac{T}{\theta_D} \right)^5 \int_0^{\theta_D/T} \frac{z^5 dz}{(e^z - 1)(1 - e^{-z})}, \quad (1.4)$$

with $z = \frac{\hbar\omega}{k_B T}$, θ_D is the Debye temperature and c denotes a temperature independent constant, which is proportional to the electron-phonon interaction strength and contains the ionic mass, the Fermi velocity, etc. U-processes decay exponentially at low temperature. At sufficiently low temperature, electron-phonon scattering is almost elastic [76, 77] and the scattering probability reaches a T^5 dependence so that $\rho_{ph} \propto T^5$ [78]. A further resistivity term $\rho_{mag}(T)$ has to be considered in magnetic materials and the resistivity can be written in the form of

$$\rho(T) = \rho_0 + \rho_{ph}(T) + \rho_{mag}(T) \quad (1.5)$$

In a localized picture and for the paramagnetic temperature region $T > T_{ord}$, where the spins are independently from each other, ρ_{mag} is given by

$$\rho_{mag}(T) = \frac{3\pi N m^*}{2\hbar e^2 E_F} |J|^2 (g - 1)^2 j(j + 1) \quad (1.6)$$

with J the exchange interaction constant between the conduction electron spin and the spin total angular momentum of the magnetic ion, j is the total angular momentum of the magnetic ion and $(g - 1)^2 j(j + 1)$ is the deGennes factor. g is the Lande-factor.

1.2 Thermal conductivity

Thermal conductivity is a fundamental and important physical parameters. The study of the underlying physics of the heat-conduction process has provided a deep and detailed understanding of the nature of lattice vibrations in solids. Heat conduction is usually quantified in terms of the thermal conductivity coefficient λ , which is defined through the macroscopic expression for the rate of heat energy flow per unit area \vec{Q} normal to the gradient ∇T

$$\vec{Q} = -\lambda \nabla T. \quad (1.7)$$

Within classical thermodynamics,

$$\lambda = \left(\frac{1}{3}\right) n c_v v l, \quad (1.8)$$

where $l = v\tau$ is the particle mean free path, v average particle velocity, τ is the relaxation time and c_v is the heat capacity. The thermal conductivity of solids, in general, is maintained by the heat conduction by electrons λ_e and by lattice vibrations λ_{ph}

$$\lambda_{tot} = \lambda_e + \lambda_{ph}. \quad (1.9)$$

The Wiedemann-Franz law compares the electronic thermal conductivity λ_e with $1/\sigma$ as given in equations 1.1 and 1.8 [79] revealing

$$\lambda_e = L_0 \sigma T, \quad (1.10)$$

with the *Lorenz number* $L_0 = (\pi^2/3)(k_B e)^2 = 2.45 \times 10^{-8} \text{W}\Omega\text{K}^{-2}$. This shows that all metals have the same electronic thermal conductivity to electrical conductivity ratio. In the scope of the free electron gas model, $v_e = v_F$ and $c_e = \pi^2 k_B^2 T / m v_F^2$, the electronic thermal conductivity λ_e can be expressed as

$$\lambda_e = (1/3) n c_e v_e l_e, \quad (1.11)$$

where c_e is the electronic heat capacity per electron, v_e the electron velocity, n the number of conduction electrons per volume and l_e the electron mean free path. According to the *Matthiessen-rule*, the electronic thermal resistivity W_e of simple metals can be written as:

$$W_e \equiv \frac{1}{\lambda_e} = W_{e,0} + W_{e,ph}. \quad (1.12)$$

Here, $W_{e,0}$ is the electronic thermal resistivity, caused by electron scattering due to impurities and defects and $W_{e,ph}$ is the lattice thermal resistivity, caused by electron scattering due to thermally excited phonons. Assuming that all defects and imperfections scatter electrons elastically, scattering processes of conduction electrons with impurities can be described as $W_{e,0} = \rho_0 / L_0 T \propto \alpha / T$, where α is a material dependent constant. The thermal resistivity $W_{e,ph}$ can be expressed by the *Wilson equation*[80]:

$$W_{e,ph} = \frac{A}{L_0 T} \left(\frac{T}{\theta_D}\right)^5 J_5(\theta_D/T) \left\{ 1 + \frac{3}{\pi^2} \left(\frac{k_F}{q_D}\right)^2 \left(\frac{\theta_D}{T}\right)^2 - \frac{1}{2\pi^2} \frac{J_7(\theta_D/T)}{J_5(\theta_D/T)} \right\}. \quad (1.13)$$

k_F is the wave vector at the Fermi surface, q_D is the phonon Debye wave vector and A is material constant, depending on the strength of the electron-phonon interaction, Debye temperature, the effective mass of electron, number of unit

cells per unit volume, Fermi velocity and on the electron wave number at the Fermi surface. The Debye integrals have the form

$$J_n(x) = \int_0^x \frac{z^n dz}{(e^z - 1)(1 - e^{-z})}, \quad (1.14)$$

with $z = \frac{\theta_D}{T}$. At high temperatures a series expansion of Eqn. 1.13 yields

$$W_{e,ph}(T) \approx \frac{A}{L_0 \theta_D} = \text{const.} \quad \text{for} \quad T \gg \theta_D \quad (1.15)$$

while at low temperatures

$$W_{e,ph}(T) \approx \text{const.} \left(\frac{124.4}{\theta_D} \right)^3 T^2 \quad \text{for} \quad T \ll \theta_D. \quad (1.16)$$

Lattice thermal conductivity is the dominant thermal conduction mechanism in non-metallic systems. λ_{ph} is constrained by scattering processes of the phonons with different scattering centers. A quantitative description of lattice thermal conductivity is possible in terms of Callaway's theory [81]. The temperature dependence of λ_{ph} follows from Eqn. 1.8. According to Callaway [81, 82, 83], this transforms for the heat carrying lattice vibrations to

$$\lambda_{ph} = \frac{k_B}{2\pi^2 v_s} \left(\frac{k_B}{\hbar} \right)^3 T^3 \int_0^{\theta_D/T} \frac{\tau_c x^4 e^x}{(e^x - 1)^2} dx + I_2, \quad (1.17)$$

with the velocity of sound $v_s = \frac{k_B \theta_D}{\hbar (6\pi^2 n)^{1/3}}$ (in the Debye model) and $x = \hbar\omega/k_B T$, where n is the number of atoms per unit volume and ω the phonon frequency. The second integral in 1.17 can be expressed as

$$I_2 = \left[\int_0^{\theta_D/T} \frac{\tau_c}{\tau_N} \frac{x^4 e^x}{(e^x - 1)^2} dx \right]^2 / \int_0^{\theta_D/T} \frac{1}{\tau_N} \left(1 - \frac{\tau_c}{\tau_N} \right) \frac{x^4 e^x}{(e^x - 1)^2} dx, \quad (1.18)$$

where τ_c^{-1} is the sum of the reciprocal relaxation times for point defect scattering (Eqn. 1.19) and τ_N^{-1} is relaxation time for the normal 3-phonon scattering processes. The various processes that scatter phonons are assumed to be independent of one another and to be described by individual scattering rates τ_i^{-1} such that:

$$\tau_c^{-1} = \tau_N^{-1} + \tau_D^{-1} + \tau_U^{-1} + \tau_B^{-1} + \tau_E^{-1}, \quad (1.19)$$

where τ_N^{-1} stands for normal three phonon scattering processes, τ_D , τ_U , τ_B and τ_E denote point defect scattering, Umklapp processes, boundary scattering and scattering of phonons by electrons. In general, the various scattering processes will depend on both temperature and phonon frequency. If all

phonon branches are scattered by resistive processes, then $\tau_N \gg \tau_U$; as a consequence, the first integral in Eqn. 1.17 predominantly contributes to the observed thermal conductivity [84]. The N -processes are, in general, important only at low temperatures and in nearly perfect, low-anharmonicity crystals.

1.3 Thermopower (Seebeck Coefficient)

A discovery by T. J. Seebeck almost 180 years ago, opened the way for modern thermoelectricity. In 1823, Seebeck [85] found that an electric current flows in a closed circuit of two dissimilar metals when one of the two junction is heated with respect to the other. In such a thermocouple circuit the current continues to flow as long as two junction are at different temperatures. The magnitude and direction of the current is a function of the temperature difference between the junctions and of the thermal properties of the metals used in the circuit. This phenomenon is known as the Seebeck Effect. Ohmic and Seebeck currents are fundamentally different in nature. When a metallic bar is subjected to a voltage (V) or a temperature (T) difference, electric current is generated. For small voltage and temperature gradients we may assume a linear relation between the electric current density j and the gradients:

$$j = \sigma E - A \nabla T \quad (1.20)$$

where σ is the electrical conductivity. In an open circuit condition no electric current flows, thus

$$\sigma E_s - A \nabla T = 0, \quad (1.21)$$

where E_s is the field generated by the thermal electromotive forces (emf). The *Seebeck coefficient*, also called the thermopower, S , is defined through

$$E = S \nabla T, \quad S \equiv A/\sigma. \quad (1.22)$$

The conductivity σ is positive but the Seebeck coefficient S can be positive or negative. Figure 1.1 represents an electric circuit consisting of the metal A and B, which are joined with their junctions and maintained at temperatures T_1 and $T_2 = T_1 + \Delta T$. The open ends are kept at a temperature T_0 . An open-circuit voltage ΔV is generated if $T_1 \neq T_2$. For homogeneous materials, this voltage is independent of the precise details of the temperature gradient and of T_0 . Only the difference $T_1 - T_2$ is important. The observed voltage

$$\Delta V_{AB} = \int_{T_1}^{T_2} [S_A(T) + S_B(T)] dT, \quad (1.23)$$

depends on the Seebeck coefficient of material A and B.

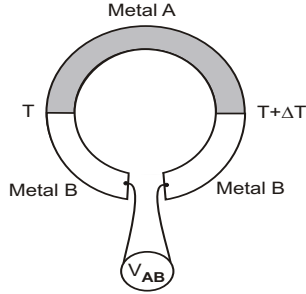


Figure 1.1: Thermoelectric circuit.

Assuming a one-band system, the coefficient of the thermoelectric power follows from

$$S = \frac{1}{eT} \frac{\int (E - E_F) j_x(E) dE}{\int j_x(E) dE}. \quad (1.24)$$

The electrical current associated with electrons of energy lying between E and $(E + dE)$ is $j_x(E)dE$. If we write the current density as $j_x = \sum_i e v_i(x)$ when the electric field is in x-direction, then in the scope of the linearized Boltzmann equation, the current in the relaxation time approximation is given as

$$j_x = \frac{-e^2 \epsilon_x}{4\pi^3 \hbar} \int \int \tau \frac{v_x^2}{v} ds \frac{df_0}{dE} dE. \quad (1.25)$$

Here the first integral is taken over a surface of constant energy and the second integral is performed over all energies. The partial electrical conductivity σ_x can be written as

$$\sigma_x = \frac{e^2}{4\pi^3 \hbar} \int \tau \frac{v_x^2}{v} ds \quad (1.26)$$

where the integration is made over constant energies E in the \vec{k} space.

$$S = \frac{1}{eT} \frac{\int_0^\infty \sigma(E) (E - E_F) \frac{df_0}{dE} dE}{\int_0^\infty \sigma(E) \frac{df_0}{dE} dE}. \quad (1.27)$$

$\sigma(E)$ is the energy dependent electrical conductivity, E_F is the Fermi energy. As equation 1.27 shows, the Seebeck coefficient is correlated to the electrical conductivity and its energy dependence. Thus, $S = 0$ if $\sigma(E)$ is constant over a range of energy $E \in (-k_B T, +k_B T)$ for which $\frac{df_0}{dE} \neq 0$. Equation 1.27 finally leads to the *Mott relation* [86], expressed by

$$S = \frac{\pi^2 k_B^2 T}{3e} \frac{1}{N(E_F)} \frac{\partial N(E)}{\partial E}|_{E=E_F}, \quad (1.28)$$

where the absolute values are depending on the energy derivative of the electronic density of states $N(E)$ right at the Fermi energy. k_B is the Boltzmann constant and e is the electron charge.

Linearity of the diffusion part of the thermopower is then predicted in terms of the free-electron model [87, 88]. For $T > \theta_D$, (θ_D is the Debye temperature) the electron phonon interaction dominates scattering mechanism and the thermopower follows from:

$$S_d(T > \theta_D) = \frac{\pi^2 k_B^2 2m_e}{e\hbar^2 (3n\pi^2)^{2/3}} T, \quad (1.29)$$

where the dominating term is the inverse proportionality of $S(T)$ on the charge carrier concentration n , m_e , the mass of the carriers and e is the respective charge. The subscript d indicates diffusion thermopower being linearly dependent on T .

In the most general case, the total Seebeck coefficient of a metal is the sum of different contributions, the diffusion term S_e originated by the movement of electrons due to a temperature gradient, the phonon-drag term S_{ph} , which represents the electron drag due to phonons and finally S_{mag} , which is caused by the electron drag caused by magnons. The thermoelectric power of a metal is given by different contributions:

$$S = S_e + S_g + S_m. \quad (1.30)$$

Since phonons interact with the electrons, there will be a momentum transfer from the phonon flow to the electron flow causing an additional contribution to the thermopower. This contribution is known as phonon drag S_{ph}

$$S_{ph} \propto \begin{cases} T^3 & T \ll \Theta_D \\ T^{-1} & T \gg \Theta_D \end{cases} \quad (1.31)$$

These interaction processes, in contradiction to the electrical - and the thermal resistivity, cannot be put together according to the *Matthiessen rule* to a certain “total effect”. Instead of it, the so called *Kohler rule* has to be used.

$$S \cdot W = \sum_i S_i \cdot W_i \quad (1.32)$$

where W is the thermal resistivity [89].

1.4 Specific heat of solids

The specific heat is a physical property of solids specifying the capability of a substance to absorb heat. For real solids, like metals, the heat capacity C_p consists of different additive terms:

$$C(T) = C_{el} + C_{ph} + C_{mag} + C_{nuc}. \quad (1.33)$$

Here, C_{el} represents the conduction electron term, C_{ph} is the contribution due to the lattice, C_{mag} is the magnetic contribution in both the ordered and the disordered temperature range, while C_{nuc} is the nuclear contribution, which is of importance just at very low temperatures.

Heat capacity of the conduction electrons in solids: The simplest model for the conduction electrons is the model of *the free electron gas*. The well-known thermodynamic result of this model is the low temperature approximation for the electronic part of the specific heat yielding a linear temperature dependence of

$$C_{el} = \frac{\pi^2}{3} N_A N(E_F) = \gamma T, \quad (1.34)$$

and is directly proportional to the density of states at the Fermi energy. Here N_A is the number of atoms per formula unit, $N(E_F)$ is the density of states at the Fermi energy and γ denote the Sommerfeld coefficient in [J/molK²] and is usually estimated from the linear coefficient of the experimental low temperature specific heat of non-magnetic metals.

Lattice contributions: An expression of the temperature dependence of the lattice contribution to the specific heat is usually based on the approximation that all lattice vibrations are strictly harmonic. Anharmonic effects can be taken into account with a perturbation series [90], but will be neglected in the following discussion. Within the harmonic approximation the 3N vibration modes of the solid consisting of N atoms can be represented by a set of 3N linear harmonic oscillators with the frequencies ν_i ($i=1, \dots, 3N$). The quantum excitations of the oscillators are called *phonons* and can be indexed with their wave vector \vec{q} and the branch index j of the dispersion relation $\omega_{\vec{q},j} = c \cdot \vec{k}$. Their quantum mechanical excitation energy is given by $\hbar\omega_{\vec{q},j}$ and their occupation number $n_{\vec{q},j}$ by the Bose-Einstein factor. The total excitation energy is thus given by

$$E = \sum_{\vec{q},j} \frac{1}{e^{\hbar\omega_{\vec{q},j}/k_B T} - 1} \hbar\omega_{\vec{q},j}. \quad (1.35)$$

In the scope of the Debye model the overall temperature dependency of the phonon part of the specific heat can be expressed as:

$$C_{ph} = 9N_i k_B \left(\frac{T}{\theta_D} \right)^3 \int_0^{\theta_D/T} \frac{e^x x^4}{(e^x - 1)^2} dx \quad (1.36)$$

with $x = \hbar\omega/k_B T$. Here θ_D is Debye temperature. For high temperatures, i.e. $T \gg \theta_D$, the phonon contribution of the specific heat becomes independent of temperature following Dulong-Petit's law, i.e. $C_{ph} = 3N_i k_B$; at low temperature a T^3 term follows. The heat capacity of simple metals at low temperatures is then given by

$$C(T) = C_{el}(T) + C_{ph}(T) = \gamma T + \beta T^3. \quad (1.37)$$

The coefficient β corresponds to the low temperature limit of the Debye-temperature Θ_D^{LT} according to

$$\Theta_D^{LT} = \sqrt[3]{\frac{1944 \cdot n}{\beta}}, \quad (1.38)$$

where n is the number of atoms per formula unit.

An attempt was made in order to evaluate the specific heat data of materials using a model proposed by Junod et al. [91, 92], which was successfully applied to a large number of A15-type compounds. If the sum in equation 1.35 is replaced by an integral introducing a phonon density of states, $F(\omega)$, one obtains the harmonic lattice heat capacity $C_{har} \equiv \partial E_{har}/\partial T$ in the general form

$$C_{ph}(T) = R \int_0^\infty F(\omega) \frac{\omega^2 \left(\frac{\omega}{2T}\right)^2}{\sinh^2 \left(\frac{\omega}{2T}\right)} d\omega. \quad (1.39)$$

In order to obtain $C_{ph}(T)$ in [J/mol K], $F(\omega)$ has to be normalized to the number of branches of the dispersion relation ($3n$ for n atoms in one unit cell) and the gas constant, $R = 8.314$ [J/mol K].

The most common assumptions of $F(\omega)$ are $F(\omega)=\delta(\omega)$ and $F(\omega) \propto \omega^2$ up to a cut-off frequency ω_D which corresponds to the well known Einstein and Debye model, respectively. The first approximation, the Einstein model assumes that all lattice atoms are in an equivalent oscillator potential, independent of each other and have therefore one common vibration frequency. The Debye model where the coupling of the oscillators is taken into account leads to $F(\omega) \propto \omega^2$. This approximation corresponds to a continuous medium with a linear dispersion relation $\omega(q) = cq$, where c denotes the velocity of sound. Since the number of atoms N is finite, a cut-off is required. The cut-off is the well-known Debye-frequency ω_D given by the $3N$ possible modes. The low temperature approximation of the Debye-model yields the cubic temperature dependence of C_{ph} already given in equation 1.37. Note that the Einstein frequencies can assume a finite spectral weight.

Magnetic contributions: In the case of magnetic materials a temperature dependent contribution $C_{mag}(T)$ has to be added to the total specific heat. C_{mag} depends sensitively on magnetic order and thermally induced excitations of electrons populating, e.g. certain crystal electric field (CEF) levels. In the scope of the molecular field model and $T < T_{ord}$, $C_{mag}(T)$ can be related to the magnetization M

$$C_{mag}(T) = -\frac{1}{2}\alpha \frac{\partial M^2}{\partial T} \quad (1.40)$$

where α is the molecular field constant. In the presence of crystal field split-

ting the contribution to the specific heat is given by:

$$C_{CEF} = \frac{R}{k_B^2 T^2} \left[\frac{1}{Z} \sum_{i=0}^n E_i^2 e^{-\beta E_i} - \left(\frac{1}{Z} \sum_{i=0}^n E_i e^{-\beta E_i} \right)^2 \right], \quad (1.41)$$

with the partition function $Z = \sum_{i=0}^n e^{-(E_i/k_B T)}$ and the universal gas constant $R=Nk_B=8.314 \text{ J/mol K}$. Eqn. 1.41 represents the so called Schottky formula.

1.5 Some aspects of the BCS theory

The main idea of the BCS (Bardeen, Cooper, Schrieffer) theory is based on the work of B. Cooper [94]. In 1956, Cooper showed that two electrons with an attractive interaction can bind together in the momentum space to form a bound pair. This bound state of two electrons is known today as the Cooper pair. As the criterion for the occurrence of superconductivity, Cooper stated that the attractive interaction between electrons mediated by phonons should overcome the screened Coulomb repulsive interaction between electrons. In 1957, Bardeen, Cooper and Schrieffer [95, 97] showed how to construct a wave function in which the electrons are paired. The wave function which is adjusted to minimize the free energy was used as the basis for a complete microscopic theory of superconductivity in metals.

An attractive interaction between electrons mediated by phonons can lead to a ground state separated from excited states by an energy gap. The critical field, the thermal properties, and most of the electromagnetic properties are consequences of the energy gap. The *penetration depth* and the *coherence length* emerges as natural consequence of the BCS theory. The way in which a superconductor expels from its interior an applied magnetic field with small magnitude (the Meissner effect) is by establishing a persistent super current on its surface which exactly cancels the applied field inside the superconductor. This surface current flows in a very thin layer of thickness λ , which is called the *penetration depth*. In the framework of the Ginzburg-Landau theory, the coherence length ξ_{GL} is the characteristic scale over which variations of the order parameter Ψ occur, for example, in a spatially-varying magnetic field or near a superconductor-normal metal boundary. Thus, the central phenomenon in superconductivity, the Meissner effect, is obtained in a natural way. The criterion for the transition temperature involves the density of states of orbitals $N(0)$ at the Fermi level and the electron lattice interaction V . In the framework of the BCS theory, one can derive an expression for the critical temperature [96]

$$k_B T_c = 1.14 \theta_D \exp \left(-\frac{1}{N(0)V} \right), \quad (1.42)$$

where θ_D is the Debye temperature. Another important BCS result is the ratio of the critical temperature T_c and the energy gap $\Delta(0)$ at $T = 0$, given by

$$\Delta(0)/k_B T_c = 3.528, \quad (1.43)$$

referring to comparable magnitudes [96]. Near the transition temperature T_c , the temperature dependent gap width can be found from the following relation:

$$\Delta(T) \approx 3.2k_B T_c \sqrt{1 - \frac{T}{T_c}}, \quad (1.44)$$

consistent with Landau's theory of second-order phase transitions. The expression for the free-energy of the superconducting state yields an exponential temperature dependence of the electronic specific heat in the superconducting state

$$C_{eS} \cong 8.5\gamma T_c \exp \left[-1.44 \left(\frac{T_c}{T} \right) \right]. \quad (1.45)$$

The BCS theory predicts that the electronic specific heat jumps abruptly at T_c from the normal state value γT_c to the superconducting state value C_{eS} [97]. The height of the specific heat jump is given by

$$\frac{\Delta C}{C_n}(T = T_c) \equiv \frac{C_{eS} - C_n}{C_n}|_{T=T_c} = 1.43. \quad (1.46)$$

Because of the gap in the electronic density of states at $E = E_F$ the specific heat falls exponentially, as the temperature decreases,

$$C_{eS} \propto \exp \left(-\frac{\Delta(T)}{k_B T} \right). \quad (1.47)$$

In the two-fluid model, the exponential temperature dependence means that below T_c , only the normal component transports heat. The Cooper-pair condensate does not contribute to the energy transfer. In the strong electron-phonon coupling regime, i.e. when $2\Delta > 3.52 k_B T_c$, the value of specific-heat jump increases, i.e. $\Delta C/C_n > 1.43$.

1.6 Some concepts of the Ginzburg-Landau Abrikosov-Gor'kov Theory

In 1950, Ginzburg and Landau [98] proposed a new phenomenological theory to explain superconductivity that contained the London theory and could account for a density of superconducting electrons varying in space. It was originally introduced as a phenomenological theory, but later Abrikosov [99] and Gor'kov [100] showed that it can be derived from the microscopic BCS

theory in a reasonable limit. The Ginzburg Landau theory makes many useful and important predictions. Macroscopic and thermodynamic properties of superconductors usually are more easily and more reliably measured than microscopic quantities like e.g. the energy gap Δ or the electron-phonon coupling function $\alpha^2 F(\omega)$.

The fundamental ideas for a basic understanding of the magnetic properties of superconductors (e.g. type II superconductivity) was worked out by Ginzburg, Landau, Abrikosov and Gor'kov, referred to as GLAG theory. Ginzburg and Landau argued that the free energy F of a superconductor near the superconducting transition can be expressed in terms of a complex order parameter ψ . The free energy F can be expanded in a Landau series of the form

$$F_s - F_{n0} = \alpha |\psi|^2 + \frac{\beta}{2} |\psi|^4 + \frac{1}{2m^*} \left| \left(-i\hbar \vec{\nabla} - \mu_0 e^* \vec{\mathbf{A}} \right) \psi \right|^2 + \frac{\mu_0 \mathbf{H}^2}{2} \quad (1.48)$$

where F_n is the free energy in the normal phase, the e and m refers to the superconducting charge carriers and α and β are phenomenological parameters. \mathbf{A} is the electromagnetic vector potential, and \mathbf{H} is the magnetic field. If $\psi = 0$, the free energy density f reduces to the free energy density of the normal state $f_n - f_{n0} = h^2/(8\pi)$ as expected. Here F and H replaced by their densities f and h . As with all Landau theories the difference in free energy between the low temperature and high temperature states is calculated by expanding the order parameter. To fourth order, the free energy in the absence of fields and gradients is

$$F_s - F_{n0} = \alpha |\psi|^2 + \frac{\beta}{2} |\psi|^4. \quad (1.49)$$

This can be interpreted as a Taylor series expansion in $n_s(T) = |\psi|^2$ stopped after the second term. This requires $n_s(T) = |\psi|^2$ to be small, i.e. the system has to be close enough to the transition temperature T_c . With $\beta > 0$, two cases arise:

- **α positive:** The minimum free energy occurs at $|\psi|^2 = 0$, corresponding to the normal state.
- **α negative:** The free energy is minimized when the derivative of Eqn.1.49 with respect to $|\psi|^2$ is cancelled, i.e. when

$$|\psi|^2 = |\psi_\infty|^2 \equiv -\frac{\alpha}{\beta}, \quad (1.50)$$

where the notation ψ_∞ suggests that ψ takes on this value infinitely deep in the superconductor where it is screened from any surface fields or currents. The case $\alpha < 0$ thus stands for the superconducting state of the system.

Therefore, α changes sign at T_c . Substituting 1.50 back into 1.49 and using the definition of the thermodynamical critical field H_c , which it discussed in subsection 1.7, the free energy difference becomes

$$F_n - F_{n0} = -\frac{H_c^2}{8\pi} = -\frac{\alpha^2}{2\beta} \quad (1.51)$$

as expected. Introducing boundary conditions and applying variational principles to minimize the overall free energy, Ginzburg and Landau derived the so-called Ginzburg-Landau equations [96]. From these equations they obtained qualitatively the temperature dependencies of the spatial variation length of the order parameter (Cooper-pair density), ξ_{GL} and the penetration depth of the local magnetic field, λ_{GL} .

Since within the GL theory these two parameters are related to each other via the thermodynamic critical field H_c , they introduced the dimensionless Ginzburg-Landau parameter κ , which is defined as the ratio of the two characteristic lengths, penetration depth λ and coherence length ξ ,

$$\kappa_{GL} \equiv \frac{\lambda}{\xi} = \frac{2\pi\sqrt{2}\mu_0 H_c(T)\lambda_{GL}^2(T)}{\Phi_0} \quad (1.52)$$

where $\Phi_0 = h/2e = 2.07 \times 10^{-15}$ Wb, is the fluxoid quantum. Ginzburg and Landau noted that the surface energy of the interface between superconducting and flux-bearing normal conducting regions is positive for $\kappa \ll 1$ and negative for $\kappa \gg 1$.

Abrikosov's [99] more detailed that magnetic flux penetrating into a type II superconductors will be subdivided to distinct flux lines each carrying a quantum of flux $\Phi_0 = h/2e$. This so-called "mixed state" reduces the diamagnetic energy and therefore superconductivity can persist up to the so-called upper critical field H_{c2} ($> H_c$). The relation of H_{c2} to the thermodynamic critical field H_c is clarified and given by [101]

$$H_{c2} = \frac{\Phi_0}{2\pi\mu_0\xi^2} = \frac{4\pi\lambda^2 H_c^2}{\Phi_0} = \sqrt{2}\kappa H_c \quad (1.53)$$

where ξ is the coherence length and κ is the Ginzburg-Landau parameter. From Eqn. 1.53 it clear that the value $\kappa = 1/\sqrt{2}$ indeed separate the materials for which $H_{c2} > H_c$ (type II superconductors) from those for which $H_{c2} < H_c$ (type I superconductors). It is inherent in the Ginzburg-Landau theory that superconductors may divided in two groups [102] according to the value of the dimensionless Ginzburg-Landau parameter κ ; for type I superconductors;

$$\kappa < 1/\sqrt{2}, \quad H_{c2} < H_c \quad \text{for type I SC} \quad (1.54)$$

the total surface energy of the normal-superconducting boundary is positive and materials exhibits ideal magnetic behavior, but for type II superconductors

$$\kappa > 1/\sqrt{2}, \quad H_{c2} > H_c \quad \text{for type II SC} \quad (1.55)$$

a negative surface energy [103, 104] and quite different magnetic behavior are expected [105].

For the case of $\kappa \gg 1$, Abrikosov derived a relation for the lower critical field H_{c1} given by

$$H_{c1} = \frac{\Phi_0}{4\pi\mu_0\lambda^2(T)} \ln \kappa. \quad (1.56)$$

Equations 1.53 and 1.56 can be used to estimate $\xi(T)$ from specific heat and magnetic measurements.

In 1959 Gor'kov [100] showed that the phenomenological Ginzburg-Landau equations follow from the microscopic BCS theory of superconductivity in the temperature region close to T_c . It terms the microscopic GL theory, Gor'kov analyzed the behaviour of superconducting alloys (i.e. type II superconductors) in a magnetic field near the critical temperature and pointed out the importance of simple material parameter namely the electron mean free path l . The essential length scale determining the results of Gor'kov calculation is of the order of l if $l \ll \xi_0$ (dirty limit) and of the order of ξ_0 if $l \gg \xi_0$ (clean limit). The BCS coherence length ξ_0 is given by

$$\xi_0 = \frac{\hbar v_F}{\pi\Delta(0)} = 0.18 \frac{\hbar v_F}{k_B T_c} \quad (1.57)$$

where v_F denotes the Fermi velocity and $\Delta(0)$ the gap in the one particle excitation spectrum at zero temperature. Since in any calculation of the magnetic properties of type II superconductors one has to distinguish between pure or clean-limit superconductors ($l \gg \xi_0$) and impure or dirty-limit superconductors ($l \ll \xi_0$), Gor'kov introduced the so-called G-L impurity parameter α^* defined as

$$\alpha^* \equiv 0.882 \frac{\xi_0}{l} = \frac{\hbar v_F}{2\pi l k_B T_c} \quad (1.58)$$

and derived the following expressions for κ close to T_c :

$$\kappa = 0.96 \frac{\lambda_L(0)}{\xi_0} \quad \text{for clean SC if, } \alpha^* \ll 1, \quad l \gg \xi_0 \quad (1.59)$$

$$\kappa = 0.725 \frac{\lambda_L(0)}{l} \quad \text{for dirty SC if, } \alpha^* \gg 1, \quad l \ll \xi_0 \quad (1.60)$$

where $\lambda_L(0) = (2\mu_0 e^2 v_f^2 N(0)/3)^{-1/2}$ is the London penetration depth at the temperature of absolute zero. Equation 1.60 shows that κ of a superconductor is increased if the electron mean free path is shortened by a high impurity concentration, which implies an increase of the electrical resistance of superconductors in the normal state region.

1.7 The thermodynamic critical field H_c

Meissner and Ochsenfeld [106] investigated the magnetic properties of elementary superconductors and revealed the fundamental thermodynamic property of the superconducting state that perfect diamagnetism persists up to a critical field $H_{crit.}(T)$. Superconductivity vanishes in external magnetic fields larger than $H_{crit.}$, because the static magnetic energy, $\mu H^2/2$, exceeds the condensation energy of the superconducting state, $F_n - F_s$. So-called type I superconductors are characterized by $M = -H$ if $H \leq H_{crit.}$ and $M=0$. The thermodynamic critical field is calculated from the free energy difference between the superconducting and normal state:

$$\Delta F(T) = F_n(T) - F_s(T) = \mu H_c^2(T)/2 = \int_{T_c}^T \int_{T_c}^{T'} \frac{(C_s - C_n)}{T''} dT'' dT'. \quad (1.61)$$

Almost all elementary superconductors belong to this group, but the much larger group of superconducting alloys and compounds show a more complex magnetic behavior, because their magnetic energy is lowered by the formation of the mixed state.

1.8 The critical magnetic field H_{c2}

From the critical field slopes near T_c several important superconducting and normal-state parameters can be estimated. These estimates are based on the evaluation of the Ginzburg-Landau (GL) parameters from the BCS-Gor'kov equations near T_c [107, 109, 110]. The main link between superconducting and normal-state properties is given by

$$-\frac{dH_{c2}}{dT}|_{T_c} = \frac{24\pi^2}{7\zeta(3)} \frac{k_B^2 c}{\hbar e} \frac{T_c}{v_F^2} \chi^{-1}(\lambda_{tr}) = \frac{\hbar c}{2e} \frac{1}{\xi_{GL}^2(0)} \frac{1}{T_c} \quad (1.62)$$

where $\xi_{GL}(0)$ is the zero-temperature Ginzburg-Landau (GL) coherence length, T_c transition temperature, $\zeta(3)=1.20205, \dots$, is the Riemann's ζ function and transport scattering length given by

$$\lambda_{tr} = \hbar v_F / 2\pi k_B T_c l_{tr} = 0.9 \xi_0 / l_{tr}, \quad (1.63)$$

with the mean free path l_{tr} and Fermi velocity v_F . Here $\chi(\lambda_{tr})$ is the Gor'kov function, also expressed as $\chi(\lambda_{tr}) = R(\lambda_{tr})/(1+\lambda_{tr})$, where $R(\lambda_{tr})$ is always of order unity [$R(0)=1$ and $R(\infty)=1.17$] [107, 109, 110]. The slope of the upper critical field $(dH_{c2}/dT)_{T_c}$ can be rewritten as [111]

$$H'_{c2} = -\frac{dH_{c2}}{dT}|_{T_c} = \frac{\eta_{H_{c2}}(T_c)}{R(\lambda_{tr})} \left[\left(\frac{24\pi^2}{7\zeta(3)} \frac{k_B^2 c}{\hbar e} \right) \frac{T_c}{v_F^2} + \left(\frac{12\pi}{7\zeta(3)} \frac{k_B c}{e} \right) \frac{1}{v_F l_{tr}} \right] \quad (1.64)$$

$$= \eta_{H_{c2}}(T_c) \frac{R(\infty)}{R(\lambda_{tr})} \left((2.17 \cdot 10^8) \frac{T_c}{v_F^2} + (3.29 \cdot 10^{-4}) \frac{1}{v_F l_{tr}} \right), \quad (1.65)$$

here, $\eta_{H_{c2}}(T_c)$ is the ratio of the strong-coupled magnetic pair-breaking parameter and can be estimated if the electron-phonon spectral function $\alpha^2 F(\omega)$ is known [112, 113, 114, 115]. Some simplifications yields:

- $R(l) = 1$; dirty limit ($l = 0$)
- $R(l) = 1.17$; clean limit ($l = \infty$)

with $R(l) = \eta_{H_{c2}}(T_c) R(\infty) / R(\lambda_{tr})$. In the clean limit only the first term contributes significantly to H'_{c2} . H'_{c2} increases with decreasing Fermi velocity v_F . The second term of equation 1.64 increases with decreasing values of the mean free path l and determines therefore H'_{c2} in the *dirty limit*. If all parameters and coefficients are taken together in the case of the dirty limit with spherical Fermi surface we have [89]:

$$H'_{c2}(\text{dirty}) = \left((4490) \frac{T m^2 K}{\Omega J} \right) \gamma \rho_0, \quad (1.66)$$

with γ the Sommerfeld value of the electronic specific heat in [$\text{J/m}^3\text{K}^2$] and ρ_0 ... the residual resistivity in [$\Omega \text{ cm}$]. The Fermi velocity v_F can be calculated according to Orlando et al. [111]:

$$\langle v_F \rangle = k_B^2 \hbar^{-1} (\pi^4/3)^{1/3} (n^{2/3} S/S_F) \gamma^{-1} = 5.77 \times 10^{-5} (n^{2/3} S_s/S_F) \gamma^{-1}, \quad (1.67)$$

where S_s is the Fermi-surface area, on which Cooper-pairs are formed; S_s/S_F is the ratio of the free Fermi-surface area S to that of a free electron gas of density n and S_F is given by

$$S_F = 4\pi (3\pi^2 n)^{2/3}. \quad (1.68)$$

The effective Fermi surface S_s can be calculated as shown by Rauchschwalbe [116]

$$S_s = \left(\frac{1.18 \times 10^{35} \cdot \gamma^2 T_c}{H'_{c2}/R(l) - (4490\gamma\rho_0)} \right)^{1/2}. \quad (1.69)$$

Combining S_s and ρ_0 derives an expression for the free path l_{tr}

$$l_{tr} = 9 \times 10^{11} \hbar (3\pi^2)^{1/3} (e^2 S \rho_n)^{-1} = 1.27 \times 10^4 [\rho_n (\Omega \text{ cm}) (n^{2/3} S_s/S_F)]^{-1} \text{ cm}. \quad (1.70)$$

Chapter 2

Experimental

2.1 Sample preparation

2.1.1 Ce–Pt–Si

The investigations were carried out on about 100 samples having masses of about 1 g. Alloys were made in an electric arc furnace under an argon atmosphere with a non consumable tungsten electrode and a water cooled copper hearth. The purity of cerium was 99.9 at.%, the purity of platinum and silicon was better than 99.9 at.%. Titanium was used as a getter prior to melting. The alloys were remelted two times in order to improve their homogeneity. The mass loss of the alloys after melting was less than 1%. After melting, the as-cast samples were cut into two pieces with a diamond wheel saw. The smaller piece of specimen cut again into two halves of which one half was used for X-ray powder diffraction and one halves of the piece used for electron probe microanalysis. After examination of the as-cast microstructures the other half of the samples were thermally heat-treated in evacuated quartz ampoules which were sealed under residual atmosphere of argon. Annealing was done in a resistance furnace at 800°C for 720 h with subsequent quenching into cold water. After annealing and standard metallography preparation, the diffusion and the equilibrated alloys were examined by light optical microscopy (LOM), electron probe microanalysis (EPMA) and X-ray diffraction (XRD) analysis was performed to identify the ternary alloys.

2.1.2 Clathrate Ba-X-Ge Systems (X=Pd, Cd, Zn)

Alloys with a weight of 1-2 grams were prepared from elemental ingots (Ba 99.9, Pd, Cd, Zn 99.99, Zn 99.99 and Ge 99.999 mass%) by melting in sealed quartz tubes at 1000°C for 2 h (weight loss less than 0.1 %). Afterwards samples were furnace cooled to 800°C and annealed at this temperature for 4-7 days prior to quenching in cold water. Single crystals were mechanically

isolated from crushed alloys. Inspection on an AXS-GADDS texture goniometer assured high crystal quality. Unit cell dimensions and Laue symmetry of the specimens prior to X-ray intensity data collection on a four-circle Nonius Kappa diffractometer equipped with a CCD area detector employing graphite monochromatic MoK α radiation ($\lambda = 0.071073$ nm). Orientation matrix and unit cell parameters for a cubic system were derived using the program DENZO [117]. No absorption corrections were necessary because of the rather regular crystal shape and small dimensions of the investigated specimens. X-ray intensity data for a single crystal with composition Ba₈Cd_{7.6}Ge_{38.4} were collected at three temperatures: 100, 200 and 300 K whereby isothermal temperatures for the crystal, mounted with transparent varnish on a glass rod, were assured by a continuous stream of nitrogen gas enclosing the crystal at preset temperature.

The Pd alloys were annealed at $T = 800^\circ\text{C}$ for 7 days before quenching in cold water. Phase diagram studies, X-ray structure determinations/refinements on powders as well as on a single crystal Ba₈Pd_{3.7}Ge_{42.3} and subsequent measurements of the various bulk properties on single phase polycrystalline material were carried out with a series of standard techniques.

Samples with nominal composition Ba₈Zn₈Ge₃₈ were annealed at 700, 600, 500 and 450 °C. Single crystals were mechanically isolated from crushed alloys. No absorption corrections were necessary because of the rather regular crystal shape and small dimensions of the investigated specimens. The structures were refined with the aid of the SHELXL-97 program [118]. Compounds Ba₈Ge₄₃ and Ba₆Ge₂₅ were used as EPMA standards.

2.1.3 Clathrate I Systems Ba₈{Pd, Pd}_xSi_{46-x}

Clathrate I Si phase samples, namely novel Ba₈{Pd, Pd}_xSi_{46-x} were also prepared by argon arc melting of the constituent metal pieces of minimum 99.9% mass purity. The alloys were sealed in evacuated quartz tubes and annealed at 900°C for 5-7 days prior to quenching in cold water. Details of the various techniques of characterization of composition have been described in detail by Melnychenko et al. [69, 70].

2.1.4 RE₂Pd_{14+x}B_{5-y}

Alloys with nominal composition M₂Pd_{14+x}B_{5-y}, M= Th, U, La, Ce, Pr, Nd, Sm, Eu, Gd, with a weight of about 1 gram each were prepared by argon arc-melting (weight loss less than 0.1%) from elemental ingots with minimal purity of 99.9 mass%. All alloys were sealed in quartz tubes and annealed at 900°C for 240 h before quenching in cold water. Single crystals were mechanically isolated from the crushed as-cast alloy Nd₂Pd₁₄B₅.

2.2 Physical and chemical investigations

2.2.1 Structure analysis

Phase conditions of the samples were checked at room temperature using X-ray powder diffraction data, which were obtained using a Huber Guinier powder camera and monochromatic CuK α -radiation with an image plate recording system. Precise lattice parameters were calculated by least squares fit of the indexed 4θ -values obtained from X-ray film recordings using Ge as internal standard ($a_{\text{Ge}}=0.5657906$ nm). For quantitative refinement of the atom positions, X-ray intensities were collected in transmission from a flat specimen in a Guinier image plate camera. Quantitative Rietveld refinement of X-ray powder diffraction data was performed with the program package FULLPROF [119, 120], with the use of its internal tables for the atomic form factors.

The as cast and annealed samples were polished using standard procedures and were examined by optical metallography and scanning electron microscopy (SEM). Additionally electron probe micro analyses were carried out for some of the compounds in order to control the correct composition. Compositions were determined via EPMA on a Carl Zeiss DSM 962 equipped with a Link EDX system operated at 20 kV and 80 μA . Ba₈Ge₄₃ and Ba₆Ge₂₅ compounds were used as EPMA standards. Samples for physical property measurements were all examined by LOM, SEM, EPMA and only specimens with an amount of secondary phases (typically Ge) of less than 2 vol. % were used. The thorium palladium boride alloy was analyzed on a CAMECA SX50 wavelength dispersive spectrograph comparing the characteristic X-rays of the three elements in the alloy with those from the pure elements and standards (ThB₆ and Pd₂B) applying a peak deconvolution and ZAF correction procedure [121]. The experimental parameters employed were: acceleration voltage of 15 kV, sample current of 15 nA and spectrometer crystals such as PET for Th, M α , PET for Pd, L α and PC3 for the B, K α radiation. Measurements of the various physical properties were carried out with a series of standard techniques.

2.2.2 Electrical resistivity measurements

Electrical resistivity measurements were carried out in a standard 4 terminal a.c. and d.c. technique, respectively. Measurements were performed from 4.2 K to room temperature in a conventional ⁴He bath cryostat with sample dimension of $1 \times 1 \times 5$ mm³. The specimen were mounted on an electrically isolated brass plate and contacted by four gold needles, serving as electrical contacts. For temperature measurements resistive sensors of Ge for T < 30 K and Pt for T > 30 K, respectively, were used. A *Lakeshore* a.c. resistance

bridge 370 with an additional low resistance scanner (Model 3716L) acquired the experimental data.

Electrical resistivity down to 400 mK as function of external magnetic fields up to 12 T was measured in a *Cryogenics* nitrogen-coated ^3He cryostat, sample geometry and contacting resembling those of the ^4He cryostat setup. Temperature was determined using calibrated *Cernox* temperature sensors supplied by *Lakeshore Cryogenics*. A description of the cryostat, the operation principles, the sample holder as well as measurement setup and equipment are given in Ref. [122, 123].

2.2.3 Thermopower measurements

Thermopower measurements were carried out from 4 K to 300 K with a so-called a differential seesaw-heating method [124]. The absolute thermopower $S_x(T)$ was calculated using the following equation:

$$S_x = S_A - \frac{V_A}{V_A - V_B}(S_A - S_B). \quad (2.1)$$

where S_A and S_B represent the absolute thermopower of Chromel and Constantan and V_A and V_B , the voltages along Chromel (AuFe0.07%) and Constantan circuits depending on the temperature difference ΔT , respectively. The spot welded junctions of thermocouple pairs Chromel-Constantan were connected to the surface of the sample by soldering or by a two component silver conductive Epoxy *Epo-TeK-H20E*. During the measurement a temperature gradient $0.2 < T < 2$ K is applied to the specimen, in both directions (seesaw heating). The heaters provides the essential temperature gradient. The voltages between the thermocouple wires were measured in both directions by a *Keithley 192* nanovoltmeter. The sample temperature and the absolute temperature were measured with a Pt sensor in the range from 40 to 300 K and a Ge sensor below 40 K, respectively.

2.2.4 Thermal conductivity measurements

Thermal conductivity measurements from 4 to 300 K were carried out by a steady state heat flow method in a ^4He Cryostat. The sample was surrounded by three radiation shields; the inner is held on the same temperature as the heat sink. Generally the rectangular shaped samples with a typical cross section A of $1\text{-}2 \text{ mm}^2$ and a length of about 10 mm were studied. One end of the sample was placed to a copper stage at a reference temperature T_0 . At the other end of the sample, a strain gauge was attached as heater establishing the temperature gradient ΔT_S . ΔT_S was determined by a differential thermocouple (AuFe0.07%/Chromel), which had its reference temperature from Pt and Ge sensors at the heat sink. The temperature gradient between the

heat sink and the lower sample end is ΔT_B . The voltage drop at the strain gauge was measured, allowing to deduce the thermal flux Q . Using these temperatures the average sample temperature T_S is given as:

$$T_S = T_0 + \frac{\Delta T_S}{2} + \Delta T_B \quad (2.2)$$

and the thermal conductivity λ is calculated

$$\lambda = \frac{l}{A} \frac{Q}{\Delta T_S}. \quad (2.3)$$

A is the sample cross-section and l the effective length. This configuration has been used for high accuracy measurements by including a radiation shield and establishing about the same temperature profile along the shield as exists along the sample. This helps to minimize the radiative losses making $T_0 \approx T_S$. The heat loss due to radiation is given by the Stefan Boltzmann law:

$$Q = \varepsilon \sigma_{SB} A (T_S^4 - T_0^4), \quad (2.4)$$

where T_S is the sample temperature, T_0 is the temperature of the heat sink and the surrounding radiation shield and A is the surface of the sample, $\sigma_{SB} = 5.710^{-8} \text{ W m}^{-2} \text{ K}^{-4}$ is the Stefan Boltzmann constant; the emissivity ε in general ranges between 0 and 1, respectively.

2.2.5 Specific heat measurements

Specific heat measurements were carried out on samples of about 1 g in the temperature range 1.8 K to 300 K employing a quasi adiabatic step heating technique in external magnetic fields up to 11 T. Temperature was obtained from a calibrated *Cernox* resistor; heat capacity data were calibrated against high purity Cu. By means of a design originating from a quasi-adiabatic Nernst setup [125], a temperature sensor (*Cernox*) is placed in the bore of a sapphire plate sample holder fixed by nylon wires and surrounded by a radiation shield. A unique feature of these specific heat experiments is the heat pulse evaluation software which was worked out by G. Schaudy [126]. Details concerning implemented algorithms as well as calibration are found in [127, 128].

Chapter 3

Structural chemistry of ternary Ce–Pt–Si system

3.1 Introduction

The recent discovery of CePt₃Si (CePt₃B type) as the first heavy fermion superconductor without a center of symmetry [11, 12, 13, 14] has triggered widespread research activities to search for a novel superconducting state in related ternary or quaternary alloy systems [15, 33]. However, not only the superconducting properties but also normal state physics of ternary CePt₃Si show a number of exceptional features which are not all fully elucidated. To gain more insight into general physical properties of such compounds, our studies were extended to rare earth-M-Si (M = Pt, Pd, Rh, Ir) systems in search for novel materials with similar property characteristics and/or a possibly high Seebeck effect due to strong electron correlations. Up to now the isothermal section of Ce-Pt-Si system at 800°C was not studied in the whole concentration range, but the existence of many ternary compounds was reported in the isothermal section of the phase diagram Ce-Pt-Si at 600°C [129], namely CePtSi, CePtSi₂, CePt₂Si₂ and Ce₂Pt₁₅Si₇. Each of them shows unusual properties: CePtSi: coherent Kondo lattice and heavy fermion compound [130]; CePtSi₂: Kondo compound with a Kondo temperature T_K = 10K [131]; CePt₂Si₂: compound with valence fluctuation [132]. In this part of work the aim was to investigate the interaction of the components in the ternary system Ce-Pt-Si in the whole concentration range and to determine the crystal structures of ternary compounds. Phase relations in the ternary system Ce-Pt-Si have been experimentally established for the isothermal section at 800°C based on X-ray powder diffraction, metallography, SEM and EPMA techniques on about 100 alloys, which were prepared by various methods employing arc melting under argon or by powder reaction sintering in closed crucibles.

3.2 Binary systems

Binary Ce-Pt is characterized by six intermediate phases [133]. Crystal structure and lattice parameter are summarised in Table 3.1 together with references [134]. The binary system Ce-Pt is used in the version of [135]. The melting temperature of Ce₇Pt₃, however, was re-measured in a DTA experiment and found to be at 860°C [136]. The binary systems bounding the ternary system were published in the literature. CePt₂ has a wide homogeneity region of ~ 9 at.%, it dissolves platinum up to the composition $\sim \text{Ce}_{25}\text{Pt}_{75}$. The solubility of Pt and Ce in each other compounds in this binary system is reported to be negligible. The Pt-Si binary-phase diagram was investigated a

Phase	Space group	Prototype	Lattice Parameters			Ref.
			<i>a</i> (nm)	<i>b</i> (nm)	<i>c</i> (nm)	
Ce ₅ Si ₃	I4/ <i>mcm</i>	Cr ₅ B ₃	0.7855(2)		1.3850(5)	[138]
Ce ₃ Si ₂	P4/ <i>mbm</i>	U ₃ Si ₂	0.77870(6)		0.43824(6)	[138]
CeSi	Pnma	FeB	0.8254(1)	0.39997(7)	0.59452(9)	[138]
Ce ₅ Si ₄	P4 ₁ 2 ₁ 2	Zr ₅ Si ₄	0.79669(6)		1.44948(2)	[138]
CeSi _{1.34}	Cmcm	V ₂ B ₃ (Nd ₂ Si _{3-x})	0.44035	2.48389	0.39517(2)	[139]
CeSi _{1.67}	Imma	GdSi _{2-x}	0.4189	0.4109	1.3917	[138]
CeSi _{2-x}	I4 ₁ mma	ThSi ₂	0.4154		1.3822	[129]
Pt ₂₅ Si ₇	Unknown	Unknown				[135, 145]
Pt ₃ Si- ht	Pnma	Fe ₃ C	0.5579	0.7697	0.5520	[135, 143]
Pt ₃ Si- rt	C2/ <i>m</i>	Fe ₃ Ge	0.7702	0.7765	0.7765	[135]
Pt ₃ Si	Unknown	Unknown				[134]
Pt ₅ Si ₂	Unknown	Unknown				[145]
Pt ₁₂ Si ₅ - ht	I4/ <i>m</i>	Ni ₁₂ Si ₅ (Ni ₁₂ P ₅)	0.9607		0.5542	[143]
Pt ₁₂ Si ₅ - rt	P4/ <i>n</i>	Pt ₁₂ Si ₅	1.34055(5)		0.55186(3)	[134]
Pt ₂ Si- ht	P6 2 <i>m</i>	Fe ₂ P	0.64567(9)		0.35772(5)	[134]
Pt ₂ Si- rt	I4/mmm	ThH ₂	0.39282(2)		0.59215(5)	[134]
Pt ₆ Si ₅	P2 ₁ / <i>m</i>	Pt ₆ Si ₅	0.6158(2)	0.34915(7)	1.5425(3)	[134]
PtSi	Pnma	MnP	0.55828(4)	0.35942(3)	0.59245(5)	[135]
Ce ₇ Pt ₃	P6 ₃ <i>mc</i>	Fe ₇ Th ₃	1.0204		0.6399	[129, 145]
Ce ₃ Pt ₂	R ₃	Er ₃ Ni ₂	0.8976(2)		1.7124(3)	[129, 145]
CePt	Cmcm	CrB	0.3974(1)	1.0940(4)	0.4479(1)	
Ce ₃ Pt ₄	R ₃	Pu ₃ Pd ₄	1.3661(7)		0.5779(3)	[134]
Ce(Ce _{1-x} Pt _x)Pt ₄	F43 _m	AuBe ₅	0.76380			[129]
CePt ₅	P6/mmm	CaCu ₅	0.5348(6)		0.4364(5)	[134]

Table 3.1: Crystal structure and Lattice parameters data for the binary system Ce-Si, Pt-Si and Ce-Pt.

couple of times. A very recent version is summarised in Ref. [137]. According to this paper there are five binary intermediate phases, Pt₃Si, Pt₁₂Si₅, Pt₂Si, Pt₆Si₅, and PtSi.

Ce-Si system was adopted from a recent investigation by [138]. There is no doubt about the formation of an additional phase, Ce₂Si_{3-x} (CeSi_{1.34}), for which crystal and magnetic structure were determined by [139]. A new investigation of the Pt-Si system by Massara et al. [135] superseded the Pt-Si diagram presented in [140] and two more compounds, Pt₂₅Si₇ and Pt₁₇Si₈, were discovered from detailed DTA-analyses of about 110 alloys. X-ray data were merely used to identify changes in the intensity patterns, however, no

details were given on the crystal structures of the binary compounds. From a comparison of the phase diagram of [141] with the new version of [135] the compound $\text{Pt}_{12}\text{Si}_5$, described by [142], [143], appears to be shifted to composition Pt_5Si_2 . In order to eliminate contradicting information in literature on formation and crystal structure of Pt–Si compounds, several alloys with compositions Pt_6Si_5 , Pt_2Si , $\text{Pt}_{17}\text{Si}_8$, $\text{Pt}_{12}\text{Si}_5$, Pt_3Si and $\text{Pt}_{25}\text{Si}_7$ were prepared and investigated by means X-ray powder diffraction in as-cast state and after annealing at 800°C. Our Rietveld refinements confirm structural details for PtSi , Pt_6Si_5 , Pt_2Si (for both the low- and high-temperature modification) whilst significant disagreement was noticed for the atom positions of Pt_3Si (Pt_3Ge -type structure [141]). Structural parameters reported for $\text{Pt}_{12}\text{Si}_5$ ($\text{Pt}_{12}\text{Si}_5$ -type [142, 144] show significant differences between calculated and observed X-ray intensities. Furthermore, Pt_3Si (Fe_3C -type), $\text{Pt}_{17}\text{Si}_8$ and $\text{Pt}_{25}\text{Si}_7$ were not observed in the investigated alloys: the X-ray powder diffraction spectrum recorded from an alloy with composition $\text{Pt}_{17}\text{Si}_8$ was indexed as a mixture of Pt_2Si and " $\text{Pt}_{12}\text{Si}_5$ " and similarly the alloy $\text{Pt}_{25}\text{Si}_7$ consists of Pt_3Si and Pt. Consequently, the phase relations derived from the present investigation at 800°C were found to be consistent with those reported by [140].

3.3 Ternary systems

The state of knowledge about the Ce–Pt–Si system before/after this work is summarised in Table 3.2 [129, 134]. The phase diagram was determined for the Ce–Pt–Si system at 800°C. Crystal growth and bulk material syntheses require detailed knowledge of phase relations as well as of crystal structures. A critical assessment by Gribanov et al. [146] summarised all data available then on the Ce–Pt–Si system with respect to phase equilibria [129] incorporating also unpublished data [147] and knowledge on physical properties. As a result of the critical review an isothermal section at 600°C [129] was presented, which, however, left many regions in the diagram (with dashed tie-lines) open for further detailed studies. Therefore a reinvestigation of the phase relations became the subject of the present work. In order to profit from enhanced diffusion in the system combining elements with rather different melting points, a temperature of 800°C was chosen in our reinvestigation for the isothermal section. Only one phase, CePt_3Si , (the most stable in this system) could be prepared as a single phase. A phase analysis of samples with different compositions was carried out. The results are schematically summarised in the presented isothermal section of the phase diagram for the Ce–Pt–Si system at 800°C, see Fig. 3.1.

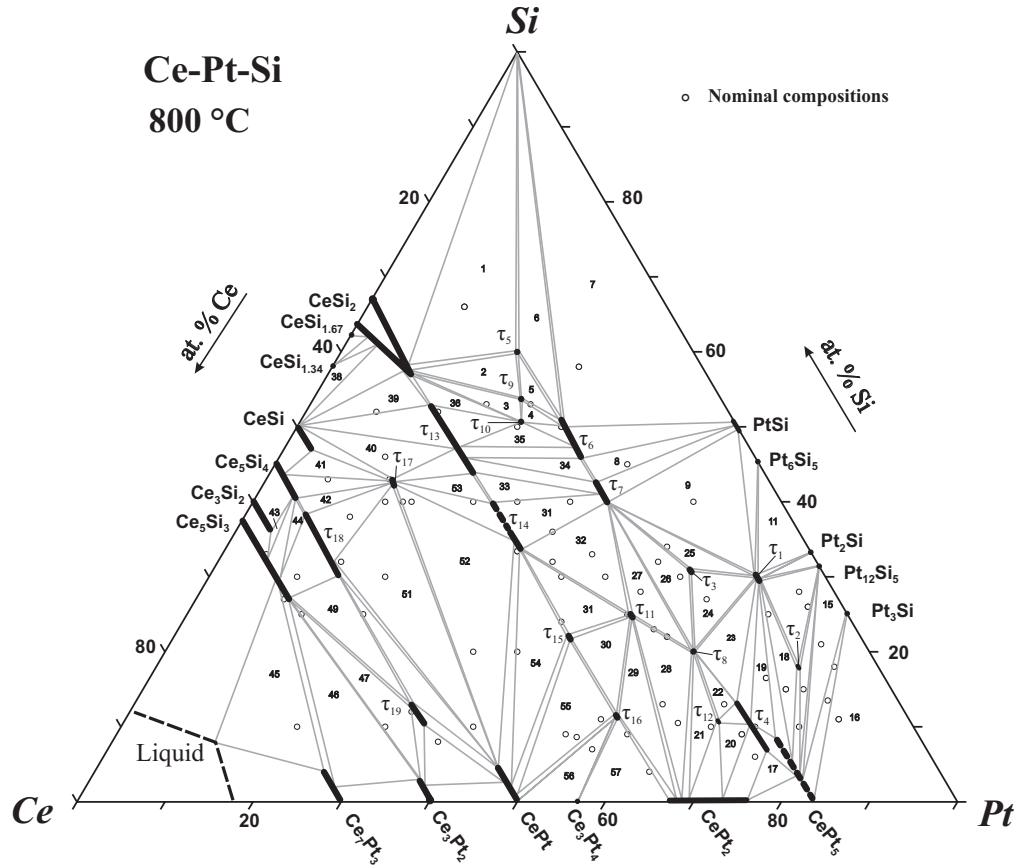


Figure 3.1: Isothermal cross-section of the Ce-Pt-Si system at 800°C.

3.4 Phase relations; the Isothermal Section Ce-Pt-Si at 800°C

Phase relations in the ternary system at 800°C are shown in Fig. 3.1. The most striking difference to the equilibria at 600°C as presented by [129, 147, 146] is the much larger amount of ternary phases as well as the absence of a significant solubility for silicon throughout the full homogeneity region of the binary compound $\text{Ce}(\text{Ce}_{1-x}\text{Pt}_x)\text{Pt}_4$. Furthermore, phase equilibria are characterized by the absence of cerium solubility in the various platinum silicides. However, mutual solubilities among cerium silicides and cerium platinides are significant. The essentially random substitution of the almost equally sized atom species platinum and silicon is reflected in extended homogeneous regions at constant Ce-content for several binary and ternary compounds such as for $\tau_{13}\text{-Ce}(\text{Pt}_x\text{Si}_{1-x})_2$ or $\tau_6\text{-CePt}_{2-x}\text{Si}_{2+x}$.

The directions of homogeneous regions of the ternary compounds indicate

Code	Phase	Space group	Prototype	Lattice Parameters			Ref.
				<i>a</i> (nm)	<i>b</i> (nm)	<i>c</i> (nm)	
τ_1	Ce ₃ Pt ₂₃ Si ₁₁	Fm ₃ <i>m</i>	Ce ₃ Pt ₂₃ Si ₁₁	1.68647(5)			[134]
τ_2	Unknown	Unknown					
τ_3	Ce ₂ Pt ₇ Si ₄	Pnma	Ce ₂ Pt ₇ Ge ₄	1.96335(2)	0.40361(1)	1.12240(2)	[134]
τ_4	Unknown	Unknown					
τ_5	CePtSi ₃	I4mm	CeNiSi ₃	0.43222(1)		0.96017(5)	[134]
τ_6	Ce ₂ Pt ₃ Si ₅	Ibam	U ₂ Co ₃ Si ₅	0.9966(6)	1.1663(8)	0.6062(3)	[134]
			presumable	0.9956(1)	1.16526(1)	0.60693(7)	
τ_7	CePt ₂ Si ₂	P4/nmm	CaBe ₂ Ge ₂	0.42441(2)		0.98341(7)	[134]
				0.42550(3)		0.97951(1)	[134]
τ_8	CePt ₃ Si	P4mm	CePt ₃ B	0.40786(4)		0.54475(4)	[134]
τ_9	Unknown	Unknown					
τ_{10}	CePtSi ₂	Cmcm	CeNiSi ₂	0.42908(3)	1.6739(2)	0.42371(5)	[134]
τ_{11}	CePt ₂ Si	Cmcm	Inv.-CeNiSi ₂	0.41008(4)	1.8046(2)	0.41734(4)	[134]
τ_{12}	Unknown	Unknown					
τ_{13}	Ce(Pt _x Si _{1-x}) ₂	P6/mmm	AlB ₂	0.41560(1)		0.42535(8)	[134]
				0.40960(4)		0.43130(3)	[134]
τ_{14}	CePt _{1-x} Si _x	I4 ₁ md	LaPtSi	0.4206(1)		1.4490(3)	[134]
				0.41866(2)		1.44914(8)	[134]
τ_{15}	Unknown	Unknown					
τ_{16}	Ce ₃ Pt ₅ Si	Imma	Ce ₃ Pd ₅ Si	0.74025(8)	1.2951(2)	0.7508(1)	[134]
τ_{17}	Ce ₃ PtSi ₃	Immm	Ba ₃ Al ₂ Ge ₂	0.41044(5)	0.43243(5)	1.8353(3)	[134]
τ_{18}	Ce ₅ (Pt,Si) ₄	Pnma	Gd ₅ Si ₄	0.77223(2)	1.53279(3)	0.80054(2)	[134]
				0.7643(1)	1.5330(3)	0.8007(2)	[134]
				0.7704(2)	1.5321(4)	0.8000(3)	[134]
τ_{19}	Unknown	Unknown					

Table 3.2: Crystal structure and Lattice parameters data for the ternary intermediate phases of the Ce–Pt–Si system at 800°C .

a substitution mechanism between Pt and Si atoms. Such a direction of solid solutions and such a mechanism with substitution between Pt and Si are typical for similar ternary systems and may be explained by the similarity of the atomic radii of Pt (1.38 Å) and Si (1.34 Å). The ternary phase CePt_{2-x}Si_{2+x} (τ_7) shows also a homogeneity region up to 4 at.%. The homogeneity range of CePt_{2-x}Si_{2+x} with CaBe₂Ge₂ structure type stretches from 38.9 at.% to 42.4 at.% Si at 800°C (Fig. 3.2). The other ternary phase at 800°C is CePt_{1-x}Si_x with LaPtSi structure type, which shows a homogeneous region up to 6.7 at.% Si. The homogeneity range of CePt_{1-x}Si_x stretches from 33.4 at.% to 40.1 at.% Si at 800°C.

In order to characterize the ternary phase Ce(Pt,Si)₂ (τ_{13}), six samples were investigated. EPMA and XRD data for τ_{13} phase indicate a wide homogeneity region up to 9 at.%. As shown in Fig. 3.2a the homogeneity range of Ce(Pt_xSi_{1-x})₂ (τ_{13}) with AlB₂ structure type stretches from 40.0 at.% to 53.2 at.% Si (13.69 at.% and 25.62 at.% Pt (0.2<*x*<0.38)) at 800°C. In order to characterize the ternary phase CePt_{2-x}Si_{2+x} (τ_7), nine samples were investigated. EPMA and XRD data for the τ_7 phase indicate a wide homogeneity region up to 4 at.% Si. Lattice parameters of this phase vary strongly from sample to sample, indicating a large homogeneity region of this phase, confirmed by microprobe measurements and by the variation of lattice pa-

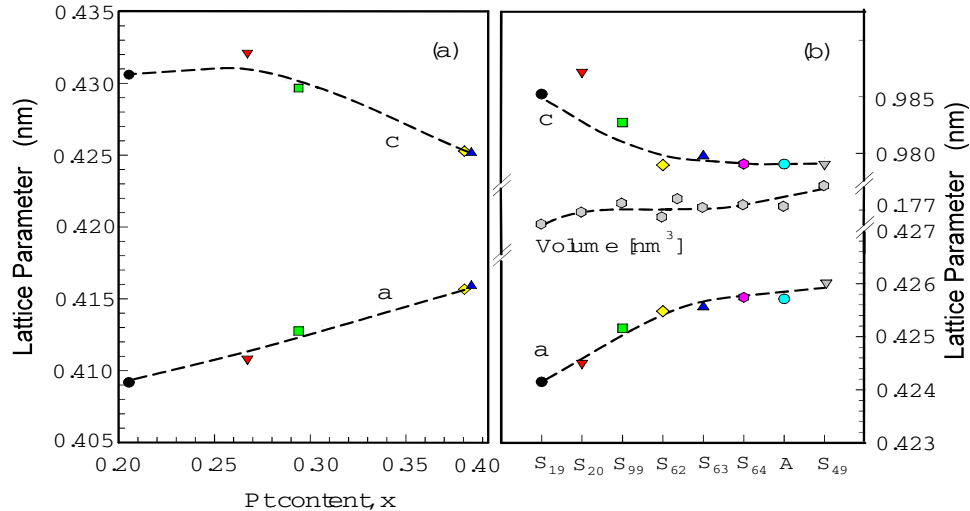


Figure 3.2: Lattice parameters as function of Pt content for ternary phases; (a) $\text{Ce}(\text{Pt}_x\text{Si}_{1-x})_2$ (τ_{13}); (b) $\text{CePt}_{2-x}\text{Si}_{2+x}$ (τ_7) and unit-cell volume.

rameters versus the Pt content (see Fig. 3.2a). A smooth increase of lattice parameter a is observed from $a = 0.42415$ nm to 0.42607 nm. On the other hand, there is a slight decrease of lattice parameter c from $c = 0.98419$ nm to 0.97925 nm (Fig. 3.2b). The unit-cell volume increases initially up to the alloy which lying in area No. 8 of the phase diagram (see Fig. 3.1). It should be noted, however, that absolute changes of the volume values are rather small. The lattice parameters a and c as well as the unit-cell volume V [nm^3] obtained from Rietveld refinement of powder X-ray diffraction data are plotted in Fig. 3.2b.

Composition and lattice parameters for phases forming three-phase equilibria at 800°C are listed in Table 3.2. It has to be noted that in addition to the ternary phases listed in Table 3.2, compounds with compositions $\text{Ce}_{30}\text{Pt}_{40}\text{Si}_{30}$ and $\text{Ce}_{22}\text{Pt}_{46}\text{Si}_{22}$ (at.%) were detected with structures still unknown, however, these phases do not participate in phase equilibria at 800°C.

The complete phase diagram was determined for the Ce-Pt-Si system at 800°C (Fig. 3.1). 19 ternary compounds were observed at 800°C. Atom order in the crystal structures of $\tau_{18}\text{-Ce}_5(\text{Pt},\text{Si})_4$ (space group Pnma ; $a = 0.77223(3)$, $b = 1.53279(8)$, $c = 0.80054(5)$ nm), $\tau_3\text{-Ce}_2\text{Pt}_7\text{Si}_4$ (space group Pnma ; $a = 1.96335(8)$, $b = 0.40361(4)$, $c = 1.12240(6)$ nm) and $\tau_{10}\text{-CePtSi}_2$ (space group Cmcm ; $a = 0.42943(2)$, $b = 1.67357(5)$, $c = 0.42372(2)$ nm) was determined by direct methods from X-ray single crystal studies and found to be isotypic with the Sm_5Ge_4 -type, the $\text{Ce}_2\text{Pt}_7\text{Ge}_4$ -type and the CeNiSi_2 -type, respectively. Rietveld refinements established atom arrangement in the structures of $\tau_{16}\text{-Ce}_3\text{Pt}_5\text{Si}$ (space group Imma) and $\tau_{17}\text{-Ce}_3\text{PtSi}_3$ (space group

$Immm$).

3.5 Determination of Crystal structures new ternary silicide

Crystal structures for all those ternary compounds, which were already reported earlier, were found to be consistent with data in literature. For a series of new compounds crystal structures were derived by single crystal X-ray diffractometry and Rietveld analyses. Crystal data are summarised in Table 3.3 and Fig. 3.8. Structural chemistry of the new compounds and solution phases follow in all cases the characteristics already outlined for the prototype structures. Interatomic distances agree well with the sum of metal atomic radii of the elements. In the system Ce–Pt–Si, nine ternary compounds with different structure types were found in preceding studies [129] which are summarised in Table 3.2: CePtSi_2 (CeNiSi_2 structure type, space group $Cmcm$) [25], CePt_2Si_2 (ThCr_2Si_2 structure type, $I4/nmm$) [148], CePtSi (LaPtSi structure type, $I4_1/md$) [149], $\text{Ce}_3\text{Pt}_{23}\text{Si}_{11}$ ($\text{Ce}_3\text{Pt}_{23}\text{Si}_{11}$ structure type, $Fm\bar{3}m$) [150] and CePt_3Si (CePt_3B structure type, space group $P4/mm$) [151]. The reinvestigation of this phase diagram yields the existence of six new ternary phases. The new ternary silicide $\text{Ce}_5(\text{Pt},\text{Si})_4$ (τ_{18}) with orthorhombic unit cell and space group $Pnma$ (No.62) crystallizes with Gd_5Si_4 structure type. In order to characterize the ternary phase $\text{Ce}_5(\text{Pt},\text{Si})_4$, five samples were investigated. The structural data and interatomic distances for $\text{Ce}_5(\text{Pt},\text{Si})_4$ are summarised in Table 3.3.

3.5.1 The crystal structure of τ_{18} - $\text{Ce}_5(\text{Pt}_{0.12}\text{Si}_{0.88})_4$ with Sm_5Ge_4 -type

Binary Ce_5Si_4 is well known to crystallize with the tetragonal Zr_5Si_4 -type structure. EMPA data (see Table 2 in Ref. [134]) indicate that the solubility of Pt at 800°C proceeds up to 4.6 at.% Pt beyond which on rising Pt content a narrow two-phase region of about 3 at.% is formed connecting to a ternary phase, τ_{18} , with an extended homogeneity region up to 15 at.% Pt. A single crystal, broken from an alloy with composition $\text{Ce}_{55.5}\text{Pt}_{5.3}\text{Si}_{39.2}$ (nominal composition in at.%) within the τ_{18} region, revealed orthorhombic symmetry with space group $Pnma$ and lattice parameters: $a = 0.77223(3)$, $b = 1.53279(8)$, $c = 0.80054(5)$ nm. The structure was solved by direct methods yielding a partial random distribution of Pt and Si sites fully compatible and isotypic with the Gd_5Si_4 -type branch of the Sm_5Ge_4 -type of structure. Results of the refinement for $\text{Ce}_5(\text{Pt}_{0.12}\text{Si}_{0.88})_4$, which converged to $R_F^2 = 0.037$ with residual electron densities smaller than $\pm 3.7 \text{ e}^-/\text{\AA}^3$, are summarised in

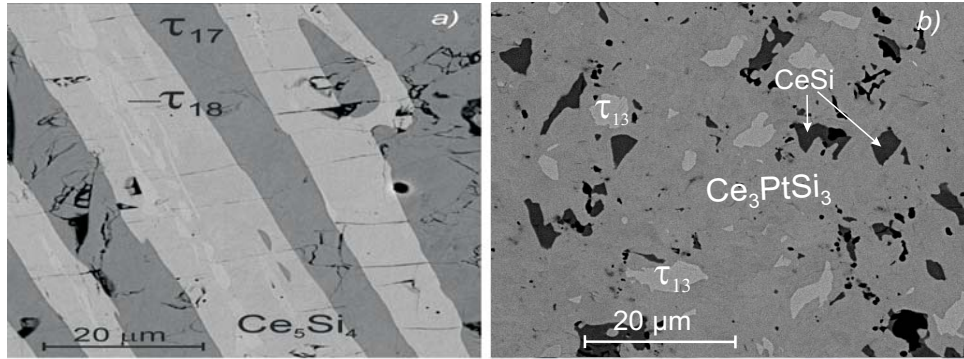


Figure 3.3: EPMA Microstructure of alloys; (a) Ce₅₃Pt₇Si₄₀ and (b) Ce₄₂Pt₁₂Si₄₆.

Table 3.3.

Fig. 3.3a shows the EPMA microstructure of alloy Ce₅₃Pt₇Si₄₀ revealing two different ternary phases and one binary phase. Analyzing the phase relations in the crystallization region one can see that the alloy Ce₅₃Pt₇Si₄₀ is in equilibrium with other phases in this part of the phase diagram (see three-phase region No.42). EPMA and X-ray diffraction analyses confirmed that the bright gray phase corresponds to Ce(Pt,Si)₂ (τ_{18}) with phase composition 55.5Ce6.7Pt37.8Si (in at.%), the dark gray region to the compounds Ce₃PtSi₃ (τ_{17}) with phase composition 43.0Ce14.0Pt42.9Si (in at.%) and the gray phase to compounds Ce₅Si₄ with phase composition 55.6Ce4.6Pt39.8Si (in at.%), respectively.

3.5.2 The crystal structure of τ_3 - Ce₂Pt₇Si₄

The phase field τ_1 (Ce₃Pt₂₃Si₁₁) - τ_7 (CePt_{2-x}Si_{2+x}) - τ_8 (CePt₃Si) was found to contain a new powder spectrum from a compound with practically no homogeneity region centered around composition Ce_{15.3}Pt_{53.9}Si_{30.8} (in at.%, from EPMA). The intensity pattern of a single crystal, isolated from the alloy Ce_{15.4}Pt_{54.1}Si_{30.5}, was indexed with a orthorhombic symmetry i.e. space group Pnma and lattice parameters: $a = 1.96335(8)$, $b = 0.40361(4)$, $c = 1.12240(6)$ nm. Direct methods yielded a completely ordered atom arrangement isotypic with the structure type of Ce₂Pt₇Ge₄. Results of the refinement for Ce₂Pt₇Si₄, which converged to $R_F^2 = 0.029$ with residual electron densities smaller than $\pm 5.9 \text{ e}^-/\text{\AA}^3$, are summarised in Table 3.3. The composition derived from the refinement is in perfect agreement with EPMA. Fig. 3.4b shows the EPMA microstructure of alloy Ce₁₈Pt₅₀Si₃₂. EPMA investigation and phase analysis of Ce₁₈Pt₅₀Si₃₂ indicate a three-phase field $\tau_3 + \tau_7 + \tau_8$ in the phase diagram (see the three-phase region No.26). Based on EPMA and XRD

Parameter	Ce ₅ (Pt, Si) ₄	Ce ₂ Pt ₇ Si ₄	CePtSi ₂
Phase code	τ_{18}	τ_3	τ_{11}
space group	Pnma	Pnma	Cmcm
Formula from refinement	Ce ₅ (Pt _x Si _{1-x}) ₄ $x=0.12$	Ce ₂ Pt ₇ Si ₄	CePtSi ₂
in at.%	55.5Ce5.3Pt39.2Si	15.4Ce53.8Pt30.8Si	25Ce25Pt50Si
Structure type	Sm ₅ Ge ₄ (branch Gd ₅ Si ₄)	Ce ₂ Pt ₇ Si ₄	CeNiSi ₂
Lattice parameter a; b[nm]	0.77223(3); 1.53279(8)	1.96335(8); 0.40361(4)	4.2943(2); 16.7357(5)
c[nm]	0.80054(6)	1.12240(6)	4.2372(2)
H_{abs} [mm ⁻¹]	38.51	120.10	61.11
Crystal size	54 \times 70 \times 80	54 \times 70 \times 27	27 \times 27 \times 54
Data collection: 2 Θ range (°)	2 \leq 2 Θ \leq 72.6	2 \leq 2 Θ \leq 72.6	2 \leq 2 Θ \leq 72.6
Total number of frames	75 sec/frame; 356 ; 5 sets	150 sec/frame; 400 ; 5 sets	220 sec/frame; 523 ; 7 sets
Reflections in refinement	1800 \geq 4 $\sigma(F_0)$ of 2238	2058 \geq 4 $\sigma(F_0)$ of 2376	428 \geq 4 $\sigma(F_0)$ of 440
mosaicity	0.45	0.50	0.55
Number of variables	53	80	18
$R_F^2 = \sum F_0^2 - F_c^2 / \sum F_0^2$	0.037	0.029	0.021
$R_{f,w}$	0.062	0.065	0.067
wR2	0.109	0.90	0.056
GOF	1.111	1.192	1.259
Extinction (Zachariasen)	0.0002(1)	0.00068(4)	0.0015(2)
Atom parameters			
Atom site 1	Ce1 in 8d (x,y,z); 0.31321(5), 0.12119(2) 0.18026(4)	Ce1 in 4c (x, $\frac{1}{4}$,z); 0.21910(4), 0.51894(7)	Ce1 in 4c (0,y, $\frac{1}{4}$); 0.39465(3)
Occ.	1.00(1)	1.00(1)	1.00(1)
U ₁₁ , U ₂₂ , U ₃₃ (10 ² nm ²)	0.0151(2), 0.0133(2), 0.0146(2)	0.0071(3), 0.0075(3), 0.0052(3)	0.0035(2), 0.0038(2), 0.0045(2)
U ₂₃ , U ₁₃ , U ₁₂ (10 ² nm ²)	0.0003(1), 0.0011(1), 0.0005(1)	U ₂₃ =U ₁₂ =0, U ₁₃ =-0.0019(2)	U ₂₃ =U ₁₃ =U ₁₂ =0
Atom site 2	Ce2 in 8d (x,y,z); 0.03037(5), 0.59774(3), 0.18278(4)	Ce2 in 4c (x, $\frac{1}{4}$,z); 0.02914 (4), 0.74378(6)	Pt1 in 4c (0,y, $\frac{1}{4}$); 0.18004(2)
Occ.	1.00(1)	1.00(1)	1.00(1)
U ₁₁ , U ₂₂ , U ₃₃ (10 ² nm ²)	0.0159(2), 0.0172(2), 0.0145(2)	0.0055(3), 0.0066(3), 0.0026(3)	0.0043(1), 0.0044(1), 0.0048(2)
U ₂₃ , U ₁₃ , U ₁₂ (10 ² nm ²)	0.0026(1), 0.0022(1), 0.0036(1)	U ₂₃ =U ₁₂ =0, U ₁₃ =0.0008(2)	U ₂₃ =U ₁₃ =U ₁₂ =0
Atom site 3	Ce3 in 4c (x, $\frac{1}{4}$,z); 0.14248(8), 0.51233(7)	Pt1 in 4c (x, $\frac{1}{4}$,z); 0.21227(3), 0.19866 (5)	Si1 in 4c (0,y, $\frac{1}{4}$); 0.7495(1)
Occ.	1.00(1)	1.00(1)	1.00(1)
U ₁₁ , U ₂₂ , U ₃₃ (10 ² nm ²)	0.0266(3), 0.0171(3), 0.0232(3)	0.0046(2), 0.0083(2), 0.0082(2)	0.0044(8), 0.0046(7), 0.0046(8)
U ₂₃ =U ₁₂ =0, U ₁₃ (10 ² nm ²)	0.0004(2)	-0.0022(2)	U ₂₃ =U ₁₃ =U ₁₂ =0
Atom site 4	M1 in 8d (x,y,z); 0.1394(1), 0.04027(8), 0.47641(1)	Pt2 in 4c (x, $\frac{1}{4}$,z); 0.03354(3), 0.06290(5)	Si2 in 4c (0,y, $\frac{1}{4}$); 0.0359(1)
Occ.	0.114(2) Pt + 0.886 Si	1.00(1)	1.00(1)
U ₁₁ , U ₂₂ , U ₃₃ (10 ² nm ²)	0.0213(6), 0.0179(5), 0.0163(5)	0.0041(2), 0.0063(2), 0.0035(2)	0.0060(8), 0.0025(6), 0.0034(9)
U ₂₃ , U ₁₃ , U ₁₂ (10 ² nm ²)	0.0032(4), -0.0005(4), -0.0029(4)	U ₂₃ =U ₁₂ =0, U ₁₃ =-0.0001(2)	U ₂₃ =U ₁₃ =U ₁₂ =0
Atom site 5	M2 in 4c (x, $\frac{1}{4}$,z); 0.0201(2), 0.0973(2)	Pt3 in 4c (0,y, $\frac{1}{4}$); 0.65850(3), 0.55722 (5)	
Occ.	0.152(2) Pt + 0.848 Si	1.00(1)	
U ₁₁ , U ₂₂ , U ₃₃ (10 ² nm ²)	0.0111(6), 0.0155(6), 0.0143(6)	0.0059(2), 0.0070(2), 0.0040(2)	
U ₂₃ =U ₁₂ =0, U ₁₃ (10 ² nm ²)	0.0010(4)	U ₂₃ =U ₁₂ =0, U ₁₃ =-0.0012(2)	
Atom site 6	M3 in 4c (x, $\frac{1}{4}$,z); 0.2528(2), 0.8784(2)	Pt4 in 4c (x, $\frac{1}{4}$,z); 0.37290(3), 0.62011 (5)	
Occ.	0.096(2) Pt + 0.904 Si	1.00(1)	
U ₁₁ , U ₂₂ , U ₃₃ (10 ² nm ²)	0.0141(8), 0.0153(7), 0.0129(7)	0.0061(2), 0.0066(2), 0.0027(2)	
U ₂₃ =U ₁₂ =0, U ₁₃ (10 ² nm ²)	-0.0005(5)	0.0010(2)	
Atom site 7		Pt5 in 4c (x, $\frac{1}{4}$,z); 0.04156(3), 0.45063(5)	
Occ.		1.00(1)	
U ₁₁ , U ₂₂ , U ₃₃ (10 ² nm ²)		0.0054(2), 0.0064(2), 0.0040(2)	
U ₂₃ =U ₁₂ =0, U ₁₃ (10 ² nm ²)		0.0009(2)	
Atom site 8		Pt6 in 4c (x, $\frac{1}{4}$,z); 0.36574(3), 0.86767(5)	
Occ.		1.00(1)	
U ₁₁ , U ₂₂ , U ₃₃ (10 ² nm ²)		0.0071(2), 0.0085(2), 0.0024(2)	
U ₂₃ =U ₁₂ =0, U ₁₃ (10 ² nm ²)		-0.0004(21)	
Atom site 9		Pt7 in 4c (x, $\frac{1}{4}$,z); 0.34850(3), 0.24305(5)	
Occ.		1.00(1)	
U ₁₁ , U ₂₂ , U ₃₃ (10 ² nm ²)		0.0046(2), 0.0162(2), 0.0043(2)	
U ₂₃ =U ₁₂ =0, U ₁₃ (10 ² nm ²)		-0.0006(2)	
Atom site 10		Si1 in 4c (x, $\frac{1}{4}$,z); 0.2446(2), 0.7976(4)	
Occ.		1.00(1)	
U ₁₁ , U ₂₂ , U ₃₃ (10 ² nm ²)		0.007(2), 0.009(2), 0.003(2)	
U ₂₃ =U ₁₂ =0, U ₁₃ (10 ² nm ²)		0.0014(12)	
Atom site 11		Si2 in 4c (x, $\frac{1}{4}$,z); 0.4131(2), 0.0615(3)	
Occ.		1.00(1)	
U ₁₁ , U ₂₂ , U ₃₃ (10 ² nm ²)		0.004(1), 0.006(2), 0.003(1)	
U ₂₃ =U ₁₂ =0, U ₁₃ (10 ² nm ²)		0.0005(11)	
Atom site 12		Si3 in 4c (x, $\frac{1}{4}$,z); 0.4136 (2), 0.4245(4)	
Occ.		1.00(1)	
U ₁₁ , U ₂₂ , U ₃₃ (10 ² nm ²)		0.003 (1), 0.008(2), 0.002 (1)	
U ₂₃ =U ₁₂ =0, U ₁₃ (10 ² nm ²)		0.0005(12)	
Atom site 13		Si4 in 4c (x, $\frac{1}{4}$,z); 0.0933 (2), 0.2515(3)	
Occ.		1.00(1)	
U ₁₁ , U ₂₂ , U ₃₃ (10 ² nm ²)		0.007(2), 0.006(2), 0.003(2)	
U ₂₃ =U ₁₂ =0, U ₁₃ (10 ² nm ²)		0.001(1)	
Residual density; e/Å ³ max; min	3.67; -3.02	7.67; -2.71	
Principal mean square atomic displacements U	Ce1 0.0161 0.0138 0.0131 Ce2 0.0218 0.0130 0.0129 Ce3 0.0266 0.0231 0.0171 M1 0.0236 0.0183 0.0136 M2 0.0155 0.0145 0.0108 M3 0.0153 0.0143 0.0127	Ce1 0.0082 0.0075 0.0040 Ce2 0.0065 0.0055 0.0026 Ce3 0.0092 0.0083 0.0036 Pt2 0.0063 0.0041 0.0035 Pt3 0.0070 0.0065 0.0035 Pt4 0.0066 0.0063 0.0024 Pt5 0.0064 0.0058 0.0036 Pt6 0.0085 0.0071 0.0024 Pt7 0.0162 0.0050 0.0039 Si1 0.0087 0.0073 0.0026 Si2 0.0062 0.0042 0.0027 Si3 0.0084 0.0036 0.0023 Si4 0.0072 0.0059 0.0026	Ce1 0.0045 0.0038 0.0035 Pt1 0.0048 0.0044 0.0043 Si1 0.0046 0.0046 0.0044 Si2 0.0060 0.0034 0.0025

Table 3.3: X-Ray single crystal data at RT for various compounds from the Ce–Pt–Si system (Mo K_α radiation); structure data are standardized with program Structure Tidy[152].

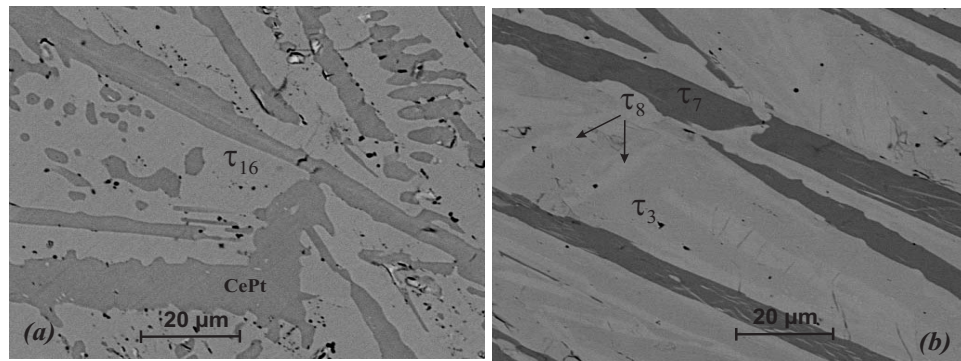


Figure 3.4: EPMA Micrograph of alloys; (a) Ce₃₈Pt₅₅Si₇ and (b) Ce₁₈Pt₅₀Si₃₂.

results, it is determined that the darkest phase is τ_7 , the light gray phase is τ_3 and the bright phase is τ_8 . It is assumed that the main phase is the light gray phase (τ_3 - Ce₂Pt₇Si₄) with phase composition 15.4Ce54.1Pt30.5Si (in at.%). The bright phase is CePt₃Si (τ_8) with composition 20.5Ce60.4Pt19.6Si (in at.%) and the darkest phase is the CePt₂Si₂ phase (τ_7) which contains 19.9Ce40.1Pt39.9Si (in at.%).

3.5.3 The crystal structure of τ_{10} - CePtSi₂

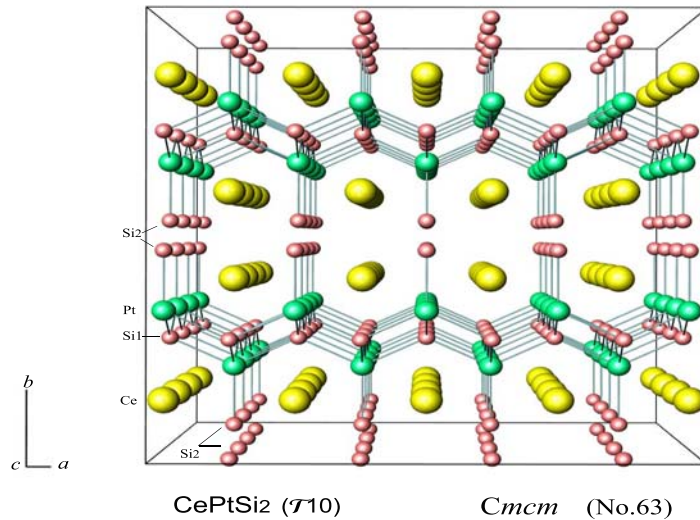


Figure 3.5: Perspective view of CePtSi₂- (τ_{10}) in a three-dimensional view along the c -axis.

Although the crystal structure of CeNiSi₂ has been elucidated in sev-

eral representatives, the X-ray intensity pattern of a single crystal, isolated from the alloy $\text{Ce}_{25}\text{Pt}_{25}\text{Si}_{50}$, was studied (space group $Cmcm$ and lattice parameters: $a = 0.42943(2)$, $b = 1.67357(5)$, $c = 0.42372(2)$ nm). From direct methods a completely ordered atom arrangement was prompted being iso-typic with the structure type of CeNiSi_2 . No site defects were observed. The refinement converged to $R_F^2 = 0.021$ with residual electron densities smaller than $\pm 7.6 \text{ e}^-/\text{\AA}^3$. The crystallographic unit cell is shown in Fig. 3.5.

All atoms occupy the $4c$ site: $(0,y,1/4)$, with different values of the position parameter y for each atom. The values of the lattice parameters a , b and c as well as of the positional parameters y , corresponding to the minimum of the appropriate reliability factor, are listed in Table 3.3.

3.5.4 Rietveld refinement of Pt_3Si

For Pt_3Si two polymorphic modifications (Fe_3C -type [143] and Pt_3Ge -type [141]) are reported in literature. However, Pt_3Si in as-cast state and after annealing at 800°C showed an X-ray powder diffraction pattern incompatible with the Fe_3C -type structure, which was reported for ht- Pt_3Si [143] and was suggested to exist in the temperature range from 440 to 876°C [135]. The structure data presented for rt- Pt_3Si (Pt_3Ge -type, space group $C2/m$ [143]) resulted in poor reliability factors, $R_F = 0.266$ and $R_I = 0.396$. But further Rietveld refinement of the atomic positions arrived at satisfactorily low residual values $R_F = 0.098$ and $R_I = 0.089$ (for results see Table 3.8).

3.5.5 Rietveld refinement of τ_{16} - $\text{Ce}_3\text{Pt}_5\text{Si}$

Due to absence of good single crystals for $\text{Ce}_3\text{Pt}_5\text{Si}$ the crystal structure of this compound was resolved by Rietveld refinements of X-ray powder diffraction intensities. EPMA of alloy $\text{Ce}_{33.3}\text{Pt}_{55.6}\text{Si}_{11.1}$ (at.%) annealed at 800°C shows almost single phase $\text{Ce}_3\text{Pt}_5\text{Si}$ with small amounts of CePt_2 . An analysis of X-ray diffraction intensities reveals complete atom order for $\text{Ce}_3\text{Pt}_5\text{Si}$ (see Table 3.8), which crystallizes in the $\text{Ce}_3\text{Pd}_5\text{Si}$ -type [145] (space group $Imma$, $Z=4$, $a = 0.74025(8)$, $b = 1.2951(2)$, $c = 0.7508(1)$ nm). Rietveld refinement of the structure (see Table 3.8) shows a complete order in the lattice: the atoms solely occupy the corresponding positions of the prototype structure that results in a small homogeneity region (from 10.6 to 11.2 at.% Si after EPMA) of this phase. The crystal structure is presented in Fig. 3.6a in a three-dimensional view along the $[100]$ -axis. The cerium atoms are located at the $4e$ - and $8j$ -site with eight-(Pt2) and ten-platinum (8 Pt2 and 2 Pt1) neighbours, respectively. Platinum atoms occupy the $4c$ - and $16j$ -site, with distances between the Pt1- and Si-site $d_{\text{Pt1-Si}}=0.2447$ nm and $d_{\text{Pt2-Si}}=0.2483$ nm. Si atoms are occupy the $4e$ -site $(0, 1/4, 0.037(2))$ with distances $d_{\text{Si-Ce1}}=0.2978$ nm, $d_{\text{Si-Pt2}}=0.2483$ nm and $d_{\text{Si-Pt1}}=0.2447$ nm,

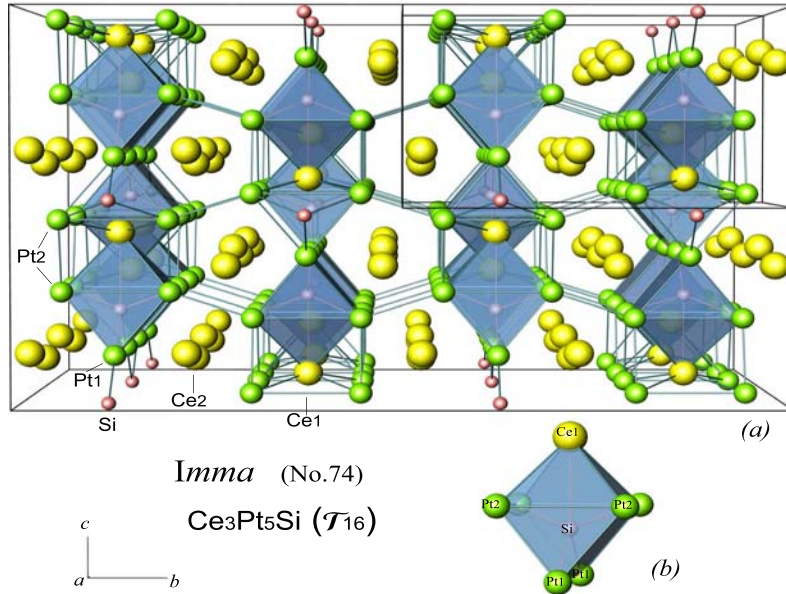


Figure 3.6: Crystal structure of $\text{Ce}_3\text{Pt}_5\text{Si}$ - (τ_{16}) in a three-dimensional view along the [100]-axis.

respectively. As one of the typical structural units for metal rich silicides, Si-atoms are found in a coordination unit formed by two trigonal *prisms* face-connected on a common quadratic base and formed by six platinum atoms and one cerium atom (Fig. 3.6b). The distance between the Pt1- and Pt2-site is $d_{\text{Pt}1-\text{Pt}2}=0.3016$ nm and the distance between the Ce2- and Pt2-site $d_{\text{Ce}1-\text{Pt}2}=0.3237$ nm. Each Ce2 atom is surrounded by 10 platinum atoms. Interatomic distances (Table 3.8) generally agree well with the metallic radii of pure elements. Figure 3.4a shows the EPMA micrograph of alloy $\text{Ce}_{38}\text{Pt}_{55}\text{Si}_7$. In order to characterize the three-phase equilibrium region τ_{16} + CePt + Ce_3Pt_4 in the phase diagram (see the three-phase region No.56) EPMA and powder X-ray diffraction of sample $\text{Ce}_{38}\text{Pt}_{55}\text{Si}_7$ show that three different phase regions exist for which the light gray region correspond to τ_{16} , the dark gray region to the CePt phase and a minor black phase to the Ce_3Pt_4 phase. As shown in Fig. 3.4a EPMA confirmed the main light gray regions with phase composition 33.5Ce55.5Pt11.0Si (in at.%), the dark gray phase with composition 48.9Ce50.2Pt0.9Si (in at.%) and a minor black phase with composition 43.1Ce56.7Pt0.2Si (in at.%).

3.5.6 Rietveld refinement of τ_{17} - Ce_3PtSi_3

Another new phase, which has been established in this study, is the ternary compound Ce_3PtSi_3 . Ce_3PtSi_3 was detected in the alloy with nominal com-

position $\text{Ce}_{43}\text{Pt}_{14}\text{Si}_{43}$. It forms incongruently and consequently the as-cast alloy contains significant amounts of secondary phases $\tau_{13} \text{Ce}(\text{Pt}_x\text{Si}_{1-x})_2$ and CeSi which both decompose slowly during annealing at temperatures from 800 to 1000°C (Fig. 3.3b). In order to overcome this problem, the sample was re-powderized, cold compacted and sintered at 800°C for 20 days. Such heat treatment reduces significantly the amount of the secondary phases to a level below 10 vol.%. Rietveld refinement for Ce_3PtSi_3 yields isotypism with

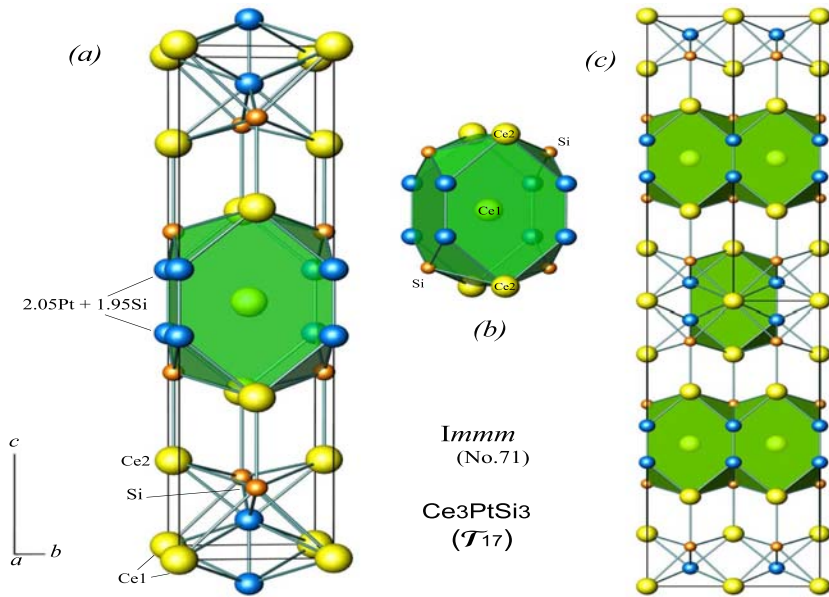


Figure 3.7: Crystal structure of Ce_3PtSi_3 - (τ_{17}) in a three-dimensional view along the [100]-axis.

the $\text{Ba}_3\text{Al}_2\text{Ge}_2$ structure type with orthorhombic unit cell and space group Immm (No.71; $Z=2$, $a= 0.41065(5)$, $b= 0.43221(5)$, $c= 1.8375(3)$ nm). Rietveld refinement of the structure (Table 3.8) shows that platinum and silicon atoms randomly share only the 4i site in ratio 2.05:1.95. Splitting this site into two 2a sites $(0,0,z)$ in the lower symmetry space group $\text{Imm}2$ does not support full order of the structure. Despite statistical distribution of platinum and silicon atoms in the 4i site of Immm , the compound has a limited homogeneity region smaller than 1 at % at 800°C . In order to characterize the new ternary phase Ce_3PtSi_3 , six samples were investigated. The structural data and interatomic distances for Ce_3PtSi_3 are summarised in Table 3.8. The crystal structure is presented in Fig. 3.7a in a three-dimensional view along the [100]-axis.

Parameter	Pt ₃ Si	Ce ₃ Pt ₅ Si(τ_{16})	Ce ₃ Pt ₃ Si(τ_{17})
Phase code		τ_{16}	τ_{17}
space group, Prototype	C2/m, Pt ₃ Ge	Imma, Ce ₃ Pd ₅ Si	Immm, Ba ₃ Al ₂ Ge ₂
Composition, EPMA at.%	Pt _{75.0} Si _{25.0}	Ce _{32.9} Pt _{55.6} Si _{10.6}	Ce _{42.8} Pt _{15.1} Si _{42.1}
Composition, refinement	Pt _{75.0} Si _{25.0}	Ce _{33.3} Pt _{55.5} Si _{11.1} , Ce ₃ Pt ₅ Si	Ce _{42.9} Pt _{14.6} Si _{42.5} , Ce ₃ Pt _{1.02} Si _{2.98}
<i>a</i> [nm], Ge standard	0.7724(2)	0.74025(8)	0.41065(5)
<i>b</i> [nm], Ge standard	0.7767(2); $\beta=133.86$	1.2951(2)	0.43221(5)
<i>c</i> [nm], Ge standard	0.5390(2)	0.7508(1)	1.8375(3)
Data collection	Image plate	Image plate	Image plate
Radiation	CuK α	CuK α	CuK α
Reflections measured	147	247	138
Θ range	8 $\leq 2\Theta \leq 100$	8 $\leq 2\Theta \leq 100$	8 $\leq 2\Theta \leq 100$
Number of variables	24	25	36
R_F	0.098	0.043	0.043
R_I	0.089	0.060	0.052
R_{wp}	0.074	0.047	0.037
R_P	0.058	0.036	0.030
R_e	0.022	0.016	0.020
$\chi^2 = (R_{wp}/R_e)^2$	11.8	8.82	3.37
Atom parameters: [nm]			
Ce1	-	4 Ce1: 4 <i>e</i> (0.1/4, 0.6393(3))	2 Ce1: 2 <i>a</i> (0,0,0)
<i>B_{iso}</i> (10 ² nm ²)	-	0.25(5)	1.34(3)
Ce2	-	8 Ce2: 8 <i>h</i> (0, 0.0502(1), 0.2840(2))	4 Ce2: 4 <i>j</i> (1/2,0, 0.18426(3))
<i>B_{iso}</i> (10 ² nm ²)	-	1.94(4)	1.88(2)
M	4 Pt1: 4 <i>i</i> (0.2843(2),0, 0.6325)	4 Pt1: 4 <i>c</i> (1/4, 1/4, 1/4)	4 M: 2.05(1)Pt+1.95Si:
<i>B_{iso}</i> (10 ² nm ²)	0.98(3)	2.71(6)	4 <i>i</i> (0,0, 0.43564(4)); 1.71(2)
Pt2;	4 Pt2: 16 <i>h</i> (0, 0.2742(2), 1/2)	16 Pt2:	-
<i>B_{iso}</i> (10 ² nm ²)	0.9(3)	16 <i>j</i> (0.2006(1), 0.60806(7), 0.0654(2))	-
Pt3;	4 Pt3: 4 <i>g</i> (0, 0.1870(2),0)	2.17(2)	-
<i>B_{iso}</i> (10 ² nm ²)	0.56(3)	-	-
Si1	4 Si1: 4 <i>i</i> (0.292(2),0, 0.061(2))	4 Si1: 4 <i>e</i> (0.1/4,0.037(2))	4 Si1: 4 <i>j</i> (1/2,0,0.3604(2))
<i>B_{iso}</i> (10 ² nm ²)	2.1(2)	3.2(3)	2.70(9)
Interatomic distances [\AA]; standard deviations generally < 0.0005 nm			
-	Ce1 - 4 Pt2: 0.2931	Ce1 - 2 M: 0.3085	
-	Ce1 - 1 Si1: 0.2978	Ce1 - 4 Si1: 0.3089	
-	Ce1 - 4 Pt2: 0.3237	Ce1 - 1 Si1: 0.3231	
-	Ce1 - 2 Pt2: 0.3457	Ce1 - 4 Ce1: 0.3834	
-	Ce1 - 2 Ce2: 0.3712		
-	Ce2 - 2 Pt2: 0.3151	Ce2 - 8 M: 0.3204	
-	Ce2 - 4 Pt2: 0.3014	Ce2 - 4 Si1: 0.3354	
-	Ce2 - 1 Si1: 0.3182		
-	Ce2 - 2 Pt1: 0.3189		
-	Ce2 - 2 Pt2: 0.3221		
-	Ce2 - 1 Ce2: 0.3489		
-	Ce2 - 1 Ce1: 0.3712		
-	Ce2 - 2 Ce2: 0.3738		
-	Pt1 - 2 Si1: 0.2447	M - 1 M: 0.2363	
-	Pt1 - 4 Pt2: 0.3061	M - 2 Si1: 0.2473	
-	Pt1 - 4 Ce2: 0.3189	M - 2 Ce1: 0.3085	
-	Pt1 - 2 Ce1: 0.3457	M - 4 Ce2: 0.3204	
-	Pt1 - 2 Pt1: 0.3703		
-	Pt2 - 1 Pt2: 0.2863		
-	Pt2 - 1 Si1: 0.2483		
-	Pt2 - 1 Ce1: 0.2931		
-	Pt2 - 1 Pt2: 0.2963		
-	Pt2 - 1 Pt2: 0.2972		
-	Pt2 - 1 Ce2: 0.3014		
-	Pt2 - 1 Pt1: 0.3016		
-	Pt2 - 1 Ce2: 0.3104		
-	Pt2 - 1 Ce2: 0.3151		
-	Pt2 - 1 Ce2: 0.3221		
-	Pt2 - 1 Ce1: 0.3237		
-	Si1 - 2 Pt1: 0.2447	Si1 - 2 M: 0.2473	
-	Si1 - 4 Pt2: 0.2483	Si1 - 4 Ce1: 0.3089	
-	Si1 - 1 Ce1: 0.2978	Si1 - 1 Ce1: 0.3231	
-	Si1 - 2 Ce2: 0.3182	Si1 - 2 Ce2: 0.3354	

Figure 3.8: Crystallographic data for Pt₃Si, Ce₃Pt₅Si(τ_{16}) and Ce₃Pt₃Si(τ_{17}) (X-ray powder diffraction, room temperature data) standardized with program Structure Tidy [152].

Chapter 4

Ge-based skutterudites: $\{\text{Sr}, \text{Ba}, \text{Eu}, \text{Th}, \text{U}\}\text{Pt}_4\text{Ge}_{12}$; crystal structure and physical properties

4.1 $\{\text{Sr}, \text{Ba}, \text{Eu}, \text{Th}, \text{U}\}\text{Pt}_4\text{Ge}_{12}$ System

4.1.1 Crystal structure

$\{\text{Sr}, \text{Ba}, \text{Th}, \text{U}\}\text{Pt}_4\text{Ge}_{12}$ and $\text{EuPt}_4\text{Ge}_{12}$ were prepared by argon arc melting from stoichiometric amounts of high purity ingots of alkaline earths and Eu plus a pre-melted $\text{Pt}_4\text{Ge}_{12}$ master alloy. Whilst $\{\text{Sr}, \text{Ba}, \text{Th}\}\text{Pt}_4\text{Ge}_{12}$ were subsequently heat treated in evacuated quartz capsules at 800°C for two weeks, $\text{UPt}_4\text{Ge}_{12}$ has to be directly quenched from the melt with nominal composition $\text{U}_{0.8}\text{Pt}_4\text{Ge}_{12}$. Phase purity and lattice parameters were checked by EPMA and x-ray diffraction. Phase purity was achieved in several steps by careful compensation of alkaline earth or europium losses during melting. The single crystals, mechanically isolated from the crushed alloys, were inspected on an AXS-GADDS texture goniometer prior to X-ray intensity data collection on a four-circle Nonius Kappa diffractometer equipped with a CCD area detector employing Graphite monochromated MoK α radiation ($\lambda = 0.071073 \text{ nm}$). Crystal structures were studied at room temperature for $\{\text{Sr}, \text{Ba}, \text{Th}, \text{U}\}\text{Pt}_4\text{Ge}_{12}$ but X-ray intensity data for $\text{BaPt}_4\text{Ge}_{12}$ were recorded at three temperatures: 100, 200 and 300 K. The crystal structure of $\{\text{Sr}, \text{Ba}, \text{Th}\}\text{Pt}_4\text{Ge}_{12}$ (from Rietveld refinements) and $\text{UPt}_4\text{Ge}_{12}$ (from Kappa-CCD single crystal X-ray data at 300 K, 200 K and 100 K) was found to be in all cases a body-centered cubic lattice with space group $Im\bar{3}$, (No. 204), isotypic with the filled skutterudite type $\text{LaFe}_4\text{Sb}_{12}$ [41]. Rietveld refinements

of the X-ray intensities with the space group $I\bar{m}\bar{3}$ in all cases converged satisfactorily for a fully ordered atom arrangement with respect to the atom site distribution among Sr, Ba and Eu atoms [54, 55, 56]. No extra reflections

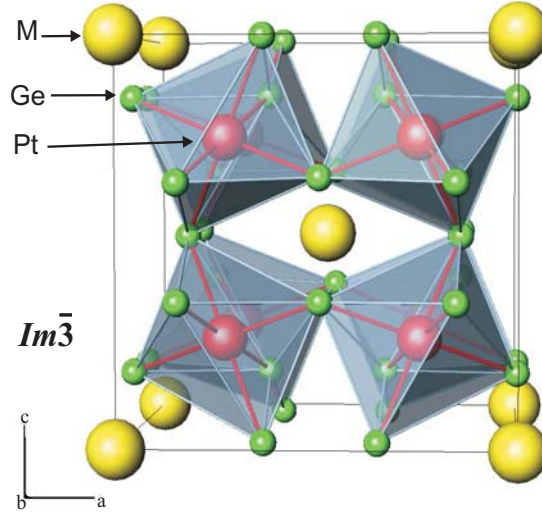


Figure 4.1: The crystal structure of MPt₄Ge₁₂ ($M=\{\text{Sr}, \text{Ba}, \text{Eu}, \text{Th}, \text{U}\}$) revealing the Ge-framework made by tilted corner connected octahedra centered by Pt-atoms. Eu-atoms are at the centers of the Ge-icosahedra.

indicating a supercell were detected in the crystals investigated. Refinements converged to low residual values generally below $R_F = 0.07$. Residual electron densities less than $2.5e/\text{\AA}^3$ for $\{\text{Sr, Ba}\}\text{Pt}_4\text{Ge}_{12}$ and less than $3.5e/\text{\AA}^3$ for a lower quality crystal EuPt₄Ge₁₂ finally provide featureless difference-Fourier maps $F_{obs} - F_{calc}$ for atom structures without any sign for deviation from full occupation. The results of the refinements for all three crystals {Sr, Ba, Eu}Pt₄Ge₁₂ are compared in Table 4.1. The crystal structure of MPt₄Ge₁₂ ($M=\{\text{Sr}, \text{Ba}, \text{Eu}, \text{Th}, \text{U}\}$) are shown in three dimensional view in Fig. 4.1. X-ray powder spectrum and the corresponding Rietveld profile are shown in Fig. 4.2 for BaPt₄Ge₁₂ and SrPt₄Ge₁₂ alloy (taken with Cu-K α_1 radiation in $8^\circ < 2\theta < 100^\circ$). The minor differences between observed $Y_{obs.}$ and the calculated intensities $Y_{calc.}$ prove the model applied as well as the sample quality (compare figures 4.2a and b). Structure and lattice parameters are collected in Table 4.1. Due to cubic low Laue symmetry (absence of 4-fold axes) the Ge-octahedra are not regular but as seen along the three-fold axes [111] are composed of two equilateral triangles, which are rotated against each other by 180° . Both types of distances along the octahedral edges (within the two equilateral triangles and within the six isosceles of the non regular octahedron) are larger than 0.3 nm and thus are no strong bonding Ge-Ge distances: Tight bonding, however, is established not only between Ge and Pt atoms at

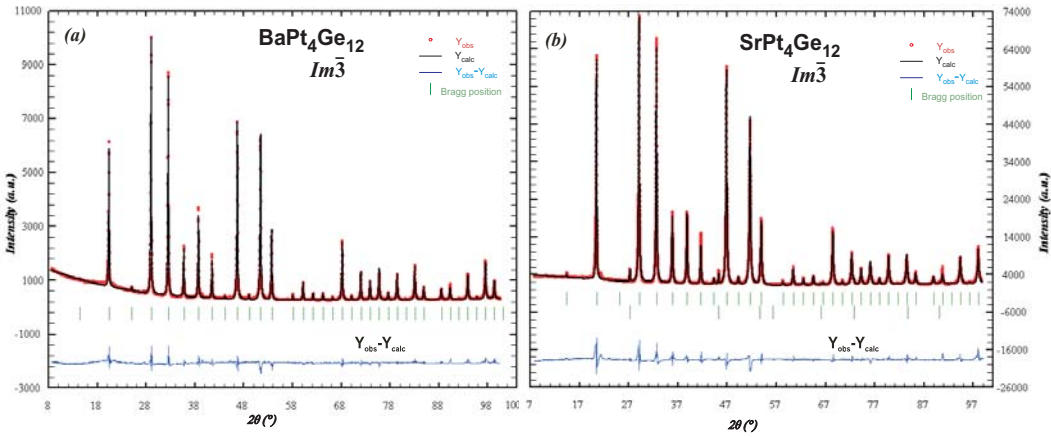


Figure 4.2: X-ray pattern of the skutterudite $\{\text{Sr}, \text{Ba}\}\text{Pt}_4\text{Ge}_{12}$. The solid line derives from the Rietveld refinement and $Y_{\text{obs}} - Y_{\text{calc}}$ is the intensity difference between experimental data and Rietveld calculations

the center of the Ge-octahedra but also to some extent between filler atoms (Eu or alkaline earth atoms) at the centers of Ge-icosahedra, thereby documenting the true intermetallic nature of the Ge-based skutterudites. In fact Ge-atoms exhibit only two homonuclear tight bonds to neighbouring octahedra tilted towards each other, altogether resulting in open Ge_4 -rectangles. As seen from data in Table 4.1 (see Refs. [54, 55, 56]) the Eu compound shows a volume only slightly smaller than isostructural $\text{SrPt}_4\text{Ge}_{12}$ indicating divalent Europium like an alkaline earth element. Although both, skutterudites and clathrates (see chapter 5), are considered as cage-compounds, bonding is essentially different in both structure types: whereas Ge atoms in skutterudites do not construct a covalently four-bonded framework but rather form strong bonds to octahedral and icosahedral filler atoms, clathrate type I structures do exist as four-bonded Ge-framework with the large filler atoms embedded in the framework cages. Occupation factors were refined, corresponding to a full occupancy of the Pt and Ge sublattices. Although not revealed from single crystal refinement, minor deviations (up to 3 %) from full occupancy are possible for the Ba and Sr atoms. Since the size of the Ge-framework is significantly smaller than the corresponding Sb-framework in $\text{Ba}_{0.3}\text{Co}_4\text{Sb}_{12}$ [43, 153], effective bonding between the framework cages (two icosahedra per unit cell) and the Ba(Sr)-center atoms is ensured. As a consequence of this stronger bond between cage and guest atom, we observe very regular thermal atom displacement factors (ADP) on all atoms. The temperature dependences of ADP's in the temperature region from 100 to 300 K reveal for all atoms similar trends: pronounced rattling modes caused by the heavy guest atoms

Parameter	BaPt ₄ Ge ₁₂	SrPt ₄ Ge ₁₂	EuPt ₄ Ge ₁₂
Crystal size <i>a</i> [nm], from Guinier(Cu-K α 1)	100×70×80 μm^3 0.86928(2)	70×70×100 μm^3 0.86601(2)	54×70×95 μm^3 0.86435(1)
μ_{abs} [mm ⁻¹]	72.29	74.20	75.31
Data collection 2 θ ($^\circ$)	2≤2 Θ ≤72.5; 70 sec/frame	2≤2 Θ ≤72.54; 70 sec/f.	2≤2 Θ ≤72.33; 70 sec/f.
Total number of frame	246 for 5 sets	236 for 5 sets	236 for 5 sets
Reflections in refinement	273 F_o ≤4 $\sigma(F_o)$ of 309	236 F_o ≤4 $\sigma(F_o)$ of 309	216 F_o ≤4 $\sigma(F_o)$ of 309
mosaicity	<0.47	<0.48	<0.45
Number of variables	11	11	11
Reflections measured	84	81	86
R_F^2	0.0172	0.0192	0.0317
R_{Int}	0.046	0.044	0.068
$wR2$	0.0456	0.0406	0.089
GOF	1.145	1.124	1.053
Extinction (Zachariasen)	0.0012(1)	0.00105(8)	0.0003(2)
Atom parameters			
M in site 2a (0,0,0); occ. $U_{11}=U_{22}=U_{33}$	1.00(1) 0.0075(2)	1.00(1) 0.0118(3)	1.00(1) 0.0142(3)
Pt in site 8c ($\frac{1}{4}, \frac{1}{4}, \frac{1}{4}$); occ. $U_{11}=U_{22}=U_{33}$ $U_{23}=U_{13}=U_{12}$	1.00(1) 0.0061(1); 0.0003(1)	1.00(1) 0.0069(1); 0.0005(1)	1.00(1) 0.0090(2); 0.0004(1)
Ge in site 24g (0,y,z); occ. <i>y, z:</i> $U_{11}; U_{22}$ $U_{33}; U_{23}$ $U_{13}=U_{12}$	1.00(1) 0.15302(7), 0.35681(6) 0.0073(2); 0.0120(3) 0.0078(3); -0.0002(2) 0.000	1.00(1) 0.15197(7), 0.35536(6) 0.0073(3); 0.0124(3) 0.0095(3); 0.0003(2) 0.000	1.00(1) 0.1512(1), 0.3544(1) 0.0102(4); 0.0135(4) 0.0120(4); 0.0001(3) 0.000
Residual density; max; min	2.45; -1.56	2.39; -1.90	4.38; -3.65
Principal mean square atomic displacements U_{ii}	Ba 0.0075 0.0075 0.0075 Pt 0.0066 0.0058 0.0058 Ge 0.0120 0.0078 0.0073	Sr 0.0118 0.0118 0.0118 Pt 0.0078 0.0064 0.0064 Ge 0.0124 0.0095 0.0073	Eu 0.0142 0.0142 0.0142 Pt 0.0099 0.0086 0.0086 Ge 0.0135 0.0120 0.0102
Interatomic distances [nm]; standard deviations generally < 0.0005 nm			
M - 12 Ge	0.3375	0.3347	0.3430
Pt - 6 Ge	0.2509	0.2498	0.2493
- 2 M	0.3764	0.3750	0.3750
Ge - 2 Pt	0.2509	0.2498	0.2493
- 1 Ge	0.2489	0.2505	0.2517
- 1 Ge	0.2660	0.2632	0.2614
- 1 M	0.3375	0.3347	0.3330

Table 4.1: X-Ray single crystal data at room temperature for {Sr, Ba, Eu}Pt₄Ge₁₂, space group $Im\bar{3}$, (No. 204), LaFe₄Sb₁₂-type. Standardized with program Structure Tidy [152].

in Sb-based skutterudites are absent in {Sr, Ba}Pt₄Ge₁₂, compare Fig.4.3.

In case of {Th, U}Pt₄Ge₁₂ occupation factors were refined, corresponding to a full occupancy of the actinoid, Pt and Ge sublattices. Although the Ge-icosahedra are significantly smaller than the corresponding Sb-framework and therefore effective bonding between the framework cages and the Th-center atoms is ensured, temperature dependent single crystal X-ray data for UPt₄Ge₁₂ unambiguously defined a strong temperature dependency of atomic displacement parameters (ADP) in the temperature region from 100 to 300 K for the smaller uranium atoms. Thus typical rattling modes caused by uranium as filler atoms are derived yielding an Einstein temperature of $\theta_E \approx 59$ K. Structure and lattice parameters are collected in Table 4.2.

4.1.2 Lattice dynamics of {Sr, Ba, Eu}Pt₄Ge₁₂

Thermal expansion of lattice parameters for BaPt₄Ge₁₂ is plotted in Fig. 4.3a shows a smooth variation from 100 to 300 K indicating stability of

Property	$\text{ThPt}_4\text{Ge}_{12}$	$\text{UPt}_4\text{Ge}_{12}$
Lattice parameter a @300 K [nm]	0.85931(3)	0.85887(4)
Ge 24g site: y	0.1515(3)	0.15048(9)
Ge 24g site: z	0.3556(3)	0.35275(9)
$R_{F2} = \sum F_o^2 - F_c^2 / \sum F_o^2$	0.057	0.026
$U_{eq}(\text{Th,U})$ [nm 2]	0.00012(1)	0.000210(3)
$U_{eq}(\text{Pt})$ [nm 2]	0.00009(1)	0.000079(2)
$U_{eq}(\text{Ge})$ [nm 2]	0.00010(2)	0.000102(1)

Table 4.2: Crystallographic properties of $\text{ThPt}_4\text{Ge}_{12}$ and $\text{UPt}_4\text{Ge}_{12}$ which crystallize in the skutterudite structure: space group $Im\bar{3}$, (No. 204); Th and U are at the $2a$ (0, 0, 0) sites, Pt at the $8c$ ($\frac{1}{4}, \frac{1}{4}, \frac{1}{4}$) sites, and Ge at the 24g (0, y, z) sites. U_{eq} is a mean value of the atomic displacement ellipsoid.

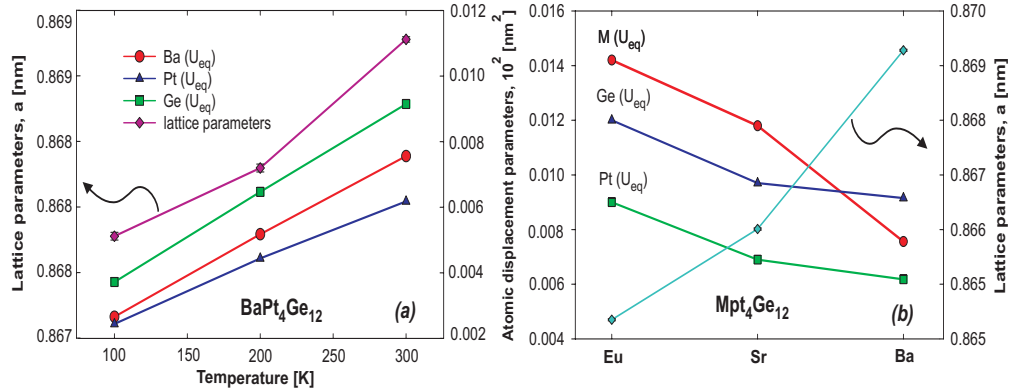


Figure 4.3: (a) Atom displacements parameters (APD) and lattice parameters versus temperature for $\text{BaPt}_4\text{Ge}_{12}$. (b) Atom displacements parameters (APD) and lattice parameters for $\{\text{Sr, Ba, Eu}\}\text{Pt}_4\text{Ge}_{12}$.

the skutterudite phase. As the size of the Ge-framework for the Ge-based compounds $\{\text{Sr, Ba, Eu}\}\text{Pt}_4\text{Ge}_{12}$ is significantly smaller than that for corresponding Sb-based skutterudites [43, 153, 154, 184], effective bonding between the Ge-framework cages (two icosahedra per unit cell) and the Eu, Sr, Ba-center atoms provides rather small thermal atom displacement parameters on all atoms. The temperature dependencies of ADP's scale with the atom masses and furthermore are practically constant for all atoms of the lattice (see Fig.4.3a). Thus no special rattling effect can be seen for Ba-atoms. The situation is similar for all compounds with Sr, Ba and Eu, although Eu and Sr show ADP's higher than Ge-atoms (see Refs. [54, 55, 56]) (see Fig.4.3b). We also tried to synthesize $\text{CaPt}_4\text{Ge}_{12}$ but our attempts were unsuccessful insofar as no ternary skutterudite compound exists in the Ca-Pt-Ge system, however,

EPMA and Rietveld refinements on Ba_{1-x}Ca_xPt₄Ge₁₂ alloys for various values of x , heat treated at 800°C, confirm a maximal solid solubility limit of about 20 mol % Ca for {Ba_{1-x}Ca_x}Pt₄Ge₁₂ with $a = 0.86842(1)$ nm.

4.1.3 Physical Properties; Electrical resistivity

Temperature dependent electrical resistivities $\rho(T)$ of {Sr, Ba, Ca, Th Eu}Pt₄Ge₁₂ and UPt₄Ge₁₂ are plotted in Figs. 4.4-4.5-4.6 and 4.8. Superconductivity is found for BaPt₄Ge₁₂ and SrPt₄Ge₁₂ from resistivity measurements using polycrystalline samples at the critical temperatures 5.3 K and 5.1 K, respectively. The normal state regions, $T > T_c$ of these ternary compounds do not behave like simple metals, since the standard model of the electrical resistivity of metallic systems, i.e., the Bloch-Grüneisen formula is not applicable. Such observations were made in many superconducting materials and may be attributed to a substantial electron-phonon interaction strength, responsible for the formation of Cooper pairs in conventional superconductors. Rather,

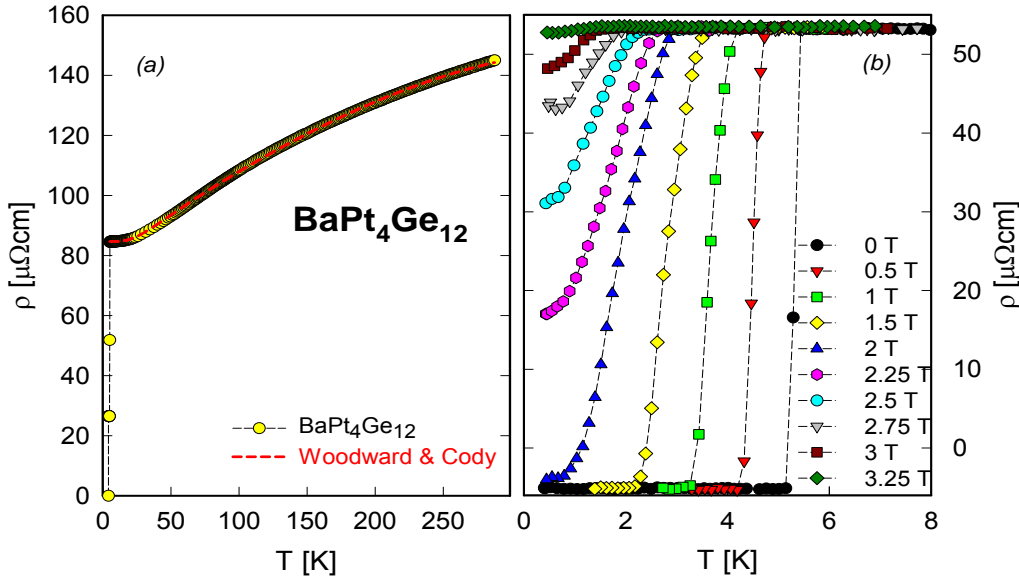


Figure 4.4: (a) Temperature dependent electrical resistivity ρ of BaPt₄Ge₁₂ (Dashed line is least squares fits of the data according to Woodard and Cody formula (Eqn.A.1)). (b) The field dependence electrical resistivity of $\rho(T)$ of BaPt₄Ge₁₂ at various applied magnetic fields.

the overall $\rho(T)$ -dependence of BaPt₄Ge₁₂ and SrPt₄Ge₁₂ skutterudites follows the model of Woodard and Cody [155], which initially was applied to A15 superconductors such as Nb₃Sn. This model reads,

$$\rho(T) = \rho_0 + \rho_1 T + \rho_2 \exp(-T_0/T), \quad (4.1)$$

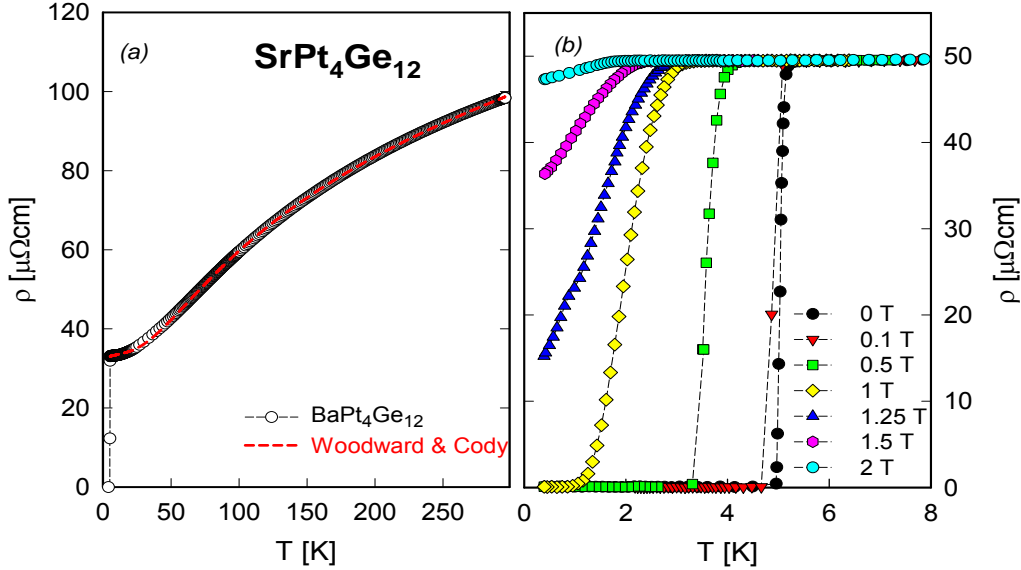


Figure 4.5: (a) Temperature dependent electrical resistivity ρ of $\text{SrPt}_4\text{Ge}_{12}$ (Dashed lines are least squares fits of the data according to the Woodward and Cody formula (Eqn.4.1). (b) The field dependence electrical resistivity of $\rho(T)$ ρ of $\text{SrPt}_4\text{Ge}_{12}$ at various applied magnetic fields.

where ρ_0 is the residual resistivity; ρ_1 , ρ_2 and T_0 are material dependent parameters. The second and third terms of Eqn. 4.1 represent the high and low temperature limits of the occupation number of a particular phonon, which assists in interband scattering according to Wilson's model [156]. A more detailed discussion on the temperature dependent resistivity of various superconductors in the normal state region is also given in Ref. [156]. Least squares fits of this model to the experimental data of $\{\text{Sr}, \text{Ba}, \text{Ca}, \text{Eu}, \text{Th}\}\text{Pt}_4\text{Ge}_{12}$ are shown in figures 4.4a-4.5a, 4.6a and 4.7a as a dashed lines, revealing reasonable agreement for characteristic temperatures of the order of 120 K. The least squares fits parameters for all compounds are summarised in Table 4.1.3. The differences of the residual resistivities may correspond to small differences in the filling of the $2a$ -sites by Ba or Sr. In case of the smaller atom Sr, filling seems to be more complete. Dashed lines in Figs. 4.4a-4.5a are least squares fits of the data according to the Eqn. 4.1.

Temperature dependent resistivity measurements of $\text{SrPt}_4\text{Ge}_{12}$ and $\text{Ba}_{0.8}\text{Ca}_{0.2}\text{Pt}_4\text{Ge}_{12}$ indicated superconductivity (SC) at $T_c=5.1$ and 5.2 K, respectively. The temperature dependent electrical resistivity $\rho(T)$ of $\text{SrPt}_4\text{Ge}_{12}$ and $\text{Ba}_{0.8}\text{Ca}_{0.2}\text{Pt}_4\text{Ge}_{12}$ are displayed in figures 4.5 and 4.6.

The suppression of superconductivity (SC) with rising external magnetic fields checked by resistivity measurements down to 300 mK and displayed

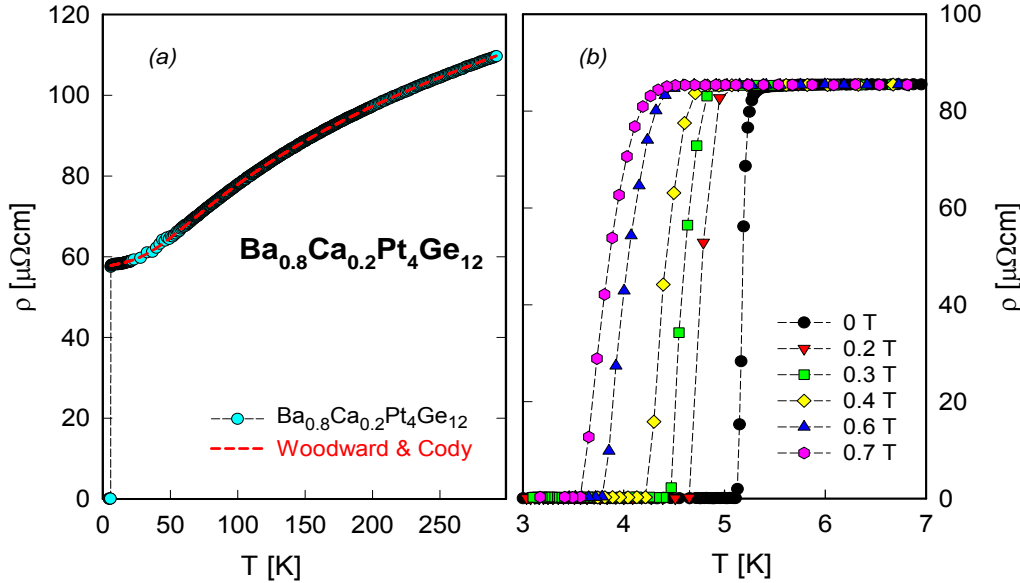


Figure 4.6: (a) Temperature dependent electrical resistivity ρ of $\text{Ba}_{0.8}\text{Ca}_{0.2}\text{Pt}_4\text{Ge}_{12}$ (Dashed line is least squares fits of the data according to the Woodard & Cody formula (Eqn.4.1). (b) The field dependence electrical resistivity of $\rho(T)$ ρ of $\text{Ba}_{0.8}\text{Ca}_{0.2}\text{Pt}_4\text{Ge}_{12}$ at various applied magnetic fields.

in Figs. 4.4b-4.5b, 4.6b. It is obvious from the zero-resistance points of the curves ($\rho(T, H) = 0$) that $T_c(H)$ varies linearly with the applied field. The critical temperatures gradually diminishes with rising field strength and already in a field of 2.25 T drops below 0.35 K in case of $\text{BaPt}_4\text{Ge}_{12}$. The same situation was observed in other compounds like in $\text{SrPt}_4\text{Ge}_{12}$ and the critical temperatures reduces with rising magnetic field and in a field of 1.25 T drops below 0.35 K.

	ρ_0 [$\mu\Omega\text{cm}$]	ρ_1 [$\mu\Omega\text{cm}$]	ρ_2 [$\mu\Omega\text{cm}$]	T_0 [K]	T_c [K]
BaPt ₄ Ge ₁₂	60.66	0.071	37.01	123.93	5.35
SrPt ₄ Ge ₁₂	32.66	0.078	64.84	121.58	5.1
EuPt ₄ Ge ₁₂	26.17	0.072	64.82	129.04	$T_N=1.7$
{Ba _{0.8} Ca _{0.2} }Pt ₄ Ge ₁₂	57.37	0.075	47.38	128.92	5.2
ThPt ₄ Ge ₁₂	2.91	0.25	113.4	131.7	4.76

Table 4.3: Least squares fits parameters result of electrical resistivity data of {Sr, Ba, Th}Pt₄Ge₁₂ and {Ba_{0.8}Ca_{0.2}}Pt₄Ge₁₂ from the model according to Woodard & Cody model (Eqn.A.1).

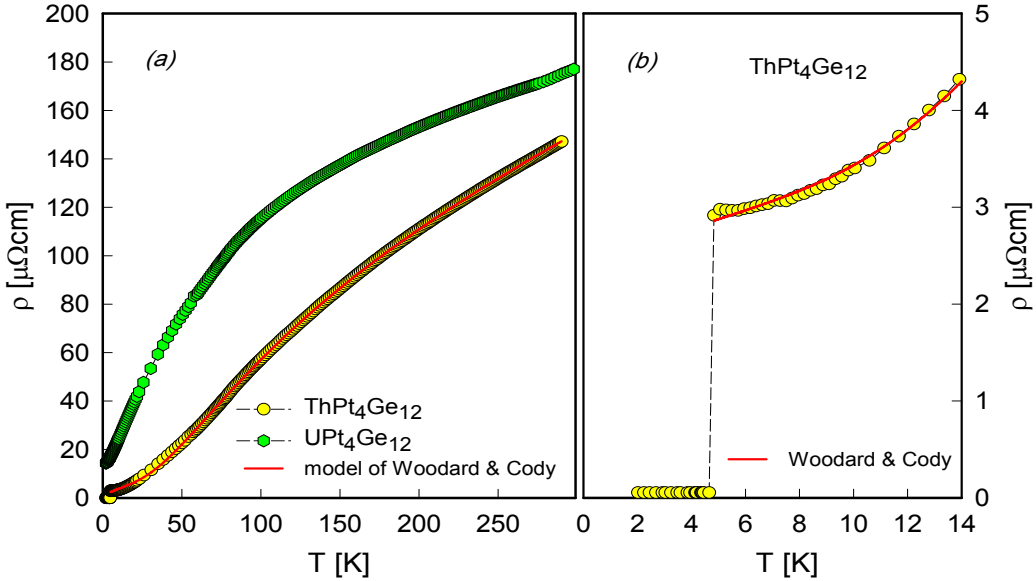


Figure 4.7: (a) Temperature dependent electrical resistivity ρ of $\text{ThPt}_4\text{Ge}_{12}$ and $\text{UPt}_4\text{Ge}_{12}$. The solid line is a least squares fit of the data according to the Woodard and Cody formula (Eqn.A.1). (b) Low temperature resistivity details evidencing superconductivity of $\text{ThPt}_4\text{Ge}_{12}$.

The application of a magnetic field suppresses the superconducting transition of $\text{BaPt}_4\text{Ge}_{12}$ (Fig. 4.4b), revealing an upper critical field of about 2 T, while for $\text{SrPt}_4\text{Ge}_{12}$ the upper critical field $H_{c2}(0) \approx 1$ T (Fig. 4.5b).

In Fig. 4.8a the metallic like resistivity behaviour and transition temperatures into the superconducting state are compared for $\{\text{Sr}, \text{Ba}, \text{Eu}, \text{Th}\}\text{Pt}_4\text{Ge}_{12}$. Temperature dependent resistivity measurements of $\text{UPt}_4\text{Ge}_{12}$ do not exhibit superconductivity down to 1.9 K. Results of resistivity measurements is shown in Fig. 4.8b. The overall $\rho(T)$ features of $\text{UPt}_4\text{Ge}_{12}$ turn out to be different at low temperatures; $\rho(T)$ behaves according to

$$\rho(T) = \rho_0 + A \cdot T^n, \quad (4.2)$$

where ρ_0 is residual resistivity in [$\mu\Omega\text{cm}$]. The inset in Fig. 4.8b shows a least squares fits to $\text{UPt}_4\text{Ge}_{12}$ according to Eqn.4.2, revealing $\rho_0 = 13.8 \mu\Omega\text{cm}$, $A = 0.36 \mu\Omega\text{cm}/\text{K}^{1.5}$ and $n = 1.5$. The latter refers to distinct deviations from a Fermi liquid ground state due to strong spin fluctuations, which are evident also from a large value of the Sommerfeld constant $\gamma = 156 \text{ mJ/molK}^2$ (see below). Moreover, classical spin fluctuation systems like YCo_2 [157] or UAl_2 exhibit at elevated temperatures a tendency towards saturation [158], which can also be conceived from Fig. 4.8b for $\text{UPt}_4\text{Ge}_{12}$.

In Fig. 4.7a the temperature dependent resistivity $\rho(T)$ of $\text{UPt}_4\text{Ge}_{12}$ is

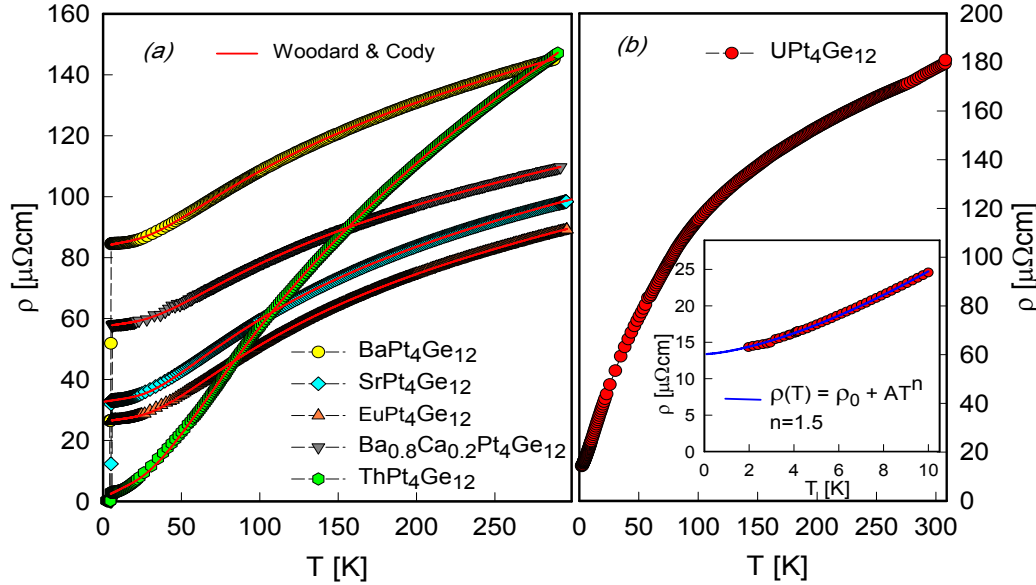


Figure 4.8: (a) A comparison of temperature dependent electrical resistivity ρ of $\{\text{Sr,Ba,Eu,Th}\}\text{Pt}_4\text{Ge}_{12}$ in the normal state regions, $T > T_c$ up to 300 K. The solid lines are least squares fits of the data according to the Woodard and Cody formula (Eqn.A.1). (b) Temperature dependent resistivity ρ of UPt₄Ge₁₂. The inset shows low temperature details and the solid line is a least squares fits based on the model as explained in the text.

compared to that of ThPt₄Ge₁₂. This significant difference in the ground states of similar compounds is already reflected in the temperature dependences of the resistivity in the normal state region. The resistivity measurements of ThPt₄Ge₁₂ indicated superconductivity at $T_c \approx 4.8$ K, but the residual resistivity values strongly differ from each other and reach values about $3 \mu\Omega\text{cm}$ at 4.76 K (see Fig. 4.8b).

4.1.4 Specific heat and phonon density of states

The Low temperature specific heat of the filled skutterudites BaPt₄Ge₁₂ and SrPt₄Ge₁₂ determined for various external magnetic fields are shown in a C_p/T vs. T representation in Fig. 4.9. The jump of $C_p(T)$ below 6 K evidences bulk superconductivity in all cases. As demonstrated by the resistivity measurements (see figures 4.4, 4.5 and 4.6) a magnetic field of 3 T is sufficient to suppress superconductivity to determine the normal state heat capacity. Assuming that the normal state heat capacity of metallic compounds at low temperature follows for $C_p(T) = C_{el} + C_{ph} \equiv \gamma T + \beta T^3$ ($\theta_D = \sqrt[3]{(1944 \times n)/\beta}$) where γ is the Sommerfeld coefficient and β is proportional to the Debye tem-

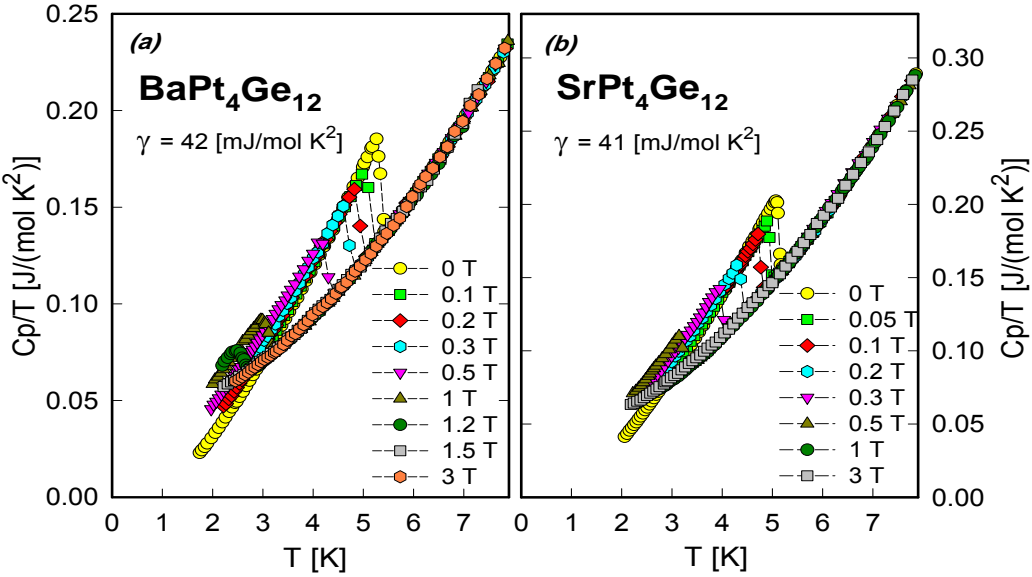


Figure 4.9: (a) Temperature dependent specific heat C_p of $\text{BaPt}_4\text{Ge}_{12}$, (b) $\text{SrPt}_4\text{Ge}_{12}$ plotted as C_p/T vs. T for various magnetic fields up to 3 T.

perature θ_D , least squares fits reveal $\gamma = 42$ mJ/molK² and $\theta_D^{LT} = 247$ K for $\text{BaPt}_4\text{Ge}_{12}$ and $\gamma = 41$ mJ/molK² and $\theta_D^{LT} = 220$ K for $\text{SrPt}_4\text{Ge}_{12}$ compound. It is worth to be noted that the Debye temperature of $\text{BaPt}_4\text{Ge}_{12}$ is larger than that of $\text{SrPt}_4\text{Ge}_{12}$. In general, however, materials with smaller masses exhibit larger Debye temperatures. This anomaly may correspond to the fact that, while the volume of the unit cells of both compounds differ by only 1%, the atomic volumes of Sr and Ba differ by about 12 %. This causes a weaker bonding of Sr to the framework, hence a weaker force constant may result in lower values of θ_D . An idealization of the heat capacity anomaly under the constraint of entropy balance between the superconducting and the normal state yields $T_c = 5.35$ and 5.1 K for the Ba and Sr based compounds, respectively. The heat capacity measurement for $\text{ThPt}_4\text{Ge}_{12}$ is plotted in Fig. 4.10a as C_p/T vs. T for various externally magnetic fields up to 0.2 T. The jump of $C_p(T)$ below 5 K evidences bulk superconductivity. Idealizing the specific heat anomaly under the constraint of entropy balance between the superconducting and the normal state we arrive at $T_c = 4.75$ K (to compare see Fig. 4.16a). As shown in Fig. 4.16a the entropy balance between the superconducting and the normal state defines $C_p/T(T = 0) = 35$ mJ/molK² and thus to extrapolate the superconducting and normal state heat capacity (i.e., measurements at 0 and 0.2 T, respectively) (dashed lines in Fig. 4.10a), indeed yielding $\Delta S(T = T_c) = 0$. To derive these extrapolations, the phonon contribution is taken from the model for phonon density of states [91, 92]

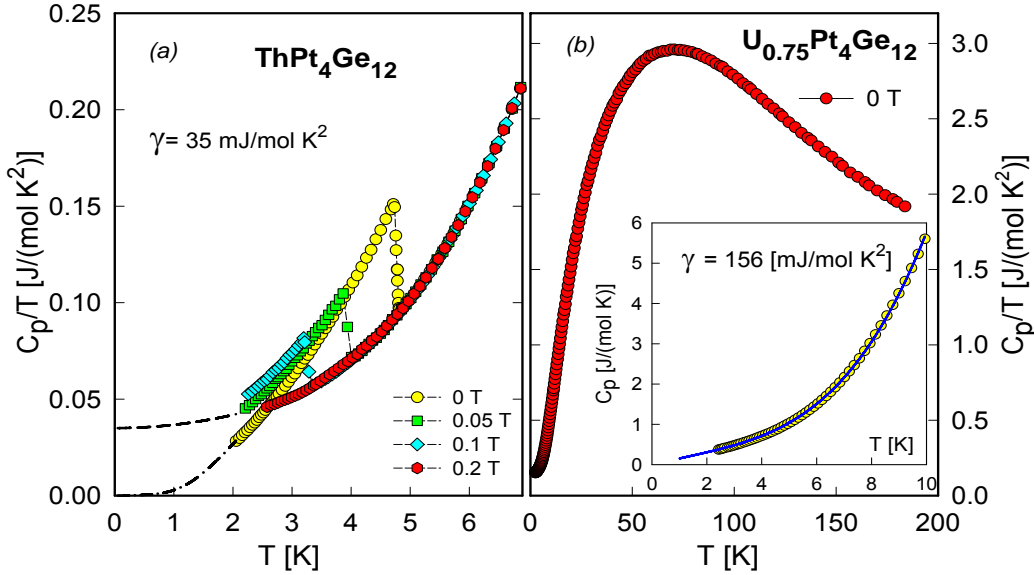


Figure 4.10: (a) Temperature dependent specific heat of ThPt₄Ge₁₂ plotted as C_p/T vs. T in various externally applied magnetic fields. The dashed and the dashed-dotted lines are extrapolations from the normal - and superconducting states, respectively. (b) Temperature dependent specific heat of UPt₄Ge₁₂ plotted as C_p/T vs. T . The inset shows low temperature details and the solid line is a least squares fit based on a spin fluctuation model.

(see discussion in section 4.1.5 and Fig. 4.12b). The sum curve is displayed as dashed line. As demonstrated by the specific heat measurements a magnetic field of 0.2 T is sufficient to suppresses superconductivity of ThPt₄Ge₁₂. Thus, the 0.2 T measurement represents the normal state heat capacity. The low temperature fit of the 0.2 T data allows to extract the Sommerfeld value $\gamma=35 \text{ mJ/molK}^2$ and the Debye temperature $\theta_D^{LT}=260 \text{ K}$ for ThPt₄Ge₁₂.

The temperature dependent specific heat C_p of UPt₄Ge₁₂ is plotted in Fig. 4.10b as C_p/T vs. T . The absence of any low temperature anomalies evidences the lack of a phase transition, in agreement with the $\rho(T)$ data in figures 4.8b and 4.7a. The inset in Fig. 4.10b shows C_p/T for T below 10 K. A standard procedure to isolate the magnetic contribution via subtraction of $C_p(T)$ of isomorphous nonmagnetic ThPt₄Ge₁₂ fails, since both C_p functions intersect each other, i.e., $C_p(T)$ of nonmagnetic ThPt₄Ge₁₂ surmounts that of UPt₄Ge₁₂ for $T > 12 \text{ K}$. The observation of such a crossover is not a unique feature of the {U,Th}Pt₄Ge₁₂ systems but frequently occurs in isostructural pairs of {La, Ce} or complementary {Yb, Lu} compounds. In all these cases, common explanations such as mass or volume differences do not apply, rather, referring to a magnetic origin [59]. Although the phonon spectra of both

compounds are more complex than that of a simple Debye solid, we attempted to fit the low temperature data of $\text{UPt}_4\text{Ge}_{12}$ with the ansatz,

$$C_p(T) = \gamma T + \beta T^3 + \delta T^3 \ln(T/T^*), \quad (4.3)$$

where the latter term accounts for spin fluctuations and T^* is characteristic temperature. Satisfactory agreement is found for $\gamma = 156 \text{ mJ/molK}^2$ and $T^* = 4.7 \text{ K}$ (solid line, inset Fig. 4.10b), suggesting spin fluctuations in the nearly localized regime. The least squares fit in inset Fig. 4.10b is based on the spin fluctuation model (Eqn.4.3); the experimental heat capacity $C_p(T)$ data reveals $\beta = 0.0021$ and $\delta = 0.0025$.

Although the combination of lattice and magnetic contributions does not allow a detailed analysis of lattice dynamics in $\text{UPt}_4\text{Ge}_{12}$, it should be noted that from temperature dependent ADP parameters an Einstein mode for the U atoms was found at $\theta_E = 59 \text{ K}$, in close analogy to the phonon spectrum derived from the specific heat analysis of $\text{ThPt}_4\text{Ge}_{12}$ [59].

4.1.5 Phonon specific heat

As phonon dynamics is a key feature for the occurrence of BCS superconductivity, a detailed analysis of the specific heat allows a definition of those phonon modes responsible for Cooper pairing. Significant deviations from the simple Debye model indicate a rather complicated phonon spectrum for this family of skutterudites. The spectrum is supposed to be composed of background vibrations originating from the cage-like structure represented by a Debye spectrum and, additionally, from specific phonon branches which are represented by Einstein-like contributions. In order to qualitatively and quantitatively describe the lattice dynamics, we have adopted a model which incorporates some fine structure in the phonon density of states as described in chapter 1.4 [91, 92]. In a first step the electronic contribution to the specific heat is subtracted from the measured specific heat data. In the second step an appropriate phonon density of states $F(\omega)$ has to be found, which explains specific heat data [159].

The latter is represented by a spectral function $F(\omega)$, allowing to express the heat capacity in the general form by Eqn. A.11. The most common assumptions on $F(\omega)$ are: $F(\omega) = \delta(\omega)$ and $F(\omega) \sim \omega^2$ up to a cut-off frequency ω_D , corresponding to the well known Einstein and Debye model, respectively. Junod et al. [91] demonstrated that certain functionals of the phonon specific heat take the form of convolutions of the phonon spectrum. The approach of Junod et al. for the phonon density of states (DOS), which was successfully applied to a large number of A15-type compounds, consists of a ω^2 -dependence but with different coefficients for different frequency regions. The phonon density of states vanishes for $\omega > \omega_D$. In particular, $(5/4)R\pi^4 C_{ph}T^3$ is an image of the spectrum $\omega^{-2}F(\omega)$ with $\omega = 4.93 \text{ T}$.

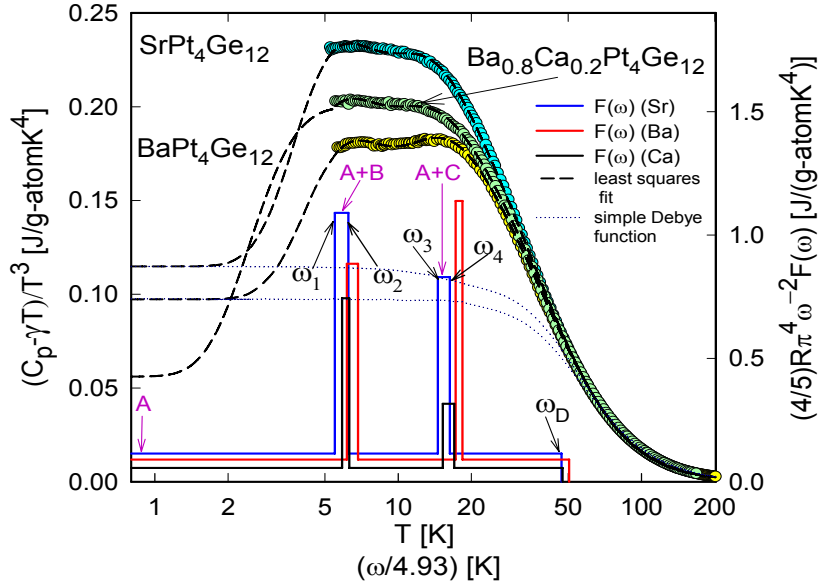


Figure 4.11: Phonon part of the temperature dependent specific heat C_p of $\{\text{Sr, Ba, Ca}\}\text{Pt}_4\text{Ge}_{12}$, plotted $(C_p - \gamma T)/T^3$ vs. $\ln T$. The dashed lines are the result of the fitting procedure of the experimental data using the model described in the text. The solid lines (referring to the right axis) sketch the phonon spectral function $F(\omega)$ plotted as $(5/4)R\pi^4\omega^{-2}F(\omega)$ vs. $\omega/4.93$.

In our case the density of states takes the following form

$$F(\omega) = \begin{cases} A\omega^2 & \omega < \omega_1 \\ (A + B)\omega^2 & \omega_1 < \omega < \omega_2 \\ A\omega^2 & \omega_2 < \omega < \omega_3 \\ (A + C)\omega^2 & \omega_3 < \omega < \omega_4 \\ A\omega^2 & \omega_2 < \omega < \omega_D \\ 0 & \omega > \omega_D \end{cases} \quad (4.4)$$

Here ω frequencies are given in degrees Kelvin. The phonon density of states vanishes for $\omega > \omega_D$.

Based on these considerations we have constructed an elementary phonon spectrum and have carried out least squares fits to the data. In a first approximation we assumed that the systems contains two additional energetically separated Einstein-type modes ω_{E1} and ω_{E2} . In contrast to the standard Einstein model of the specific heat, a certain frequency width $\Delta\omega$ for each of these branches is allowed.

Results of this ansatz are shown in Fig. 4.11 for $\{\text{Sr, Ba, Ca}\}\text{Pt}_4\text{Ge}_{12}$ as dashed lines. The phonon spectra are constructed and plotted in Fig. 4.11 referring to the right axis (solid line). The spectral weight follows from the

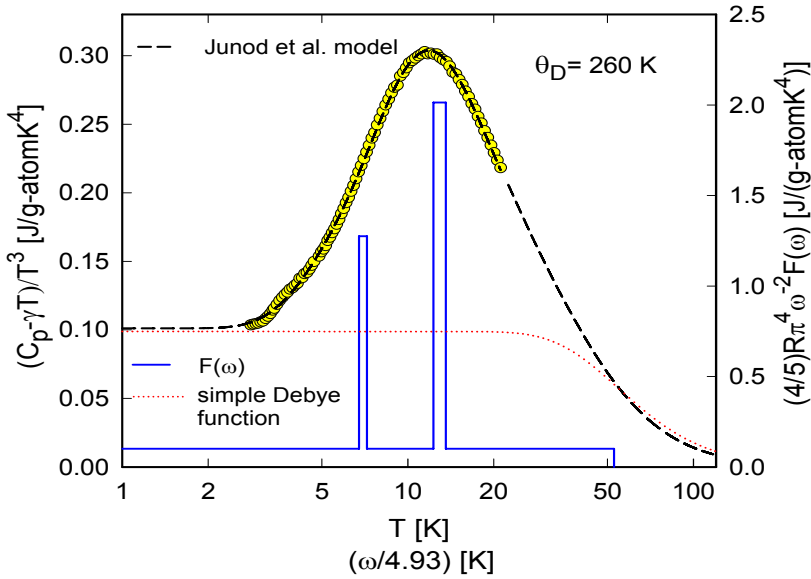


Figure 4.12: Temperature dependent specific heat C_p of ThPt₄Ge₁₂, plotted as $(C_p - \gamma T)/T^3$ vs. $\ln T$. The dashed line is a least squares fit of the experimental data using model Junod et al. [91, 92] (see Eqn. A.11) with a Debye spectrum ($\theta_D = 260$ K) and two Einstein-like modes $\omega_{EL1} = 34.7$ K with a width of 2.2 K and $\omega_{EL2} = 63.8$ K with a width of 6.4 K. The solid line (referring to the right axis) describes the phonon spectral function $F(\omega)$ plotted as $(4/5)R\pi^4\omega^{-2}F(\omega)$ vs. $\omega/4.93$. ω is given in degrees Kelvin.

constraint that for $T \rightarrow 0$ the height of the phonon density of states (DOS) coincides with the value of C_p/T^3 for $T \rightarrow 0$. The low lying phonon branch in each of the samples investigated may render those lattice vibrations which couple to the electron system and hence promote Cooper pairing, thereby enabling BCS-type superconductivity.

In all cases of the MPt₄Ge₁₂ skutterudites the phonon part of the specific heat is well described by a Debye spectrum together with two Einstein-like contribution in the frequency regions $27 \text{ K} < \omega < 33 \text{ K}$ and $71 \text{ K} < \omega < 90 \text{ K}$.

Details of these fits are summarised in Table 4.4. For BaPt₄Ge₁₂ the width of these contributions $\Delta\omega$ in low and high frequency regions ($30 \text{ K} < \omega < 33 \text{ K}$ and $85 \text{ K} < \omega < 90 \text{ K}$) are significantly smaller than for SrPt₄Ge₁₂ (see Table 4.4). A narrow contribution to $F(\omega)$ at high frequencies can be expected due to the most regular lattice in this compound. It should be noted that besides the increase of the $2a$ occupancy, an increase of the Ba content renders the skutterudite structure more regular.

The reconstruction of the phonon density of states (DOS) in the case of SrPt₄Ge₁₂ is plotted in Fig. 4.11. The overall goodness of the fit is high,

property	SrPt ₄ Ge ₁₂	BaPt ₄ Ge ₁₂	Ba _{0.8} Ca _{0.2} Pt ₄ Ge ₁₂	ThPt ₄ Ge ₁₂
γ [mJ/molK ²]	41	42	44	35(1)
θ_D^{LT} [K]	220	247	213	260
ω_{E1} [K]	28.5	32	30	34.7
$\Delta\omega_{E1}$ [K]	1.6	1.7	1	2.2
ω_{E2} [K]	72	85	75	63.8
$\Delta\omega_{E2}$ [K]	4.3	2.8	4.4	6.4
ω_D [K]	231	248	233	256
A	2.1	1.7	1.58	
A+B	22.7	18.9	22.4	
A+C	17.7	24	10.4	

Table 4.4: Debye frequencies ω_D , Einstein frequencies ω_{E_i} and with corresponding spectral widths according to least squares fits to the data with Eqn. A.11. Parameters for the phonon density of states $F(\omega)$ and normalized to $(4/5)R\pi^4\omega^{-2}F(\omega)$ [mJK⁻⁴ g atom⁻¹], γ and θ_D values were evaluated in the temperature region below 6 K.

revealing reasonable sets of parameters, summarised in Table 4.4. The best fit the specific heat data $(C_p - \gamma T)/T^3$ of SrPt₄Ge₁₂ with $\gamma = 41$ [mJ/molK²] revealed that the Debye temperature $\theta_D = 220$ K.

From the experimental data it is obvious that the filling of the $2a$ position with calcium atoms in {Ba_{0.8}Ca_{0.2}}Pt₄Ge₁₂ influences also the phonon spectrum $F(\omega)$ of the host lattice in comparison with BaPt₄Ge₁₂. A rather sharp Einstein-like contribution occurs at around 30 K which is slightly lower than in the case of Ba and Sr filled compounds.

The inapplicability of a Debye-like extrapolation of $C_p(T)$ towards high temperatures (as usually applied in simple metallic systems) demonstrates the existence of a complicated phonon spectrum in ThPt₄Ge₁₂. Based on Eqn.A.11, the phonon spectra are constructed and plotted in Fig. 4.12b referring to the right axis (solid line). The overall goodness of the fit is extremely high, revealing reasonable sets of parameters (see Table 4.4).

4.1.6 Superconducting and normal state

Superconductivity only occurs in a phase space spanned by three key parameters, i.e, the critical temperature T_c , the critical current I_c and the critical magnetic field $H_c(T)$ which are specific for each material. The superconducting state is characterized by various length scales, and the ratio of such scales $\lambda_{GL}/\xi_{GL} \equiv \kappa_{GL}$ (λ_{GL} is the penetration depth and ξ the coherence length) determines whether the material is a type I superconductor ($\kappa < 1/\sqrt{2}$) with perfect diamagnetism up to a critical field above which the

material becomes normal conducting or it is a type II superconductor ($\kappa > 1/\sqrt{2}$).

Determination of the electron-phonon coupling strength λ_{ep} :

An evaluation of the electron-phonon enhancement factor λ_{ep} from data for T_c and Θ_D is based on the McMillan formula [160] and postulates an assumption on the Coulomb pseudopotential. Within this model, the superconducting transition temperature T_c is given by:

$$T_c = \frac{\Theta_D}{1.45} \exp \left[\frac{-1.04(1 + \lambda_{ep})}{\lambda_{ep} - \mu^*(1 + 0.62\lambda_{ep})} \right], \quad (4.5)$$

where λ_{ep} is dimensionless electron-phonon coupling constant, Θ_D is Debye temperature for the characteristic phonon frequency. λ_{ep} determines the attractive part of the Cooper pair bonding, while μ^* is the repulsive screened Coulomb part ($\mu^* \approx 0.1 - 0.13$). For weak coupling superconductors, electron-phonon mass enhancement λ_{ep} depends importantly on the value assigned to μ^* . Thus, it is widely accepted to approximate μ^* by a typical mean value. McMillan proposed $\mu^* = 0.13$ for transition metal superconductors [160]. Taking into account the McMillan model allows calculation of the dimensionless electron-phonon coupling constant λ_{ep} , related in terms of the Eliashberg theory to the phonon density of states. Applying this simple model yields for Ba and Sr cases $\lambda_{ep} \approx 0.7$ and in case of Th $\lambda_{ep} = 0.66$. This refers to superconductors well beyond the weak coupling limit. In comparison, μ^* of different cage forming compounds have been found to cover a range from ≈ 0.1 to ≈ 0.3 [51, 52, 53]. The applicability of this approximation can be checked with the empirical formula by Bennemann and Garland [161]

$$\mu^* = 0.26N(0)/[1 + N(0)], \quad (4.6)$$

where $N(0)$ is the electronic density of states at the Fermi-energy E_F which has to be taken in the unit [states/eV atom]. In the following, λ_{ep} will be evaluated with the Bennemann and Garland formula. Using Eqn. 4.6 and taking $N(E_F)$ from band structure results yields $\mu^* \approx 0.113$ for BaPt₄Ge₁₂ ($N(E_F) = 13.2$ states eV⁻¹ f.u⁻¹ [54]), $\mu^* \approx 0.108$ for SrPt₄Ge₁₂ ($N(E_F) = 12.1$ states eV⁻¹ f.u⁻¹ [54]) and $\mu^* \approx 0.094$ in the case of ThPt₄Ge₁₂ ($N(E_F) = 9.63$ states eV⁻¹ f.u⁻¹ [59]). These values are close to the value of $\mu^* = 0.13$ estimated for transition metal superconductors. Note that $N(E_F)$ is usually given in [states/eV f.u.], but Eqn. 4.6 requires the use of $N(E_F)/(number of atoms in unit cell)$. In section 4.1.9 of this chapter, more detail of the band-structure calculations of {Sr, Ba, Th}Pt₄Ge₁₂ and the electron-phonon enhancement parameter taken from the McMillan will be given. In Table 4.5 are collected the results of λ_{ep} from McMillan formula (calculated with $\mu^* = 0.13$), the estimates of μ^* obtained from empirical formula by

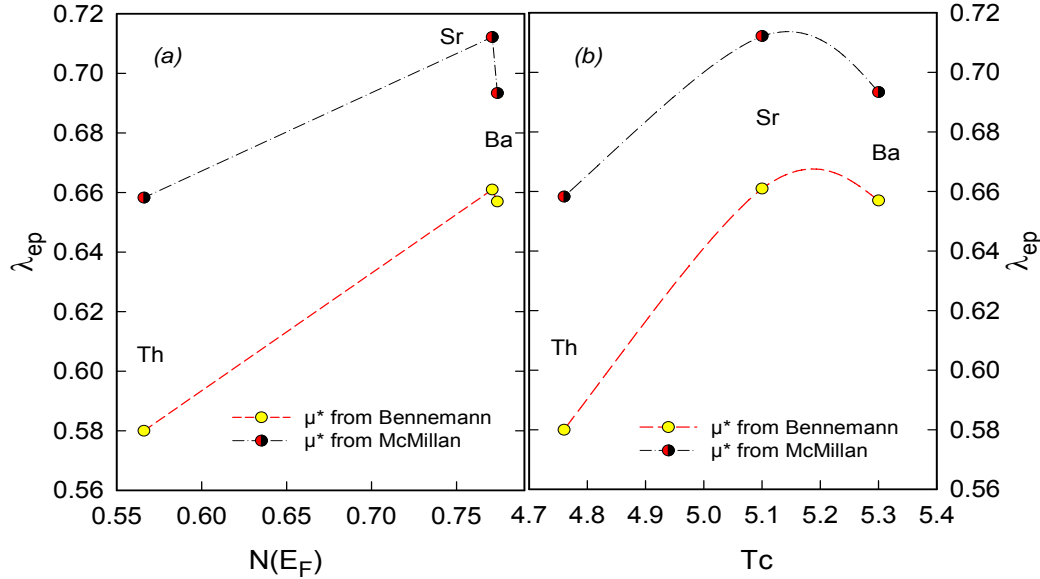


Figure 4.13: Comparison of the electron-phonon mass enhancement factors λ_{ep} ($= \gamma_{obs}/\gamma_{band} - 1$) with λ_{ep} estimated from Bennemann et. al. [161] and McMillan [160] as function of T_c/θ_D .

	$N(E_F)$ [states eV ⁻¹ atom ⁻¹]	μ^* Eqn.4.6	λ_{ep} Eqn.4.5	μ^* Eqn.4.6	λ_{ep} Eqn.4.5
BaPt ₄ Ge ₁₂	0.774	0.113	0.65	0.13	0.69
SrPt ₄ Ge ₁₂	0.711	0.108	0.66	0.13	0.71
ThPt ₄ Ge ₁₂	0.566	0.094	0.58	0.13	0.66

Table 4.5: Comparison of the electron-phonon mass enhancement factors λ_{ep} ($= \gamma_{obs}/\gamma_{band} - 1$) with λ_{ep} estimated from Bennemann et. al. [161] and McMillan [160]. More detail discussed in section 4.1.9.

Bennemann and Garland are compared with value of $\lambda_{ep} = \gamma_{obs}/\gamma_{band} - 1$. Figure 4.13 illustrates the electron-phonon mass enhancement factors λ_{ep} ($= \gamma_{obs}/\gamma_{band} - 1$) with λ_{ep} estimated from Bennemann et. al. [161] and McMillan [160] as a function of T_c/θ_D .

Thermodynamic BCS ratios:

Fig. 4.14a displays the zero-field and normal state (3 T and in case of Th compound 0.2 T) specific heat of {Sr,Ba,Th}Pt₄Ge₁₂ in C_p/T versus T representation. The idealization of the superconducting transition conforming the constraint of entropy conservation is shown by the solid line which

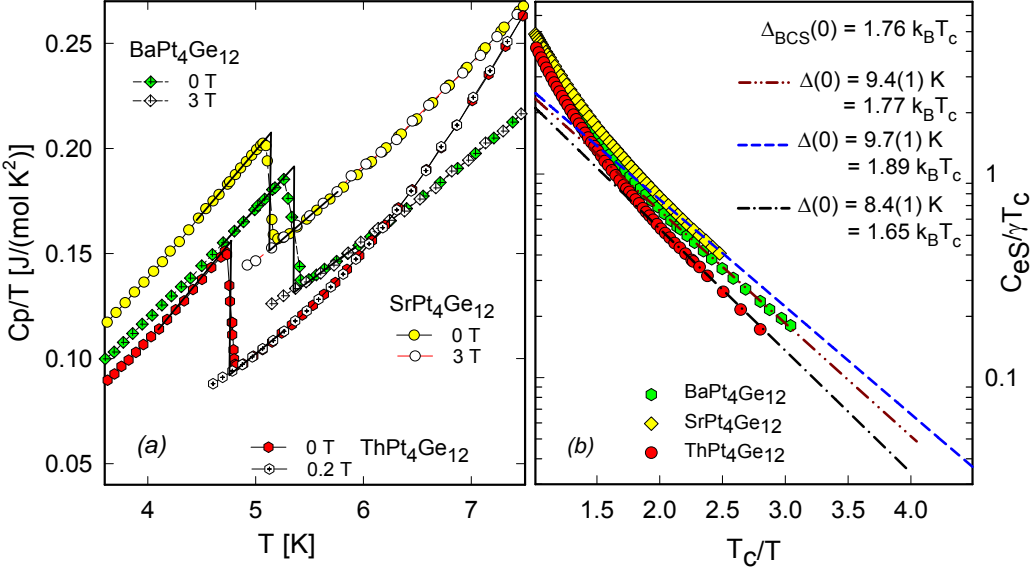


Figure 4.14: (a) Temperature dependent specific heat in the superconducting and normal state plotted as C_p/T vs. T for 0 and 3 T; the solid line accounts for an ideally sharp transition. The filled symbols correspond to the zero field and open symbols to the 3 and 0.2 T measurements. (b) The normalized electronic specific heat C_{eS} of $\{\text{Sr}, \text{Ba}, \text{Th}\}\text{Pt}_4\text{Ge}_{12}$ plotted as semi-logarithmic $C_{eS}/\gamma T_c$ as a function of the inverse reduced temperature T_c/T .

yields the height of the specific heat jump $(\Delta C_p)/T|_{T_c} = (C_s - C_n)/T|_{T_c}$ at T_c and the thermodynamic mean value of superconducting transition at \bar{T}_c , summarised in Table 4.6. The jump of the specific heat $(\Delta C_p/T)_{T=T_c} \approx 58 \text{ mJ/molK}^2$ for BaPt₄Ge₁₂ and $\approx 57 \text{ mJ/molK}^2$ for SrPt₄Ge₁₂ allows calculation of $\Delta C_p/\gamma_n T_c \approx 1.38$ as well as 1.39 for BaPt₄Ge₁₂ and SrPt₄Ge₁₂, which is near to the figure expected from BCS theory [$\Delta C_p/\gamma T_c \approx 1.43$], respectively. In the case of Ba_{0.8}Ca_{0.2}Pt₄Ge₁₂ the same analysis yields a specific heat jump $\Delta C_p/\gamma_n T_c \approx 1.2$, where $(\Delta C_p)/T|_{T_c} \approx 53 \text{ mJ/molK}^2$ is determined from the zero field data assuming an idealized sharp drop at the superconducting transition at T_c .

$\Delta C_p/T$ of ThPt₄Ge₁₂ and SrPt₄Ge₁₂ is displayed in Fig. 4.15a. As shown in Fig. 4.15a, in the case of ThPt₄Ge₁₂, taking the jump of the specific heat $\Delta C_p/T|_{T=T_c} = 61(2) \text{ mJ/molK}^2$, $\Delta C_p/\gamma_n T_c$ is calculated to be ≈ 1.74 , above the value expected from the BCS theory ($\Delta C_p/\gamma T_c \approx 1.43$) [54, 55, 56, 59]. As the magnetic field strength increases, both the transition temperature and the anomaly right at T_c are suppressed, defining the phase diagram shown in figures 4.17 and 4.18(b). The results of these evaluation are summarised in Table 4.6.

property	SrPt ₄ Ge ₁₂	BaPt ₄ Ge ₁₂	ThPt ₄ Ge ₁₂	Ba _{0.8} Ca _{0.2} Pt ₄ Ge ₁₂
T_c [K]	5.1	5.35	4.75	5.2
θ_D^{lt} [K]	220	247	260	213
γ [mJ/molK ²]	41	42	35(1)	44
$\Delta C_p/T(T = T_c)$	58	57	61(2)	53
$\Delta C_p/\gamma_n T_c$	1.39	1.38	1.74	1.2
$\mu_0 H_{c2}$ [T]	1	1.8	0.22	1.75
BCS: $\Delta(0)$ [K]	9.7(1)	9.4(1)	8.4(1)	8.8(1)

Table 4.6: The basic quantities describing the thermodynamic properties of superconducting state of MPt₄Ge₁₂, M = {Ca, Sr, Ba, Th}.

Superconducting gap:

The analysis of the zero-field superconducting state heat capacity of {Ca, Sr, Ba, Th}Pt₄Ge₁₂ for $T < T_c/2$ reveals a BCS-like exponential temperature dependence. The BCS expression for the electronic specific heat in the superconducting state well below T_c (Eqn.1.45) can be written as [162, 163]

$$C_{eS}(T) = 8.5\gamma T_c \exp\left(-0.82\frac{\Delta_{BCS}(0)}{k_B T}\right), \quad (4.7)$$

where $\Delta_{BCS}(0)$ represents the superconducting gap width at $T = 0$. The superconducting gap $\Delta(0)$ of {Ca, Sr, Ba, Th}Pt₄Ge₁₂ can be derived from a comparison of the modified BCS expression (Eqn.4.7) with the experimental heat capacity data. The temperature dependence of the electronic specific heat C_{eS} of {Ca, Sr, Ba, Th}Pt₄Ge₁₂ in the superconducting state, is obtained by subtracting the phonon contributions C_{ph} (derived from the normal state heat capacity data) from zero-field measurements (see dashed-dotted line in Fig. 4.12a in case of ThPt₄Ge₁₂). Fig. 4.14b shows a semi-logarithmic plot of the normalized electronic specific heat $C_{eS}/\gamma T_c$ as a function of the reduced temperature T_c/T for {Sr, Ba, Th}Pt₄Ge₁₂. The exponential temperature dependency of the electronic specific heat C_{eS} in all cases indicating a ratio $\Delta(0)/k_B T_c$ in close agreement with the weak coupling BCS value. From the exponential dependence curve, the superconducting energy gap at zero temperature $\Delta(0)$ can be estimated to be 0.81 meV (9.4 K) for BaPt₄Ge₁₂ and 0.83 meV (9.7 K) for SrPt₄Ge₁₂, respectively. These yielding a ratio $\Delta(0)/k_B T_c \approx 1.77(1)$ for BaPt₄Ge₁₂ and 1.89(1) in case of SrPt₄Ge₁₂ in close agreement with the weak coupling BCS value ($\Delta_{BCS}(0) = 1.76 k_B T_c$). From the exponential dependence curve of ThPt₄Ge₁₂ (for $T < T_c/2$), the superconducting energy gap at zero temperature $\Delta(0)$ can be estimated to be 0.72(1) meV. By using these values, the ratio $\Delta(0)/k_B T_c \simeq 1.75$ is in fine

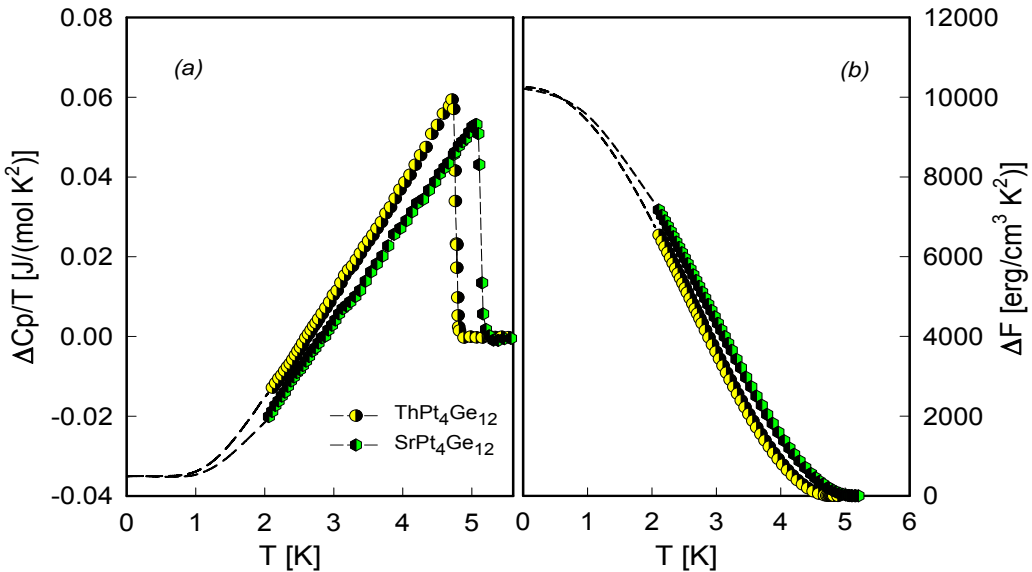


Figure 4.15: (a) comparison of $\Delta C_p/T(T = T_c)$ between ThPt₄Ge₁₂ and SrPt₄Ge₁₂. (b) comparison of free energy difference $\Delta F(T) = F_n - F_s$ between the superconducting and normal state (see Eqn. 1.61) of ThPt₄Ge₁₂ and SrPt₄Ge₁₂. The dashed lines are extrapolations from the normal- and superconducting states, respectively.

agreement with the BCS value. The reason why these values are not identical to the BCS weak-coupling values is probably the sample inhomogeneities.

The thermodynamic critical field:

Figure 4.16b displays the thermodynamic critical field $\mu_0 H_c$ of ThPt₄Ge₁₂ and SrPt₄Ge₁₂. $H_c(T)$ is obtained by integrating the entropy difference between the normal and superconducting state. The temperature dependent entropies ΔS of ThPt₄Ge₁₂ and SrPt₄Ge₁₂ with $\Delta S(T) = S_n - S_s$ are displayed in Fig. 4.16a. The application of equation 1.61 to the data in figures 4.9a,b - 4.12a reveals the thermodynamic critical field $H_c(T)$. The entropy of any system is the derivative of the free energy $S = -(\partial F/\partial T)_B$ and the specific heat is $C_p = T(\partial S/\partial T)_B$. By starting with experimental specific heat data and integrating twice, the free energy can be recovered for each state, and the difference can be calculated at any temperature. The results of calculation of free energy difference $\Delta F(T) = F_n - F_s = \mu_0 H_c^2(T)/2$, where F_n and F_s are evaluated from the specific heat data in the normal and superconducting state, respectively, are displayed in Fig. 4.15b for ThPt₄Ge₁₂ and SrPt₄Ge₁₂ as $\mu_0 H_c$ vs. temperature. $C_s(T)$ is obtained from the zero field specific heat measurements and $C_n(T)$ are taken from the

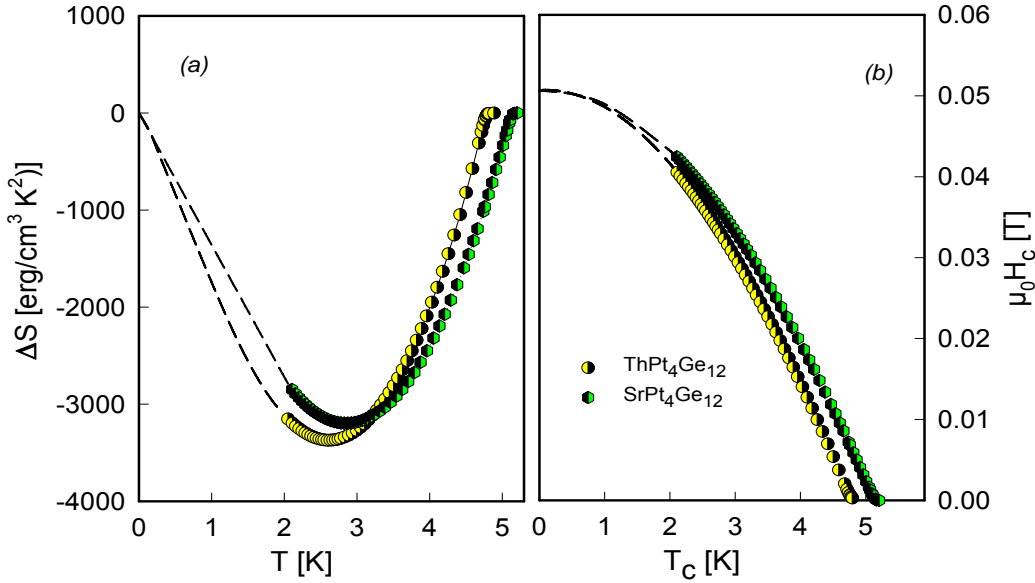


Figure 4.16: (a) comparison of $\Delta S(T)$ between ThPt₄Ge₁₂ and SrPt₄Ge₁₂. (b) comparison of thermodynamic critical field $\mu_0 H_c$ of ThPt₄Ge₁₂ and SrPt₄Ge₁₂. The dashed lines are extrapolations from the normal- and superconducting states, respectively.

0.2 T data for the Th compound and 3 T for the Sr compound, respectively. The thermodynamic critical field (filled symbol) and the upper critical field values for ThPt₄Ge₁₂ are displayed in Fig. 4.18b; an extrapolation $T \rightarrow 0$ yields $\mu_0 H_c(0) \approx 50$ mT, very similar to the figures derived for SrPt₄Ge₁₂ and BaPt₄Ge₁₂ ($\mu_0 H_c(0) \approx 53(2)$ and $52(2)$ mT for the Ba and the Sr-based compound, respectively) [54].

Upper critical field:

The upper critical field H_{c2} is one of the most fundamental quantities in type-II superconductors. After the pioneering work by Abrikosov [99] based on the Ginzburg-Landau (GL) equations [98], theoretical efforts have been made for its quantitative description at all temperatures [100, 164]. The temperature dependent upper critical field $\mu_0 H_{c2}$ of SrPt₄Ge₁₂ and BaPt₄Ge₁₂ as deduced from field dependent resistivity, magnetisation and heat capacity measurements is illustrated in Fig. 4.17. The slopes of the upper critical field $\partial(\mu_0 H_{c2})/\partial T \equiv \mu_0 H'_{c2}$ are collected in Table 4.1.6, yielding slightly larger values deduced from magnetisation and resistivity data (surface effects) than those from specific heat. The further evaluation of $\mu_0 H_{c2}$ is thus based on the specific heat measurement data. $\mu_0 H'_{c2}$ of BaPt₄Ge₁₂ is larger than $\mu_0 H'_{c2}$ of SrPt₄Ge₁₂. The temperature dependent upper critical field $\mu_0 H_{c2}$

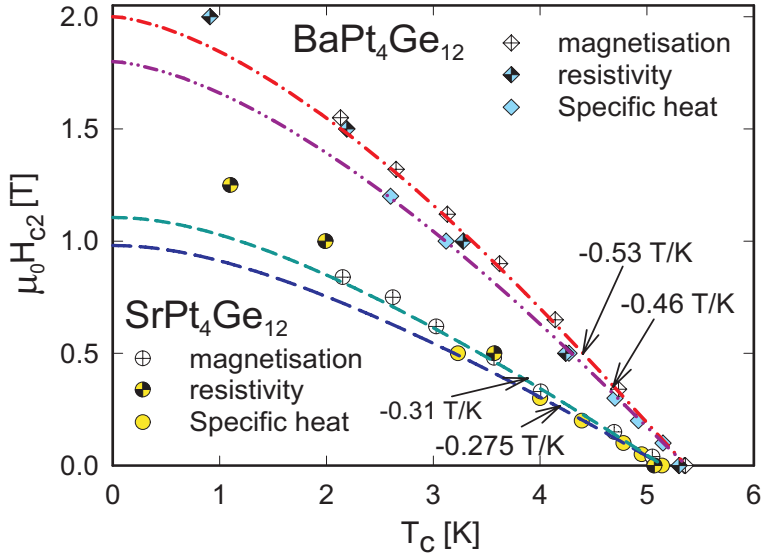


Figure 4.17: (a) Temperature dependent upper critical field $\mu_0 H_{c2}$ of $\text{BaPt}_4\text{Ge}_{12}$ and $\text{SrPt}_4\text{Ge}_{12}$ as obtained from resistivity, magnetisation and specific heat measurements. The dashed and the dashed-dotted lines represent the WHH model.

of $\text{ThPt}_4\text{Ge}_{12}$ as deduced from the specific heat measurements $C_p(T, H)$ is displayed in Fig. 4.18b, with $\partial(\mu_0 H_{c2})/\partial T \equiv \mu_0 H'_{c2} = -0.064 \text{ T/K}$ [59].

Essentially two mechanisms limit the value of $\mu_0 H_{c2}$: orbital pair breaking and Pauli limiting. Werthamer et al. [165] derived an expression (Werthamer, Helfand, Hohenberg, *WHH model*) for the upper critical field $\mu_0 H_{c2}$ in terms of orbital pair-breaking, including the effect of Pauli spin paramagnetism and spin-orbit scattering.

Werthamer noted that the expression for the upper critical field $\mu_0 H_{c2}$ of dirty limit type II superconductors can be expressed in terms of the digamma function. Orlando [111] showed for bulk type II superconductors in the *dirty limit*, that $\mu_0 H_{c2}(t)$ is an implicit function of

$$\ln t = \psi\left(\frac{1}{2}\right) - \frac{1}{2} \left(1 + \frac{\lambda_{so}/4}{X}\right) \psi\left(\frac{1}{2} + \frac{Y + \lambda_{so}/4 - X}{t}\right) - \frac{1}{2} \left(1 - \frac{\lambda_{so}/4}{X}\right) \psi\left(\frac{1}{2} + \frac{Y + \lambda_{so}/4 + X}{t}\right), \quad (4.8)$$

where ψ is the digamma function, $t = T/T_c$,

$$Y = \frac{2h}{\pi^2} \quad \text{with} \quad h = H_{c2}(T)/\left[\frac{dH_{c2}}{dT}|_{T_c} \cdot T_c\right] \quad (4.9)$$

and

$$X = \left[(\lambda_{so}/4)^2 - 4h^2\alpha^2/\pi^4 \right]^{1/2} \quad \text{with} \quad \alpha = \frac{2^{1/2}\pi^2}{8e^\gamma} \frac{-(dH_{c2}/dT|_{T_c}) T_c}{H_p(0)} \quad (4.10)$$

here $H_p(0) = \pi k_B/(2^{1/2}e^\gamma\mu_B)T_c[(1 + \lambda_{ep})^{1/2}\eta_{H_c}(0)]$ is the Pauli limiting field (with no other pair breaker and in the absence of spin-orbit scattering) [111] and α is Maki¹ parameter [164].

A comparison of the experimental results with the WHH model is based on two parameters, α , the Pauli paramagnetic limitation (*Maki parameter*) and λ_{so} describing spin-orbit scattering (see A.3.1). If the atomic numbers of the elements constituting the material under investigation increase, λ_{so} is expected to increase as well.

For an interpretation of the experimental data and a comparison of the experimental results we used the WHH model Eqn. 4.8 and 4.9. $\mu_0 H_{c2}$ is almost linear near T_c and saturates at lowest temperatures. Using the approach by Werthamer et al. yields $\mu_0 H_{c2}(0) = 0.7\mu_0 T_c H'_{c2}|_{T_c} = 0.22$ T for ThPt₄Ge₁₂ (Fig. 4.18b), 1.8 and 1 T for BaPt₄Ge₁₂ and SrPt₄Ge₁₂, respectively. The best fit for Ba_{0.8}Ca_{0.2}Pt₄Ge₁₂ using equation 4.8 yields $\mu_0 H_{c2}(0) = 0.7\mu_0 T_c (dH_{c2}/dT)|_{T_c} = 1.75$ T.

The Maki parameter α can be estimated via the Sommerfeld value γ and ρ_0 [165], i.e.,

$$\alpha = (3e^2\hbar\gamma\rho_0)/(2m\pi^2k_B^2) \quad (4.11)$$

where γ is the normal state electronic specific heat coefficient in [erg/cm³K²], ρ_0 is the residual resistivity in [Ω cm], \hbar the Boltzmann's constant in [erg/K] and e the electron charge and m the electron mass. Taking the experimental residual resistivity ρ_0 and the Sommerfeld value γ yields $\alpha = 0.18$ for BaPt₄Ge₁₂, $\alpha = 0.14$ for SrPt₄Ge₁₂ and $\alpha = 0.016$ for ThPt₄Ge₁₂, respectively. A value of similar magnitude can be derived from [164]

$$\alpha = 5.3 \cdot 10^{-5} \left(\frac{-dH_{c2}(T)}{dT} \right) |_{T=T_c}. \quad (4.12)$$

An increasing value of α reduces H_{c2} from the upper limit $h^* = H_{c2}/(T_c \partial \mu_0 H_{c2} / \partial T|_{T=T_c}) = 0.693$. Spin-orbital scattering, on the contrary, compensates for the decrease due to the paramagnetic limitation and restores $h^* \approx 0.693$ for $\lambda_{so} \rightarrow \infty$. Wong et al. [166] pointed out that $\lambda_{so} > 10$ for 5d compounds, which also should hold for the present Pt-based system. We have adjusted the WHH model to the experimental data (dashed and dashed-dotted lines in Fig. 4.17 and solid line in Fig. 4.18b), revealing $\lambda_{so} \approx 15$ for all data-sets. Note, however, $H_{c2}(T \rightarrow 0)$, is quite insensitive for

¹In memoriam: on 10 September 2008 Kazumi Maki, world-renowned physicist in the field of superconductivity, died at age 72 (1936 - 2008).

$\lambda_{so} > 10$. Both enhancement effects as well as strong coupling are expected to have only minor influence on these data [166].

Ginzburg-Landau parameter κ and the characteristic lengths ξ and λ_{GL} :

The thermodynamic and the upper critical field are used to calculate the ratio of the penetration depth $\lambda_{GL}(0)$ to the coherence length $\xi_{GL}(0)$ via Abrikosov's relation

$$\lambda_{GL}(0)/\xi_{GL}(0) \equiv \kappa_{GL}(0) = H_{c2}/[\sqrt{2}H_c(0)], \quad (4.13)$$

yielding the Ginzburg-Landau parameter $\kappa_{GL} = 24(2)$ and $14(2)$ for the Ba-, Sr- and $\kappa_{GL} = 3$ for Th-based compounds, respectively. In case Ba and Sr compounds the coherence length ξ_0 for $T \rightarrow 0$ was obtained from two independent relations. One follows from the BCS equation (Eqn.1.57), yielding about 13.8×10^{-8} m, 18.1×10^{-8} m for the Ba and Sr compounds, respectively. A second expression stems from the well known formula

$$\xi = \left(\frac{\Phi_0}{2\pi\mu_0 H_{c2}} \right)^{1/2} = 14(1) \times 10^{-8} \text{ m} \quad (4.14)$$

for the Ba- and $18(1) \times 10^{-8}$ m for Sr-based compound, respectively, in fair agreement with the former. The absolute values of ξ_0 and $\lambda(0)$ can be evaluated via the isotropic Ginzburg-Landau-Abrikosov-Gor'kov (GLAG) theory (Eqn.1.52 and Eqn.1.53), resulting in $\xi_0 = 4 \times 10^{-8}$ m and $\lambda(0) = 1.2 \times 10^{-7}$ m for ThPt₄Ge₁₂. The values for ξ and λ are collected in Table 4.1.6.

Gor'kov [100] has derived an expression for Ginzburg-Landau parameter κ to be valid when the electronic mean free path l_{tr} is much smaller than the intrinsic coherence length ξ_0 . This was shown by Goodman [105] to have the convenient form

$$\kappa = \kappa_0 + 0.0237\sqrt{\gamma}\rho_0, \quad (4.15)$$

where κ_0 is the clean limit value of the Ginzburg-Landau parameter, γ is the Sommerfeld coefficient in units [J/m³K²] and ρ_0 the residual resistivity in [Ω cm]. Using the Gor'kov-Goodman relation the experimental value $\kappa \approx 2.9$ provides a rough estimate of $\kappa_0 = 1.9$ for {Sr, Ba, Th}Pt₄Ge₁₂ in the hypothetical clean limit case. The results of these evaluation are given in Table 4.1.6 and will be compared with direct estimation from the Abrikosov's relation Eqn.4.13 and the Gor'kov-Goodman relation Eqn.4.15. These findings are illustrated in Fig.4.18a, where $\kappa_{GL}(0)$ calculated from the Abrikosov's relation and the Gor'kov-Goodman relation are compared. Good agreement is obtained between Ginzburg-Landau parameter $\kappa_{GL}(0)$ calculated from the Abrikosov's relation and the Gor'kov-Goodman relation for all compounds.

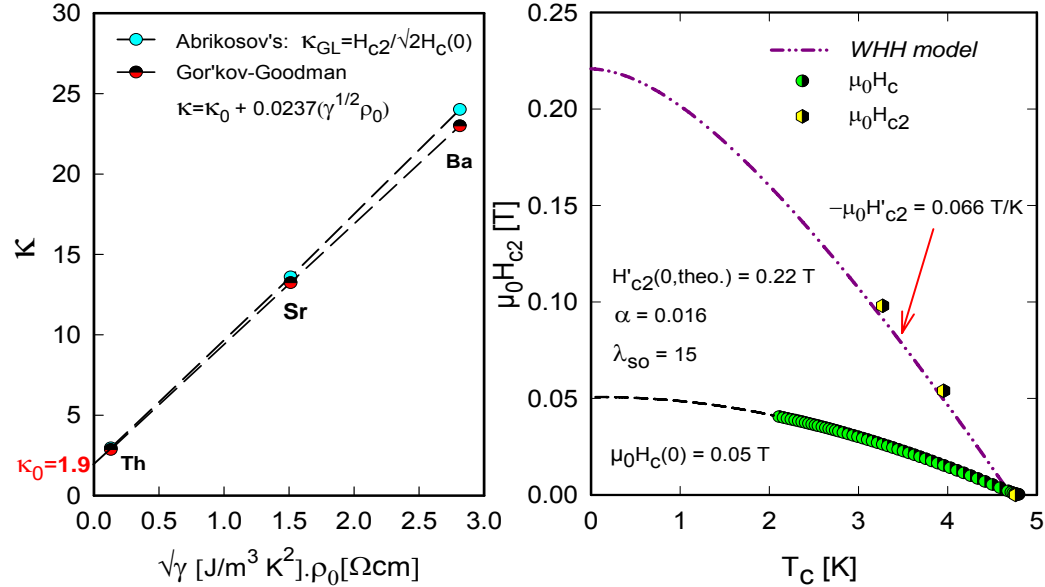


Figure 4.18: (a) comparison of the Ginzburg-Landau parameter $\kappa_{GL}(0)$ calculated values from the Abrikosov's relation and the Gor'kov-Goodman relation. (b) Upper critical field $\mu_0 H_{c2}$ and the thermodynamic critical field $\mu_0 H_c$ (filled green symbol) of ThPt₄Ge₁₂. Data are taken from the heat capacity data. The dashed and the dashed-dotted lines corresponds to the *WHH* model as explained in the text.

For interpretation of the experimental data these relations are collected in Appendix A.3.

The fact that $\mu_0 H'_{c2}$ of ThPt₄Ge₁₂ is substantially smaller than that of isomorphous {Sr, Ba}Pt₄Ge₁₂ ($\mu_0 H'_{c2}(Sr) \approx -0.275 \text{ T/K}$, $\mu_0 H'_{c2}(Ba) \approx -0.46 \text{ T/K}$) [54, 55, 56, 59] might be a consequence of the observed variation of the Sommerfeld value γ and the residual resistivity ρ_0 .

As shown in Fig. 4.17 $\mu_0 H'_{c2}$ of BaPt₄Ge₁₂ is larger than that of SrPt₄Ge₁₂, a fact that can be understood in terms of the Ginzburg-Landau theory. Hake et al. [167] and Orlando et al. [111] derived a model equation for $\mu_0 H'_{c2}$ with the assumption of a spherical Fermi surface which primarily depends on two parameters: on the inverse of the square of Fermi velocity v_F and on the inverse of the electronic mean free path l_{tr} (see Eqn. 1.64). The Fermi velocity v_F can be calculated from

$$v_F = \frac{\xi_0 k_B T_c}{0.18 \hbar} [\text{m/s}], \quad (4.16)$$

with coherence length ξ_0 in [m].

Taking into account the parameters deduced from the above analyses ex-

property	$\text{BaPt}_4\text{Ge}_{12}$	$\text{SrPt}_4\text{Ge}_{12}$	$\text{ThPt}_4\text{Ge}_{12}$
transition temperature T_c [K]	5.35	5.10	4.75
upper critical field $\mu_0 H_{c2}$ [T]	1.8	1	0.22
thermod. critical field $\mu_0 H_c$ [T]	0.053	0.052	0.050
slope of $\mu_0 H_{c2}$, $\mu_0 H'_c(C_p)$ [T/K]	-0.46	-0.275	-0.067
Fermi velocity v_F [m/s]	52500	67000	136000
effective Fermi surface S_s^{cl} [m^{-2}]	2.74×10^{20}	3.43×10^{20}	5.69×10^{20}
coherence length ξ_0 [nm] (BCS Eq.)	13.8	18.1	39.4
coherence length ξ [nm]	14(1)	18(1)	40(1)
penetration depth λ [nm]	320(10)	250(10)	120 (10)
mean free path l_{tr} [m]	1×10^{-8}	1.4×10^{-8}	6.5×10^{-8}
G.L. parameter κ_{GL}	24(1)	14(1)	3(1)
G.L. parameter κ_{GL} (Goodman Eq.)	23.7	13.65(1)	3.01
α	0.18	0.14	0.016
λ_{ep}	0.7	0.7	0.66
l_{tr}/ξ	0.5(2)	0.7(2)	3.2(2)

Table 4.7: The normal and superconducting state properties of $\text{SrPt}_4\text{Ge}_{12}$, $\text{BaPt}_4\text{Ge}_{12}$ and $\text{ThPt}_4\text{Ge}_{12}$.

plains in all cases, at least qualitatively, differences of $\mu_0 H'_{c2}$. While the decrease of v_F from the Sr case ($v_F = 0.67 \times 10^5$ m/s) to the Ba case ($v_F = 0.52 \times 10^5$ m/s) [54] and finally to the Th compound can be conceived by the increase of the unit cell volume ($v_F \propto (N/V)^{1/3}$, for free electrons), the increase of the electronic mean free path l_{tr} corresponds to the very low residual resistivity ($\rho_0 = 3 \mu\Omega\text{cm}$) of $\text{ThPt}_4\text{Ge}_{12}$ and the decrease of the mean free path l_{tr} corresponds to the increase of the residual resistivity from $\text{SrPt}_4\text{Ge}_{12}$ to $\text{BaPt}_4\text{Ge}_{12}$, respectively. Both of these parameters are larger in the case of $\text{ThPt}_4\text{Ge}_{12}$, explaining straightforwardly the reduced value of $\mu_0 H'_{c2}$. Values are summarised in Table 4.1.6. The importance of the latter parameter is obvious from $\mu_0 H'_{c2} = const \cdot \gamma \rho_0$ [111], which is valid within the dirty limit case ($const$ is a numerical constant, Eqn. 1.66). For the mean free path, l_{tr} , we then followed the scheme of Rauchschwalbe [116] developed for s-wave superconductors:

$$l_{tr} = 1.533 \times 10^6 \frac{1}{\rho_0 S_s} \quad (4.17)$$

with ρ_0 the residual resistivity in [$\Omega \text{ cm}$] and the effective Fermi surface S_s in [m^2]. Combining S_s and ρ_0 according to Eqn. 4.17, a mean free path l_{tr} of about $\approx 1.0 \times 10^{-8}$ m and $\approx 1.4 \times 10^{-8}$ m for the Ba and Sr compound, respectively, is derived. For the Th compound we derived $l_{tr} \approx 6.5 \times 10^{-8}$ m.

From $l_{tr}/\xi \approx 1$ we classify $\{\text{Sr}, \text{Ba}\}\text{Pt}_4\text{Ge}_{12}$ as a dirty limit superconduc-

tor, and κ of the order of 10 to 20 refers to a pronounced type II superconducting behaviour and the ThPt₄Ge₁₂ as a SC grouped between the clean ($l_{tr} \gg / \xi$) and the dirty ($l_{tr} \ll / \xi$) limit; κ of the order of 3 refers to a type II SC behaviour.

4.1.7 Magnetic properties

Magnetisation measurements were carried out down to 2 K with a SQUID magnetometer on the {Sr, Ba, Eu, Th, U}Pt₄Ge₁₂. The low field susceptibility $\chi(T)$ of BaPt₄Ge₁₂ is plotted as a function of temperature in Fig. 4.19a for the magnetic field up to 0.1 T. The susceptibility χ exhibits a rather sharp transition at $T_C = 5.3$ K, dropping from an initially small positive value to the diamagnetic value of $[-1/(4\pi)]$ for zero field cooling, which corresponds to a full Meissner Ochsenfeld effect. The irreversibility upon field

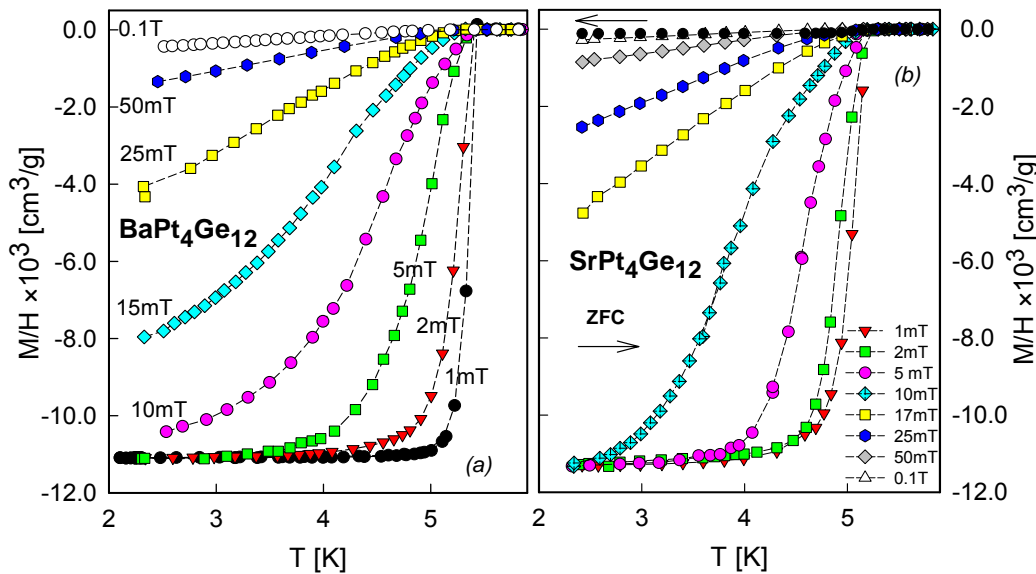


Figure 4.19: (a) Temperature dependent susceptibility χ of BaPt₄Ge₁₂, plotted as MH vs. T at various applied magnetic fields after zero-field cooling. (b) Temperature dependent magnetic susceptibility $\chi(T)$ of SrPt₄Ge₁₂, plotted as MH vs. T at various applied fields after cooling the specimen in zero-field.

and zero-field cooling can be attributed to type II superconductivity. The temperature dependent magnetic susceptibility $\chi(T)$ of SrPt₄Ge₁₂ is shown in Fig. 4.19b for applied fields up to 0.1 T. In a field of 1 mT, the onset of the superconducting state occurs at 5.1 K. The strong diamagnetic signal observed at 3.3 K upon cooling the sample in zero field (ZFC) corresponds

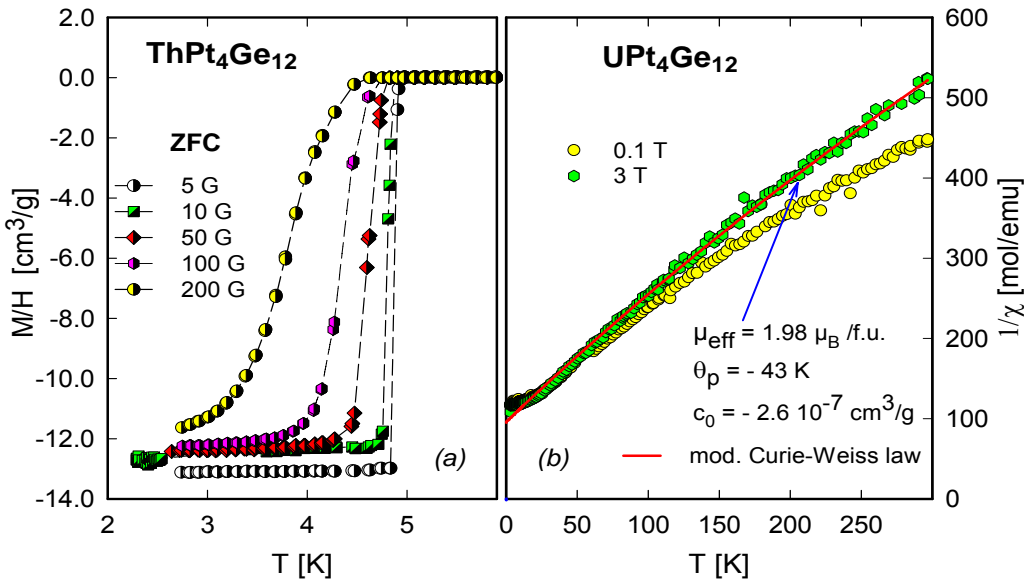


Figure 4.20: (a) Temperature dependent susceptibility M/H of $\text{ThPt}_4\text{Ge}_{12}$. The jump at $T = T_c$ for 5 G reveals a full Meissner effect. Filled and open symbols refer to zero field and field cooling, respectively. The jump at T_c reveals a full Meissner effect. (b) Temperature dependent magnetic susceptibility χ of $\text{UPt}_4\text{Ge}_{12}$ compound, plotted as χ^{-1} vs. T . The solid line is a least squares fit using the modified Curie-Weiss law.

to the perfect shielding of the total volume of the sample by super currents. With rising magnetic field strength the critical temperature T_c gradually decreases, and the superconductivity becomes hardly observable by means of $\chi(T)$ measurement already in fields above 0.15 T. The temperature dependent magnetic susceptibility $\chi(T)$ of $\text{ThPt}_4\text{Ge}_{12}$ is displayed in Fig. 4.20a at various magnetic field, plotted as M/H vs. T . The magnetic susceptibility, χ , of $\text{ThPt}_4\text{Ge}_{12}$ is diamagnetic in the normal state region, revealing a temperature independent susceptibility $\chi = -1.5 \cdot 10^{-7} \text{ g/cm}^3$. At $T = 4.8$ K, the sharp transition evidences bulk superconductivity, in perfect agreement with the specific heat and the resistivity data. The diamagnetic value of $[-1/(4\pi)]$ for zero-field cooling (ZFC) corresponds to a complete flux exclusion of the total sample volume due to the screening currents. In the low field limit (< 5 mT) the shielding signal is in good agreement with the value expected for perfect diamagnetism (using the X-ray density 9.063 g/cm^3 and a correction for demagnetisation due to the macroscopic sample geometry). The flux expulsion (Meissner-Ochsenfeld effect) for field cooling (FC) in 5 and 20 mT is only 21% and 17% of the shielding signal, which indicates a rather strong flux pinning in a type II superconductor. With growing external fields the

transition is washed out and shifted to lower temperatures and is suppressed in fields larger than 0.13 T above 2.2 K.

The inverse magnetic susceptibility $\chi^{-1}(T)$ of UPt₄Ge₁₂ at a magnetic field of $\mu_0 H = 0.1$ and 3 T is plotted as a function of temperature in Fig. 4.20b. Above about 30 K a Curie-Weiss like behaviour indicates a simple paramagnetic state. At high temperatures, a least squares fit to the modified Curie-Weiss law, i.e., $\chi = \chi_0 + C/(T - \theta_p)$ yields an effective magnetic moment $\mu_{eff} = 1.98 \mu_B$ and a paramagnetic Curie temperature $\theta_p = -43$ K. Such value, however, is lower than the expected moment for a free uranium in either 5f² or 5f³ configuration, which resulting $\mu_{eff} = 3.58 \mu_B$ and $\mu_{eff} = 3.62 \mu_B$, respectively [168]. This may refer to a loss of localisation in favour of an itinerant 5f state. Similar low effective moments are known for other U-intermetallics such as the heavy fermion superconductors of UPt₃, UPd₂Al₃ and URu₂Si₂, for which the 5f-bands lie very close to the Fermi level tending to delocalise [169, 170, 171, 172].

4.1.8 Seebeck coefficient

The temperature dependent thermopower $S(T)$ of {Sr, Ba, Eu}Pt₄Ge₁₂ skutterudites as well as of (Ba_{0.8}Ca_{0.2})Pt₄Ge₁₂ is displayed in Fig. 4.21. Data were collected between 4.2 to 300 K. Throughout the series, positive thermopower is observed, reaching room temperature values of about 5.4 μ V/K in the case of SrPt₄Ge₁₂, 6.7 μ V/K in the case of BaPt₄Ge₁₂ and 4.4 μ V/K in the case of EuPt₄Ge₁₂. For BaPt₄Ge₁₂ and Ba_{0.8}Ca_{0.2})Pt₄Ge₁₂, $S(T)$ shows an almost linear behaviour. Most remarkable is the fact that for (Ba_{0.8}Ca_{0.2})Pt₄Ge₁₂, $S_{RT} \approx 9.7 \mu$ V/K, is even higher than the value for BaPt₄Ge₁₂. $S(T)$ of EuPt₄Ge₁₂ is slightly reduced in comparison to the $S(T)$ of SrPt₄Ge₁₂. It shows a steep increase at low temperatures up to 100 K, reaching a maximum value $S_{max} \approx 5.1 \mu$ V/K followed by a plateau from 100 K up to room temperature, where it reaches a value $S_{RT} \approx 4.4 \mu$ V/K comparable to SrPt₄Ge₁₂ with $S_{RT} \approx 5.4 \mu$ V/K. At temperatures below about 100 K $S(T)$ for SrPt₄Ge₁₂ and EuPt₄Ge₁₂ is larger than that of corresponding BaPt₄Ge₁₂ as well as (Ba_{0.8}Ca_{0.2})Pt₄Ge₁₂.

4.1.9 Electronic structure

Lastly, in this section the superconducting state from a theoretical perspective of the calculated electronic band structure was discussed. For the band-structure calculations, density functional theory (DFT) was applied using the Vienna *ab initio* simulation package (VASP) [173, 174] with a fully relativistic spin-orbit coupling approach [175, 176]. The Brillouin zone was sampled with 5×5×5 Monkhorst-Pack \vec{k} -point grids. The exchange-correlation functional was treated within the local density approximation. The calculated total

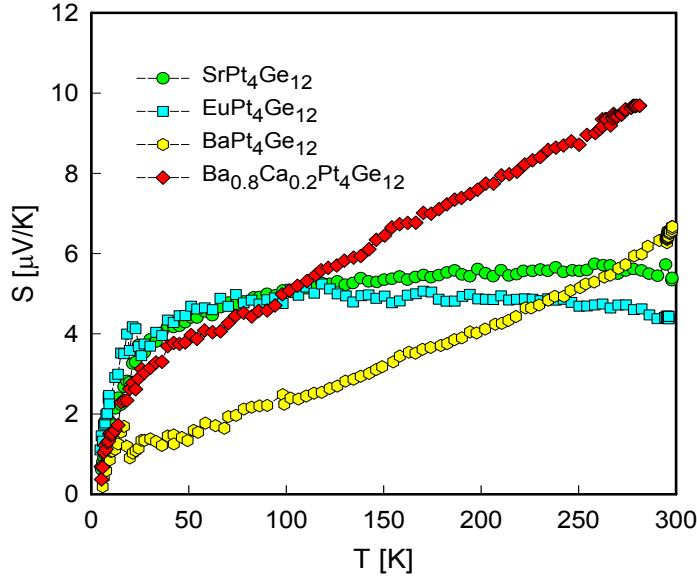


Figure 4.21: Temperature dependent thermopower $S(T)$ of $\{\text{Sr}, \text{Ba}\}\text{Pt}_4\text{Ge}_{12}$ and $\{\text{Ba}_{0.8}\text{Ca}_{0.2}\}\text{Pt}_4\text{Ge}_{12}$.

density of states (DOS) for $\text{BaPt}_4\text{Ge}_{12}$ in comparison to $\text{SrPt}_4\text{Ge}_{12}$ is plotted in left panel of Fig. 4.22. The broken line at $E=0$ indicates the Fermi energy. The calculated total density of states (DOS) reveal the individual contributions of $X=(\text{Ba}, \text{Sr})$, Pt and Ge atoms showing that Ge states, which are of p - and s -like states, are dominating at Fermi energy. The Ge states hybridize with Pt 5d-like states by which the spin-orbit coupling effect is transmitted to the DOS at E_F . Consequently, by making use of the electron localization function technique [177], expressive Ge-Ge covalent bonds and typical metallic Pt bonding are being deduced. The metallic features of the DOS around E_F convincingly confirm that the Zintl concept no longer applies to $\{\text{Sr}, \text{Ba}\}\text{Pt}_4\text{Ge}_{12}$, while its applicability is quite obvious among pnictogen-based skutterudites.

The right panel of Fig. 4.22 shows the total calculated DOS for $\text{ThPt}_4\text{Ge}_{12}$. The calculated DOS reveals the individual contributions of the Th, Pt, and Ge atoms. The relativistic effect of spin-orbit coupling does not significantly influence the DOS at E_F . The directed covalent bonds of Ge intermixed with the more metal-like charge distribution of Pt states contribute to the peak of the DOS at E_F . From Bader's charge analysis [178], about 0.13 electrons are transferred from each Ge to Pt, indicating only weakly ionic Pt-Ge bonds.

The electron-phonon coupling parameter can be obtained directly from

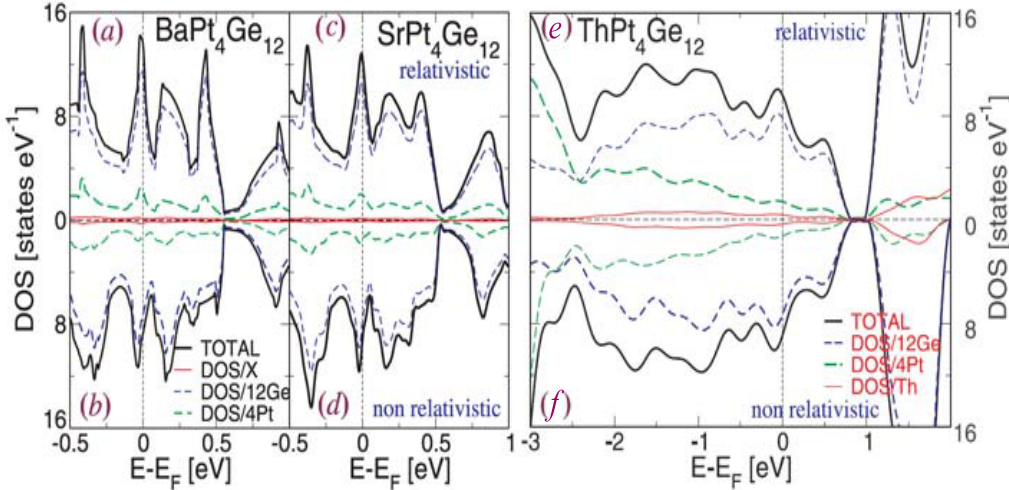


Figure 4.22: DOS for BaPt₄Ge₁₂ (a,b),SrPt₄Ge₁₂ (c,d) and ThPt₄Ge₁₂ (e,f) as derived from DFT calculations. Fermi energy is situated at zero energy. The upper half (a),(c) shows the density of states for a fully relativistic calculation, which includes spin-orbit (SO) coupling. The lower half (b),(d) of the figure presents the DOS of a standard non-relativistic calculation. The total DOS is decomposed into the local DOS representative for one Ba(Sr), four Pt, and twelve Ge atoms. The upper half (e) shows the density of states for a fully relativistic calculation, which includes spin-orbit (SO) coupling. The lower half (f) of the figure presents the DOS of a standard non-relativistic calculation. The total DOS is decomposed into the local DOS representative for one Th, four Pt, and twelve Ge atoms. The graphs clearly demonstrate the very dominant character of Ge states particularly at Fermi energy. These states are of expressed *p*-like character. The relativistic effect is small but important, because it shifts the Fermi level of the non-relativistic DOS almost into the maximum of the relativistic DOS.

the relation

$$\gamma_{obs} = \gamma_{band}(1 + \lambda_{ep}), \quad (4.18)$$

where index *band* means that band structure, $\gamma_{band}(0) = 1/3\pi^2k_B^2N(E_F)$ and λ_{ep} is the electron–phonon mass enhancement parameter. The experimental observed values γ_{obs} slightly larger than 40 mJ/molK² for the Ba and Sr compounds, along with an electron-phonon enhancement factor $\lambda_{ep} = 0.7$ (estimated via the McMillan formula Eqn.4.5) would require a bare DOS equivalent to ≈ 25 mJ/molK², which compares favorably with the DOS calculations involving spin-orbit coupling: 31 mJ/molK² for the Ba ($N(E_F) = 13.2$ states eV⁻¹ f.u⁻¹) and 28 mJ/molK² for the Sr compound ($N(E_F) = 12.1$ states eV⁻¹ f.u⁻¹). Without spin-orbit coupling, the specific heats, γ ,

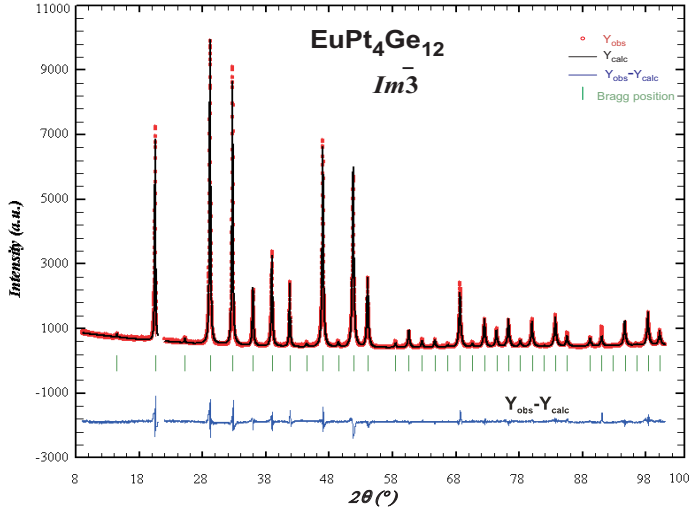


Figure 4.23: X-ray pattern and Rietveld refinement of the skutterudite EuPt₄Ge₁₂. The solid line derives from the Rietveld refinement and Y_{obs} - Y_{calc} is the intensity difference between experimental data and Rietveld calculations.

are 19.5 and 21.0 mJ/molK² for Ba and Sr, respectively.

The total DOS at E_F can be compared with the Sommerfeld value of the specific heat $\gamma = \frac{1}{3}\pi^2 N(E_F)k_B^2$. The experimental values of about 35 mJ/molK² for ThPt₄Ge₁₂ along with an electron-phonon enhancement factor $\lambda_{ep} = 0.66$ (estimated via the McMillan formula Eqn. 4.5) would require a bare DOS equivalent of ≈ 21 mJ/molK², which compares favorably with the DOS calculation involving spin-orbit coupling: 22.7 mJ/molK², $N(E_F) = 9.63$ states eV⁻¹ f.u⁻¹. Without spin-orbit coupling, $\gamma = 20.1$ mJ/molK², documenting the insignificance of relativistic effects. For UPt₄Ge₁₂, however, standard Perdew-Burke-Ernzerhof (PBE) [179] calculations (not shown here) do not disclose any magnetic ordering, thereby confirming experimental observations. The total DOS at E_F of 16.21 states eV⁻¹ f.u⁻¹ is significantly larger than that of ThPt₄Ge₁₂. The corresponding Sommerfeld value $\gamma = 38.2$ mJ/molK² turns out to be smaller than the experimental value of 156 mJ/molK² pointing towards the pronounced effect of spin fluctuations.

4.2 Bulk properties of EuPt₄Ge₁₂

The powder X-ray diffraction pattern of a EuPt₄Ge₁₂ sample was perfectly indexed by considering the skutterudite structure with a body-centered cubic lattice, space group $Im\bar{3}$, (No. 204), isotypic with the filled skutterudite

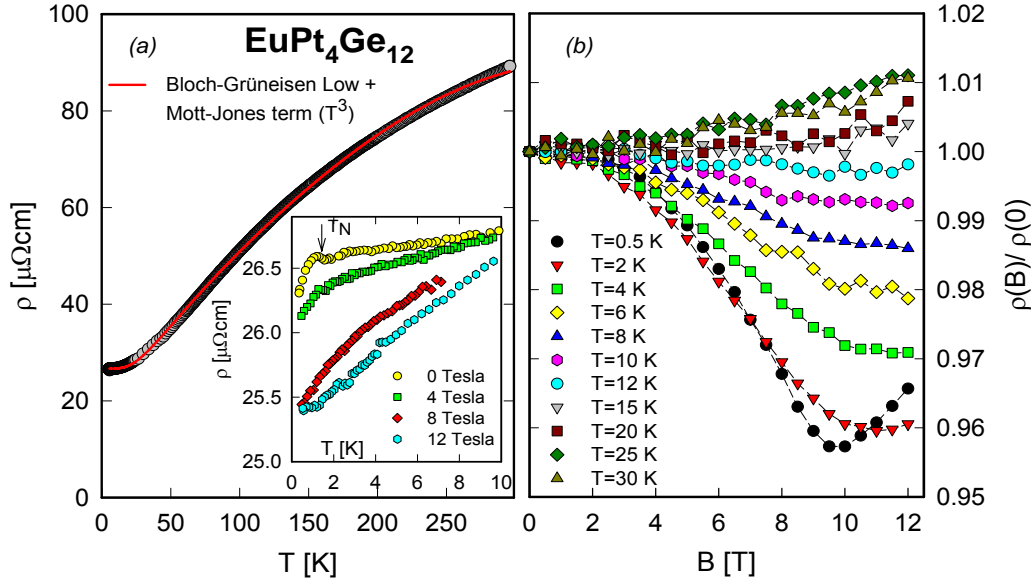


Figure 4.24: (a) Temperature dependent electrical resistivity ρ of EuPt₄Ge₁₂. The inset shows ρ for different field values; the arrow indicates the magnetic ordering temperature. (b) Isothermal magnetoresistance $\rho(B)/\rho(0)$ vs. B ($\rho(B)$ and $\rho(0)$ are the resistivities with and without magnetic fields, respectively) of EuPt₄Ge₁₂ at various temperatures.

type EuFe₄Sb₁₂ [41]. Rietveld refinements of the X-ray intensities with the space group Im $\bar{3}$, (No. 204) in this case converged satisfactorily for a fully ordered atom arrangement (compare crystal structure in Fig. 4.1). A representative Rietveld profile is shown in Fig. 4.23. The lattice parameter for the Eu compound calculated from a least squares fit of the observed powder X-ray pattern and is $a=0.8689(9)$ nm. Rietveld refinements converged to low residual values below $R_F=0.054$.

4.2.1 Electrical resistivity of EuPt₄Ge₁₂

The temperature dependent resistivity $\rho(T)$ of EuPt₄Ge₁₂ is shown in Fig. 4.24a. Runs at various magnetic fields carried out down to 350 mK are displayed in the inset of Fig. 4.24a. These results clearly evidence long range magnetic order around 1.7 K, presumably of antiferromagnetic nature. The latter is inferred from the specific features of $\rho(T)$ below about 1.7 K, which can be accounted for in terms of superzone-boundary effects. Antiferromagnetism is also favoured by the negative paramagnetic Curie-temperature. The application of a sufficiently large external magnetic field suppresses magnetic order. A Fermi-liquid ground state, however, is not recovered since measure-

ments even at 12 T do not reveal a T^2 dependence of $\rho(T)$ at low temperatures. At elevated temperatures, $\rho(T)$ follows the behaviour of a simple metal, but the strong curvature found experimentally requires adding of a Mott-Jones term to the Bloch-Grüneisen formula. The former is a consequence of conduction electron scattering on a narrow feature in the electronic density of states below the Fermi energy. Results of such a fit are shown as solid line in Fig. 4.24a. Scattering of conduction electrons on disordered Eu moments reveals only a temperature independent contribution, since CEF effects are absent.

The isothermal magnetoresistance $\rho(B)/\rho(0)$ as function of external magnetic fields up to 12 T for various temperatures between 0.5 K and 30 K is shown in Fig. 4.24b. At lowest temperatures ($T = 0.5$ K), the system is in its magnetically ordered state, and the pronounced minimum around 10 T may indicate a field induced re-orientation of the antiferromagnetic spin-structure. Above the ordering temperature, the quenching of magnetic fluctuations by the applied magnetic field decreases the electric resistivity as obvious from the data for runs from 4 to 12 K. Above those temperatures, a small positive contributions due to the classical magnetoresistance is observed.

4.2.2 Magnetic properties of $\text{EuPt}_4\text{Ge}_{12}$

The rare earth element Eu exhibits either the magnetic Eu^{2+} state, which is equivalent to Gd^{3+} with only a spin component to the total angular momentum j , i.e., $j = s = 7/2$, while the Eu^{3+} electronic configuration (EC) is non-magnetic. To prove the EC of Eu in $\text{EuPt}_4\text{Ge}_{12}$ we have carried out magnetic measurements. Results regarding the temperature dependent magnetic susceptibility $\chi(T)$, plotted as χ^{-1} vs. T , are shown in Fig. 4.25a. Above about 50 K a Curie-Weiss like behaviour indicates a simple paramagnetic state. A least squares fit to the modified Curie-Weiss law, i.e., $\chi = \chi_0 + C/(T - \theta_p)$ yields an effective moment $\mu_{\text{eff}} = 7.35 \mu_B$ and a paramagnetic Curie temperature $\theta_p = -11.5$ K.

The effective magnetic moment is close to the theoretical value associated with the Eu^{2+} state ($\mu_{\text{eff}}^{\text{theo}} = 7.91 \mu_B$), while the negative paramagnetic Curie temperature indicates antiferromagnetic interactions between conduction electrons and the almost localized $4f$ electrons. The slight curvature of $1/\chi(T)$ originates from a temperature independent Pauli contribution $\chi_0 = 0.001 \text{ emu/mol}$. Distinct crystalline electric field effects are absent in this compound because of the spin-only contribution to the total angular momentum. A magnetic phase transition is not obvious from these measurements, at least, down to 2 K, although the system holds a very large effective magnetic moment. The small deviation of the observed effective magnetic moment from the theoretical value may be a result of various features: *i*) a filling grade slightly below 100 % of Eu on the $2a$ site cannot completely

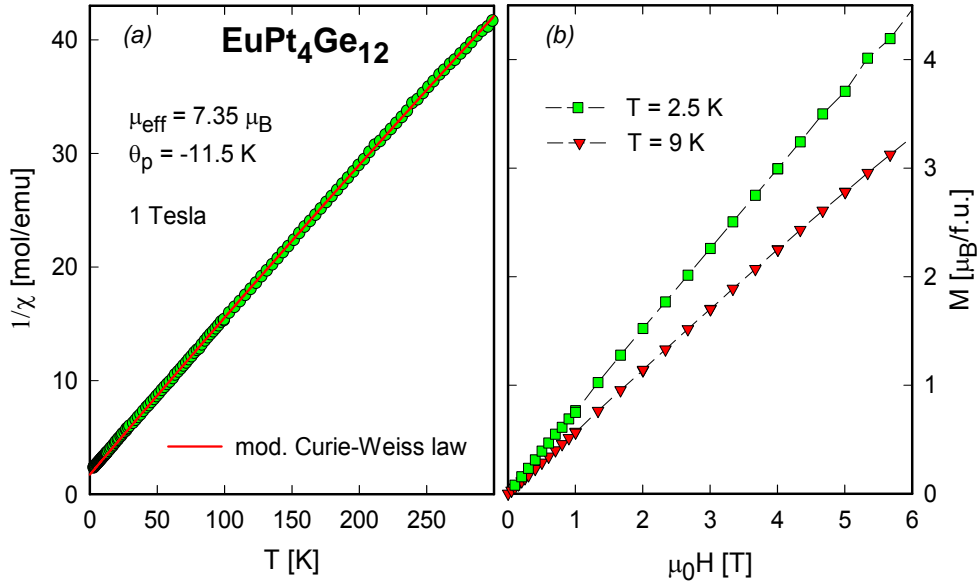


Figure 4.25: (a) Temperature dependent magnetic susceptibility χ of EuPt₄Ge₁₂ compound, plotted as χ^{-1} vs. T . The solid line is a least squares fit using the modified Curie-Weiss law. (b) Isothermal magnetisation of EuPt₄Ge₁₂ compound.

be excluded from our x-ray study and/or *ii)* the valency of the Eu ion may not fully match the integer 2+ state. Specifically, L_{III} measurements carried out on EuFe₄Sb₁₂ [180] have shown that about 13 % of the Eu ions have formally a valence of 3+, associated with the nonmagnetic EC of this element. Isothermal magnetisation curves shown in Fig. 4.25b also demonstrate that magnetic order does not occur above 2.5 K. Furthermore, the linear $M(H)$ dependence of EuPt₄Ge₁₂ reflects the absence of CEF effects as well as of significant magnetic correlations.

4.2.3 Density of states DOS of EuPt₄Ge₁₂

The calculated DOS of EuPt₄Ge₁₂ is shown in Fig. 4.26. Because the Eu-4f states are strongly localized, these states are treated in terms of the LDA+ U approach as proposed by Dudarev et. al. [181]. Only the difference $\Delta = U - J$ of the on-site Coulomb and exchange parameters enters then the calculation. Similar to the study of EuB₆[182], $\Delta = 7$ eV is selected for Eu. Similar calculations performed for $\Delta = 6, 8$, and 9 (without optimization of the internal parameter) showed that the bulk properties are almost unaffected by the choice of Δ . As can be realized from Fig. 4.26, the choice of $\Delta = 7$ eV yields the f bands ≈ 2 eV below the Fermi level. Switching off Δ causes a

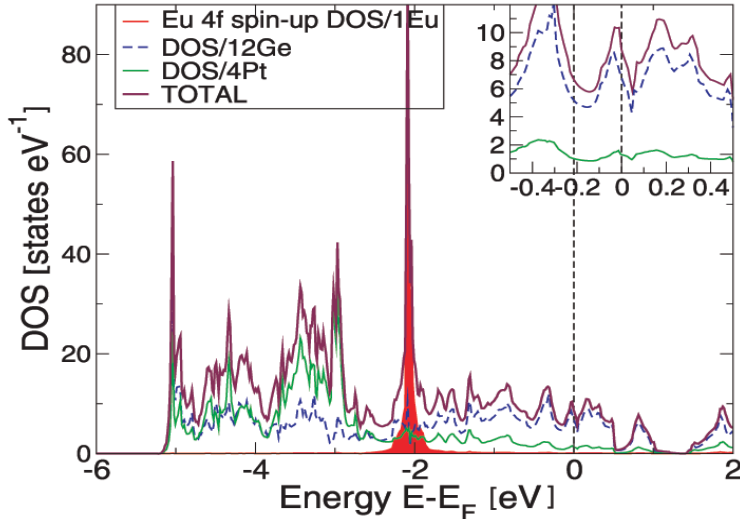


Figure 4.26: Density of states (DOS) for EuPt₄Ge₁₂ as derived from DFT LDA+U ($U - J = 7$ eV) calculations. Fermi energy is situated at zero energy. The total DOS is split into the local DOS corresponding to all the Ge and Pt atoms. The effect of spin polarization on Pt and Ge states is negligible. For Eu the local *f* DOS is shown for the majority spin occupation and is fully occupied resulting in a total localized moment of $\mu_{eff} = 7 \mu_B$. Inset: DOS around Fermi energy.

shift of the Eu-4*f* states to energies just below the Fermi energy. The long range magnetic coupling is very weak, because both the ferromagnetic and antiferromagnetic calculation for EuPt₄Ge₁₂ results in the same total energy, and consequently the same structural parameters as well as in the same local moment of $7 \mu_B$ for Eu. The magnetic moment of $7 \mu_B$ is in agreement to the above susceptibility data. The states at the Fermi level are mainly composed of Ge 4*p* states (about 90%) and a small Pt-5*d* contribution (10%). The total DOS value at E_F is 9.2 states eV⁻¹ f.u.⁻¹ [55].

Although Eu²⁺ has a rather large magnetic moment, the ordering temperature is small. In general, magnetic order of metallic rare earth systems is maintained by the oscillating RKKY interaction between the localized magnetic moment and the conduction electron system. The electronic density of states as well as the distance between magnetic moments are playing a crucial role. A comparison with the Eu-based skutterudite EuFe₄Sb₁₂ reveals for the latter a much larger phase transition temperature, $T_c \approx 84$ K, exhibiting a ferrimagnetic ordered state. The striking difference between both isomorphous compounds, however, is due to the fact that the [Fe₄Sb₁₂] host lattice is nearly ferromagnetic [180, 183], with a moment of about $0.21 \mu_B$, antiferromagnetically coupled to the Eu moment. The resulting

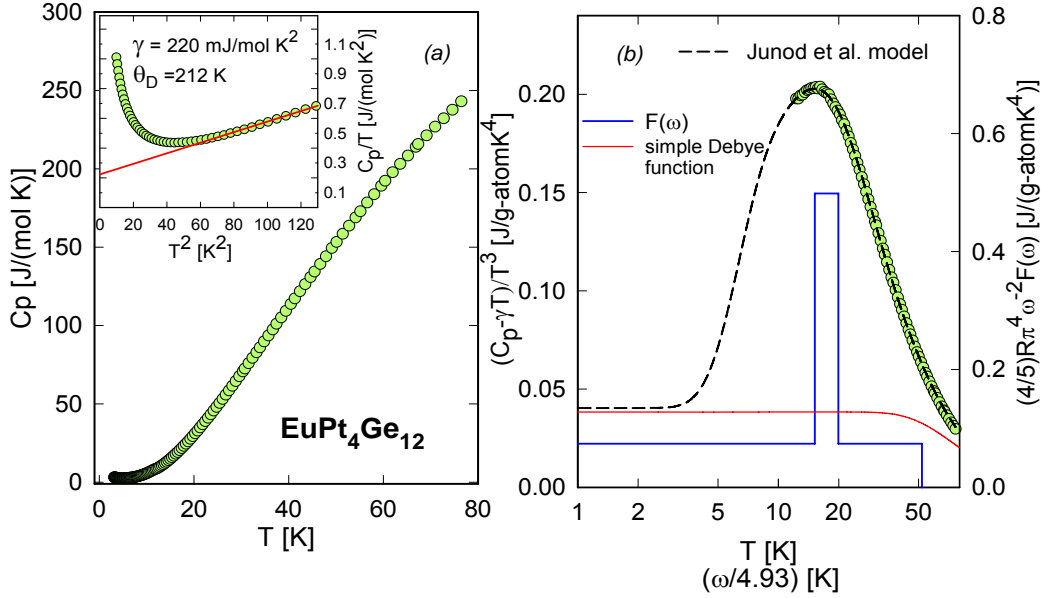


Figure 4.27: (a) Temperature dependent specific heat C_p of EuPt₄Ge₁₂ plotted as C_p vs. T for 0 T. The inset shows C_p/T vs. T^2 for the low temperature region. (b) Phonon part of the temperature dependent specific heat C_p of EuPt₄Ge₁₂, plotted $(C_p - \gamma T)/T^3$ vs. $\ln T$. The dashed lines are the result of the fitting procedure of the experimental data using the model described in the text. The solid lines (referring to the right axis) sketch the phonon spectral function $F(\omega)$ plotted as $(5/4)R\pi^4\omega^{-2}F(\omega)$ vs. $\omega/4.93$.

f -electron interaction with nearly ferromagnetic [Fe₄Sb₁₂] is then the origin of the relatively high transition temperature observed for EuFe₄Sb₁₂. Since [Pt₄Ge₁₂] does not possess a magnetic moment, the above indicated enhancement mechanism is absent. Thus, the spin-only moment of Eu considerably fluctuates, and ordering can be easily destroyed with increasing temperature, as observed experimentally. This scenario is corroborated from ordering temperatures below 3 K if Fe in EuFe₄Sb₁₂ is replaced by isovalent Ru [184].

4.2.4 Heat capacity of EuPt₄Ge₁₂

The temperature dependent specific heat C_p of EuPt₄Ge₁₂ above 2 K is shown in Fig. 4.27a. The smooth $C_p(T)$ dependence indicates phonon-dominated specific heat. The application of the simple Debye model in the whole temperature range, however, fails. Plotting the data as C_p/T^3 vs. T (Fig. 4.27b) reveals a local maximum around 15 K which refers to an Einstein-like phonon branch around 75 K. A plot of C_p/T vs. T^2 is shown in the inset of Fig. 4.27.

Clearly visible is the rapid upturn below 5 K, reflecting short range order effects above the magnetic phase transition at 1.7 K. Apart from this upturn, a standard specific heat analysis (solid line, inset, Fig. 4.27a) allows to obtain the electronic contribution to the specific heat $\gamma = 220$ [mJ/molK²] and the Debye temperature $\theta_D \approx 212$ K. γ of the present compounds consists of the pure electronic contribution due to the distinct DOS at E_F as well as of enhancement factors such as the electron-phonon term and a term due to magnetic fluctuations above ordering. Previously we have shown that for $\{\text{Sr}, \text{Ba}\}\text{Pt}_4\text{Ge}_{12}$ $\lambda_{e,ph} \approx 1.7$ [54]. Adopting the value ($1 + \lambda_{e,ph} \approx 1.7$) in the context of the theoretically calculated DOS at E_F (9.2 states eV/f.u., corresponding to a specific heat coefficient $\gamma \approx 21$ [mJ/molK²]) would reveal a contribution of about 35 [mJ/molK²]. The remaining share to the observed value $\gamma \approx 220$ mJ/molK² is thus a result of fluctuations of the Eu magnetic moment.

Chapter 5

Clathrate Ba-X-Ge Systems (X=Cd, Pd, Zn)

5.1 Ba-Cd-Ge Clathrate System; crystal structure and physical properties

5.1.1 Crystal Chemistry of $Ba_8Cd_xGe_{43-5x/8}\square_{3-3x/8}$

In order to evaluate atom site preferences in $Ba_8Cd_xGe_{43-5x/8}\square_{3-3x/8}$ X-ray diffraction data from single crystals with $x = 2.4, 4.7, 6.5$ and 7.6 were collected at room temperature. In all cases extinctions and diffraction intensities were consistent with a primitive cubic lattice (space group $Pm\bar{3}n$, $a \approx 1.1$ nm) and indicated isotypism with the structure of Clathrate type I. No extra reflections indicating a larger unit cell $a' = 2a$ as reported by [194] for Ba_8Ge_{43} were detected in the investigated ternary crystals.

The composition dependence of the lattice parameters for $Ba_8Cd_xGe_{46-x-y}\square_y$ is shown in Fig. 5.1a and compares well with available literature data. The increase of the unit cell parameters with cadmium content is in line with the difference of atomic radii of the elements. The sample $Ba_8Cd_8Ge_{38}$ (nominal composition) is a single phase Clathrate with lattice parameter $a = 1.09499(3)$ nm, but ternary alloys with higher Cd content were found to be multiphase with a similar lattice parameter for the clathrate phase.

The heavy barium atoms were unambiguously found in sites $2a$ (0, 0, 0) and $6c$ ($1/4, 0, 1/2$) and the electron density distribution for the remaining sites appeared as two features.: (i) constant electron densities of about 32 e/atom in both lattice sites $16i$ and $24k$, (ii) an increasing number of electrons in the $6d$ site from 16 e/atom for binary $Ba_8Ge_{43}\square_3$ (data of Ref.[194]) to ~ 46 e/atom for $Ba_8Cd_{6.5}Ge_{39.1}\square_{0.4}$ and $Ba_8Cd_{7.6}Ge_{38.4}$.

X-ray diffraction data for crystals with smaller Cd contents

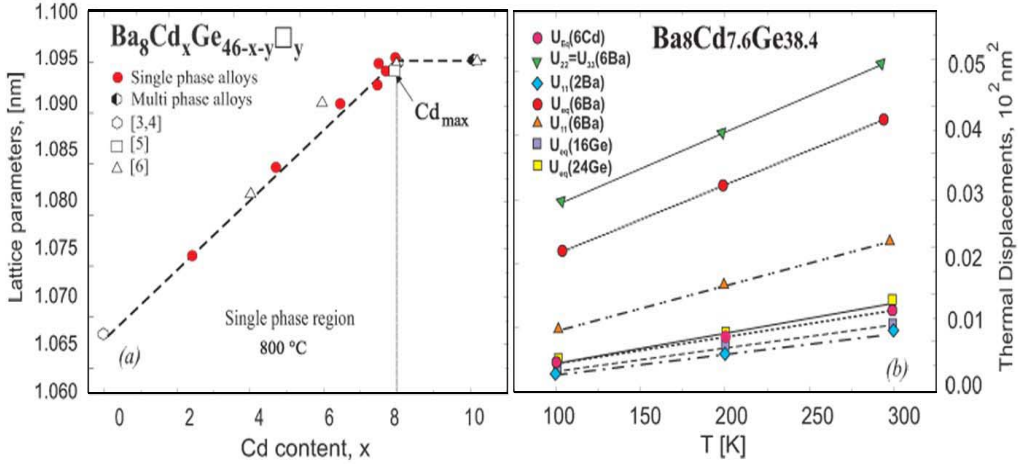


Figure 5.1: (a) Thermal displacement parameter of $\text{Ba}_8\text{Cd}_{7.6}\text{Ge}_{38.4}$ vs temperature. (b) Lattice parameters versus Cd-content for $\text{Ba}_8\text{Cd}_x\text{Ge}_{46-x-y}\square_y$ alloys. The dashed line denotes the solubility limit of Cd at 800°C.

($\text{Ba}_8\text{Cd}_{2.4}\text{Ge}_{41.4}\square_{2.2}$ and $\text{Ba}_8\text{Cd}_{4.7}\text{Ge}_{40.3}\square_{1.0}$) were refined with fixed vacancy or/and Cd content in the $6d$ site. For all refinements anisotropic thermal displacement parameters (ADP) were employed.

Analyzing the thermal atomic displacement parameters ADP's we encountered a large anisotropy of electron densities in two cases (*i*) Ba atoms in the $6c$ site for all investigated single crystals and (*ii*) Ge atoms in $24k$ site (Ge3) for Cd-concentrations smaller than $x = 5$. However, with increasing Cd-content the anisotropy of ADP's for Ge3 decreases and finally vanishes for $x \geq 6$. As the direction of the ADP ellipsoids point towards the nearest neighbours in the $6d$ site (M1), we may associate this behaviour with vacancy formation: the three species (Ge- or Cd- atoms or vacancy) occupying the $6d$ site engage in different interactions with Ge atoms located in the $24k$ site and interatomic distances d_{M1-Ge3} increase in the sequence $\square\text{-Ge}$, Ge-Ge , Cd-Ge . Accordingly the shape of the $6d$ site electron density adopts an ellipsoid elongated along the direction of the M-Ge3 bonds (Fig. 5.2).

The change of the crystallographic parameters (lattice parameter, atomic coordinates and site occupancy) with Ge/Cd substitution is well reflected by a compositional dependence of the interatomic distances (Tables 2 and 3 in Ref.[69]).

The ADP parameters for Ba atoms located in the $6c$ site (Ba2) show significant anisotropy in contrast to Ba1 atoms in site $2a$, which seem to have normal behaviour (Tables 3 and 4 in Ref.[69]). Coordination polyhedra for both barium atoms are shown on Fig. 5.2. If the $\text{Ba}_8\text{Cd}_{7.6}\text{Ge}_{38.4}$ crystal is considered as a simple Debye solid and additionally with Ba2 atoms be-

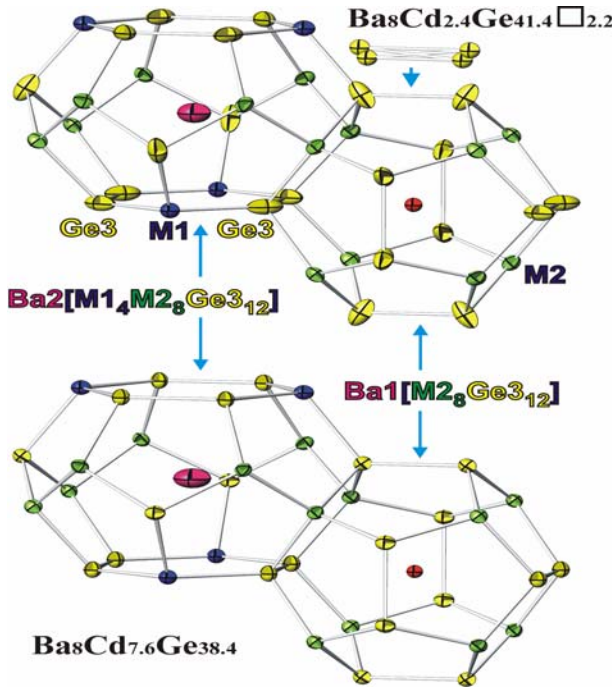


Figure 5.2: Cages and atom thermal displacement parameters in Clathrate $\text{Ba}_8\text{Cd}_{x}\text{Ge}_{43-5x/8}\square_{3-3x/8}$ (Ge3 atoms in unsplit model). The replacement of Ge3 by split Ge31 and Ge32 sites is indicated in the right upper corner.

having like Einstein-oscillators, the thermal displacements and the Einstein temperatures $\Theta_{E,ii}$ are related by Eqn. 5.1

$$U_{ii} = \frac{\hbar^2}{2m_{\text{Ba}}k_B\theta_{E,ii}} \coth\left(\frac{\theta_{E,ii}}{2T}\right), \quad (5.1)$$

where m_{Ba} is the atomic mass of Ba. From symmetry constraints U_{11} is different from $U_{22} = U_{33}$, yielding $\theta_{E,ii} = 78K$ and $\theta_{E,ii} = 58K$ in line with the flat rotational ellipsoid of Ba2 atoms squeezed between the two hexagons of the framework tetradecahedron (see Fig. 5.2). It is interesting to note that Ba1 atoms in the smaller pentagonal dodecahedral cage do not show a thermal displacement factor (spherical by symmetry) enhanced over the general ADP values for framework atoms. Thus no special rattling effect can be expected from Ba1 atoms.

5.1.2 Physical Properties; Heat Capacity

Specific heat measurements were performed on the clathrate having the highest content of Cd, i.e., $\text{Ba}_8\text{Cd}_{7.6}\text{Ge}_{38.4}$. Results of this investigation are displayed in figures 8a,b. The heat capacity at low temperature ($T < 4 \text{ K}$) can be

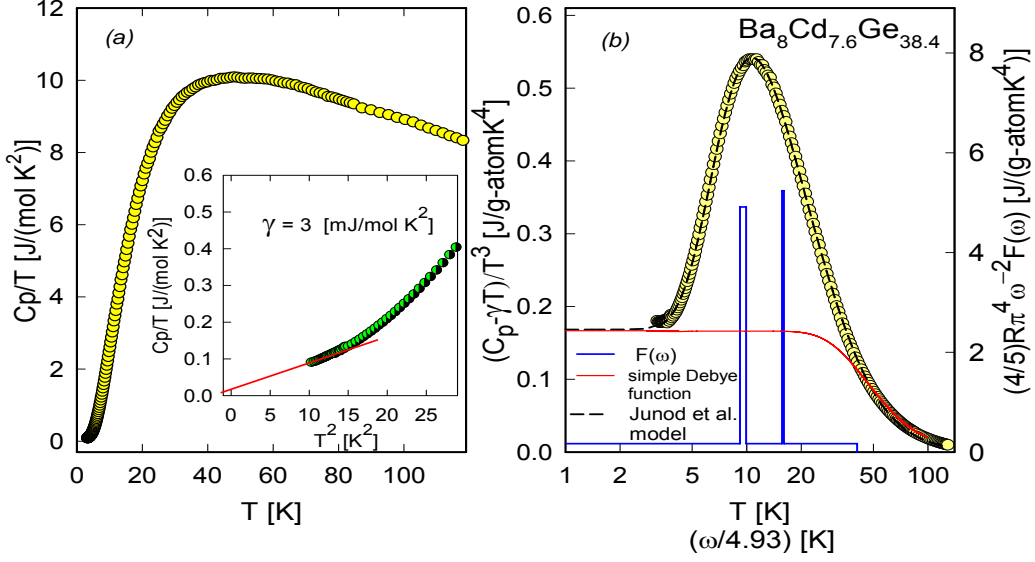


Figure 5.3: (a) Temperature dependent specific heat C_p of $\text{Ba}_8\text{Cd}_{3-x}\text{Ge}_{43-5x/8}\square_{3-3x/8}$, plotted as C_p versus T . (b) Temperature dependent specific heat of $\text{Ba}_8\text{Cd}_{7.6}\text{Ge}_{38.4}$, plotted as $(C_p - \gamma T)/T^3$ vs. $\ln T$. The dashed line is a least squares fit of the experimental data using the model described in the text(Eqn.A.11). The solid and the dashed-dotted lines sketch the phonon spectral function $F(\omega)$ plotted as $\omega/4.93$ vs. $(5/4)R\pi^4\omega^{-2}F(\omega)$ for which ω is given in Kelvin. The essential parameters of the model used to construct the spectral function $F(\omega)$ (solid lines, right axis), are $\theta_D = 220$ K, $\theta_{E1} = 47 \pm 2$ K and $\theta_{E2} = 78 \pm 1.6$ K.

described in terms of an electronic contribution $\gamma = 3$ mJ/molK² and a lattice contribution $\beta = 0.0085$ J/molK⁴, yielding a low temperature Debye temperature $\theta_D^{LT} = 231$ K. This standard description, however, breaks down already above about 4 K, referring to a rather complicated phonon spectrum due to the distinct crystal structure of $\text{Ba}_8\text{Cd}_{7.6}\text{Ge}_{38.4}$, filled by the electropositive element Barium.

Results of least squares fits of $\text{Ba}_8\text{Cd}_{7.6}\text{Ge}_{38.4}$ based on the Junod's model [91, 92] are shown in Fig. 5.3b. The Sommerfeld value γ is subtracted, thus, the experimental points in Fig. 5.3b refer to the phonon contribution only. A proper description of the temperature dependent specific heat is obtained employing a Debye temperature $\theta_D = 220$ K and two Einstein-like contributions, $\theta_{EL1} = 47$ and $\theta_{EL2} = 78$ K, with corresponding spectral widths of 3.7 and 1.9 K, respectively. Accordingly, both contributions have different spectral weights. Adding these additional branches means to account for very localized phonon branches. In a first view, the cage like structure

formed by the (Cd,Ge) network may constitute the background Debye-like spectrum, while the electropositive element barium, which fills the over sized cages, gives rise to rattling modes, represented by two Einstein-branches. Here, it should be noted that the Einstein contribution is not a δ -function, rather, it replenishes a temperature width of a few Kelvins. However, when comparing this type of analysis with data available for skutterudites [185], a much narrower temperature range regarding the Einstein branches is obtained for clathrates.

Although the treatment of the temperature dependent specific heat coincides with the Einstein temperatures obtained from the ADP's, a 1:1 correspondence between both sets of temperatures may be somehow artificial. Assuming that the smaller Einstein temperature belongs to the Ba2 sites, the cage structure around Ba2 atoms and its elastic deformation may then give rise to a further Einstein mode, $\Theta_{EL2} = 78.5 \pm 1.6$ K.

5.1.3 Electrical resistivity

Materials under investigation are characterized by their proximity to a metal-to-insulator transition because of a significantly reduced charge carrier concentration. As a result, the overall resistivities are quite large, exceeding those of typical intermetallic compounds by more than one order of magnitude (see Fig. 5.4a). The room temperature resistivities are 8322, 10330, 401 and $453 \mu\Omega \text{ cm}$ for the $\text{Ba}_8\text{Cd}_x\text{Ge}_{46-x-y}\square_y$, $x = 2.4, 4.7, 6.5$ and 7.6 samples, respectively. $\text{Ba}_8\text{Cd}_x\text{Ge}_{46-x-y}\square_y$, $x = 6.5$ and 7.6 exhibit metallic like behaviour, i.e., $\rho(T)$ increases steadily with increasing temperature, however, particular features in $\rho(T)$ do not follow a simple temperature dependence originated by scattering of charge carriers (electrons or holes) on thermally excited phonons. The latter is usually expressed by the Bloch-Grüneisen formula 1.4 where C is a temperature independent electron-phonon interaction constant and Θ_D is the Debye temperature. Bloch-Grüneisen formula (Eqn. 1.4) causes a T^5 behaviour of $\rho(T)$ at low temperatures ($T \ll \Theta_D$), whilst at elevated temperatures $\rho(T)$ should behave linearly. A closer inspection of the data of Fig. 5.4a shows that $\rho(T)$ at low temperatures follows roughly a $T^{2.5}$ dependence, which never can be reproduced applying Eqn. 1.4. Moreover, the tendency of the data towards a positive slope, i.e., $d\rho/dT > 1$, is not accounted for in terms of Eqn. 1.4. Deviations from the Bloch-Grüneisen behaviour become even worse if the number of charge carriers is changed, varying the Cd content (Fig. 5.4a).

The temperature dependent resistivity $\rho(T)$ evidences a crossover from a metallic-like behaviour for large Cd contents, to a more complex temperature dependence for $x = 2.4$ and 4.7 . Both latter compounds exhibit around room temperature a semiconducting-like temperature dependence of $\rho(T)$, while below a maximum, a metallic like behaviour becomes obvious. Additionally,

a small upturn of $\rho(T)$ can be observed for $T < 10$ K. In order to get rid of those rather uncommon features, we have developed a model [69], which combines the description of simple metals via the Bloch-Grüneisen law with a temperature dependent charge carrier density. The latter follows from distinct features of the electronic density of states (DOS) around the Fermi energy E_F . To simplify the calculations, we have assumed that the DOS can be represented by rectangular bands. The proximity of the present systems to isolating states has to be reflected by a gap in the DOS slightly above E_F having an appropriate width E_g (compare the inset in Fig. 5.4b). These assumptions allow to calculate both, the density of electrons, n_n , as well as the density of holes, n_p , using standard statistics and involving the Fermi-Dirac distribution function $f(E, T)$. Considering this rectangular density of states model, $N(E)$, n_n follows from

$$n_n(T) = \int_{E_F}^{\infty} N(E) f(E, T) dE \quad (5.2)$$

as

$$n_n(T) = -NE_g + Nk_B T \ln(1 + \exp(E_g/k_B T)) \quad (5.3)$$

where N is the band height. With similar arguments, the hole density n_p can be derived:

$$n_p(T) = \int_{-\infty}^{E_F} N(E) (1 - f(E, T)) dE \quad (5.4)$$

revealing $n_p(T) = -Nk_B T \ln 2$. The total charge carrier density is then simply given by

$$n(T) = \sqrt{n_n(T)n_p(T)} + n_0 \quad (5.5)$$

where n_0 is a residual density of states, accounting for the fact that at $T = 0$ the samples investigated exhibit finite residual resistivity. Finally, the overall resistivity of such systems can be expressed as

$$\rho(T) = \frac{\rho_0 n_0 + \rho_{ph}}{n(T)} \quad (5.6)$$

where ρ_0 is the residual resistivity and ρ_{ph} is given by Eqn.1.4.

A least squares fit to the data of Fig. 5.4a was carried out considering Eqn. 5.6. Results of such a procedure are plotted in Fig. 5.4b as solid blue lines. Despite of the fact that the model is simple, the results describe astonishingly well the experimentally derived temperature dependences. The most important parameter appears to be the gap width E_g , which for $\text{Ba}_8\text{Cd}_{2.4}\text{Ge}_{41.4}\square_{2.2}$ and $\text{Ba}_8\text{Cd}_{4.7}\text{Ge}_{40.3}\square_{1.0}$ amounts to 2570 and 3230 K, respectively. Besides other features in $\rho(T)$ within the model outlined, a very narrow region of the DOS right above E_F , also defining the gap distance from E_F , is responsible for the metallic $\rho(T)$ dependence of the present clathrates at lower temperatures. Note also, that features, like a small upturn in $\rho(T)$ at lowest temperatures, are quite well reproduced, too.

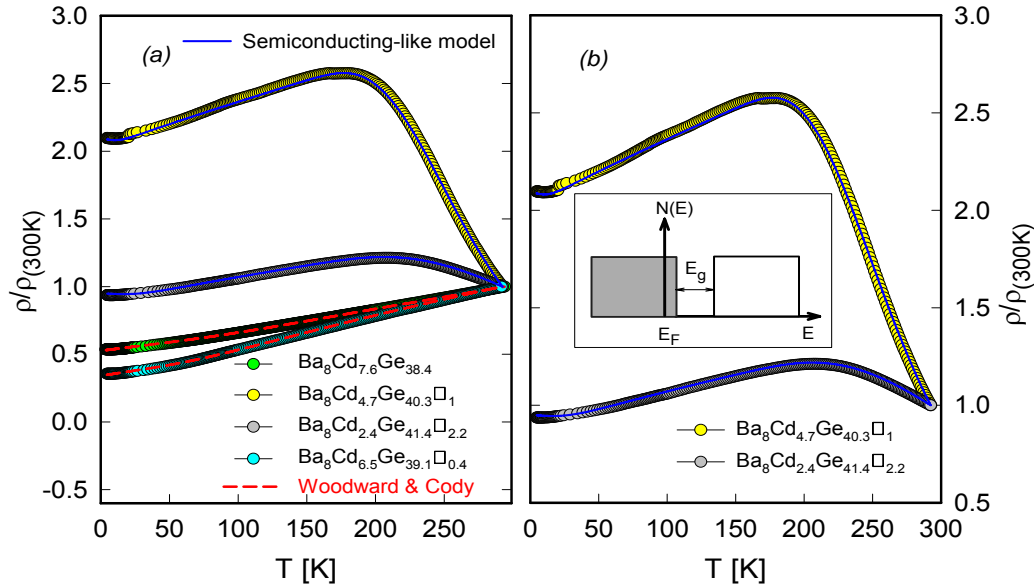


Figure 5.4: (a) Temperature dependent normalized resistivity $\rho/\rho_{(295K)}$ of $Ba_8Cd_xGe_{43-5x/8}\square_{3-3x/8}$. Dashed red lines are least squares fits of the data according to Woodard and Cody formula (Eqn.A.1). The solid blue lines are least squares fits according to model which explained in the text. (b) Normalized electrical resistivity ρ of $Ba_8Cd_{2.4}Ge_{41.4}\square_{2.2}$ and $Ba_8Cd_{4.7}Ge_{40.3}\square_1$. The solid lines are least squares fits explained in the text. The inset is a sketch of the electronic density of states model in the vicinity of the Fermi energy E_F .

5.1.4 Thermal conductivity

The temperature dependent thermal conductivity, λ , of $Ba_8Cd_xGe_{43-5x/8}\square_{3-3x/8}$ is displayed in Fig. 5.5a for the temperature range from 4 K to room temperature. As expected for clathrates, overall $\lambda(T)$ values are small and are dominated by the lattice thermal conductivity λ_{ph} at low temperatures.

A more quantitative description of $\lambda(T)$ is possible in terms of Callaway's theory [81, 82, 83] of lattice thermal conductivity, λ_{ph} . To derive λ_{ph} from the total thermal conductivity λ , the Wiedemann-Franz law is applied to the $\rho(T)$ data, allowing to define the electronic thermal conductivity, λ_e . Although this model is valid in extended temperature ranges only for free electron systems, it is widely used even for complex materials such as skutterudites or clathrates. The Wiedemann-Franz relation states that increasing electrical resistivities cause decreasing λ_e values.

In the Eqn. 1.17 second integral is $I_2 = I_2(\tau_c, \tau_N, \tau_U)$, where τ_N denotes

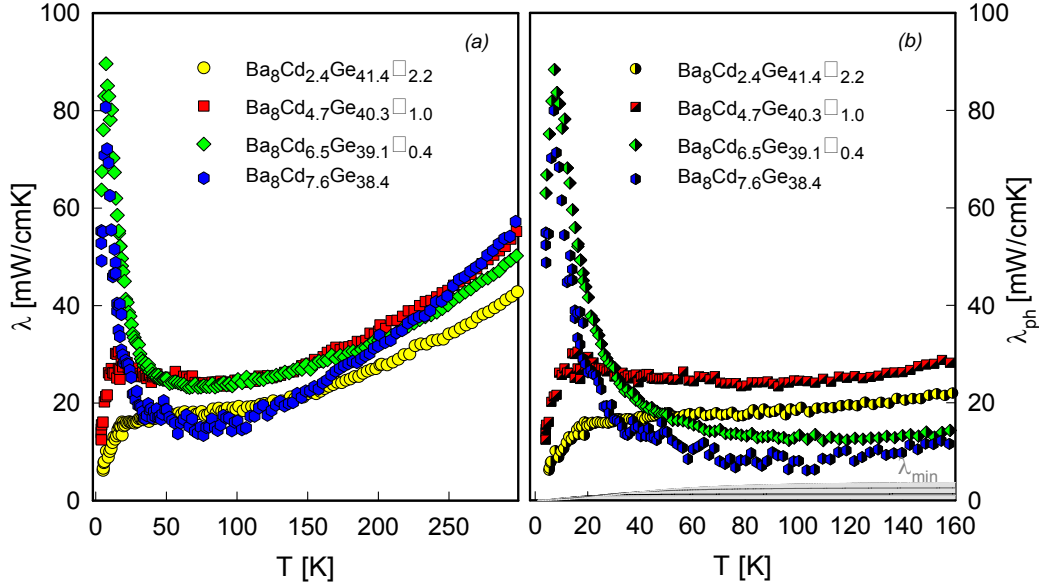


Figure 5.5: (a) Temperature dependent thermal conductivity λ of $\text{Ba}_8\text{Cd}_x\text{Ge}_{43-5x/8}\square_{3-3x/8}$ with $x = 2.4, 4.7, 6.5, 7.6$. (b) Temperature dependent lattice thermal conductivity λ_{ph} for the same samples.

normal 3-phonon processes. If all phonon branches are scattered by resistive processes, then $\tau_N \gg \tau_U$; as a consequence, the first integral in Eqn. 1.17 predominantly contributes to the observed thermal conductivity [84]. The N -processes are, in general, important only at low temperatures and in nearly perfect, low-anharmonicity crystals. The rather large resistivity values, typical for skutterudites and clathrates, allow in a first approximation to neglect contributions from the Integral I_2 of Eqn. 1.17. Thus, I_2 in the Eqn. 1.17 is disregarded in the present analysis. In order to get rid of radiation losses, proprietary to the steady state heat flow method used, a T^3 term was added to Eqn. 1.17 for the analysis. In the relaxation times Eqn. 1.19 does not contain terms for resonance scattering, since they seem to be of minor importance in both compounds studied. The initial rise of λ_{ph} may be referred to boundary and point defect scattering; it becomes large when both quantities are small. Note that defects comprise also vacancies. If the strength of Umklapp scattering increases, λ_{ph} starts to strongly decrease, thereby forming a maximum at lower temperatures. The latter depends also weakly on the Debye temperature but occurs in general well below $\theta/10$. Additionally, an increase of θ slightly reduces overall λ_{ph} values. Enhanced scattering of phonons on electrons also efficiency reduces the lattice reduces the lattice thermal conductivity.

The lattice thermal conductivity (see Fig. 5.5) shows very small values at

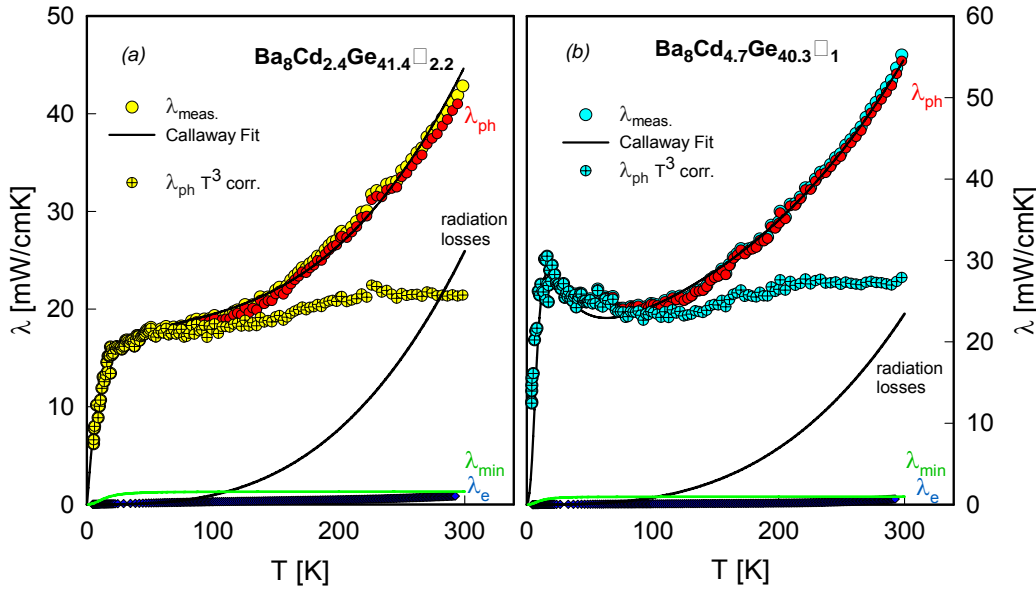


Figure 5.6: (a) Separation of the total thermal conductivity $\lambda(T)$ of $\text{Ba}_8\text{Cd}_{2.4}\text{Ge}_{41.4}\square_{2.2}$ (b) $\text{Ba}_8\text{Cd}_{4.7}\text{Ge}_{40.3}\square_{1.0}$ into the electronic part λ_e and the lattice part λ_{ph} . The electronic λ_e (filled blue diamonds) and the lattice contribution λ_{ph} (filled red circles) are derived from the Wiedemann-Franz law. The filled \oplus symbol indicate thermal conductivity data obtained from a correction procedure taking radiation losses into account. The solid and the dashed lines are least squares fits applying the model of Callaway with a T^3 term for radiation losses. The green lines are calculations of the theoretical lower limit of thermal conductivity λ_{\min} .

medium temperatures, thereby evidencing an important interaction process to substantially lowering λ_{ph} : scattering of the phonons on charge carriers (compare Eqn. 1.19).

In fact the compounds richest in Cd content ($x = 6.5$ and 7.6) exhibit the lowest lattice thermal conductivity. This is referred to the previously-indicated mechanism since the compounds $\text{Ba}_8\text{Cd}_{7.6}\text{Ge}_{38.4}$ and $\text{Ba}_8\text{Cd}_{6.5}\text{Ge}_{39.1}\square_{0.4}$ show the least resistivity, giving rise to an enhanced interaction of the heat carrying phonons with the conduction electron system. On the other hand, the $\text{Ba}_8\text{Cd}_{4.7}\text{Ge}_{40.3}\square_{1.0}$ compound exhibits a almost doubled lattice thermal conductivity around 150 K. This coincides with the largest overall electrical resistivity of the present series. One can then conclude that the reduced charge carrier density and/or smaller mobility yields only to weak interactions of both phonons and the charge carriers. Hence, the lattice thermal conductivity keeps relatively large.

The temperature dependent thermal conductivity $\lambda(T)$ of

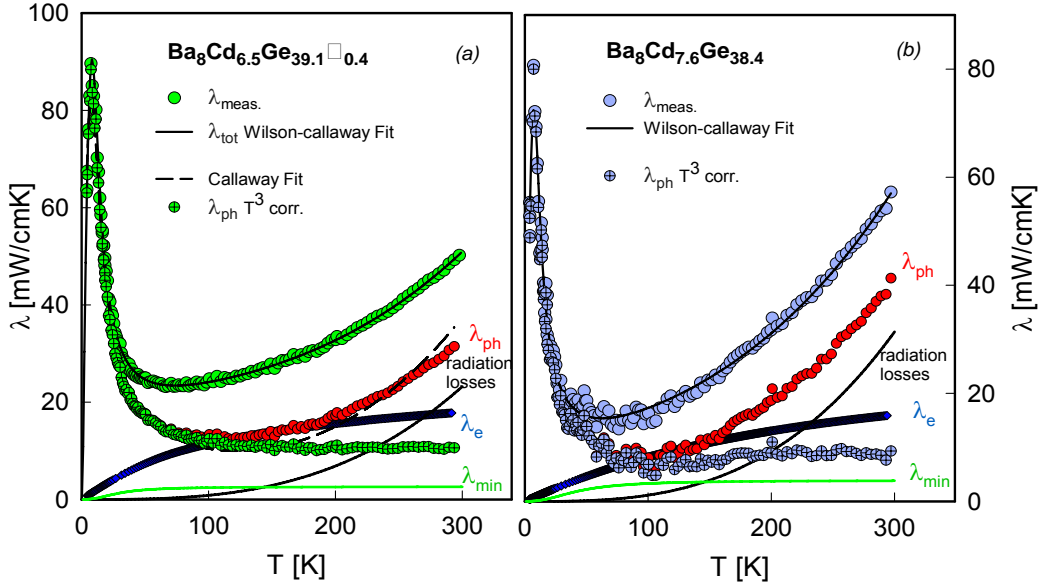


Figure 5.7: (a) Separation of the total thermal conductivity $\lambda(T)$ of $\text{Ba}_8\text{Cd}_{6.5}\text{Ge}_{39.1}\square_{0.4}$ (b) $\text{Ba}_8\text{Cd}_{7.6}\text{Ge}_{38.4}$ into the electronic part λ_e and the lattice part λ_{ph} . The electronic λ_e (filled blue diamonds) and the lattice contribution λ_{ph} (filled red circles) are derived from the Wiedemann-Franz law. The filled \oplus symbol indicate thermal conductivity data obtained from a correction procedure taking radiation losses into account. The solid and the dashed lines are least squares fits applying the model of Callaway with a T^3 term for radiation losses. The green lines are calculations of the theoretical lower limit of thermal conductivity λ_{min} .

$\text{Ba}_8\text{Cd}_{2.4}\text{Ge}_{41.4}\square_{2.2}$ and $\text{Ba}_8\text{Cd}_{4.7}\text{Ge}_{40.3}\square_{1.0}$ is displayed in Figs. 5.6a,b. The separation of the total thermal conductivity $\lambda(T)$ into the electronic contribution λ_e and the lattice contribution λ_{ph} was done in terms of the Wiedemann-Franz law. The solid bold lines correspond to the radiation losses data. Application of the Wiedemann-Franz law (Eqn. 1.10) in both cases reveals only small electronic thermal conductivities λ_e only ≤ 1 mW/cmK. The filled symbol in Figs. 5.6a,b denote the corrected lattice thermal conductivities. The overall values of $\lambda(T)$ in cases of $\text{Ba}_8\text{Cd}_{2.4}\text{Ge}_{41.4}\square_{2.2}$ and $\text{Ba}_8\text{Cd}_{4.7}\text{Ge}_{40.3}\square_{1.0}$ are lower than those of $\text{Ba}_8\text{Cd}_{6.5}\text{Ge}_{39.1}\square_{0.4}$ and $\text{Ba}_8\text{Cd}_{7.6}\text{Ge}_{38.4}$ at low temperature, typically in the range of 15 to 30 mW/cmK. Results of least squares fits are shown as solid and dashed lines in Fig. 5.6, where the bold solid line corresponds to the T^3 correction.

The experimentally observed fact that an increase of the Cd content enhances the low temperature maximum in $\lambda_{ph}(T)$ (compare figures 5.5(a,b)-5.7(a,b)) would refer to a lowering of boundary and/or point defect scattering.

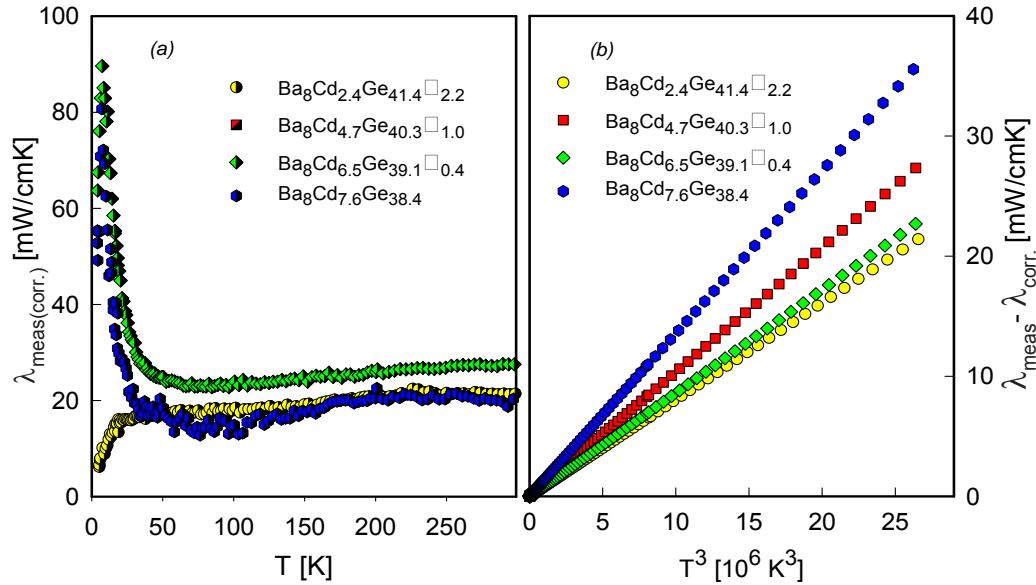


Figure 5.8: Temperature dependent thermal conductivity λ of $\text{Ba}_8\text{Cd}_x\text{Ge}_{43-5x/8}\square_{3-3x/8}$ with $x = 2.4, 4.7, 6.5, 7.6$ (a) thermal conductivity $\lambda_{\text{meas. corr.}}(T)$ indicate measured thermal conductivity data obtained from a correction procedure taking radiation losses into account (b) The right panels displays the difference between the measured and the corrected thermal conductivity $\lambda_{\text{meas.}} - \lambda_{\text{corr.}}$ as a function of T^3 .

Although the Ge/Cd substitution creates increasing statistical disorder, the replenishing of the vacancies is made responsible for this observed low temperature feature. According to Cahill and Pohl [187], the theoretical lower limit of the lattice thermal conductivity is primarily defined by the number of atoms per unit volume and by the Debye temperature. The minimum thermal conductivity shown in Fig. 5.6 as solid green line was calculated using a Debye temperature $\theta_D = 211$ K and a number of atoms per unit volume $n = 4.3446 \times 10^{28}/\text{m}^3$ for $\text{Ba}_8\text{Cd}_{2.4}\text{Ge}_{41.4}\square_{2.2}$. The outcome of this is a room temperature value λ_{\min} of 1.3 mW/cmK. Figure 5.6b also demonstrates that the lattice thermal conductivity of $\text{Ba}_8\text{Cd}_{4.7}\text{Ge}_{40.3}\square_{1.0}$, yields 54.5 mW/cmK at room temperature.

Larger overall thermal conductivity were obtained for $\text{Ba}_8\text{Cd}_{7.6}\text{Ge}_{38.4}$. Similar observations was done also for a $\text{Ba}_8\text{Cd}_{6.5}\text{Ge}_{39.1}\square_{0.4}$. The separation of the total thermal conductivity $\lambda(T)$ of $\text{Ba}_8\text{Cd}_x\text{Ge}_{43-5x/8}\square_{3-3x/8}$ with $x = 6.5, 7.6$ into the electronic contribution λ_e and the lattice contribution λ_{ph} is plotted in Fig. 5.7. The solid bold lines correspond to the radiation losses. The filled symbol in Figs. 5.7a,b denote the corrected lattice thermal conductivities. The application of the Wiedemann-Franz law in both cases yields

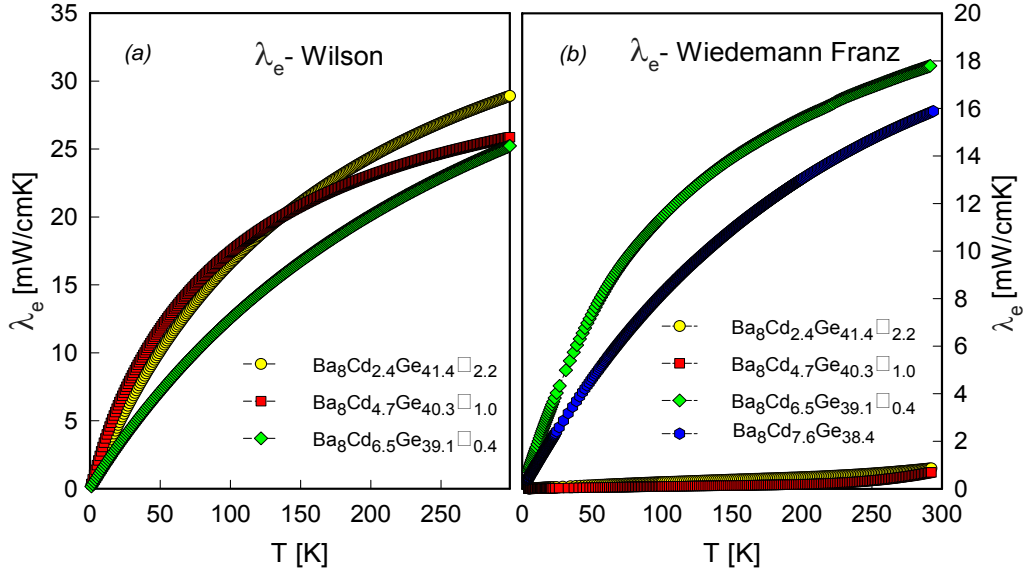


Figure 5.9: (a) Comparison of the electronic contribution $\lambda_e(T)$ deduced from the Wilson's equation (Eqn.1.13)(right panels) and (b) Wiedemann-Franz law (left panels). The curves for $Ba_8Cd_xGe_{43-5x/8}\square_{3-3x/8}$ with $x= 2.4, 4.7, 6.5, 7.6$ show a remarkably good agreement.

large electronic contribution λ_e for $Ba_8Cd_{6.5}Ge_{39.1}\square_{0.4}$ 17.9 mW/cmK and 15.8 mW/cm for $Ba_8Cd_{7.6}Ge_{38.4}$, respectively. The lattice thermal conductivity λ_{ph} of $Ba_8Cd_xGe_{43-5x/8}\square_{3-3x/8}$ with $x= 6.5, 7.6$ at room temperature varies between 31 and 41 mW/cmK. In case of $Ba_8Cd_{6.5}Ge_{39.1}\square_{0.4}$ the thermal conductivity at room temperature reaches 50 mW/cmK. The theoretical value of λ_{min} of $Ba_8Cd_{6.5}Ge_{39.1}\square_{0.4}$ is calculated, revealing 2.6 mW/cmK. Although λ_{ph} of this compound is larger than λ_{min} , they are of the same order of magnitude. Thus the phonons appear to be not very different from the glassy state (see Fig. 5.7a). Figure 5.7b also demonstrates that the lattice thermal conductivity of $Ba_8Cd_{7.6}Ge_{38.4}$ is near to theoretical limit of thermal conductivity, a necessity for thermoelectric applications of such materials. The lattice thermal conductivity λ_{ph} of $Ba_8Cd_{6.5}Ge_{39.1}\square_{0.4}$ and $Ba_8Cd_{7.6}Ge_{38.4}$ at room temperature varies between 31 and 41 mW/cmK. With increasing x content to 6.5 and 7.6, λ_{ph} increases strongly up to 20 K and decreasing up to 100 K, the $Ba_8Cd_{7.6}Ge_{38.4}$ compound shows the lowest λ_{ph} (31 mW/cmK) at room temperature. Essentially the minimum thermal conductivity is a lower limit of λ_{ph} , which is achieved if the phonon spectrum resembles that of glass-like or in general amorphous systems especially at high temperatures. The glass-like λ_{ph} is realized in some rattling systems where the phonon mean free path becomes extremely short due to the scattering by rattling guest atoms.

According to Einstein model [186] the phenomenological expression for λ_{min} is given by [187, 188],

$$\lambda_{min} = \left(\frac{3n}{4\pi}\right)^{\frac{1}{3}} \frac{k_B^2 T^2}{\hbar \theta_D} \int_0^{\theta_D/T} \frac{x^3 e^x}{(e^x - 1)^2} dx. \quad (5.7)$$

Here n is the number of atoms per unit volume and x is a dimensionless parameter connected to the phonon frequency ω via $x = \hbar\omega/k_B T$. The theoretical lower limit of the lattice thermal conductivity is primarily defined by the number of atoms per unit volume and by the Debye temperature [187]. Taking $n = 4.11 \times 10^{28} \text{ m}^{-3}$, two curves are calculated for $\theta_D = 192 \text{ K}$ and $\theta_D = 230 \text{ K}$, respectively. Results are shown in Fig. 5.7b as dashed-dot and dashed-dot-dot lines, respectively, revealing $\lambda_{min}(300 \text{ K}, \theta_D = 192 \text{ K}) = 3.65 \text{ mW/cmK}$ and $\lambda_{min}(300 \text{ K}, \theta_D = 230 \text{ K}) = 4.34 \text{ mW/cmK}$. In fact, these calculations demonstrate that the lattice thermal conductivity of $\text{Ba}_8\text{Cd}_{7.6}\text{Ge}_{38.4}$ at elevated temperatures is in the proximity of the theoretical minimum. This refers to the fact that at least $\text{Ba}_8\text{Cd}_{7.6}\text{Ge}_{38.4}$ behaves within the concept of a phonon glass.

Figure 5.8 displays $\lambda_{meas.}(T)$ contribution corrected for radiation losses (left) of $\text{Ba}_8\text{Cd}_x\text{Ge}_{43-5x/8}\square_{3-3x/8}$ with $x = 2.4, 4.7, 6.5, 7.6$. Due to poor electrical conductivities, λ_e may also stay below about 10% of the overall quantity, compare e.g. $\text{Ba}_8\text{Cd}_{2.4}\text{Ge}_{41.4}\square_{2.2}$ or $\text{Ba}_8\text{Cd}_{4.7}\text{Ge}_{40.3}\square_1$. The right panel (Fig. 5.8b) displays the difference between the measured and the corrected thermal conductivity $\lambda_{meas.} - \lambda_{corr.}$ as a function of T^3 . The derived curves are plotted in the right panel as a function of T^3 evidencing rough linearity. Fig. 5.9 displays a comparison of $\lambda_e(T)$ derived from the Wiedemann-Franz law and from the Wilson equation. It should be noted that both models provide comparable values. For $x = 2.7, 4.7$ the curves derived by Wiedemann-Franz are slightly different to the other compounds, which is due to the small electrical resistivity $\rho(T)$ of these compounds. The curves for $x = 6.5, 7.6$ show remarkably good agreement.

5.1.5 Thermopower

Measurements of the temperature dependent thermopower, S , are shown in Fig. 5.10a for $\text{Ba}_8\text{Cd}_x\text{Ge}_{43-5x/8}\square_{3-3x/8}$ with $M = \text{Cu}, \text{Zn}, \text{Cd}$. Common to all systems displayed are negative thermopower values referring to electrons as majority charge carriers. Moreover, $S(T)$ does not exhibit much structure in its temperature dependence, evidencing electronic transport without significant correlations within the system of charge carriers. This absence follows also from the Sommerfeld value of the specific heat being as low as 2 mJ/molK^2 . Moreover, the moderate thermopower values of the present family of clathrates may also follow from a rather weak energy dependence of the

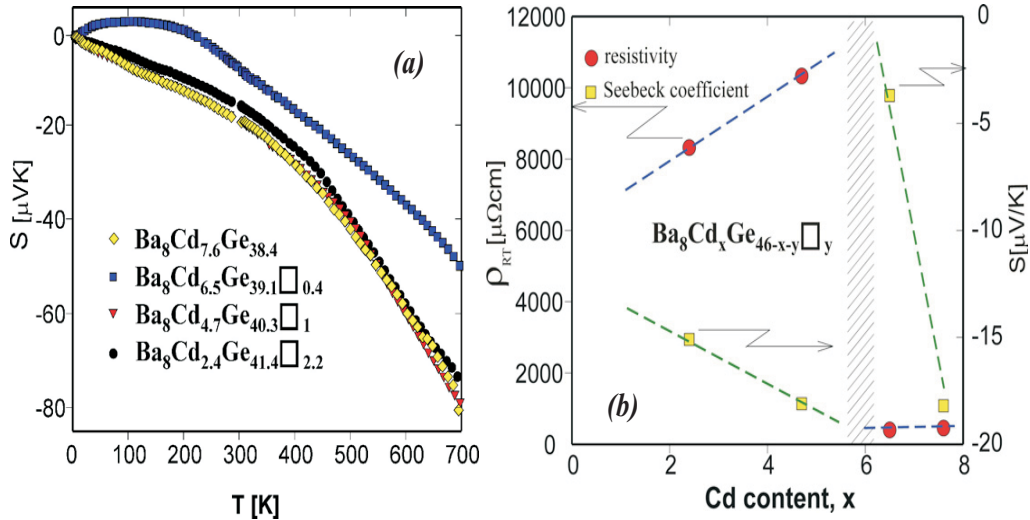


Figure 5.10: (a) Temperature dependent thermopower of $\text{Ba}_8\text{Cd}_x\text{Ge}_{43-5x/8}\square_{3-3x/8}$ with $x = 2.4, 4.7, 6.5, 7.6$. (b) Concentration dependence of the resistivity ρ (circles) and of the Seebeck coefficient S (square symbols) at room temperature (RT).

DOS right at E_F . This, in turn, somehow justifies the use of a simple DOS as considered for the analysis of the temperature dependent resistivity. Figure 5.10b shows the concentration dependent variation of the room temperature resistivity and of the Seebeck coefficient. Both quantities are characterized by a significant variation around a Cd content of 6 Cd atoms per formula unit. These abrupt changes correlate well with the filling of the $6d$ site by Cd atoms, simultaneously reducing the vacancy concentration. Above a Cd content of 6, Cd subsequently enters the $16i$ sites. This distinct substitution mechanism obviously changes details of the electronic density of states at the Fermi level, thereby altering electronic transport such as resistivity and the Seebeck coefficient.

5.2 Ba-Pd-Ge Clathrate System

5.2.1 Heat Capacity

Temperature dependent heat capacity measurements were carried out on $\text{Ba}_8\text{Pd}_{3.3}\text{Ge}_{42.5}\square_{0.2}$ and $\text{Ba}_8\text{Pd}_{3.82}\text{Ge}_{42.18}$ as representatives of this family of clathrates. Results of these investigations are displayed in Figs. 5.11a,b as C_p/T vs. T and as $(C_p - \gamma T)/T^3$ vs. $\ln T$ for $\text{Ba}_8\text{Pd}_{3.82}\text{Ge}_{42.18}$. The latter representation can be used to visualize deviations of the lattice dynamics from

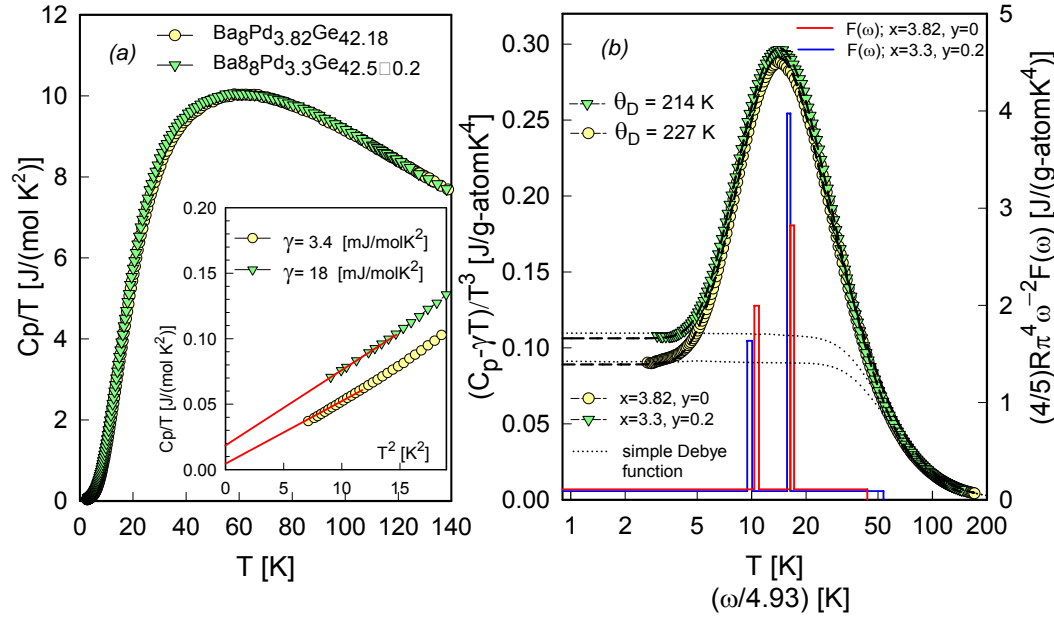


Figure 5.11: (a) Temperature dependent specific heat C_p of $\text{Ba}_8\text{Pd}_x\text{Ge}_{46-x-y}\square_y$ at $x = 3.3, 3.82$ and $y = 0, 0.2$ plotted as C_p vs. T . (b) $(C_p - \gamma T)/T^3$ vs. $\ln T$. The dashed line is a least squares fits of the experimental data using the model described in the text with two Einstein-like modes. The dotted and the solid lines sketch the simple Debye model and the phonon spectral function $F(\omega)$ plotted as $\omega/4.93$ vs. $(5/4)R\pi^4\omega^{-2}F(\omega)$ for which ω is given in Kelvin.

that expected in terms of the simple Debye model, plotted in Fig. 5.11b as dotted line. Obviously, $\text{Ba}_8\text{Pd}_{3.82}\text{Ge}_{42.18}$ does not follow the Debye model in the whole temperature range studied. The same holds for $\text{Ba}_8\text{Pd}_{3.3}\text{Ge}_{42.5}\square_{0.2}$, shown in Fig. 5.11b. Using only data below 4 K and applying a standard analysis of the specific heat of metals at low temperatures allows to extract the Sommerfeld value γ and the low temperature Debye temperature θ_D^{LT} . The electronic contributions γ to the specific heat for $\text{Ba}_8\text{Pd}_{3.3}\text{Ge}_{42.5}\square_{0.2}$ and $\text{Ba}_8\text{Pd}_{3.82}\text{Ge}_{42.18}$, respectively are deduced as 3.4 and 18 mJ/mol K², whereas θ_D^{LT} yields 260 and 268 K. The observed electronic contribution to the specific heat refers to distinctly different density of states (DOS) features around the Fermi energy E_F . While the former compound shows a metallic-like behaviour, the latter refers to a DOS almost vanishing at E_F . The significant deviations from the simple Debye model indicate a rather complicated phonon spectrum for this family of clathrates. The spectrum is supposed to be composed of background vibrations originating from the cage-like structure represented by a Debye spectrum and, additionally, from the rattling modes

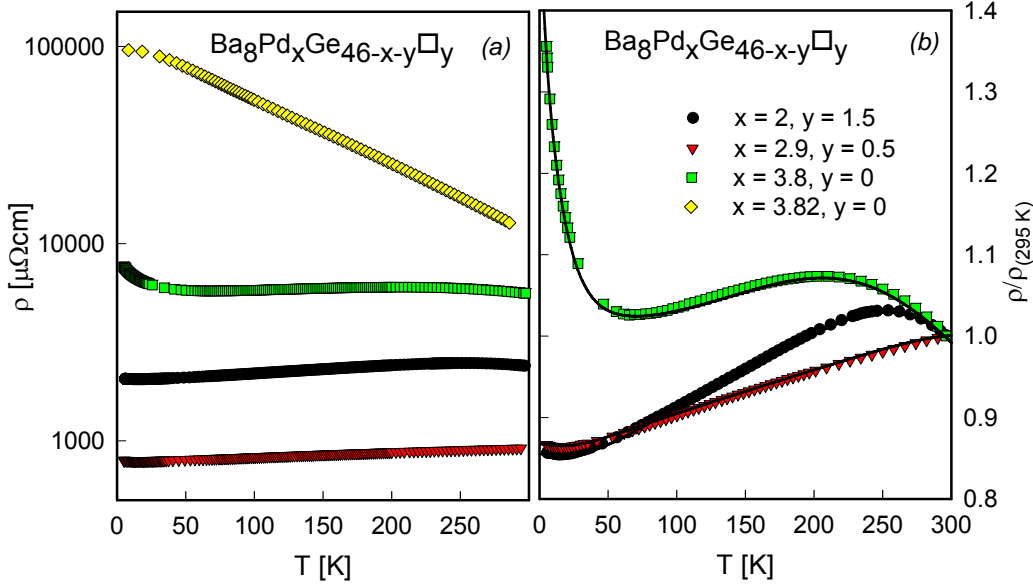


Figure 5.12: (a) Temperature dependent resistivity ρ of various concentrations of $\text{Ba}_8\text{Pd}_x\text{Ge}_{46-x-y}\square_y$. (b) Normalized resistivity of $\text{Ba}_8\text{Pd}_x\text{Ge}_{46-x-y}\square_y$. The solid lines are least squares fits as explained in the text.

of the loosely bound electropositive Ba-atoms. The latter should follow the behaviour Einstein-like frequencies.

In the case of $\text{Ba}_8\text{Pd}_{3.3}\text{Ge}_{42.5}\square_{0.2}$ and $\text{Ba}_8\text{Pd}_{3.82}\text{Ge}_{42}$ the phonon part of the specific heat is well described by a simple Debye-function with a Debye temperature of 215 K and 227 K together with two additional Einstein-like contributions. Results of the least squares fits to the data according to model Junod et al. model performed for $\text{Ba}_8\text{Pd}_{3.3}\text{Ge}_{42.5}\square_{0.2}$ and $\text{Ba}_8\text{Pd}_{3.83}\text{Ge}_{42}$ are shown in Fig. 5.11b.

The overall goodness of the fit is extremely high in case $\text{Ba}_8\text{Pd}_{3.82}\text{Ge}_{42}$, revealing a Debye temperature $\theta_D = 227$ K and two narrow structures at $\theta_{EL1} = 53.4$ K with width of $\Delta\omega_{EL1} = 2.3$ K and $\theta_{EL2} = 84.7$ K with a corresponding spectral width of $\Delta\omega_{EL2} = 2.1$ K, respectively. Based on this fit, the phonon spectrum is constructed and plotted in 5.11(b) referring to the right axis (solid line). The spectral weight follows from the constraint that for $T \rightarrow 0$ the height of the phonon density of states coincides with the value of C_p/T^3 for $T \rightarrow 0$. Very similar figures are derived for $\text{Ba}_8\text{Pd}_{3.3}\text{Ge}_{42.5}\square_{0.2}$ (shown Fig. 5.11b) ($\theta_D = 214$ K, $\theta_{EL1} = 54$ K and $\theta_{EL2} = 85.4$ K, with corresponding spectral widths of 2.3 and 2.2 K, respectively). A comparison of the phonon density of states of $\text{Ba}_8\text{Pd}_{3.82}\text{Ge}_{42}$ with a higher Debye temperature ($\theta_D = 227$ K) and the phonon density of states of $\text{Ba}_8\text{Cd}_{7.6}\text{Ge}_{38.4}$ clearly signals a shift of the Einstein-like contribution to higher frequencies (see Fig 5.3).

5.2.2 Electrical resistivity

Results of our resistivity study on various concentrations of $\text{Ba}_8\text{Pd}_x\text{Ge}_{46-x-y}\square_y$ are displayed in Figs. 5.12a,b. Data in Fig. 5.12a are plotted on a logarithmic resistivity scale in order to get rid of the large variation of the absolute resistivity values. Obviously, the temperature dependent resistivity, $\rho(T)$, changes from a metallic like behaviour for smaller Pd concentrations to a semiconducting one (for the whole temperature range studied) for the compound containing 3.82 Pd. The semiconducting behaviour of the latter compound is in excellent agreement to the observation that the Sommerfeld value of the specific heat $\gamma < 0.05 \text{ mJ/molK}^2$ refers to a vanishing density of states right at the Fermi energy.

A closer inspection of the data (except $x = 3.82$), shows that even the system containing the smallest amount of Pd does not behave according to simple metals, compare Fig. 5.12b. Rather, specific structures of $\rho(T)$ indicate that all the materials investigated are in fact very near to the semiconducting state. The overall behaviour reminds to both, metallic and activation-like behaviours as reflected from positive and negative slopes in $\rho(T)$. Least squares fits according to Eqn. 5.6 are shown in Fig. 5.12b as solid lines. The principal parameter is the gap width Δ , which increases from about 1000 K for $x = 2$ to 2200 K for $x = 3.8$. Although the applied model is quite simple, it fairly well describes the temperature dependent resistivity of $\text{Ba}_8\text{Pd}_x\text{Ge}_{46-x-y}\square_y$. The metallic behaviour derives from scattering of conduction electrons into unoccupied sites in reciprocal space just above the Fermi energy. Once this region of the DOS becomes occupied, electrons have to be promoted across the gap, originating in semiconducting features. However, a distinct exponential behaviour does not become obvious due to the proximity to the metallic state.

5.2.3 Thermal conductivity

The temperature dependence of the thermal conductivity $\lambda_{meas.}(T)$ has been measured for $\text{Ba}_8\text{Pd}_x\text{Ge}_{46-x-y}\square_y$ for concentrations $x = 2, 3.8$ and $y = 1.5, 0$, and the results are displayed in Fig. 5.13. The overall thermal conductivity values are rather small, expectable for cage forming compounds which are filled by loosely bound electropositive elements. The increasing Pd content enables a low temperature maximum to evolve. An analysis of the data relies on the Wiedemann-Franz law, which, in a first approximation, allows to split the measured thermal conductivity into an electronic part, λ_e and into the lattice part, λ_{ph} .

The large overall resistivity of the present samples is thus the cause that λ_e is clearly the minority channel of the total measured effect in both cases, compare Figs. 5.14a,b. Results of a separation of the total thermal conduc-

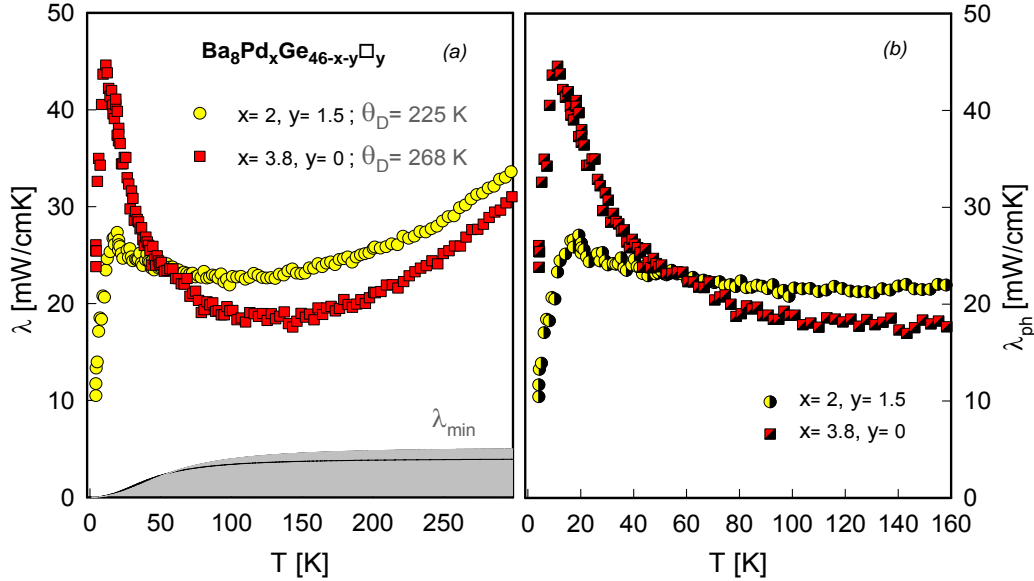


Figure 5.13: (a) Temperature dependent thermal conductivity λ of two concentrations of $\text{Ba}_8\text{Pd}_x\text{Ge}_{46-x-y}\square_y$. (b) Temperature dependent lattice thermal conductivity λ_{ph} for the same samples.

tivity $\lambda(T)$ of $\text{Ba}_8\text{Pd}_2\text{Ge}_{42.5}\square_{1.5}$ and $\text{Ba}_8\text{Pd}_{3.8}\text{Ge}_{42.2}$ into the electronic part λ_e and the lattice part λ_{ph} plotted as a function of temperature in Figs. 5.14a,b.

The filled symbol in Figs. 5.14a and 5.14b denote the corrected thermal conductivities data. The λ_{ph} -curves are calculated by applying the Wiedemann-Franz law and subtracting the radiation losses, assuming a T^3 -dependence. Least squares fits according to Eqn. 1.17 are shown in Figs. 5.14a,b as solid line, revealing only rough agreement with the data observed. Comparing the set of fit parameters indicates that the relaxation time referring to point defect scattering, i.e., $\tau_D^{-1} = Dx^4T^4$, with the material dependent parameter D decreases by more than a factor of 2 when proceeding from the sample with $x=2$ to the sample $x = 3.8$. In turn, the strength of the Umklapp processes increases simultaneously. The remaining parameters do not show significant changes. These results, which should be used only in a qualitative manner, although the disorder due to the Ge/Pd substitution rises, the overall disorder of the crystal decreases much stronger due to the vanishing of the vacancies provoked the growing Pd content. A comparison of the lattice thermal conductivity λ_{ph} of $\text{Ba}_8\text{Pd}_2\text{Ge}_{42.5}\square_{1.5}$ with $\text{Ba}_8\text{Pd}_{3.8}\text{Ge}_{42.2}$ clearly signals an overall and significant reduction of λ_{ph} for the $\text{Ba}_8\text{Pd}_2\text{Ge}_{42.5}\square_{1.5}$ case. With decreasing Pd content λ_{ph} increases, $\text{Ba}_8\text{Pd}_{3.8}\text{Ge}_{42.2}$ shows the highest λ_{ph} (45 mW/cmK) at 10 K. For the compound $\text{Ba}_8\text{Pd}_{3.8}\text{Ge}_{42.2}$, λ_{ph}

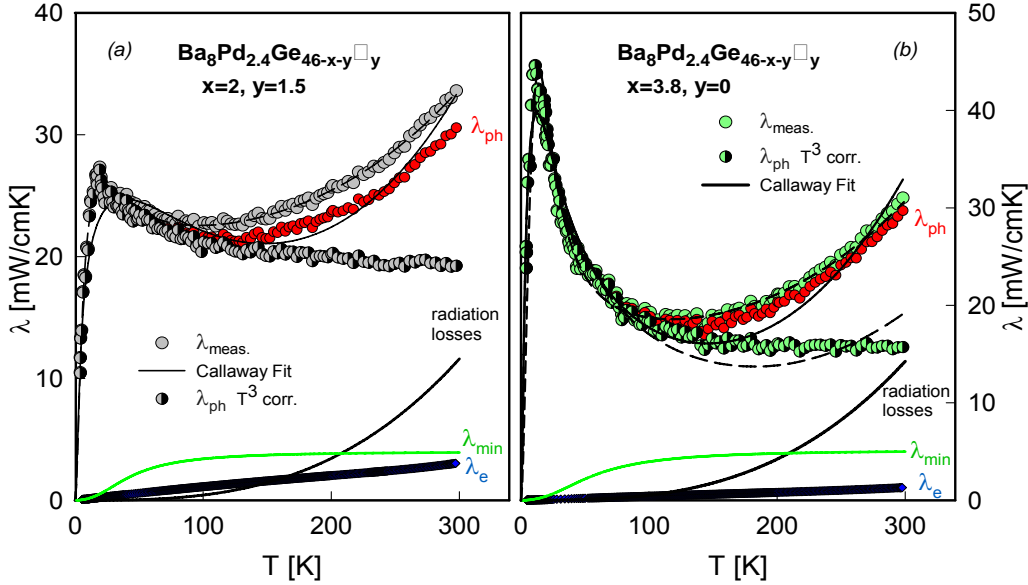


Figure 5.14: (a) Separation of the total thermal conductivity $\lambda(T)$ of $\text{Ba}_8\text{Pd}_2\text{Ge}_{42.5}\square_{1.5}$ (b) $\text{Ba}_8\text{Pd}_{3.8}\text{Ge}_{42.2}$ into the electronic part λ_e and the lattice part λ_{ph} . The electronic λ_e (filled blue diamonds) and the lattice contribution λ_{ph} (filled red circles) are derived from the Wiedemann-Franz law. The half filled symbol indicate thermal conductivity data obtained from a correction procedure taking radiation losses into account. The solid and the dashed lines are least squares fits applying the model of Callaway (Eqn. 1.17) with a T^3 term for radiation losses. The green lines are calculations of the theoretical lower limit of thermal conductivity λ_{min} .

at room temperature is already reduced to a value 30 mW/cmK. The evaluation of the measured $\lambda_{meas.}$ and corrected thermal conductivity $\lambda_{corr.}$ of $\text{Ba}_8\text{Pd}_x\text{Ge}_{46-x-y}\square_y$ for the Pd content $x = 2, 3.8$ and $y = 1.5, 0$ are plotted in Fig. 5.15. The left panel of this figure displays the corrected $\lambda_{corr.}$ thermal conductivity data, obtained from a correction procedure taking radiation losses T^3 into account ($\lambda_{corr.} = \lambda_{meas.} - \beta T^3$). The right panel of this figure convincingly demonstrates the T^3 behaviour of $\lambda_{meas.} - \lambda_{corr.}$ which is expected, if the error is caused by radiation losses.

Taking $n = 4.32 \times 10^{28} \text{ m}^{-3}$ and $\theta_D = 225 \text{ K}$ for $\text{Ba}_8\text{Pd}_2\text{Ge}_{42.5}\square_{1.5}$ reveals the lower limit of the lattice thermal $\lambda_{min}(300 \text{ K}) = 4.3 \text{ mW/cmK}$. A slightly larger value of 5 mW/cmK is derived taking $\theta_D = 268 \text{ K}$, obtained from the low temperature extrapolation of the heat capacity data. Results below room temperature are shown in Figs. 5.13 and 5.14 as solid green lines and filled area for both sets of parameters.

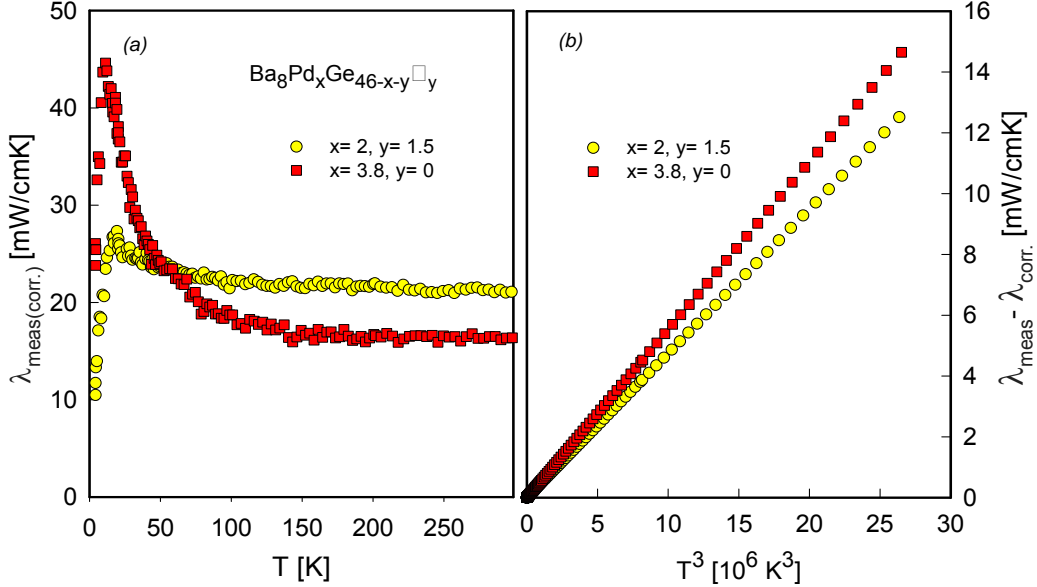


Figure 5.15: (a) Temperature dependent thermal conductivity, $\lambda_{\text{meas.}}(T)$, of $\text{Ba}_8\text{Pd}_x\text{Ge}_{46-x-y}\square_y$ for the content $x= 2, 3.8$ and $y= 1.5, 0$. (b) $\lambda_{\text{meas.}} - \lambda_{\text{corr.}}$ of $\text{Ba}_8\text{Pd}_x\text{Ge}_{46-x-y}\square_y$ vs. T^3 .

5.2.4 Thermopower

Results regarding the temperature dependent thermopower, $S(T)$, are plotted in Figs. 5.16a,b for various concentrations of $\text{Ba}_8\text{Pd}_x\text{Ge}_{46-x-y}\square_y$. $S(T)$ is characterized by a Pd-dependent evolution of the absolute $S(T)$ values up to about $x = 3.8$. Within this concentration range $S(T)$ is negative, referring to electrons as the principal charge carriers. In contrast, $S(T)$ becomes positive for $x = 3.82$, indicative of holes as majority charge carriers. The compound with $x = 3.8$ exhibits thermopower values up to $-145 \mu\text{V/K}$ well below room temperature and thus belongs to those members of clathrates having the largest $S(T)$ values. The almost linear temperature dependence of $S(T)$, except those compounds with very large Pd concentrations, suggests a simple origin, depending primarily on the charge carrier density n . As demonstrated e.g., in Ref. [88], the diffusion part of the thermopower can simply be represented by

$$S_d(T > \theta_D) = \frac{\pi^2 k_B^2 2m_e}{e\hbar^2 (3n\pi^2)^{2/3}} T \quad (5.8)$$

where m_e is the mass of the carriers and e is the respective charge. Approaching the data of Fig. 5.16 by a linear dependence, at least for concentrations from $x = 2$ up to $x = 3.6$, and $T < 350$ to 400 K allows calculating the charge carrier density (Eqn. 5.8), which decreases almost by one order of magnitude

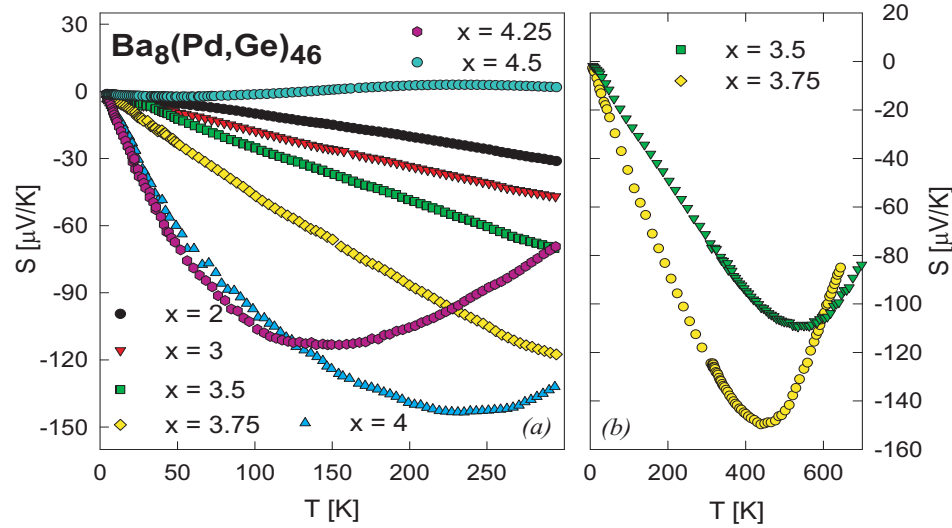


Figure 5.16: (a) Temperature dependent thermopower for various concentrations of $\text{Ba}_8\text{Pd}_x\text{Ge}_{46-x-y}\square_y$. (b) $S(T)$ of $x=3.3$ and $x=3.6$ in an extended temperature range.

from $n = 2.9 \times 10^{21} \text{ cm}^{-3}$ for $x = 2$ to $n = 3.4 \times 10^{20} \text{ cm}^{-3}$ for $x = 3.75$. A further justification for such an estimation of n from thermopower data regarding clathrate I systems was obtained previously from measurements of the optical conductivity in $\text{Ba}_8(\text{Ge}, \text{Zn})_{46}$ compounds, where n deduced from the plasma frequency excellently agreed with an estimation of n based on Eqn. 5.8 [189].

Figure 5.16b demonstrates that the almost linear dependence of $S(T)$ is restricted to lower, concentration dependent temperatures. Above the nearly linear dependence, a minimum develops, followed by a decrease of $|S(T)|$. A possible explanation of this observation may follow from the concentration dependent gap in the electronic density of states above E_F : Once, thermal energy is sufficient to appreciably populate the states above the gap, the number of charge carriers increases, accordingly $|S(T)|$ becomes reduced (compare Eqn. 5.8).

In order to understand the non-monotonous variation of the absolute resistivity, we have carried out Hall measurements at low temperatures and have analyzed the data in terms of the free electron model, i.e. $R_H = -1/(ne)$ and $\rho = R_H/\mu$ (R_H is the Hall resistance, n is the charge carrier density, e is the electron charge and μ is the mobility). At $T = 10 \text{ K}$ and $\mu_0 H = 3 \text{ T}$, n is found to be -3.5 , -3.2 , -0.83 and $0.56 \times 10^{21} \text{ cm}^{-3}$ for $x = 2$, 2.9 , 3.6 and 3.82 , respectively. The mobility μ of these carriers is, respectively, 0.64 , 1.6 , 0.9 and $-0.07 \text{ cm}^2/\text{Vs}$. These results refer to electrons as main charge carriers,

except for $x = 3.82$, which seems to be dominated from holes (compare also the thermopower data in Fig. 5.16). The charge carrier density in the context of the mobility derived for the present series, directly renders the sequence of the resistivity data observed. The material with the highest mobility and reasonable charge carrier density was found for $x = 2.9$ which, in fact, shows the lowest overall resistivity. The compound with $x = 2$ has similar values of n , but the mobility is smaller, hence $\rho(T)$ is larger, in agreement with the experimental data. The largest resistivity is found for $x = 3.82$, owing to both small n and small μ values.

5.3 Ba-Zn-Ge Clathrate System

5.3.1 Heat Capacity

Temperature dependent heat capacity measurements were carried out on $\text{Ba}_8\text{Zn}_{7.7}\text{Ge}_{38.3}$. Results of this investigation are displayed in Figs. 5.17a,b as C_p vs. T and as $(C_p - \gamma T)/T^3$ vs. $\ln T$. The latter representation allows emphasizing deviations from the simple Debye model, which at low temperatures causes a T^3 dependence. Note that the Sommerfeld value $\gamma \approx 2 \text{ mJ/molK}^2$ is also subtracted in Fig. 5.17b. Obviously, the heat capacity of $\text{Ba}_8\text{Zn}_{7.7}\text{Ge}_{38.3}$ exhibits distinct deviations from a Debye-like behaviour in the entire temperature range studied. In fact, a standard plot of the heat capacity data according to C_p/T vs. T^2 does not reveal any sufficiently extended temperature range, where the simple behaviour of metals holds, i.e., $C_p/T = \gamma T + \beta T^3$. The finite value of γ refers to a finite electronic density of states at the Fermi energy, thus indicating a metallic state, at least, for $\text{Ba}_8\text{Zn}_{7.7}\text{Ge}_{38.3}$. Also, the complete Debye function is unable as well to account for the temperature dependent specific heat of $\text{Ba}_8\text{Zn}_{7.7}\text{Ge}_{38.3}$ in an extended temperature range. Figure 5.17a also shows that there are no phase transitions below about 80 K.

Based on Eqn. A.11 as mentioned in the previous sections (see Pd and Cd clathrates) we have constructed an elementary phonon spectrum and have carried out least squares fits to the data. Results of this procedure are also shown in Fig. 5.17b. In a first approximation we have assumed that besides a Debye density of states, the system is composed of two additional, energetically separated Einstein-like modes.

The parameters obtained by least squares fits of the experimental data reveal for $\text{Ba}_8\text{Zn}_{7.7}\text{Ge}_{38.3}$ a Debye temperature of $\theta_D = 225 \text{ K}$ and two narrow structures at $\theta_{EL1} = 46.2 \text{ K}$ and $\theta_{EL2} = 77.1 \text{ K}$, with corresponding spectral widths of $\Delta\omega_{EL1} = 5.6$ and $\Delta\omega_{EL2} = 3.4 \text{ K}$, respectively. A similar set of frequencies and Debye temperature were obtained also for the related Pd and Cd clathrates. Based on this fit, the phonon spectrum is constructed and

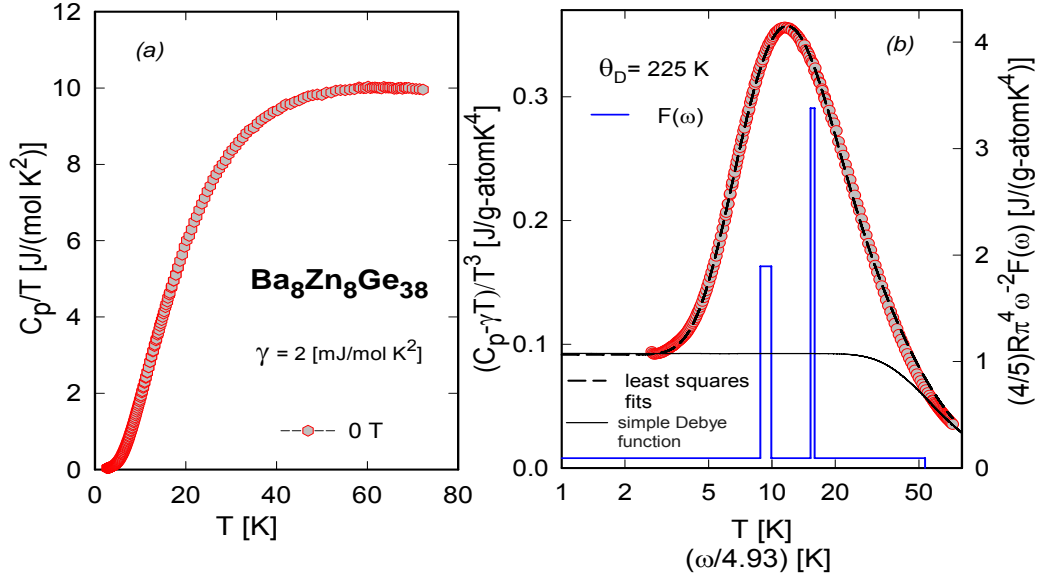


Figure 5.17: (a) Temperature dependent specific heat C_p of $\text{Ba}_8\text{Zn}_{7.7}\text{Ge}_{38.3}$, plotted as C_p/T vs. T and (b) $(C_p - \gamma T)/T^3$ vs. $\ln T$. The dashed line is a least squares fit of the experimental data using the model described in the text with two Einstein-like modes ($\theta_D = 225$ K, $\theta_{EL1} = 46.2$ K with width of 5.6 K and $\theta_{EL2} = 77.1$ with a width of 3.4 K). The bold solid line sketch the phonon spectral function $F(\omega)$ plotted as $\omega/4.93$ vs. $(5/4)R\pi^4\omega^{-2}F(\omega)$ for which ω is given in Kelvin.

plotted in Fig. 5.17b referring to the right axis (solid line).

5.3.2 Electrical resistivity

The temperature dependent electrical resistivity $\rho(T)$ of $\text{Ba}_8\text{Zn}_x\text{Ge}_{46-x-y}\square_y$ is plotted in Fig. 5.18. Doping and substitutions are valuable tools to reduce the charge carrier density of a certain family of compounds to an optimum level. Resistivities of such materials, however, become large, frequently behaving in-between a simple metallic state and semiconducting features. Moreover, relatively small gaps Δ in the electronic density of states near the Fermi energy drive a continuous crossover from metallic-like transport to a more semiconducting-like behaviour. Such features are also obvious for the series $\text{Ba}_8\text{Zn}_x\text{Ge}_{46-x-y}\square_y$, $x = 2.1, 4.6, 5.7$ and 7.7 , respectively; compare Figs. 5.18a,b. While samples with larger Zn concentrations behave metallic, the $\text{Ba}_8\text{Zn}_{2.1}\text{Ge}_{41.5}\square_{2.4}$ compound obviously shows at low temperatures a metallic-like resistivity. At higher temperatures, however, there is a crossover to an activation-like dependence of $\rho(T)$.

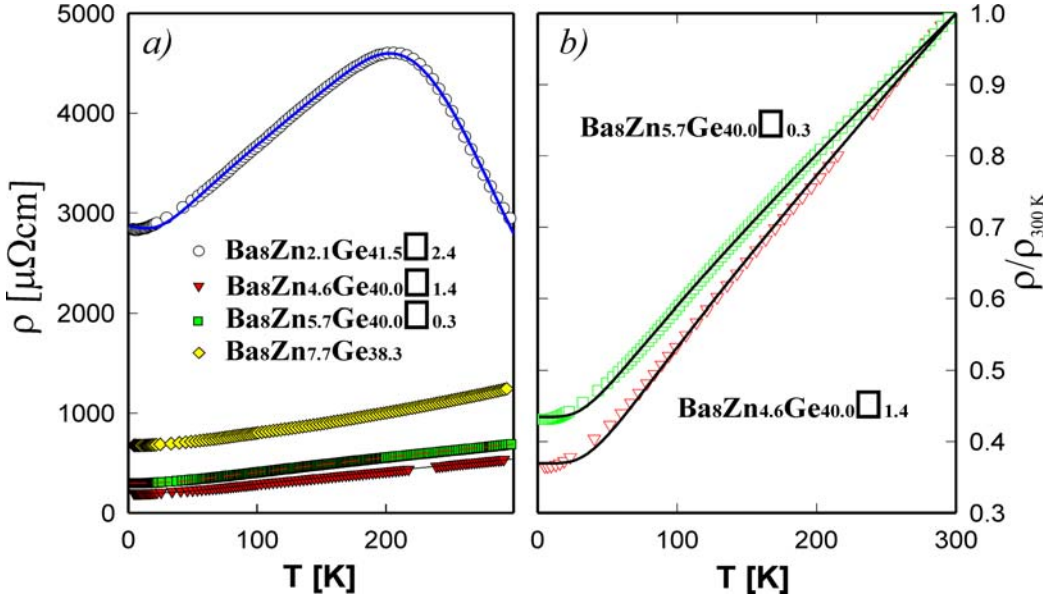


Figure 5.18: (a) Temperature dependent resistivity ρ of $\text{Ba}_8\text{Zn}_x\text{Ge}_{46-x-y}\square_y$. The solid line is a fit to the compound $\text{Ba}_8\text{Zn}_{2.1}\text{Ge}_{41.5}\square_{2.4}$ (see text). (b) Normalized resistivity of $\text{Ba}_8\text{Zn}_{4.6}\text{Ge}_{40.0}\square_{1.4}$ and $\text{Ba}_8\text{Zn}_{5.7}\text{Ge}_{40.0}\square_{0.3}$. The solid lines are least squares fits according to the Bloch-Grüneisen formula.

Since there are no magnetic interactions between conduction electrons and magnetic ions, electrical resistivity should be well described by a temperature independent residual resistivity ρ_0 together with the Bloch-Grüneisen law ρ_{ph} (Eqn. 1.4). Least squares fits to the data in the temperature range from 4.2 K to 300 K reveal the values for ρ_0 , the Debye temperature θ_D and the electron phonon interaction strength \mathcal{R} . Least squares fits according to Eqn. 1.4 (solid lines, Fig. 5.18b) reveal $\Theta_D = 235$ and 210 K for the $\text{Ba}_8\text{Zn}_{4.6}\text{Ge}_{40.0}\square_{1.4}$ and $\text{Ba}_8\text{Zn}_{5.7}\text{Ge}_{40.0}\square_{0.3}$ compounds, respectively. While above about 30 K the fit is convincing, at lower temperatures distinct differences between the experimental data and Eqn. 1.4 occur, most likely as a consequence of the insufficient phonon model, missing a pronounced Einstein-like contribution. A description of $\rho(T)$ of the $\text{Ba}_8\text{Zn}_{7.7}\text{Ge}_{38.3}$ sample in terms of Eqn. 1.4 totally fails since the data exhibit a positive slope, i.e., $d\rho/dT > 1$; such behaviour can never be traced by Eqn. 1.4. The $\text{Ba}_8\text{Zn}_{2.1}\text{Ge}_{41.5}\square_{2.4}$ sample, however, shows a low temperature behaviour reminiscent of metals, whilst at higher temperatures an activation type resistivity becomes evident. In order to account for such these distinct features, we used the model given in section 5.1, *Electrical resistivity* [185]. A least-squares fit according to this procedure (Eqn. 5.6) is shown in Fig. 5.18a as a solid line. The principal parameter is the gap width Δ , derived as 1650 K. Although the applied model

is quite simple, it fairly well describes the temperature dependent resistivity of $\text{Ba}_8\text{Zn}_{2.1}\text{Ge}_{41.5}\square_{2.4}$. The metallic behaviour derives from scattering of conduction electrons into unoccupied sites in reciprocal space just above the Fermi energy. Once this region of the DOS becomes occupied, electrons have to be promoted across the gap, originating semiconducting features.

5.3.3 Thermal conductivity

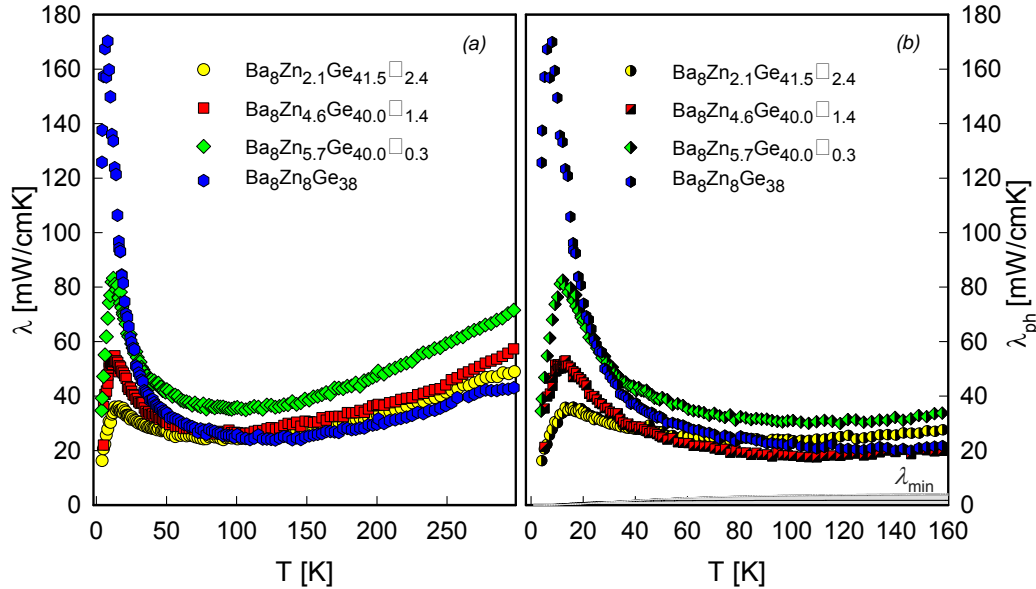


Figure 5.19: (a) Temperature dependent thermal conductivity λ of $\text{Ba}_8\text{Zn}_x\text{Ge}_{46-x-y}\square_y$ with $x = 2.1, 4.6, 5.7, 7.7$. The hatched area renders the minimum thermal conductivity (see text). (b) Lattice thermal conductivity λ_{ph} of $\text{Ba}_8\text{Zn}_x\text{Ge}_{46-x-y}\square_y$.

The thermal conductivity, λ , of $\text{Ba}_8\text{Zn}_x\text{Ge}_{46-x-y}\square_y$ is displayed as a function of temperature in Fig. 5.19a for a temperature range from 4 K to room temperature. The main characteristics of all the samples measured are pronounced maxima at low temperatures. This feature is opposite to a number of clathrates, e.g. $\text{Eu}_8\text{Ga}_{16}\text{Ge}_{30}$, [192], where $\lambda(T)$ does not exhibit a maximum in this temperature range. The suppression of these kinds of maxima is attributed to *resonance scattering* as demonstrated recently by Nolas et al. [193]. This scattering of the heat carrying phonons is based on static and dynamic disorder associated with the *rattling* motion of the guest atoms, i.e. Ba2, in the large voids of the structure formed by Zn and Ge atoms. In general, this mechanism has a large impact on thermal transport and is considered responsible for the glass-like transport in cage forming compounds

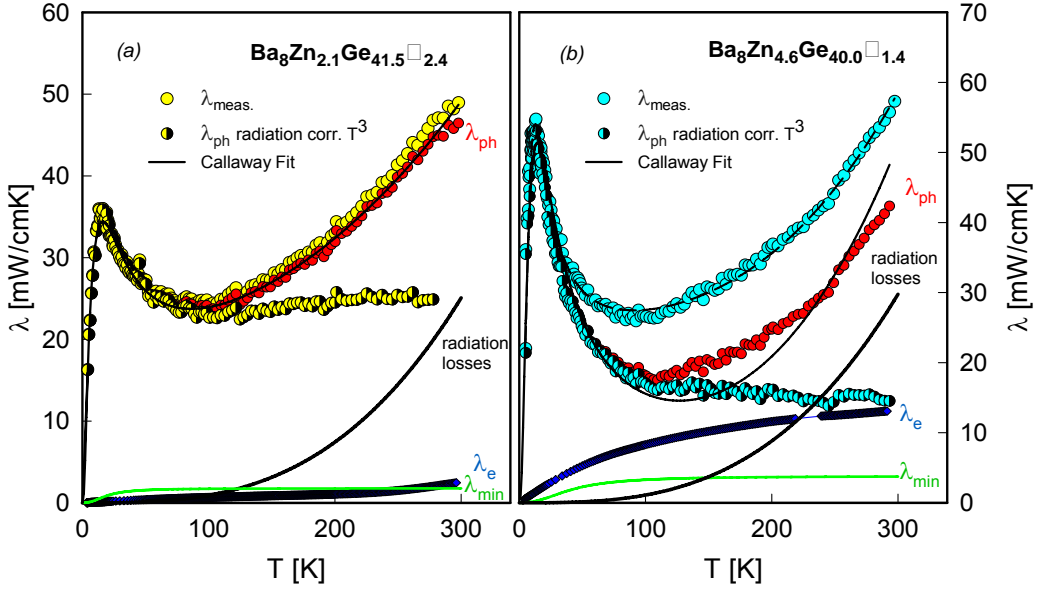


Figure 5.20: (a) Separation of the total thermal conductivity $\lambda(T)$ of $\text{Ba}_8\text{Zn}_{2.1}\text{Ge}_{41.5}\square_{2.4}$ (large circles) and (b) $\text{Ba}_8\text{Zn}_{4.6}\text{Ge}_{40.0}\square_{1.4}$ (large circles). The electronic λ_e (blue symbols) and the lattice contribution λ_{ph} (red filled circles) are derived from the Wiedemann-Franz law. The small filled circles represent the lattice contribution corrected for radiation losses. The solid and the dashed lines are least squares fits applying the model of Callaway with and without a T^3 term for radiation losses. The green lines correspond to the upper border of the theoretical lower limit of the lattice thermal conductivity λ_{min} according to Eqn. 5.7.

such as clathrates and skutterudites. In comparison to already mentioned $\text{Eu}_8\text{Ga}_{16}\text{Ge}_{30}$, the Zn-based compounds have overall larger thermal conductivities.

Taking into account the most relevant scattering processes present in the clathrates investigated, the relaxation time can be expressed by Eqn. 1.19. Equation 1.19 does not contain terms for resonance scattering, since they seem to be of minor importance in the series of compounds studied. Additionally, a T^3 term was added to Eqn. 1.17 in order to get rid of radiation losses. Equation 1.17 highlights that the lattice thermal conductivity can be influenced from scattering on the charge carrier system, too ($\tau_E^{-1} = E\omega$, E is a material constant). This seems to significantly influence λ_{ph} at somewhat elevated temperatures. The compound having the lowest electrical resistivity, and thus the largest charge carrier density, i.e., $\text{Ba}_8\text{Zn}_{4.6}\text{Ge}_{40.0}\square_{1.4}$, exhibits a well reduced lattice thermal conductivity above about 100 K. On the other hand, the lattice thermal conductivity of $\text{Ba}_8\text{Zn}_{2.1}\text{Ge}_{41.5}\square_{2.4}$ becomes much

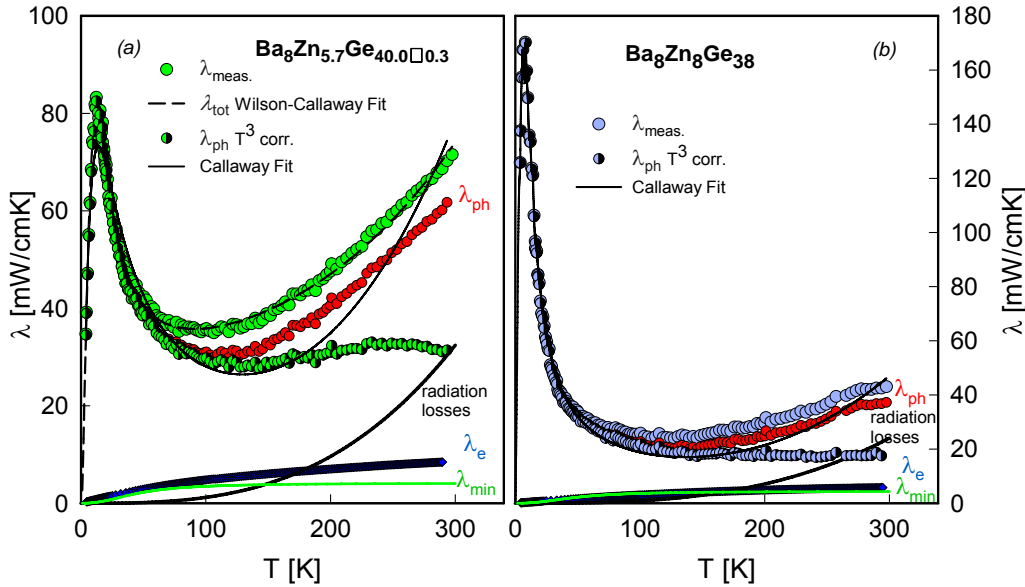


Figure 5.21: (a) Separation of the total thermal conductivity $\lambda(T)$ of $\text{Ba}_8\text{Zn}_{5.7}\text{Ge}_{40.0}\square_{0.3}$ (large circles) and (b) $\text{Ba}_8\text{Zn}_{7.7}\text{Ge}_{38.3}$ (large circles). The electronic λ_e (blue symbol) and the lattice contribution λ_{ph} (red circles) are derived from the Wiedemann-Franz law. The small filled circles represent the lattice contribution corrected for radiation losses. The solid and the dashed lines are least squares fits applying the model of Callaway with and without a T^3 term for radiation losses. The green lines correspond to the upper border of the theoretical lower limit of the lattice thermal conductivity λ_{min} according to Eqn. 5.7.

larger, most likely due to the reduced efficiency of phonon scattering on conduction electrons. As indicated above, this compound is next to a metal to insulator transition.

The thermal conductivity $\lambda(T)$ shows a distinct increase with increasing x at low and high temperatures for all compounds except $\text{Ba}_8\text{Zn}_{7.7}\text{Ge}_{38.3}$, which shows lower thermal conductivity values at high temperature (from 100 K to room temperature). Most notably is the suppression of the maximum at about 10 K. In a basic theory of thermal conductivity, the atomic masses distinctly influence the absolute values of $\lambda(T)$. The heavier the masses involved, the lower is the overall $\lambda(T)$. Taking $n = 4.329 \times 10^{28} \text{ m}^{-3}$ and $\theta_D = 225 \text{ K}$ for $\text{Ba}_8\text{Zn}_{7.7}\text{Ge}_{38.3}$ reveals $\lambda_{\text{min}}(300 \text{ K}) = 4.3 \text{ mW/cmK}$ (Eqn. 5.7). Results below room temperature are shown in Fig. 5.19a as hatched area. Owing to the strong interaction of the phonons with the weakly bound, the lattice thermal conductivity of such Clathrates systems is strongly reduced and the theoretical minimum thermal conductivity, as found for glass-like

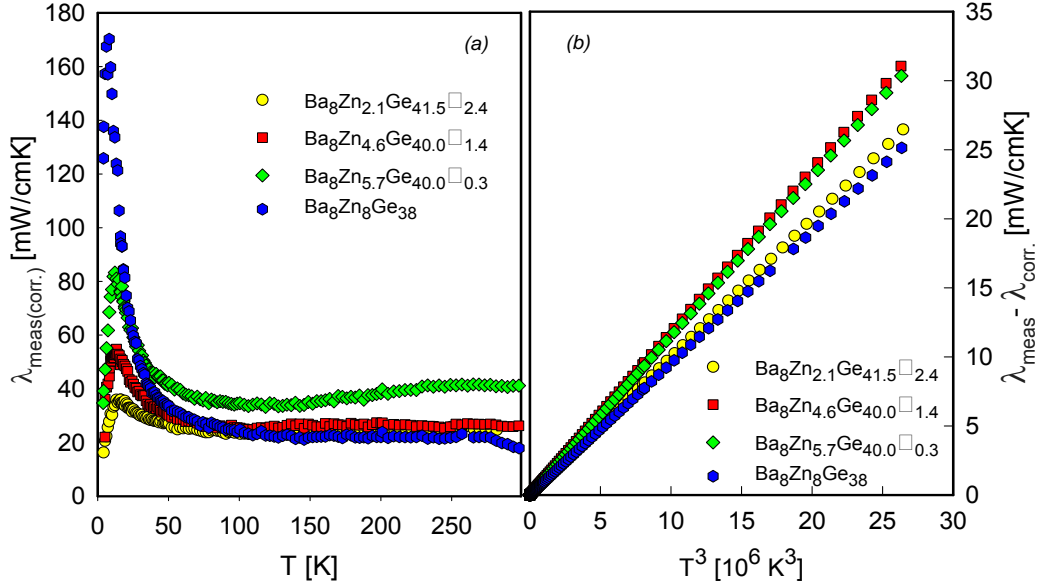


Figure 5.22: (a) The corrected thermal conductivity $\lambda_{meas-corr.}$ of $Ba_8Zn_xGe_{46-x-y}\square_y$ for concentrations $x = 2.1, 4.6, 5.7, 7.7$. (b) $\lambda_{meas.} - \lambda_{corr.}$ of $Ba_8Zn_xGe_{46-x-y}\square_y$ with $x= 2.1, 4.6, 5.7, 7.7$ vs. T^3 .

materials. Although the Wiedemann-Franz law is valid in extended temperature ranges only for free electron systems, it is widely used even for complex materials such as skutterudites or clathrates. The Wiedemann-Franz relation states that increasing electrical resistivities cause decreasing λ_e values. If, e.g., $\rho(295\text{ K}) = 720\text{ }\mu\Omega\text{cm}$, $\lambda_e = 10\text{ mW/cmK}$; a resistivity of $100\text{ }\mu\Omega\text{cm}$ is equivalent to 72 mW/cmK . The relatively large resistivities of the series investigated cause λ_e values well below λ_{ph} , (Fig. 5.21b). In Fig. 5.22a data corrected for radiation losses are displayed. The right panel of Fig. 5.22b displays the difference between the measured and the corrected thermal conductivity $\lambda_{meas.} - \lambda_{corr.}$ as a function of T^3 . $\lambda_{meas-corr.}$ -curve in the right panel indicate thermal conductivity data obtained from a correction procedure taking radiation losses into account. This is in fine agreement with the Stefan Boltzmann

To evaluate procedure $\lambda_{ph}(T)$ theoretical model of Callaway et al. [81, 82, 83] was used. The filled symbol in Fig. 5.20a show $\lambda_{ph}(T)$ and corrected with respect to radiation losses.

The temperature dependent thermal conductivity $\lambda(T)$ of $Ba_8Zn_{5.7}Ge_{40.0}\square_{0.3}$ and $Ba_8Zn_{7.7}Ge_{38.3}$ is displayed in Figs. 5.21a,b. The filled symbols in Figs. 5.20a,b correspond to λ_{ph} corrected for radiation losses ($\lambda_{corr.} = \lambda_{meas.} - \beta T^3$). The lattice thermal conductivity λ_{ph} of $Ba_8Zn_{5.7}Ge_{40.0}\square_{0.3}$ at room temperature shows the highest λ_{ph} value in this

series (62 mW/cmK). In case $\text{Ba}_8\text{Zn}_{7.7}\text{Ge}_{38.3}$ the values have to be compared with the theoretical minimum thermal conductivity obtained from Eqn. 5.7. In case $\text{Ba}_8\text{Zn}_{5.7}\text{Ge}_{40.0}\square_{0.3}$ the minimum thermal conductivity as shown in figures was calculated using a Debye temperature θ_D of 210 K and a number of atoms per unit volume $n = 4.3453 \times 10^{28}/\text{m}^3$. The outcome of this is a room temperature value λ_{min} of 4 mW/cmK.

A further interesting feature is the observation that the low temperature maximum in $\lambda(T)$ of the present series becomes more pronounced with increasing Zn content and reaches its maximum for $\text{Ba}_8\text{Zn}_{7.7}\text{Ge}_{38.3}$. Although this sequence is expected to introduce some disorder in the crystal structure and thus enhances the thermal resistivity, the vanishing of the vacancies in the lattice due to the Zn/Ge substitution, which obviously completes for the $\text{Ba}_8\text{Zn}_{7.7}\text{Ge}_{38.3}$ compound, seems to overcompensate by far the former mechanism. Results of least squares fits according to Eqn. 1.17 and 1.19 are shown as solid and dashed lines in Fig. 5.21b for $\text{Ba}_8\text{Zn}_{7.7}\text{Ge}_{38.3}$. The filled symbols correspond to the T^3 correction of the experimental lattice thermal conductivity and demonstrate that the corrected thermal conductivity $\lambda_{ph}(T)$ of this compound is in proximity of the theoretical limit of thermal conductivity, a necessity for thermoelectric applications. The initial rise of $\lambda_{ph}(T)$ may be referred to boundary and point defect scattering; it becomes large when both quantities are small. It should be noted that defects comprise also vacancies. If the strength of Umklapp scattering increases, $\lambda_{ph}(T)$ starts to strongly decrease above a certain temperature, thereby forming a maximum at lower temperatures. The latter weakly depends on the Debye temperature but occurs well below $\theta_D/10$. Additionally, an increase of θ_D slightly reduces overall $\lambda_{ph}(T)$ values (see Figs. 5.20-5.21).

While λ_e increases strongly from $\text{Ba}_8\text{Zn}_{2.1}\text{Ge}_{41.5}\square_{2.4}$ to $\text{Ba}_8\text{Zn}_{4.6}\text{Ge}_{40.0}\square_{1.4}$, which shows the highest λ_e in these series (according to the decrease of the electrical resistivity owing to an increasing carrier number), the observed decrease of λ_{ph} is assigned to scattering of the phonons on the filler element. The application of the Wiedemann-Franz law yields there an electronic contribution of $\text{Ba}_8\text{Zn}_x\text{Ge}_{46-x-y}\square_y$ where $x= 2.1$ only 2.4 mW/cmK and for $x= 4.6$ is 13 mW/cmK at room temperature, respectively. Thermal conductivity $\lambda(T)$ and lattice thermal conductivity λ_{ph} at room temperature of $\text{Ba}_8\text{Zn}_{2.1}\text{Ge}_{41.5}\square_{2.4}$ ranges between 46 and 49 mW/cmK. Due to the small values of $\lambda(T)$ in this case, in contrast to ordinary metals, radiation losses during the measurement process at elevated temperatures have to be taken into account. For the compound $\text{Ba}_8\text{Zn}_{4.6}\text{Ge}_{40.0}\square_{1.4}$, λ_{ph} at room temperature is already reduced to values as small as 43 mW/cmK . The filled symbol in Figs. 5.20a,b denote the corrected lattice thermal conductivities.

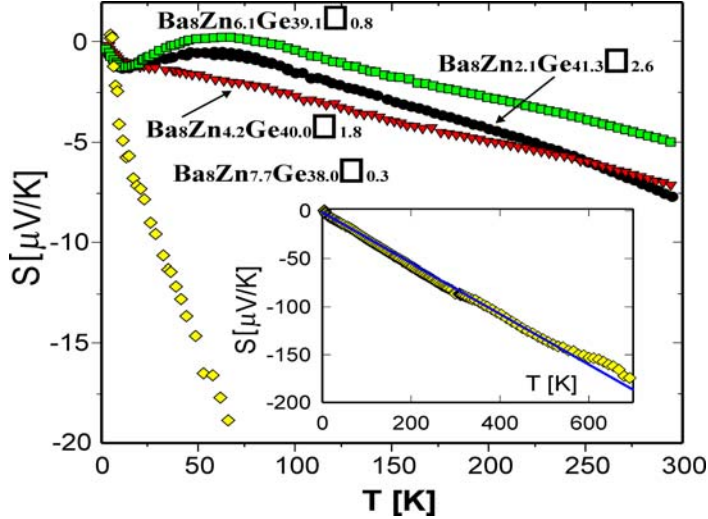


Figure 5.23: Temperature dependent thermopower of $\text{Ba}_8\text{Zn}_x(\text{Ge}_{46-x-y}\square_y)$ with $x = 2.1, 4.6, 5.7, 7.7$.

5.3.4 Thermopower

Measurements of the temperature dependent thermopower are shown in Fig. 5.23 for $\text{Ba}_8\text{Zn}_x(\text{Ge}_{46-x-y}\square_y)$. Common to all systems displayed are negative $S(T)$ values, referring to electrons as majority charge carriers. Moreover, $S(T)$ exhibits weak low temperature structures, most likely a consequence of phonon-drag effects. The compound richest in Zn, however, behaves almost linearly up to the 600 K range (inset, Fig. 5.23). Deviations from linearity are most likely measurement errors. $\text{Ba}_8\text{Zn}_{7.7}\text{Ge}_{38.3}$ is characterized by a slope of $-0.28 \mu\text{V}/\text{K}$. Linearity of the diffusion thermopower is predicted in terms of the free-electron model (see Eqn.5.8) [88]. For $T > \theta_D$, electron phonon interaction dominates. This simple relation (Eqn.5.8) allows an estimation of the charge carrier densities. Taking $m = m_e$, which should hold at high temperatures for systems without significant electronic correlations, the charge carrier density is estimated to be $n \approx 6.1 \times 10^{20} \text{ cm}^{-3}$, in excellent agreement with the optical data [189]. These numbers appear reasonable in comparison to e.g. $\text{Ba}_6\text{Ge}_{25}$ [88], where a charge carrier density $n \approx 7.8 \times 10^{21} \text{ cm}^{-3}$ was observed from Hall data; the Seebeck effect for that compound is about 10 times smaller than that of $\text{Ba}_8\text{Zn}_{7.7}\text{Ge}_{38.3}$.

5.4 $\text{Ba}_8\{\text{Pd}, \text{Pd}\}_x\text{Si}_{46-x}$ Clathrate I systems; crystal structure and physical properties

5.4.1 Crystal chemistry of $\text{Ba}_8\text{Pd}_x\text{Si}_{46-x}$ and $\text{Ba}_8\text{Pt}_x\text{Si}_{46-x}$

Atom site preferences were studied for $\text{Ba}_8\text{Pd}_x\text{Si}_{46-x}$ and $\text{Ba}_8\text{Pt}_x\text{Si}_{46-x}$ by room temperature X-ray powder diffraction from single-phase samples with $2 \leq x \leq 5$. For four single crystals, selected from samples with nominal composition $\text{Ba}_8\text{Pd}_{4.2}\text{Si}_{41.8}$, $\text{Ba}_8\text{Pt}_{2.5}\text{Si}_{43.5}$, $\text{Ba}_8\text{Pt}_{3.1}\text{Si}_{42.9}$, $\text{Ba}_8\text{Pt}_{3.8}\text{Si}_{42.2}$, X-ray intensity data were recorded at three temperatures: 100, 200 and 300 K. In all cases extinctions were consistent with a primitive cubic lattice (space group $Pm\bar{3}n$, $a \sim 1.035 \text{ nm}$) and inferred isotypism with the structure of clathrate type I. A plot of the unit cell dimensions of the clathrate type I solution (κ_1) versus increasing Pd, Pt content shows a volume expansion in accordance with the atomic size of Pd, Pt and Si (Fig. 5.24a and Fig. 5.25a). The data derived by Cordier and Woll [68] from single crystals selected from alloys melted at $T = 1400^\circ\text{C}$ ($\text{Ba}_8\text{Pd}_{2.5}\text{Si}_{43.5}$ and $\text{Ba}_8\text{Pt}_{2.7}\text{Si}_{43.3}$). In contrast to binary $\text{Ba}_8\text{Ge}_{43}\square_3$ [194] where the 6d site contains vacancies, the Si-containing samples did not reveal any defects in the 6d-sites. The site preference shown in Fig. 5.24b and Fig. 5.25b demonstrates that Pd or Pt atoms essentially occupy the 6d sites with only a small but significant fraction of Pd, Pt atoms gradually entering the 24k sites. The crystal analyses confirm earlier single crystal data by Cordier and Woll [68] which from our phase diagram study turned out to be at the low-(Pd, Pt) side of the ternary homogeneity region of the clathrate phases.

Thermal atomic displacement parameters (ADP) in all crystals investigated are consistent with features generally observed for clathrate type I compounds: whereas Ba2 atoms in the 6c site showed a large anisotropy of electron densities, Ba1 in 2a behave rather normal. However, in contrast to Ge-containing clathrates with (M = Pd, Pt, Zn, Cd) [69, 70, 202, 203], ADP's of Si atoms in 24k (Si3) show only slight deviations from spherical shape without any tendency to split into two 24k sites.

The small differences among the atomic radii of Pd, Pt and Si are reflected in an insignificant variation of the crystallographic parameters with the noble metal content (lattice parameter, atomic coordinates and site occupancy). Distances monotonically increase following the trend defined by the unit cell dimensions (Fig. 5.24 and 5.25). As generally observed in clathrates [69, 70, 202], the ADP parameters for Ba2 atoms in the 6c site show a significant anisotropy in contrast to Ba1 atoms, which behave normal with respect to the framework atoms. Although the ADP's of Ba2 atoms are significantly larger (by a factor of 3) than those of Ba1 atoms, the temperature dependences of ADP's are practically constant for all atoms of the lattice. Thus no

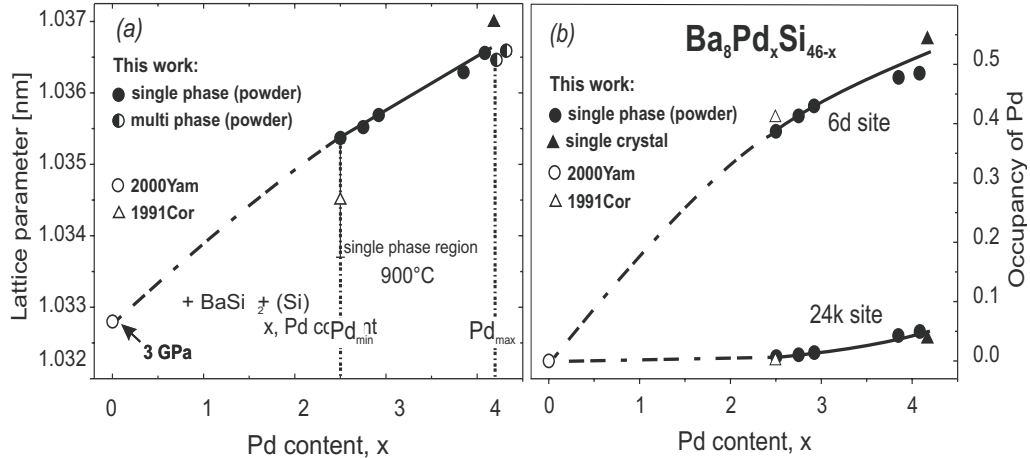


Figure 5.24: (a) lattice parameters vs. Pd-content for $\text{Ba}_8\text{Pd}_x\text{Si}_{46-x}$ alloys. The homogeneity region at $T = 900^\circ\text{C}$ is indicated. (b) compositional dependence of Pd occupancy in 6d and 24k sites. Filled circles - Rietveld refinements; filled triangles - single crystal data.

special rattling effect can be seen for Ba-atoms and an evaluation of Einstein-oscillations is not justified. Thermal expansion of lattice parameters shows a smooth variation in the temperature region from 100 to 300 K indicating continuous stability of the clathrate type I phase.

5.4.2 Physical Properties; Electrical Resistivity

Corresponding to the substitution of Si/Pd and Si/Pt distinct changes of carrier concentration and thus of transport quantities such as resistivity or thermopower are expected in $\text{Ba}_8\{\text{Pd}, \text{Pt}\}_x\text{Si}_{46-x}$.

Results of resistivity measurements for various concentrations of $\text{Ba}_8\{\text{Pd}, \text{Pt}\}_x\text{Si}_{46-x}$ are displayed in Figs. 5.26a,b in a normalized representation. The absolute values at room temperature are 59990, 1660 and 1685 [$\mu\Omega\text{cm}$] for $x = 2.5, 2.9$ and 3.9 in the case of the Pd-based series, and 1997, 448 and 990 [$\mu\Omega\text{cm}$] for $x = 2.8, 3.2$ and 3.8 for the Pt-based materials.

As obvious from Figs. 5.26a,b, the temperature dependent resistivity $\rho(T)$ does not behave metallic-like and the absolute $\rho(T)$ values are large, in a range of typical semi-metals or semiconductors. Two features may dominate the distinct $\rho(T)$ behaviour observed: *i)* The exchange of Si/Pd or Si/Pt distinctly changes the charge carrier density of the system. Following the Zintl concept, the removal of one Si atom creates 4 uncompensated charges which can be compensated - or even overcompensated - by the electrons provided by Ba as well as by Pd and Pt. While the valence state of Ba is rather clear,

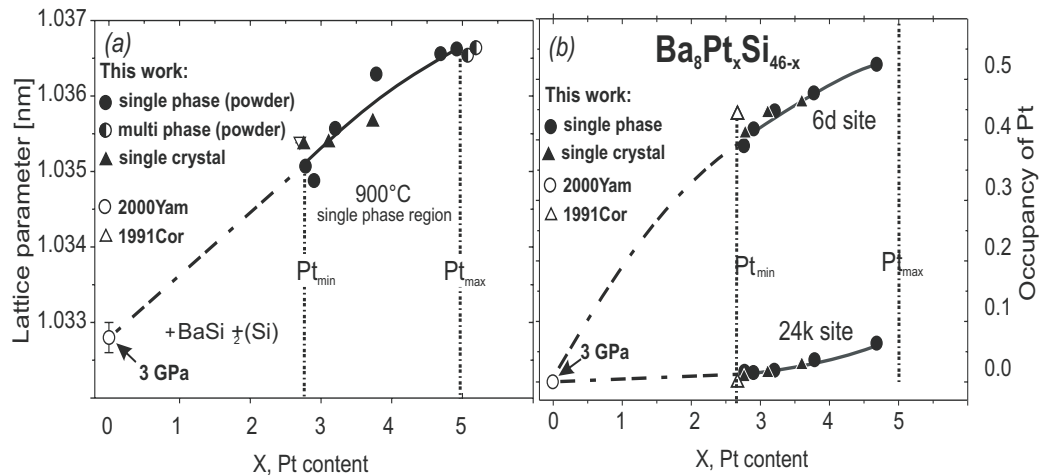


Figure 5.25: (a) lattice parameters vs. Pt-content for $\text{Ba}_8\text{Pt}_x\text{Si}_{46-x}$ alloys. The homogeneity region at $T = 900^\circ\text{C}$ is indicated. (b) compositional dependence of Pt occupancy in 6d and 24k sites. Filled circles - Rietveld refinements; filled triangles - single crystal data.

i.e., Ba^{2+} , giving rise to an extra of 2 electrons/Ba. In general, Pd and Pt are assumed to be neutral and do not allocate extra electrons. Such a scenario causes that the increase of the Pd or Pt content in the present Si-based type I clathrates reduces the charge carrier density from about 6 electrons/f.u. in the case of $x = 2.5$ to about 0.4 electrons/f.u. for the sample with $x = 3.9$. This indicates that a further increase of Pd or Pt would cause a compensated state, or even a crossover to an electronic transport guided by holes as predominant charge carriers. The scenario described follows from:

$$\left. \begin{array}{l} \text{Ba}_8; \quad 8 \times 2e = 16e \\ \text{Pt}_2; \quad 2 \times 0 = 0 \\ \text{Si}_{44}; \quad (46 - 44) \times 4h = 8h \end{array} \right\} \Rightarrow 8e \qquad \left. \begin{array}{l} \text{Ba}_8; \quad 8 \times 2e = 16e \\ \text{Pt}_4; \quad 4 \times 0 = 0 \\ \text{Si}_{42}; \quad (46 - 42) \times 4h = 16h \end{array} \right\} \Rightarrow 0$$

where the index *e* and *h* denotes *electrons* and *holes*, respectively. A fully compensated states, however, is not reached in the present substitution study.

ii) As clearly demonstrates in Fig. 5.26a the material shows temperature ranges with metallic behaviour but also ranges where a semiconducting scenario would better apply. Similar to Ge-based type I clathrates such a behaviour can be explained in terms of a density of states (DOS) model, where a narrow gap in the DOS is located slightly above the Fermi level. As a result both the metallic and the semiconducting features are accounted for [69, 70, 202, 203]. The metallic behaviour derives from scattering of conduction electrons into unoccupied states in reciprocal space just above the Fermi energy. Once this region of the DOS becomes occupied, electrons have to be

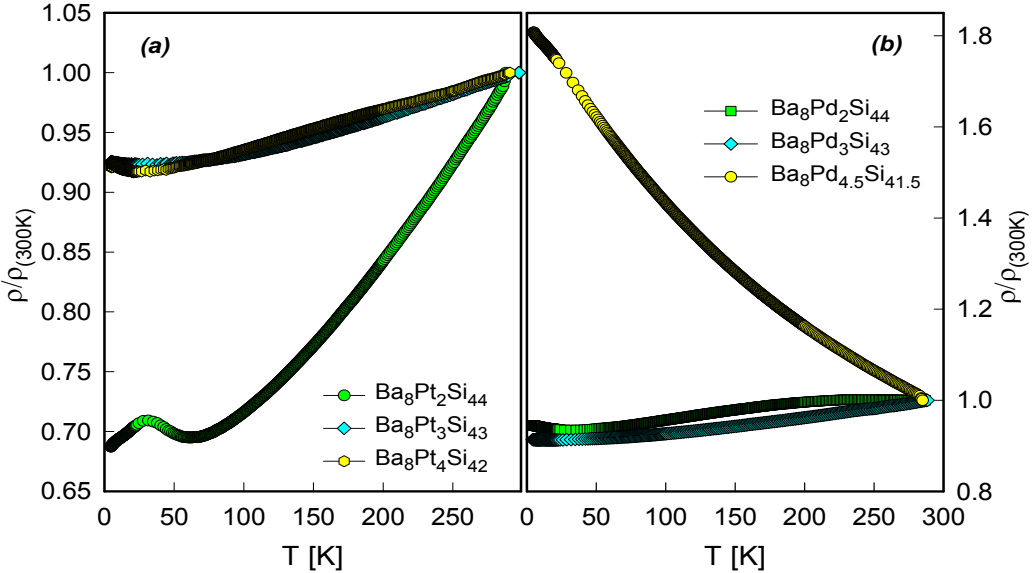


Figure 5.26: Temperature dependent electrical resistivity, ρ , of $\text{Ba}_8\text{Pt}_x\text{Si}_{46-x}$ (a) and $\text{Ba}_8\text{Pd}_x\text{Si}_{46-x}$ (b) for various concentrations x .

promoted across the gap, originating in a semiconducting behaviour. A distinct exponential temperature dependence, however, is not observed because of the proximity to the metallic state.

5.4.3 Thermal conductivity of $\text{Ba}_8(\text{Pd}, \text{Pt})_x\text{Si}_{46-x}$

The temperature dependent thermal conductivity, λ , of $\text{Ba}_8\text{Pd}_x\text{Si}_{46-x}$ and $\text{Ba}_8\text{Pt}_x\text{Si}_{46-x}$ has been measured from 4 K to room temperature. Results are shown in Figs. 5.27-5.28. Overall, thermal conductivity of both sets of samples is larger than required for thermoelectric materials. The comparison of $\text{Ba}_8\text{Pd}_x\text{Si}_{46-x}$ and $\text{Ba}_8\text{Pt}_x\text{Si}_{46-x}$ with Ge-based Pd and Pt compounds shows that the Ge-based type I clathrates have significantly smaller $\lambda(T)$ -values throughout the temperature range investigated. Within a first approximation, the substantial mass difference between the Si and the Ge based compounds is made responsible for this observation since, in general [67],

$$\lambda = 8 \left(\frac{k_B}{h} \right)^3 \frac{MV^{1/3}\theta_D^3}{\gamma^2 T}. \quad (5.9)$$

γ is the Grüneisen parameter, M is an average atomic mass and V the average atomic volume. The Debye temperature follows from $\theta_D \propto 1/M$. Thus, Eqn. 5.9 points to a decrease of the thermal conductivity as the average

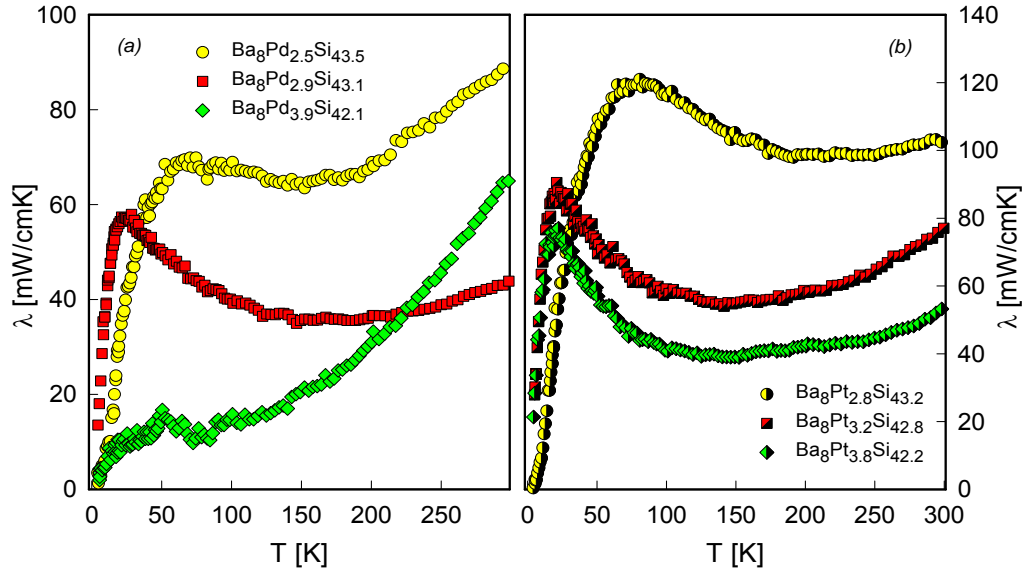


Figure 5.27: (a) Temperature dependent thermal conductivity, $\lambda(T)$, of $\text{Ba}_8\text{Pd}_x\text{Si}_{46-x}$ (b) $\text{Ba}_8\text{Pt}_x\text{Si}_{46-x}$ for various concentrations $x = 2.5, 2.9, 3.9$.

masses of a certain system increases. Consequently, a reduced Debye temperature associated with the higher Ge mass naturally explains the experimental findings.

Based on the Wiedemann-Franz law, the data observed are separated into the lattice (λ_{ph}) and the electronic contribution (λ_e), with $\lambda = \lambda_e + \lambda_{ph}$. Results are shown in Fig. 5.29a for λ_{ph} of $\text{Ba}_8\text{Pd}_{2.5}\text{Si}_{43.5}$. Due to the large electrical resistivities of the present series, the electronic contribution λ_e is small, of the order of several percent at room temperature of the total measured quantity, i.e., 0.15, 4.7 and 4.5 mW/cmK for $x = 2.5, 2.9$ and 3.9, respectively. Thermal conductivity at room temperature of Pd clathrates varies between 43 and 89 mW/cmK at room temperature. Similar observations were done also for a Pt clathrates. The overall values of $\lambda(T)$ are higher, typically in the range of 53 to 103 mW/cmK at room temperature. With increasing Pt content λ decreases; $\text{Ba}_8\text{Pt}_{2.8}\text{Ge}_{43.2}$ shows the highest λ values (~ 100 mW/cmK). The minimum thermal conductivity as shown in the figures 5.29, 5.30 and 5.31 as solid green lines was calculated using a Debye temperature θ_D and a number of atoms per unit volume n . Adding Pd to $\text{Ba}_8\text{Pd}_x\text{Si}_{46-x}$ causes that the low temperature maximum in $\lambda(T)$ becomes suppressed, converging a glass-like behaviour. However, none of the samples investigated is characterized by a dip in $\lambda(T)$ at lower temperatures, attributed to resonance scattering. This mechanism is expected to have a significant impact on thermal transport and is considered responsible for the

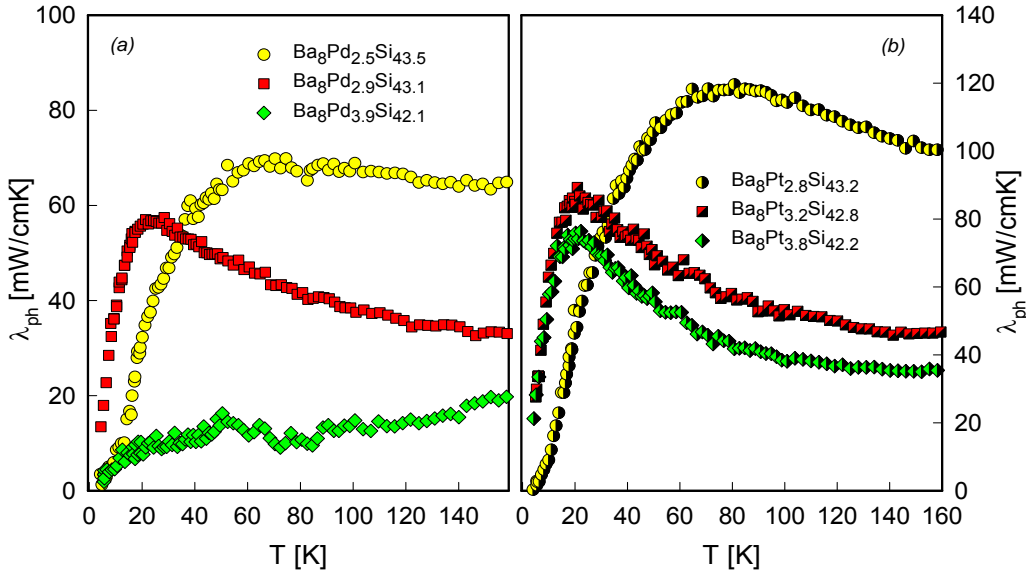


Figure 5.28: (a) Temperature dependent lattice thermal conductivity, $\lambda_{ph}(T)$, of $Ba_8Pd_xSi_{46-x}$ for various concentrations $x = 2.5, 2.9, 3.9$ (b) $Ba_8Pt_xSi_{46-x}$ for $x = 2.8, 3.2, 3.8$.

glass-like temperature dependence of $\lambda(T)$ in some cage forming compounds. An archetypal example for the latter is $Eu_8Ga_{16}Ge_{30}$ [192]. To obtain such true glass-like thermal conductivity, not only resonance scattering on the rattling modes is of importance, rather, tunneling states are necessary for this occurrence. A very intriguing proof of that fact was provided from a study on α - $Eu_8Ga_{16}Ge_{30}$ (type VIII Clathrate) and β - $Eu_8Ga_{16}Ge_{30}$ (type I Clathrate) [200]. While the former is the low temperature modification, the latter exists in a range of only 3°C, melting congruently at 699°C. β - $Eu_8Ga_{16}Ge_{30}$ is characterized by a plate-like displacement ellipsoid, referring to a split-site of Eu, which is entirely absent in α - $Eu_8Ga_{16}Ge_{30}$. As a consequence, tunneling states are missing and the thermal conductivity becomes much larger, the glass like behaviour got lost. It was pointed out that a large carrier concentration ($n \approx 10^{21}$) also can be responsible for “washing out” the resonance dip in $\lambda(T)$ due to enhanced phonon-electron scattering processes [201]. As already noted in the previous subsection a quantitative description of $\lambda(T)$ is possible in terms of Callaway’s theory [82, 83] (Eqn.1.17) of lattice thermal conductivity.

A comparison of the lattice thermal conductivity of the Pd with Pt compounds clearly signals an overall and significant reduction of $\lambda(T)$ for the Pd cases. The separation of the total thermal conductivity $\lambda(T)$ of $Ba_8Pd_{2.5}Si_{43.5}$ and $Ba_8Pt_{2.8}Ge_{43.2}$ into the electronic part λ_e and the lattice part λ_{ph} plotted

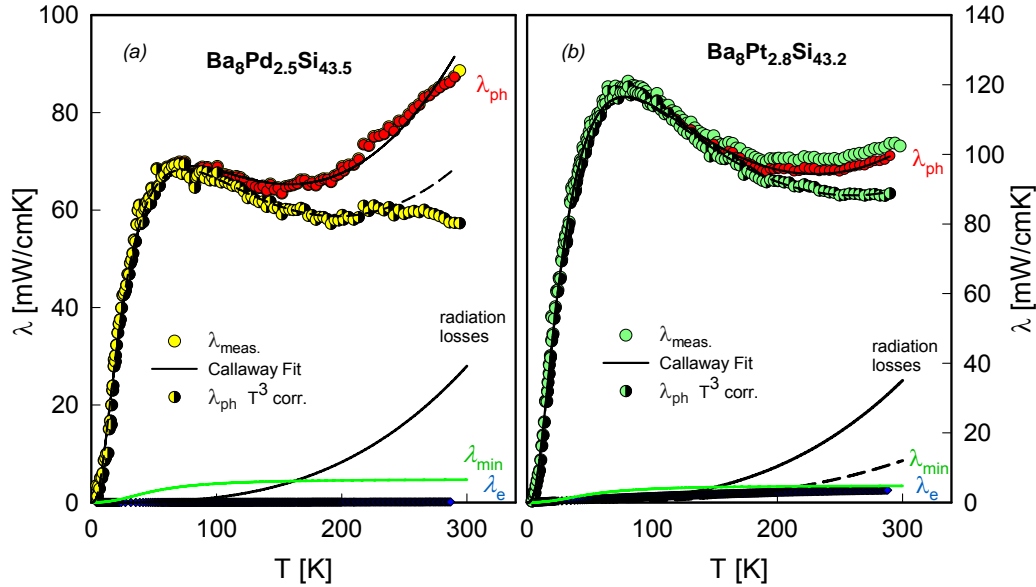


Figure 5.29: Separation of the total thermal conductivity $\lambda(T)$ of $\text{Ba}_8\text{Pd}_x\text{Si}_{46-x}$ for $x = 2.5$ (b) $\text{Ba}_8\text{Pt}_x\text{Si}_{46-x}$ for $x = 2.8$ into the electronic part λ_e and the lattice part λ_{ph} . The electronic contribution λ_e is deduced from the Wiedemann-Franz law. The solid lines are least squares fits according to Callaway model (Eqn. 1.17). The green lines correspond to the upper border of the theoretical lower limit of the lattice thermal conductivity λ_{min} . The black line demonstrates the radiation losses, the corresponding T^3 term. The half filled symbols indicate lattice thermal conductivity data obtained from a correction procedure taking radiation losses into account.

as a function of temperature in Figs. 5.29a,b. In both cases upon an increasing Pd and Pt content, λ_{ph} decreases. Among the Pd series $\text{Ba}_8\text{Pd}_{2.5}\text{Si}_{43.5}$ compound shows the highest λ_{ph} (87 mW/cmK) at 300 K while for the Pt case $\text{Ba}_8\text{Pt}_{2.8}\text{Ge}_{43.2}$ is largest, $\lambda_{ph} = 87$ mW/cmK at room temperature (see Fig. 5.29b).

The application of the Wiedemann-Franz law yields an electronic contribution of only about 0.1 mW/cmK in case of $\text{Ba}_8\text{Pd}_{2.5}\text{Ge}_{43.5}$ and 3.5 mW/cmK in case of $\text{Ba}_8\text{Pt}_{2.8}\text{Ge}_{43.2}$, respectively. With decreasing Pd content λ_e is reduced strongly from $\text{Ba}_8\text{Pd}_{2.9}\text{Si}_{43.1}$ to $\text{Ba}_8\text{Pd}_{2.5}\text{Si}_{43.5}$. As already noted in the previous subsection the λ_{ph} -curves are calculated by applying the Wiedemann-Franz law and subtracting the radiation losses assuming a T^3 -dependence. The filled symbol in Figs. 5.29a and 5.29b denote the corrected thermal conductivities data.

A comparison of the lattice thermal conductivity λ_{ph} of the $\text{Ba}_8\text{Pd}_{2.5}\text{Si}_{43.5}$ with $\text{Ba}_8\text{Pt}_{2.8}\text{Si}_{43.2}$ compound clearly signals an overall and significant re-

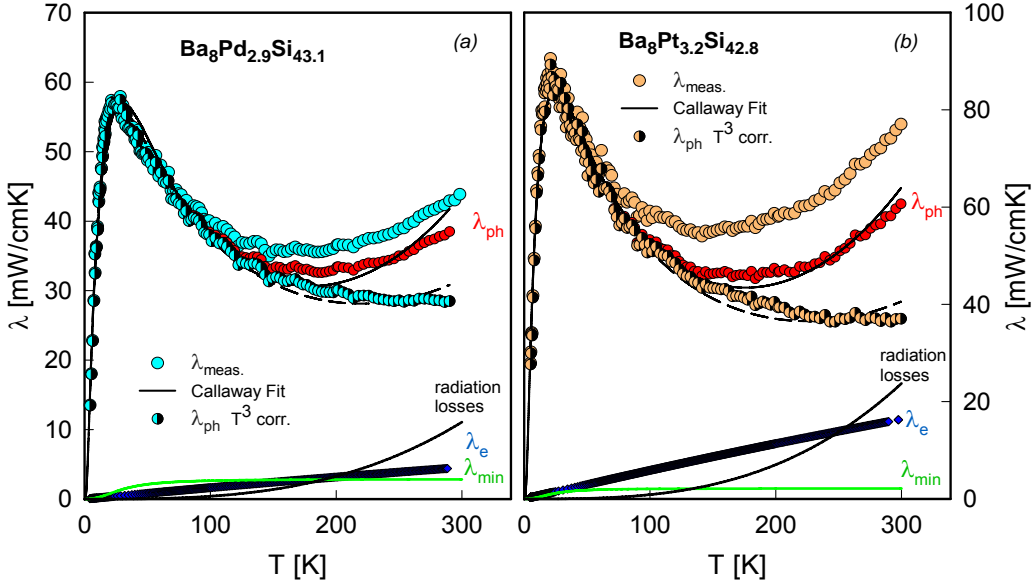


Figure 5.30: Separation of the total thermal conductivity $\lambda(T)$ of $\text{Ba}_8\text{Pd}_x\text{Si}_{46-x}$ for $x = 2.9$ (b) $\text{Ba}_8\text{Pt}_x\text{Si}_{46-x}$ for $x = 3.2$ into the electronic part λ_e and the lattice part λ_{ph} . The electronic contribution λ_e is deduced from the Wiedemann-Franz law. The solid lines are least squares fits according to Callaway model (Eqn. 1.17). The green lines correspond to the upper border of the theoretical lower limit of the lattice thermal conductivity λ_{min} . The black line demonstrates the radiation losses. The half filled symbols indicate lattice thermal conductivity data obtained from a correction procedure taking radiation losses into account.

duction of λ_{ph} for the $\text{Ba}_8\text{Pd}_{2.5}\text{Si}_{43.5}$ case. With increasing Pd content λ_{ph} decreases, the $\text{Ba}_8\text{Pd}_{2.5}\text{Si}_{43.5}$ compound shows the highest λ_{ph} values (about 71 mW/cmK at 70 K. For the compound $\text{Ba}_8\text{Pt}_{2.8}\text{Si}_{43.2}$, λ_{ph} at room temperature is about 103 mW/cmK. On the other hand $\text{Ba}_8\text{Pt}_{2.8}\text{Si}_{43.2}$ shows highest λ_{tot} and λ_{ph} values in the whole temperature range in this series. The minimum thermal conductivity was calculated using a Debye temperature θ_D of 233, 238 K and a number of atoms per unit volume $n = 4.8652 \times 10^{28}/\text{m}^3$ in case Pd compounds, $4.8695 \times 10^{28}/\text{m}^3$ in case Pt compounds, respectively. The outcome of this for $\text{Ba}_8\text{Pd}_{2.5}\text{Si}_{43.5}$ is a room temperature values of λ_{min} about 4.7 mW/cmK and 4.8 mW/cmK in case of $\text{Ba}_8\text{Pt}_{2.8}\text{Si}_{43.2}$, respectively.

The separation of the total thermal conductivity $\lambda(T)$ of $\text{Ba}_8\text{Pd}_{2.9}\text{Si}_{43.1}$ (left panel) and $\text{Ba}_8\text{Pt}_{3.2}\text{Si}_{42.8}$ (right panel) into the electronic part λ_e and the lattice part λ_{ph} plotted as a function of temperature in Figs. 5.30a,b. The thermal conductivity $\lambda(T)$ of $\text{Ba}_8\text{Pd}_{2.9}\text{Si}_{43.1}$ and $\text{Ba}_8\text{Pt}_{3.2}\text{Si}_{42.8}$ is about 44 and 77 mW/cmK at 300 K, respectively. Least squares fits according to

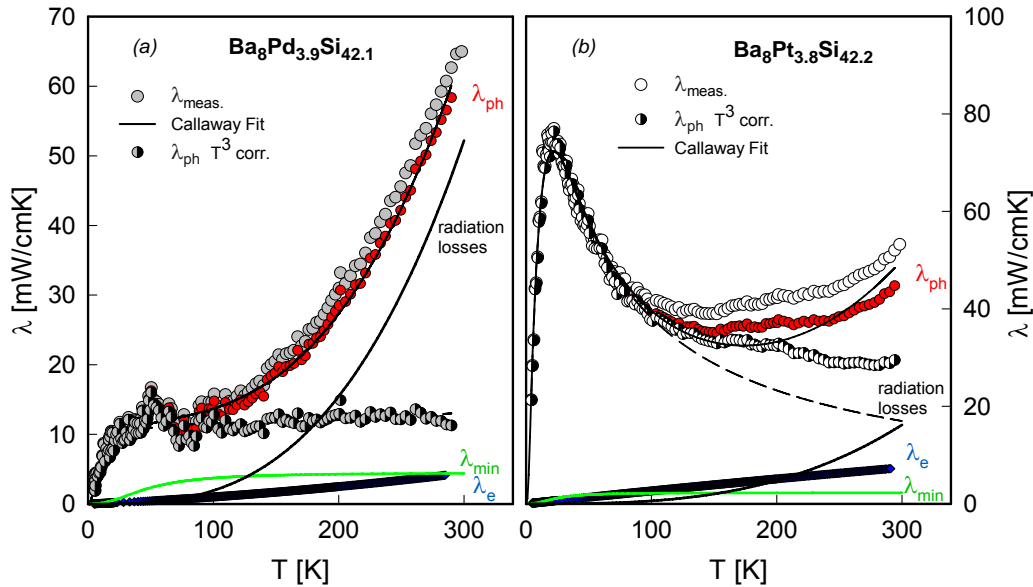


Figure 5.31: Separation of the total thermal conductivity $\lambda(T)$ of (a) $\text{Ba}_8\text{Pd}_x\text{Si}_{46-x}$ for $x = 3.9$ (b) $\text{Ba}_8\text{Pt}_x\text{Si}_{46-x}$ for $x = 3.8$ into the electronic part λ_e and the lattice part λ_{ph} . The electronic contribution λ_e is deduced from the Wiedemann-Franz law. The solid lines are least squares fits according to Callaway model (Eqn. 1.17). The green lines correspond to the upper border of the theoretical lower limit of the lattice thermal conductivity λ_{min} . The black line demonstrates the radiation losses. The half filled symbols indicate lattice thermal conductivity data obtained from a correction procedure taking radiation losses into account.

Eqn. 1.17 are shown in Fig. 5.30 as dashed lines, revealing fine agreement with the data observed. Filled symbols in Figs. 5.30a,b indicate thermal conductivity data obtained from the correction procedure taking radiation losses into account. In all cases lattice thermal conductivity λ below ~ 200 K can be described by means of Callaway's model. This procedure allows an extrapolation of $\lambda(T)$ towards higher temperatures and helps to account for the radiation losses. For the compound $\text{Ba}_8\text{Pt}_{3.2}\text{Si}_{42.8}$ with respect to radiation losses, λ_{ph} at room temperature is already reduced from 77 mW/cmK to 60 mW/cmK. Similar features for $\text{Ba}_8\text{Pd}_{2.9}\text{Si}_{43.1}$ reveals at room temperature λ_{ph} 38 mW/cmK. The electronic thermal conductivity λ_e for $\text{Ba}_8\text{Pt}_{3.2}\text{Si}_{42.8}$ at room temperature shows the highest value (17 mW/cmK). The minimum thermal conductivity as shown in Fig. 5.30a (solid green line) was calculated using a Debye temperature θ_D of 202 K, and $n = 4.86 \times 10^{28}/\text{m}^3$; thus $\lambda_{min} = 4$ mW/cmK (at room temperature). In case of $\text{Ba}_8\text{Pt}_{3.2}\text{Si}_{42.8}$ λ_{min} is lower compared to the Pd compound. Debye temperature $\theta_D = 123$ K, and $n =$

$4.862 \times 10^{28}/m^3$ reveals $\lambda_{min} = 2.5$ mW/cmK at 300 K.

Similar observations were made also for $Ba_8Pd_xSi_{46-x}$ and $Ba_8Pt_xSi_{46-x}$ for $x = 3.9, 3.8$. The temperature dependent thermal conductivity $\lambda(T)$ of $Ba_8Pd_{3.9}Ge_{42.1}$ and $Ba_8Pt_{3.8}Ge_{42.2}$ is displayed in Figs. 5.31a,b. The left panel of Fig. 5.31 shows $\lambda(T)$ of $Ba_8Pd_{3.9}Ge_{42.1}$ (large circles). $\lambda_{ph}(T)$ and $\lambda_e(T)$ are separated according to equation 1.9. The measured thermal conductivity is indicated by large circles, the lattice thermal conductivity by filled symbols and the electronic thermal conductivity by triangle symbols. The phonon contribution $\lambda_{ph}(T)$ is further interpreted by using the model of Callaway, according to Eqn. 1.17. The filled symbols in Figs. 5.31a,b show $\lambda_{ph}(T)$ derived from the Wiedemann-Franz law (Eqn. 1.10) and corrected with respect to radiation losses. The left panel of Fig. 5.31 shows the measured data in case $Ba_8Pd_{3.9}Ge_{42.1}$ with an oversized slope of the curves at higher temperatures due to radiation losses. The different contributions to $\lambda(T)$ as well as the corrected thermal conductivities of $Ba_8Pt_{3.8}Ge_{42.2}$ are plotted in Fig. 5.31b as examples of this correction procedure. Thermal conductivities of $Ba_8Pd_{3.9}Ge_{42.1}$ and $Ba_8Pt_{3.8}Ge_{42.2}$ are 64 mW/cmK and 53 mW/cmK at room temperature, respectively. The electronic thermal conductivity, deduced from the Wiedemann-Franz law yields larger λ_e for $Ba_8Pt_{3.2}Si_{42.8}$, 7.5 mW/cmK at 300 K. Correcting the $\lambda(T)$ data for radiation losses demonstrates that the lattice thermal conductivity of $Ba_8Pd_{3.9}Si_{42.1}$ reaches at room temperature about 10 mW/cmK (lower curve, Fig. 5.31a). The radiation-corrected lattice thermal conductivity of $Ba_8Pd_{3.9}Si_{42.1}$ is of the same order of magnitude as λ_{min} , suggesting that phonons behave like in a glassy state. Taking $n = 4.8523 \times 10^{28} m^{-3}$ and $\theta_D = 230$ K reveals $\lambda_{min}(300 K) = 4.4$ mW/cmK. Results below room temperature are shown in Fig. 5.31a as solid green line. A similar scenario is valid for $Ba_8Pt_{3.2}Si_{42.8}$. The minimum thermal conductivity was calculated using a Debye temperature $\theta_D = 221$ K and $n = 4.8523 \times 10^{28}/m^3$. The outcome of this is a room temperature value λ_{min} of 4.42 mW/cmK. With increasing x , λ_{ph} decreases in whole temperature range and $Ba_8Pt_{3.2}Si_{42.8}$ shows the lowest value of λ_{ph} (44 mW/cmK) at room temperature.

The fit parameters A , B , C and D from Eqn. 1.19 are listed in Table 5.1 and obtained by least squares fits of the lattice thermal conductivity data λ_{ph} according to Callaway's model (Eqn. 1.17). Table 5.1 shows the influence of each parameter and, therefore, of each physical process of the phonon contribution λ_{ph} to thermal conductivity. The probability for Umklapp-processes ($\tau_U^{-1} = BT^3x^2e^{-\frac{\theta_D}{3T}}$) represents by the parameter B and indicate that the probability of Umklapp-processes increases with the more platinum and less silicon atoms a unit cell contains. Since Umklapp-processes become dominant as the temperature increases above 15 K the influence of the grain size (parameters C) decreases as the platinum/palladium content increases in both cases.

	θ_D [K]	A [$\text{K}^{-4}\text{s}^{-1}$]	B [$\times 10^{-4}\text{K}^{-3}\text{s}^{-1}$]	C [$\times 10^9\text{s}^{-1}$]	D [$\times 10^7\text{K}^{-1}\text{s}^{-1}$]
$\text{Ba}_8\text{Pt}_2\text{Si}_{44}$	238	551.7	5.4	9.9	1.07
$\text{Ba}_8\text{Pt}_3\text{Si}_{43}$	200	6306.1	11.85	0.14	0.51
$\text{Ba}_8\text{Pt}_4\text{Si}_{42}$	126	10458.5	23.4	0.104	0.0002
$\text{Ba}_8\text{Pd}_2\text{Si}_{44}$	234	1087.05	8.08	9.9	9.8
$\text{Ba}_8\text{Pd}_3\text{Si}_{43}$	204	7683.7	16.83	0.42	0.36
$\text{Ba}_8\text{Pd}_{4.5}\text{Si}_{41.5}$	311	15990	13.64	0.24	1.3

Table 5.1: The fit parameters A , B , C and D were obtained by least squares fits of the lattice thermal conductivity data λ_{ph} in the temperature range $4.2 \text{ K} < T < 300 \text{ K}$ according to Callaway's model Eqn. 1.17.

While the added platinum/palladium atoms replace the silicon atoms in the crystal lattice scattering of phonons on crystal defects such as unoccupied places become more important. Parameter A indicates for phonon scattering on the crystal defects. Comparing the set of fit parameters indicates that the scattering rate referring to point defect scattering, i.e., $\tau_D^{-1} = Ax^4T^4$ (A is a material dependent parameter) increases by several orders of magnitude upon the increasing Pd/Pt content. Thus, scattering on point defects as created by the Pd/Si substitution turns out to be an extremely efficient scattering process. Parameter D denotes the electron-phonon scattering processes. Since the probability for the electron-phonon interaction increases with increasing electron concentration, the values of parameter D is larger for the compounds containing less platinum and palladium atoms. It should be noted that the values of the Debye temperature θ_D do not correspond to those calculated by the fit for heat capacity or electrical resistivity because the Debye temperature is temperature dependent. For the lattice thermal conductivity the low temperature range is more important. Thus θ_D was optimized in this range in order to improve the quality of the fit. Consequently, the Debye temperature resulting from the lattice thermal conductivity fits is lower than that resulting from the fits for specific heat or electrical resistivity measurements.

5.4.4 Thermopower

Results regarding the temperature dependent thermopower, $S(T)$, are plotted in Fig. 5.32 for various concentrations of $\text{Ba}_8\{\text{Pd}, \text{Pt}\}_x\text{Si}_{46-x}$. Different to most of the clathrates studied previously [69, 70, 202, 203], both series exhibit a rather complicated temperature dependence. This refers to distinct electronic correlations, particularly in the case of the Pd-based materials. As a consequence, $S(T)$ differs from the linear dependence evident in simple met-

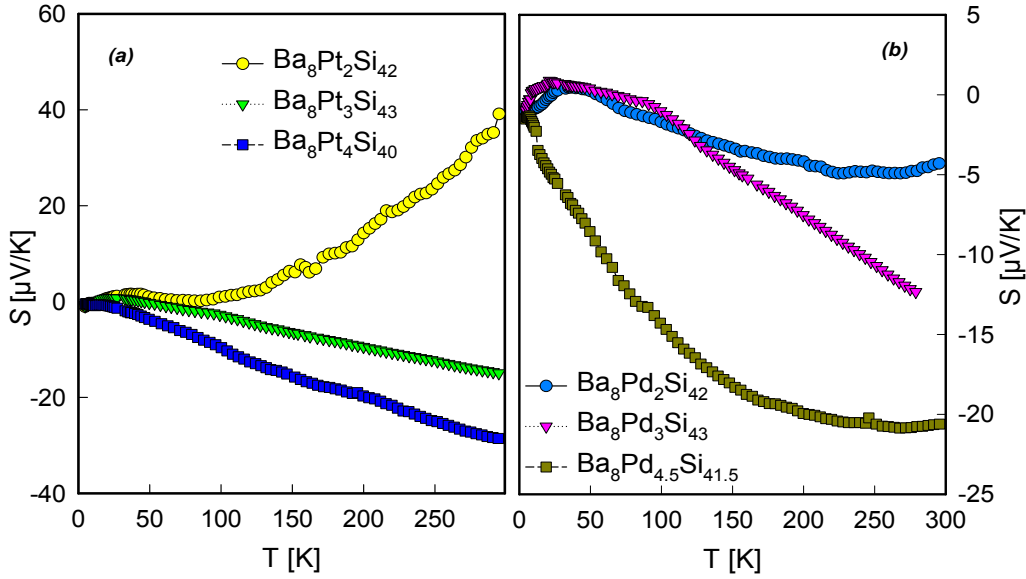


Figure 5.32: Temperature dependent thermopower $S(T)$ for various concentrations of $\text{Ba}_8\text{Pt}_x\text{Si}_{46-x}$ (a) and $\text{Ba}_8\text{Pd}_x\text{Si}_{46-x}$ (b).

als. The largest values [$S(RT) \approx 30 \mu\text{V/K}$ for $\text{Ba}_8\text{Pt}_{3.8}\text{Si}_{42.2}$] is well above $S(T)$ of simple metals, but still below those values sufficient for thermoelectric applications [$S(RT) \approx 150 - 200 \mu\text{V/K}$].

$S(T)$ is negative in the high temperature range for both series, indicating electrons as the dominant charge carriers. Exceptionally, however, $\text{Ba}_8\text{Pt}_{2.8}\text{Si}_{43.2}$ behaves positive, referring to holes as predominant charge carriers in electronic transport.

Using Eqn. 5.8 for the linear $S(T)$ dependence as observed for $\text{Ba}_8\text{Pt}_{3.2}\text{Si}_{42.8}$ and $\text{Ba}_8\text{Pt}_{3.8}\text{Si}_{42.2}$, the charge carrier density n can be calculated. Approaching the data of Fig. 5.32 by a linear dependence for $150 \leq T \leq 300 \text{ K}$ reveals the charge carrier density which for the $\text{Pt}_{3.2}$ compound amounts to $n = 6.3 \times 10^{21} \text{ cm}^{-3}$ and for $\text{Pt}_{3.8}$ to $n = 3.2 \times 10^{21} \text{ cm}^{-3}$. These figures are about two orders of magnitude above the charge carrier concentration providing the optimum power value $\alpha = S^2/\rho$ of degenerate semiconductors with a narrow gap in the electronic density of states.

Chapter 6

Non-centrosymmetric BCS superconductor BaPtSi₃

6.1 Introduction

The research on superconductivity in non-centrosymmetric materials has attracted growing interest in recent years. The ternary barium transition-metal silicides are new intermetallic superconductors where SC without inversion symmetry can be studied in non strongly correlated electron systems. For most superconductors, the atomic lattice is centrosymmetric. Due to the Pauli principle and the parity conservation Cooper-pairs with orbital even parity should have antiparallel spin states, namely spin singlets (total spin $S = 0$), while those having orbital odd parity should have a parallel spin state, i.e., a spin triplet (total spin $S = 1$).

Non-centrosymmetric structures allow for the existence of a mixture of spin singlet and spin triplet pairing. From a detailed investigation of the Ba-Pt-Si system at 800°C the formation of a novel compound, BaPtSi₃, was identified which is a representative of the non-centrosymmetric structure BaCuSn₃.

6.2 Crystallographic details

BaPtSi₃ was prepared by argon arc melting and subsequent heat treatment under high vacuum at 900°C for 100 h. X-ray powder diffraction data from as-cast and annealed alloys were collected on a Guinier-Huber image plate recording system with CuK_α-radiation ($8 \leq 2\Theta \leq 100^\circ$).

The crystal structure of BaPtSi₃ was determined from X-ray Rietveld refinement. Typical final observed, calculated, and difference X-ray powder diffraction patterns for BaPtSi₃ are shown in Fig. 6.1a. The low residual value confirmed isotropic with the tetragonal unit cell. Indexing of the X-ray powder

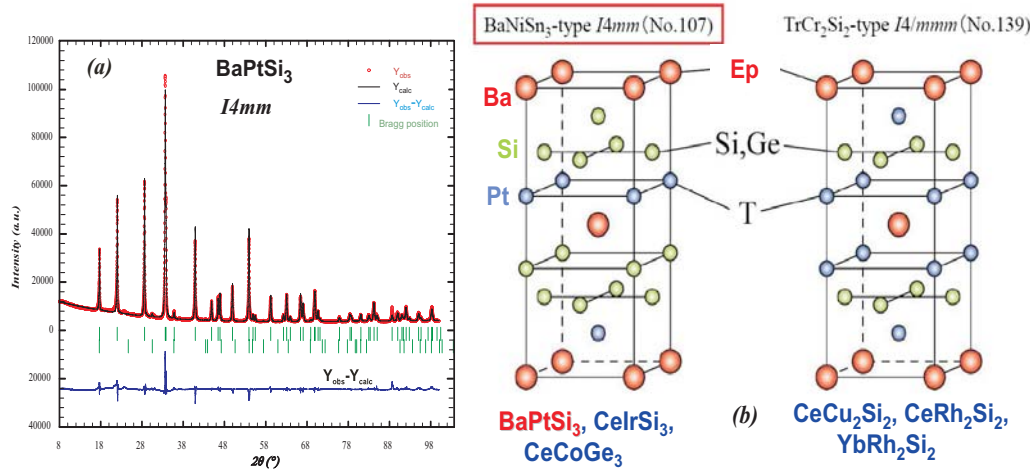


Figure 6.1: (a) X-ray pattern and Rietveld refinement of BaPtSi₃. The solid line derives from the Rietveld refinement and $Y_{obs.}-Y_{calc.}$ is the intensity difference between experimental data and Rietveld calculations. (b) The crystal structure of BaPtSi₃ in three-dimensional view.

pattern prompted space group I4mm (No. 107), isotropic with BaNiSn₃-Type. The crystal structure of BaPtSi₃ is shown in Fig. 6.1b in three-dimensional view in comparison with the TrCr₂Si₂ structure type. Crystallographic data (standardized) are: $a = 0.44071(2)$ nm, $c = 1.0018(3)$ nm in as-cast condition and $a = 0.44080(3)$, $c = 1.0022(4)$ nm in 900°C; Ba in 2a site at (0, 0, 0.6040); Pt in site 2a at (0, 0, 0.25322), Si(2) in 2a site at (0,0,0) (fixed) and Si(1) in 4b site with (0, 0.5, 0.3640).

6.3 Electrical resistivity of BaPt_xSi_y

The temperature dependent electrical resistivity $\rho(T)$ of BaPtSi₃ is displayed in Fig. 6.2a in comparison with $\rho(T)$ of BaPt₅Si_{y12} and Ba₁₂Pt₂₃Si₆₅. All compounds are characterized by temperature dependencies implying metallic behaviour throughout the whole temperature range. The resistivity $\rho(T)$ in the normal state region is similar to that of simple metals and can be described in terms of a temperature independent residual resistivity ρ_0 and a Bloch-Grüneisen term (compare expression 1.4) in combination with a Mott-Jones contribution KT^3 allowing to account for the strong curvature of $\rho(T)$. With increasing Pt and Si content the absolute resistivity increases in the whole temperature region.

The respective room temperature values of the electrical resistivity in cases of BaPt₅Si₁₂ and Ba₁₂Pt₂₃Si₆₅ are 423.5, 378.4 [$\mu\Omega\text{cm}$] and 35.3 [$\mu\Omega\text{cm}$] for

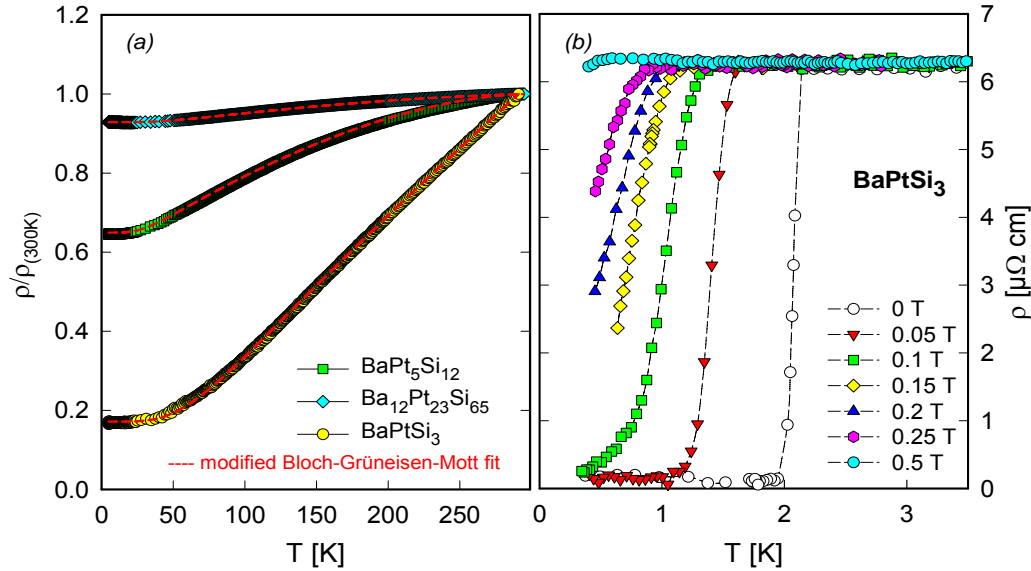


Figure 6.2: (a) Temperature dependent electrical resistivity, $\rho(T)$ for various concentrations x and y of BaPt_xSi_y plotted in a normalized representation. The solid lines are least squares fits according to the modified Bloch-Grüneisen model (see Eqn. 1.4). (b) Temperature dependent electrical resistivities of BaPtSi_3 measured in various externally applied magnetic fields of up to 0.5 T.

BaPtSi_3 , respectively. The Debye temperatures θ_D , ranging between 180 K and 346 K, are typical for intermetallic compounds. Further fit data are listed in Table 6.1. Least squares fits to the data of BaPtSi_3 in the temperature range from 4.2 to 300 K reveal the values for $\rho_0 = 6$ [$\mu\Omega\text{cm}$], the Debye temperatures $\theta_D = 346$ K and the electron phonon interaction strength $\mathcal{R} = 36.7$ [$\mu\Omega\text{cm}$].

Figure 6.2b show temperature dependent electrical resistivities measured in various externally applied magnetic fields of up to 0.5 T for BaPtSi_3 . These data demonstrate that BaPtSi_3 undergoes a sharp superconducting transition around 2.3 K, which becomes suppressed already at small magnetic fields.

The evaluation of the electron-phonon coupling constant λ of BaPtSi_3 can be made in terms of the McMillan formula (see Eqn. 4.5). For weak coupling superconductors (SC), $\lambda_{e,ph}$ depends crucially on the value attributed to μ^* , but not in the case of strong coupling SC, because the possible variation of the Coulomb pseudopotential is small compared to $\lambda_{e,ph}$. Taking repulsive screened Coulomb part $\mu^* = 0.13$ (for transition metal superconductors and their intermetallic counterparts) and $\theta_D = 370$ K one obtains $\lambda_{e,ph} \approx 0.5$, referring to a superconductor in the weak coupling limit.

	ρ_0 [$\mu\Omega\text{cm}$]	θ_D [K]	\mathcal{R} [$\mu\Omega\text{cm}$]
BaPt ₅ Si ₁₂	273	180	135
Ba ₁₂ Pt ₂₃ Si ₆₅	351	268	35.1
BaPtSi ₃	6	346	36.7

Table 6.1: Fit-parameters for the electrical resistivity obtained by the Bloch-Grüneisen law, $\rho(T) = \rho_0 + \rho_{ph}(T)$, and Residual resistivity ρ_0 , Debye temperature θ_D , electron-phonon interaction strength \mathcal{R} .

6.4 Low-temperature specific heat and phonon specific heat of BaPt_xSi_y

The low-temperature specific heat of BaPtSi₃ is shown in a C_p/T versus T representation for various external magnetic fields in Fig. 6.3a. BaPt₅Si₁₂ is non-superconducting down to 2 K while BaPtSi₃ shows a pronounced anomaly, which, in agreement to the resistivity data, follows from superconductivity with an onset temperature of about 100 mK. As can be seen from Fig. 6.3a, a field of 0.05 T is sufficient to suppress superconductivity to below 2 K. Thus, the 0.05 T and the zero-field data of BaPtSi₃ represent the superconducting- and normal-state specific heat. Approximating normal-state data at lowest temperatures by $C_p/T = \gamma T + \beta T^3$ yields the Sommerfeld coefficient $\gamma = 5.7 \text{ mJ/molK}^2$ (see inset Fig. 6.3a) and the Debye temperature $\theta_D \approx 370 \text{ K}$. Idealization of the heat capacity anomaly under the constraint of entropy balance between the superconducting and the normal state is shown in Fig. 6.3a, yields $T_c = 2.3 \text{ K}$ and the height of the specific heat jump $\Delta C_p/T|_{T_c} = (C_s - C_n)/T|_{T_c} = 7.1 \text{ mJ/molK}^2$. The normalized specific heat jump $(\Delta C_p)|_{T_c}/(\gamma_n T_c) \approx 1.2$, which is slightly below the figure expected from BCS theory ($\Delta C_p/(\gamma T_c) \approx 1.43$). BCS type superconductivity follows also from an application of the data set of Mühlischlegel [196] to the heat capacity results of BaPtSi₃. Results of this procedure are shown as a solid line in the Fig. 6.3a, revealing fine agreement with a fully gapped BCS superconductivity. The residual deviation at the lowest temperatures might be due to same impurities or measurement uncertainties.

In order to obtain more aspects on the lattice dynamics, we employ in Fig. 6.3b a $(C_p - \gamma T)/T^3$ vs. $\ln T$ representation. This particular representation allows us to emphasize deviations from the simple Debye model, which, at low temperatures, follows $C_p \propto T^3$. Based on the already discussed model of Junod et al.[91] the phonon spectra $F(\omega)$ (right axis, solid line) are reconstructed and plotted as $(C_p - \gamma T)/T^3$ vs. $\ln T$ for BaPtSi₃ and BaPt₅Si₁₂ in Fig. 6.3b. The low lying phonon branch in BaPtSi₃ may render those lattice

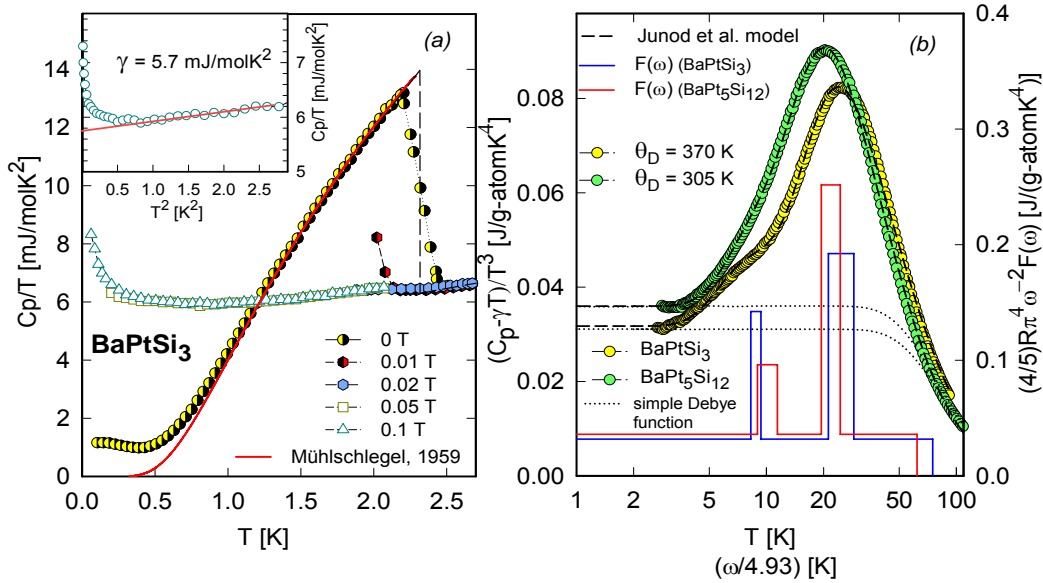


Figure 6.3: (a) Temperature dependent specific heat C_p of BaPtSi₃ plotted as C_p/T vs. T for various magnetic fields up to 0.1 T. The solid line adjusts the numerical data of Mühlischlegel (Ref. [196]) to the present experiment. Inset: low temperature heat capacity C_p of BaPtSi₃ plotted as C_p/T vs. T^2 . (b) Phonon part of the specific heat of BaPtSi₃ and BaPt₅Si₁₂ plotted as $(C_p - \gamma T)/T^3$ vs. $\ln T$. The dashed line is a least squares fits of the experimental data using the model described in the text with two Einstein-like modes $\theta_D = 369$ K in case BaPtSi₃ and $\theta_D = 305$ K in case of BaPt₅Si₁₂. The solid and the dashed-dotted lines sketch the phonon spectral function $F(\omega)$ plotted as $\omega/4.93$ vs. $(5/4)R\pi^4\omega^{-2}F(\omega)$ for which ω is given in Kelvin.

vibrations which couple to the electron system, thereby enabling BCS-type superconductivity. The phonon part of the specific heat of BaPtSi₃ is well described by a simple Debye-function with a Debye temperature $\theta_D = 369$ K together with two Einstein modes $\omega_{EL1} = 43.4$ K with a width of 5.3 K in the frequency regions 40 K $< \omega < 46$ K and $\omega_{EL2} = 123.3$ K with a width of 37.7 K in the frequency regions 104 K $< \omega < 142$ K. For BaPtSi₃ the width of contributions is significantly larger than for BaPt₅Si₁₂ (see also Table 6.2).

The reconstruction of the phonon density of states in the case of BaPt₅Si₁₂ is plotted in figure 6.3(b). The essential parameters of the model used to construct the spectral function $F(\omega)$ (solid lines, right axis), are $\theta_D = 305$ K, $\omega_{EL1} = 50.2$ with width of 12.1 K and $\omega_{EL2} = 108.2$ with a width of 24.8 K. The parameters of least squares fits are summarised in Table 6.2.

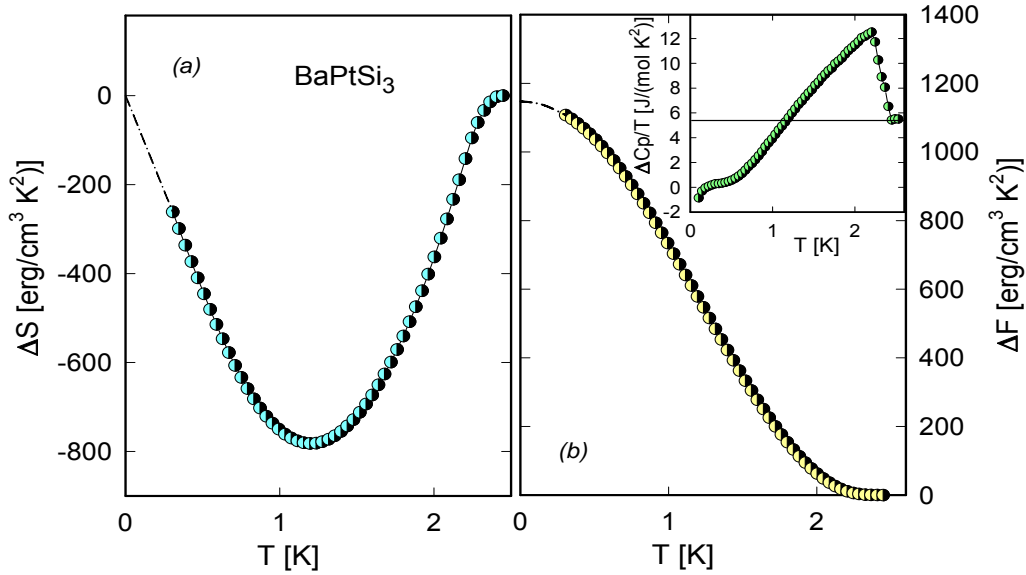


Figure 6.4: (a) The temperature dependent entropy $\Delta S(T)$ by integration of $\Delta C/T$ according to the data. (b) The free energy difference $\Delta F(T)$ of BaPtSi_3 . The dashed lines are extrapolations from the normal- and superconducting states, respectively. Inset; $\Delta C_p/T(T = T_c)$ obtained from $\Delta C_p[C_p(H = 0) - C_p(H = 0.1 \text{ T})]$ data.

6.5 Determination superconducting and normal state properties

The thermodynamic critical field $H_c(T)$ is calculated from the free energy difference between the superconducting and normal state: $\Delta F(T) = F_n - F_s = \mu_0 H_c^2(T)/2 = \int_{T_c}^T \int_{T_c}^{T'} \frac{C_s - C_n}{T'} dT'' dT$ (Fig.6.4b). The difference curves is displayed in inset of Fig.6.4b. C_s is obtained from the zero field specific heat measurement and C_n is taken from the normal state specific heat by $C_n = \gamma T + \beta T^3$, respectively. The superconducting gap $\Delta(0)$ of BaPtSi_3 can be estimated from the modified BCS expression (Eqn. 4.7). $T < T_c/2$ C_{eS} data are used to estimate the superconducting gap $\Delta(0)$. Adjusting Eqn. 4.7 to $C_{eS}(T) = C_p(T) - C_{ph}(T)$ reveals $\Delta = 0.34(1)$ meV ($= 3.96 \text{ K}$). The ratio $\Delta(0)/k_B T_c \approx 1.72$ is in good agreement with the BCS value $\Delta_{\text{BCS}}(0) = 1.76 k_B T_c$. Results are displayed in Fig. 6.5a in a semi-logarithmic plot of the normalized electronic specific heat $C_{eS}/\gamma T_c$ versus T_c/T . C_{eS} vanishes almost exponentially at low temperatures. For comparison, the temperature dependence according to BCS theory with $\Delta_{\text{BCS}}(0)/k_B T_c = 1.76$ is included as dashed line. The application of a magnetic field suppresses T_c with

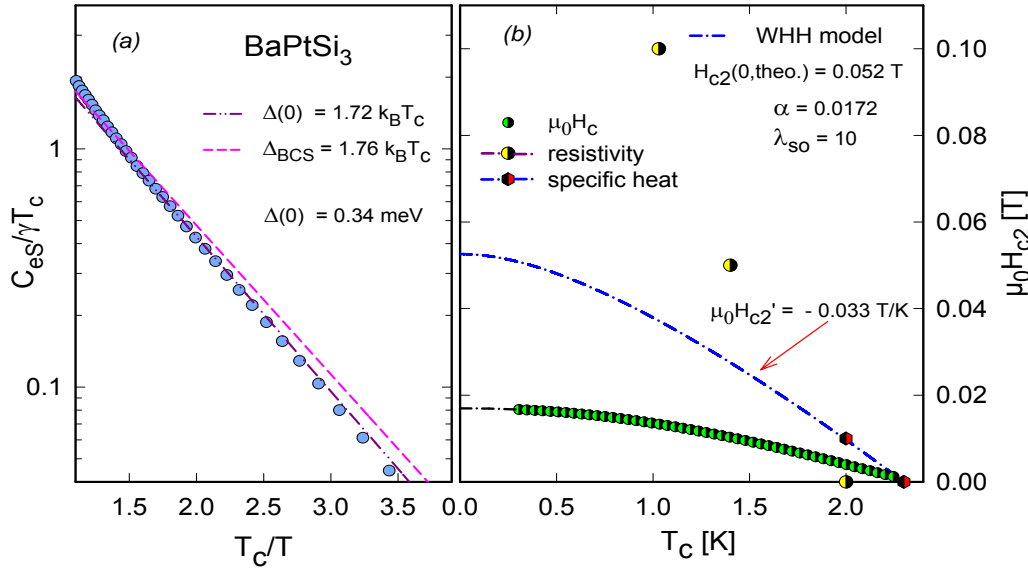


Figure 6.5: (a) The normalized electronic specific heat C_{es} of BaPtSi_3 plotted as semi-logarithmic $C_{es}/\gamma T_c$ as a function of the inverse reduced temperature T_c/T . The exponential temperature dependence according to BCS (with $\Delta_{BCS}(0)/k_B T_c = 1.76$ and 1.72), are shown by dashed-dotted lines, respectively. (b) Temperature dependent upper critical field of BaPtSi_3 as deduced from resistivity measurements. The initial slope of $\mu_0 H_{c2}(T)$ is about -0.03 T/K . The dashed-dotted line corresponds to $\mu_0 H_{c2}$ derived in terms of the model of Werthamer et al.[165], revealing $\mu_0 H'_{c2} = -0.033 \text{ T/K}$.

an initial slope of about $\partial(\mu_0 H_{c2})/\partial T \equiv \mu_0 H'_{c2} = -0.033 \text{ T/K}$ from specific heat data, extrapolating to an upper critical field at $T = 0$ well below 0.1 T . The strong upturn of experimental H_{c2} data from resistivity measurement refers to some deviation from standard WHH-type behaviour of the upper critical field. The initial slope of the upper critical field $\mu_0 H'_{c2} \approx -0.1 \text{ T/K}$, yielding slightly larger values deduced from resistivity data than those from specific heat, which may be attributed to pinning and surface effects. An estimation of $\mu_0 H_{c2}(0)$ using the WHH-model yields $\mu_0 H_{c2}(0) = 0.69 T_c H'_{c2}(T_c) = 0.052 \text{ T}$, a value significantly smaller than that obtained from resistivity data (0.144 T). To explain this, the behaviour near the surfaces must be considered, since real superconductors are finite in size [96]. De Gennes and Saint-James [195] showed that superconductivity can nucleate at an interface in a parallel field H_{c3} , larger by a factor of 2.77 than H_{c2} , yielding $H_{c3} = 0.144 \text{ T}$. In case of BaPtSi_3 our conclusion is that in a magnetic field parallel to the surface, superconductivity will nucleate in a surface layer of sample at a field more as double higher than at which nucleation occurs in the volume of the material.

property	BaPtSi ₃	BaPt ₅ Si ₁₂
crystal structure	tetragonal	
space group	<i>I4mm</i>	
lattice parameter a @300 K [nm]	$a = 0.44080(3)$	
	$c = 1.0022(4)$	
T_c [K]	2.3	
γ [mJ/molK ²]	5.7	8.1(1)
θ_D [K]	370	305
$\Delta C_p(T = T_c)$	15.7	
$\Delta C_p/\gamma_n T_c$	1.2	
$\mu_0 H_{c2}$ [mT]	52	
$\mu_0 H_c(0)$ [mT]	16.7	
$\mu_0 H_c(0)_{calc.}$ [mT]	17.5	
BCS: $\Delta(0)$ [meV]	0.34	
upper critical field $\mu_0 H_{c2}(0)$ [mT]	52	
slope of $\mu_0 H_{c2}$, $\mu_0 H'_{c2}$ [T/K]	-0.033	
$\mu_0 H'_{c2}(calc.)$ [T/K] (clean)	-0.055	
(dirty)	-0.052	
thermod. critical field $\mu_0 H_c$ [mT]	16.7	
λ_{ep}	0.5	
α	0.0172	
λ_{so}	10	
θ_D [K]	370	305
ω_{E1} [K]	43.4	50.2
$\Delta\omega_{E1}$ [K]	5.3	12.1
ω_{E2} [K]	123.3	108.2
$\Delta\omega_{E2}$ [K]	37.7	24.8

Table 6.2: The characteristic parameters of BaPtSi₃ in the superconducting and normal state and BaPt₅Si₁₂.

Fig. 6.5b displays the temperature dependent upper critical field $\mu_0 H_{c2}$ of BaPtSi₃ as deduced from both resistivity and specific heat data $C_p(T, H)$ and the thermodynamic critical field. An extrapolation $T \rightarrow 0$ reveals $\mu_0 H_c(0) \approx 16.7$ mT, close to theoretical value of the thermodynamic critical field, which follows from $\gamma T_c^2 = 0.168 \mu_0 H_c^2$, thus $\mu_0 H_c(0, theor) = 17.5$ mT. The upper critical field can be estimated with the WHH-model [165] (see appendix A.3.1), $\mu_0 H_{c2}(0) = 0.69 \mu_0 T_c H'_{c2}|_{T_c} \approx 0.052$ T (dashed-dotted line in Fig. 6.5b). Two parameters determine the WHH-model [165], the Pauli paramagnetic $\alpha = (3e^2 \hbar \gamma \rho_0) / (2m\pi^2 k_B^2) = 0.0172$ as well as the spin-orbit scattering $\lambda_{so} \approx 10$. A similar value of α follows from $\alpha = 5.3 \cdot 10^{-1} \left(\frac{-dH_{c2}(T)}{dT} \right) |_{T=T_c}$

parameter	0.1 T	0.05 T	0.02 T
$\mu_0 H'_c(\text{calc.})$ [T/K]	-0.011	-0.016	-0.025
effective Fermi surface S_s [m^{-2}]	2.17×10^{20}	2.17×10^{20}	2.17×10^{20}
Fermi velocity v_F [m/s]	95935	135732	214611
mean free path l_{tr} [nm]	87	87	87
mean free path l_{tr} [nm] ([116])	95	95	95
coherence length ξ_0 [nm] (BCS Eq.)	57	81	128
coherence length ξ_0 [nm]	57	81	128
penetration depth $\lambda_L(T \rightarrow 0)$ [nm]	243	172	109
G.L. parameter κ_{GL}	4.04	2.02	0.81
κ (from Eqn.1.53)	4.24	2.12	0.84
l_{tr}/ξ_0	1.5	1.07	0.7
SC in the	dirty limit	dirty limit	dirty limit

Table 6.3: Comparison of the determined parameters characterizing the superconducting and normal state of BaPtSi₃ for upper critical field $\mu_0 H_{c2}(0) = 0.02, 0.05$ and 0.1 T.

= 0.0174. Here $\mu_0 H'_{c2}$ given in T/K. Results of this model are displayed in Fig. 6.5b as dashed-dotted line. Orbital pair breaking is the most relevant mechanism in the low field limit and therefore determines $\mu_0 H'_{c2}$. The Maki parameter $\alpha = 0.0172$ of BaPtSi₃ corresponds with a dominating orbital pair breaking, almost excluding Pauli limiting. In the framework of BCS superconductivity, we estimate in the following section a number of parameters from an analysis of superconducting and normal state properties [111] assuming a spherical Fermi surface and incorporating clean and dirty limit terms.

Starting parameters are $\gamma = 0.0057(1)$ J/molK², the slope of the upper critical field $\mu_0 H'_{c2} = -0.033$ T/K and $\rho_0 = 6 \mu\Omega\text{cm}$. The effective Fermi surface area S_s as shown by Orlando et al.[111] yields $S_s = 1.169 \times 10^{20}$ [m^{-2}] in the clean case. The mean free path l_{tr} was obtained from two independent relations. Combining the Fermi surface with Sommerfeld value γ yields the Fermi velocity $v_F \approx 95935$ m/s and in the context of the residual resistivity, $\rho_0 = 6 \mu\Omega\text{cm}$, a mean free path $l_{tr} \approx 95$ nm can be derived. A second expression originates from the well known formula [197] $\rho = \frac{3\pi^2\hbar}{e^2 k_F^2 l_{tr}}$, assuming a three-dimensional system with a spherical Fermi surface [198, 199]. This results in $l_{tr} = 87$ nm, which is slightly smaller than the mean free path computed from the model of Ref.[116]. Here, we used the conversion $\hbar a_0/e^2 = 0.022$ mΩcm and the Bohr radius $a_0 = 0.529$ Å, the Fermi wave vector $k_F = \sqrt{2\pi}/a'$, where $a' = a\sqrt[3]{2}$ is the lattice parameter in the cubic unit cell.

The low temperature extrapolations of the thermodynamic critical field $H_c(T)$ and the upper critical field $\mu_0 H_{c2}(0)$ allows evaluation of the Ginzburg Landau parameter $\kappa_{GL}(0) \equiv \lambda_{GL}(0)/\xi_{GL}(0) = H_{c2}/[\sqrt{2}H_c(0)]$. Starting with

$H_{c2}(0)=0.1$ T reveals the ratio of the penetration depth $\lambda_{GL}(0)$ to the coherence length $\xi_{GL}(0)$, $\kappa_{GL}(0) = 4.24$. The absolute value of the penetration depth $\lambda(0)$ can be evaluated via the isotropic Ginzburg-Landau-Abrikosov-Gor'kov theory (Eqn. 1.52), resulting $\lambda_{GL}(0) \approx 243$ nm. The coherence length ξ_0 for $T \rightarrow 0$ was obtained from the BCS equation (Eqn.1.57), $\xi_0=57$ nm, and from the well known formula $\mu_0 H_{c2} = \Phi_0/(2\pi\mu_0\xi^2) \approx 57$ nm, respectively, in excellent agreement with the former.

Results of evaluations for $H_{c2}(0)=0.05$ T, 0.02 T are given in Table 6.5 and are compared with the upper critical field $H_{c2}(0)=0.1$ T.

The parameters κ , $\xi(0)$ and $\lambda_L(0)$, evaluated from the upper and the thermodynamic critical field, excellently agree with model calculations based on the free electron model. $l_{tr}/\xi \approx 1$ allows to classify BaPtSi₃ as a dirty limit superconductor, while $\kappa \approx 4.27$ indicates a type II superconducting behaviour.

Chapter 7

Structure and Physical Properties of $M_2Pd_{14+x}B_{5-y}$, M= Th, Ce, Pr, Nd, Sm, Eu, Gd

7.1 Introduction

Our search for novel compounds also focused on a yet unknown series of borides, i.e. $M_2Pd_{14+x}B_{5-y}$ (M= Th, Ce, Pr, Nd, Sm, Eu, Gd). In the course of the present study, it turned out that besides the well known perovskite phases REPD₃B_{1-x} [204, 205] (RE is one of the light rare earth elements) novel and hitherto unknown compounds were found to exist near the composition REPd₇B_{2.5} for all light rare earth elements from La to Gd. Furthermore the investigation was extended to include the actinoid elements Th and U. The present study characterizes the crystal structure, thermodynamic, electric and magnetic behaviour and elucidate ground states and phase transitions appearing in this series.

7.2 Crystal structures of $\{Nd, Th\}_2Pd_{14.9}B_{4.9}$.

Crystal structure of Nd₂Pd_{14.9}B_{4.9}. Systematic extinctions, besides those for a body-centered unit cell, (hk0) for $h=2n+1$ and $k=2n+1$, (hkl) for $2h+l=4n+1$, (00l) for $l=4n+1$, are compatible with the highest possible symmetry for the tetragonal space group type $I4_1/AMD$. Determination of the atom arrangement in this space group type (origin at center) was successful employing direct methods prompting one Nd- and four Pd-sites in the asymmetric unit. Two boron sites were located from a difference Fourier synthesis. This structure model refined to a residual value $R_{F^2} = 0.12$

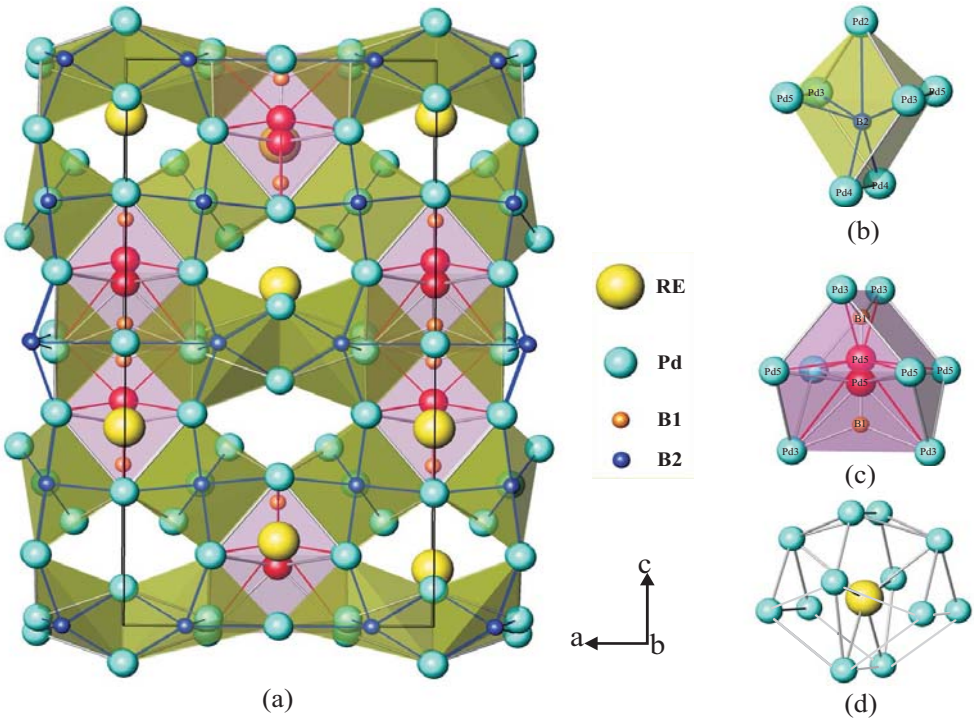


Figure 7.1: Crystal structure of $Nd_2Pd_{14}B_5$ in a three-dimensional view along the [010]-axis

adopting anisotropic thermal displacement factors for the metal atoms but isotropic temperature factors for the borons, resulting in the chemical formula $Nd_2Pd_{14}B_5$. Standardization of the structure model with program Structure Tidy [152] revealed at this stage identity with the structure type of $Y_2Pd_{14}B_5$ [206]. Due to the rather high residual densities of $85\text{ e}^-/\text{\AA}^3$ left in $(0, \frac{1}{4}, 0.3989)$, the refinement at that stage was highly unsatisfactory. Therefore firstly occupancies of all metal sites were refined but did not reveal any significant deviations from full occupation. Inserting an additional Pd-atom (Pd5) into the site $(0, \frac{1}{4}, 0.3989)$ reduced the residual density as well as the residual value to $R_{F^2} = 0.12$, however, at the expense of unacceptably high $ATD's$ for Pd5 and unacceptably short distances among Pd5-atoms and between Pd5- and B2-atoms in the 4b-site $(0, \frac{1}{4}, \frac{3}{8})$ ($d_{B2-Pd5} = 0.0438\text{ nm}$, $d_{Pd5-Pd5} = 0.0875\text{ nm}$). Furthermore the residual density of $24\text{ e}^-/\text{\AA}^3$ shifted to $(0, \frac{1}{4}, 0.4680)$. Relieving the occupancy of Pd5 to 45% and compensating the residual peak at $(0, \frac{1}{4}, 0.4680)$ by releasing the constraint on z_{B2} for the B2-atoms at an occupancy of $\sim 42\%$, finally rendered normal $ATD's$ for all atoms and reduced the total residual density below $2\text{ e}^-/\text{\AA}^3$. As both the Pd5 as well as the B2 site, however, are only partially occupied (about 50% occu-

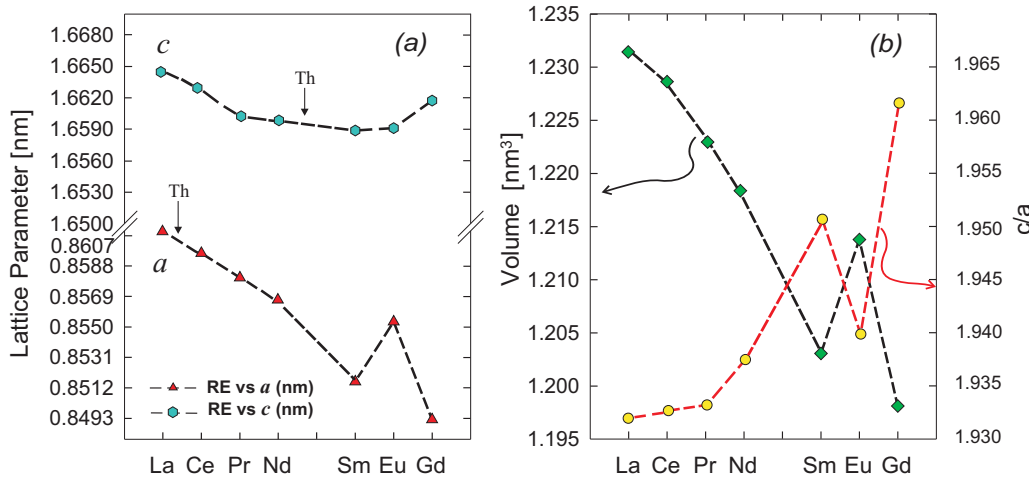


Figure 7.2: (a) Lattice parameters variation vs. light rare earth; (b) volume and c/a ratio of $M_2 Pd_{14} B_5$

pancy in each site), a complicated defect structure arises in which only one Wyckoff position (either Pd5 or B2) per unit cell is half filled. It should be emphasized here, that neither Pd5-atoms nor B2-atoms with z fixed at $(0, \frac{1}{4}, \frac{3}{8})$ supply a satisfying solution ($R_{F^2} \sim 0.050$; residual densities $\geq 10e^-/\text{\AA}^3$). It shall be noted that the final structure in all its details is closely related to the $Sc_4 Ni_{29} Si_{10}$ -type [207].

Results of the structure determination show a final R-value as low as 0.02, thus confirm the structure model. The chemical formula turns out to be $Nd_2 Pd_{14.9} B_{4.9}$. The crystal structure is presented in Fig. 7.1a in a three-dimensional view along the [010]-axis. As one of the typical structural units for metal rich borides, B1-atoms are found in deformed *Archimedian antiprisms* capped on one side by an additional Pd-atom (Pd5-atoms) (Fig. 7.1c) whereas B2-atoms (defect site) are in a coordination unit formed by two trigonal prisms face-connected on a common quadratic base and formed by seven palladium atoms Fig. 7.1b. Each rare earth atom is surrounded by 6 palladium atoms and 6 neighboring palladium atoms at a larger distance of 0.30326 nm (Fig. 7.1d). Interatomic distances generally agree well with the metallic radii of pure elements.

Crystal structure of $Th_2 Pd_{15} B_5$. Determination of the crystal structure of $Th_2 Pd_{15} B_5$ revealed essentially the same atom arrangement as found for $Nd_2 Pd_{14.9} B_{4.9}$. Small differences concern Pd5 atoms which for the Th-compound occupy the 4d position with a slight defect. Results of the structure determination show a final R-value as low as 0.026, thus confirm the structure model. Whilst no indications were found for formation of an isostructural compound $U_2 Pd_{14} B_5$, X-ray intensities and unit cell dimensions of the

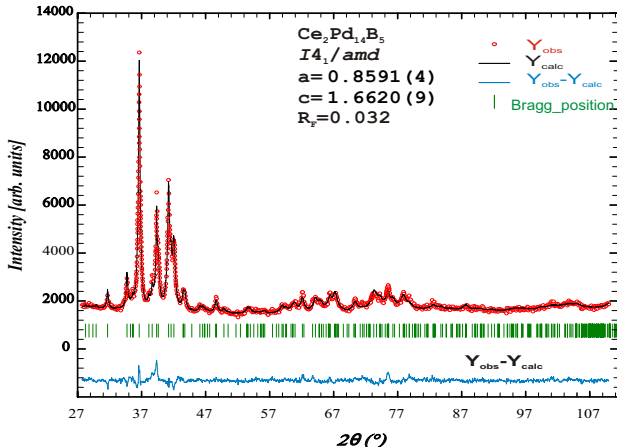


Figure 7.3: X-ray diffraction pattern of $Ce_2Pd_{14}B_5$. The solid line derives from the Rietveld refinement. $Y_{obs}-Y_{calc}$ is the intensity difference between experimental data and Rietveld calculations.

thorium analog compare well with the $Nd_2Pd_{14.9}B_{4.9}$ structure implying structural analogy and suggesting similar size of Nd and Th atoms. The measured composition (from EMPA, in at.%), $Th_{9.3}Pd_{68.1}B_{22.5}$, is fully consistent with the formula $Th_2Pd_{14.9}B_{4.9}$ (in at.% $Th_{9.2}Pd_{68.3}B_{22.5}$). Crystallographic results of $Nd_2Pd_{15}B_5$ and $Th_2Pd_{15}B_5$ are collected in Table 7.1.

7.3 Isotypic compounds $M_2Pd_{14}B_5$

Indexing of the X-ray powder patterns of $M_2Pd_{14}B_5$ alloys for $M = Ce, Pr, Nd, Sm, Eu, Gd$ in all cases was complete and prompted a tetragonal unit cell close to that established for $Nd_2Pd_{14.9}B_{4.9}$. Analysis of the X-ray intensities, systematic extinctions, and size of unit cells suggest isotypism with the structure of $Nd_2Pd_{14.9}B_{4.9}$ ($Sc_4Ni_{29}B_{10}$ -type). Rietveld refinements with residual values generally below $R_F=0.07$ confirmed this isotypism. A small but significant scatter in the lattice parameters (Fig. 7.2a) may indicate the existence of limited homogeneity regions. In Fig. 7.2b, volume vs. rare earth, indicates a 3+ ground state for Ce to Sm. The monotonic decrease of both a and c parameters with rising ordinal number of the rare earths complies with a shrinking unit cell volume i.e the lanthanide contraction. The minor increase of the c/a ratio throughout the stability range of the $Nd_2Pd_{14.9}B_{4.9}$ structure type yields only a small increase of the lattice anisotropy. Different from the light rare earth analogs, the Eu-containing compound exhibits a strong positive deviation from the unit cell volume variation vs. the rare earths i.e. a valance state close to divalent. Typical final observed, calcu-

Parameter / compound	$Nd_2Pd_{14}B_5$	$Th_2Pd_{14}B_5$
Crystal size	$27 \times 54 \times 41 \mu m^3$	$50 \times 54 \times 90 \mu m^3$
$a; c$ [nm]	$a=0.85776(3); c=1.66278(4)$	$a=0.86102(2); c=1.66019(5)$
Data collection $MoK\alpha$, 2Θ range ($^\circ$)	$2 \leq 2\Theta \leq 72.6$	$2 \leq 2\Theta \leq 72.6$
Total number of frames	70 sec/frame; 242 frames; 7 sets	50 sec/frame; 222 frames; 7 sets
Reflections in refinement	$793 \geq 4\sigma(F_o)$ of 823	$763 \geq 4\sigma(F_o)$ of 827
Number of variables	40	38
$R_{F^2} = \Sigma F_o^2 - F_c^2 / \Sigma F_o^2 $	0.020	0.026
$wR2$	0.058	0.062
R_{int}	0.062	0.069
GOF	1.227	1.081
Secondary extinction (Zachariasen)	0.00043(1)	0.00026(2)
Atom parameters		
Nd or Th in 8e ($0, \frac{1}{4}, z$); z	0.10022(3)	0.09804(2)
occ.	1.0	1.0
$U_{11}, U_{22}, U_{33} [10^2 (nm)^2]$	0.0110(2), 0.0099(1), 0.062(2)	0.0128(2), 0.0099(1), 0.066(2)
Pd1 in 8d ($0, 0, \frac{1}{2}$)	-	-
occ.	1.0	1.0
$U_{11}, U_{22}, U_{33} [10^2 (nm)^2]$	0.0160(2), 0.0131(1), 0.107(2)	0.0168(3), 0.0149(3), 0.0130(3)
Pd2 in 16h ($0, y, z$); y, z	0.02537(5); 0.23640(3)	0.02978(7); 0.23706(3)
occ.	1.0	1.0
$U_{11}, U_{22}, U_{33} [10^2 (nm)^2]$	0.0139(2), 0.0086(2), 0.0084(2)	0.0203(2), 0.0104(2), 0.0093(2)
Pd3 in 16h ($0, y, z$); y, z	0.58884(5); 0.06585(2)	0.58831(6); 0.06605(3)
occ.	1.0	1.0
$U_{11}, U_{22}, U_{33} [10^2 (nm)^2]$	0.0098(2), 0.0078(2), 0.0053(2)	0.0148(2), 0.0094(2), 0.0064(2)
Pd4 in 16g ($x, x + \frac{1}{4}, \frac{7}{8}; x$)	0.28179(4)	0.28409(5)
occ.	1.0	1.0
$U_{11}, U_{22}, U_{33} [10^2 (nm)^2]$	0.0130(2), 0.0119(2), 0.0096(3)	0.0221(2), 0.0135(2), 0.0110(3)
Pd5 in 8e ($0, \frac{1}{4}, z$); z	0.35465(9)	Pd5 in 4b ($0, \frac{1}{4}, \frac{3}{8}$)
occ.	0.45(1)	0.830(4)
$U_{iso} [10^2 (nm)^2]$	0.0146(4)	0.036(2)
B1 in 8e ($0, \frac{1}{4}, z$); z	0.2827(15)	0.2851(35)
occ.	0.43(1)	0.170(4)
$U_{iso} [10^2 (nm)^2]$	0.017(6)	0.006(6)
B2 in 16f ($x, 0, 0$); x	0.1992(7)	0.2009(11)
occ.	1.0	1.0
$U_{iso} [10^2 (nm)^2]$	0.011(1)	0.016(1)
Residual density in $e^-/\text{\AA}^3$; max; min	1.78; -2.10	4.12; -4.14

Table 7.1: X-Ray Single Crystal Data for $Nd_2Pd_{14.9}B_{4.9}$, and $Th_2Pd_{14.9}B_{4.9}$; (structure type related to $Sc_4Pd_{29}B_{10}$ -type, Space Group $I4_1/amd$; No. 141) standardized with program Structure Tidy [152], standard deviations generally < 0.0005 nm.

lated, and difference X-ray powder diffraction patterns for the $Ce_2Pd_{14}B_5$ is shown in Fig. 7.3. A full profile Rietveld refinement performed on powder x-ray diffraction data of all alloys, however, cannot differentiate between the two slightly different atom arrangements in the Nd and Th cases. Therefore for all RE-homologs the structure model of $Nd_2Pd_{14.9}B_{4.9}$ was applied. The only minor differences between the observed ($Y_{obs.}$) and the calculated intensity ($Y_{calc.}$) confirm the structure as well as the sample quality (see Fig. 7.3). Attempts to synthesize the corresponding La-containing compound in single phase condition failed, particularly due to the rather small temperature window of existence for this compound. Inspection by EMPA of an as-cast sam-

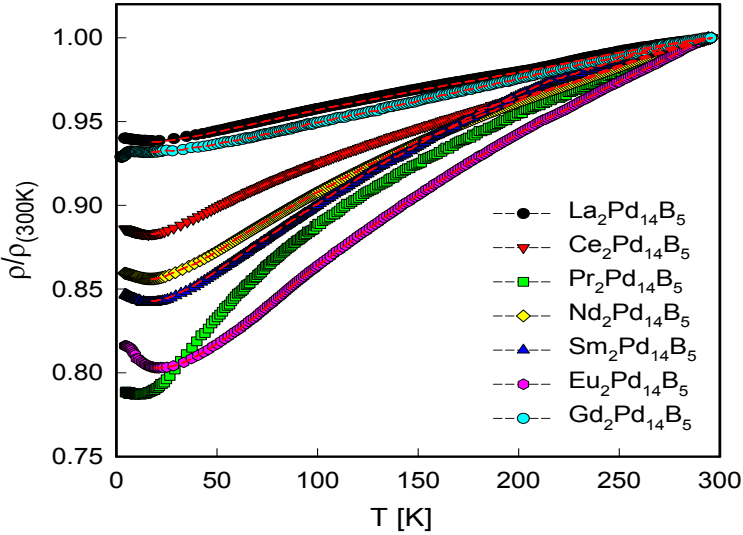


Figure 7.4: Temperature dependent electrical resistivity of $M_2Pd_{14}B_5$ as ρ in a normalized representation.

ple with nominal composition $La_2Pd_{14.9}B_{4.9}$ revealed a two-phase structure, which from Rietveld refinements confirmed the minor phase $La_2Pd_{14.9}B_{4.9}$ to comply with the tetragonal structure model of $Nd_2Pd_{14.9}B_{4.9}$ at a residual value of $R_F = 0.037$. On annealing, however, the tetragonal phase disappears, yielding a single main phase (also seen in cast condition), which was indexed with a monoclinic X-ray powder spectrum. The detailed elucidation of the latter structure, $La_3Pd_{25-x}B_{8-y}$ ($x=1.75$, $y=0.07$; space group $P2_1/c$ with $a = 1.17567(2)$ nm, $b = 1.05757(2)$ nm, $c = 1.60664(3)$ nm, $\beta = 102.1788(10)$ deg, $R_{F^2} = 0.03$), is the subject of discussion in Ref. [208]. In lack of the La-compound and in order to isolate the magnetic part of the physical properties we used as an isotypic nonmagnetic analog the newly discovered $Lu_2Pd_{14+x}B_{5-y}$ (with the structure type of $Nd_2Pd_{14.9}B_{4.9}$) [209].

7.4 Electrical resistivity

Physical properties of ternary $M_2Pd_{14+x}B_{5-y}$, $M=(Th, La, Ce, Pr, Nd, Sm, Eu, Gd)$, were investigated by means of temperature dependent resistivity, susceptibility and heat capacity measurements. The electrical resistivity, ρ , of $M_2Pd_{14+x}B_{5-y}$, in general, is characterized by small RRR values originated by defects inherent to the crystal structure. The temperature dependent electrical resistivity $\rho(T)$ of $M_2Pd_{14}B_5$ is shown in Fig. 7.4 in a normalized representation for temperatures above 4.2 K. Low temperature $\rho(T)$ data of the

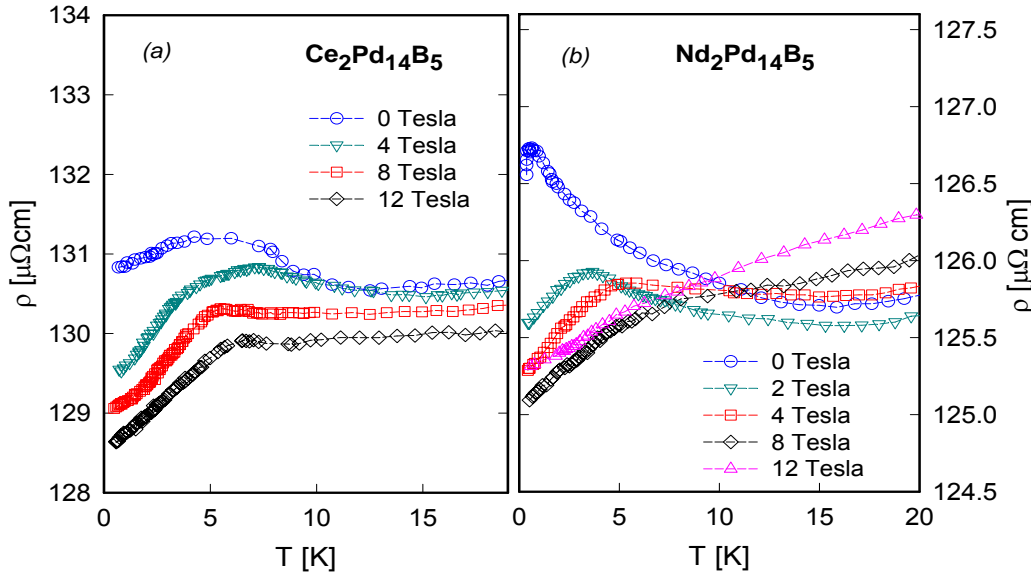


Figure 7.5: Temperature dependent electrical resistivity ρ of (a) $\text{Ce}_2\text{Pd}_{14}\text{B}_5$, (b) $\text{Nd}_2\text{Pd}_{14}\text{B}_5$ at various applied magnetic fields up to 12 T.

compounds based on Ce, Nd, Sm, Eu and Gd exhibit a minimum in the vicinity of 20 K followed by an increase towards lower temperatures. Although a nonmagnetic origin like variable range hopping is conceivable due to statistical disorder of atoms within the crystal structure, a magnetic source is more likely, since magnetic fields of the order of several Tesla completely suppress the anomalies indicated above. This behaviour is shown in figures 7.4, 7.5 and 7.6. Note that ρ decreases monotonically with temperature without any other feature down to about 17 K. This establishes that all these compounds behave similar to simple metals. Low temperature $\rho(T)$ data of the compounds based on Ce, Nd, Sm and Eu exhibit a minimum in the vicinity of 10 K followed by increase towards lower temperatures. Such minimum has been seen in many antiferromagnetic metals [210]. The room temperature resistivities are 197, 66, 147, 120, 142 and 136 $\mu\Omega\text{ cm}$ for the Ce, Pr, Nd, Sm, Eu, Gd-based samples, respectively.

The temperature dependent electrical resistivity for various values of external magnetic fields up to 12 T is displayed in Figs. 7.5 - 7.6. As is shown in Fig. 7.5a the resistivity of $\text{Ce}_2\text{Pd}_{14}\text{B}_5$ decreases up to 10 K and rises again with decreasing temperature. It should be noted that this feature is similarly observed for $\text{Nd}_2\text{Pd}_{14}\text{B}_5$ (Fig. 7.5b).

The temperature dependent electrical resistivity of $\text{Sm}_2\text{Pd}_{14}\text{B}_5$ in external magnetic fields up to 12 T is shown in inset of Fig. 7.6a. For temperature below 10 K the resistivity firstly decreases with fields, but above 8 T the

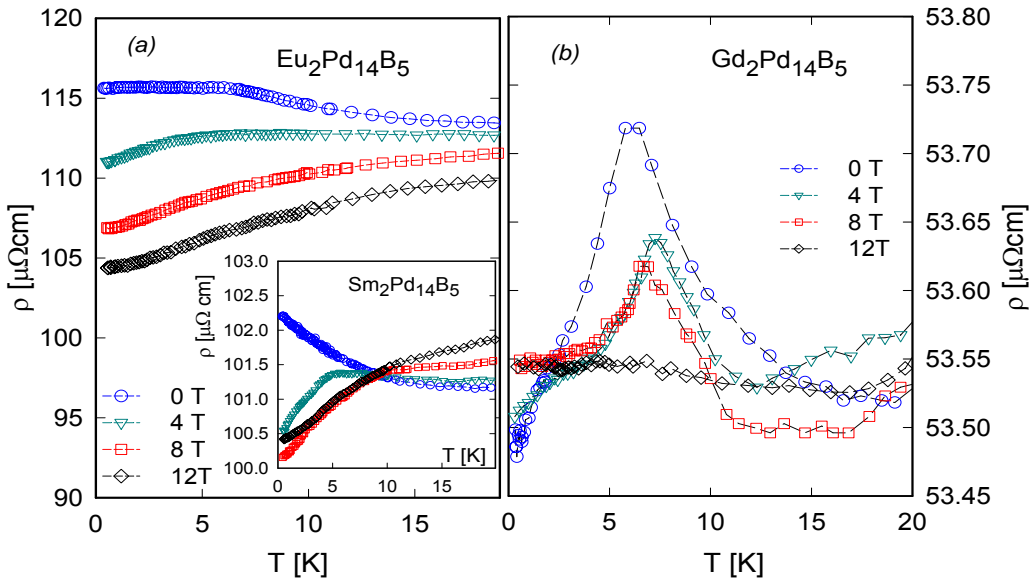


Figure 7.6: Temperature dependent electrical resistivity ρ of (a) $\text{Eu}_2\text{Pd}_{14}\text{B}_5$ Inset: Electrical resistivity $\rho(T)$ of $\text{Sm}_2\text{Pd}_{14}\text{B}_5$. (b) $\text{Gd}_2\text{Pd}_{14}\text{B}_5$ at various applied magnetic fields up to 12 T.

trend is inverted yielding higher resistivity value for 12 T at about 0.5 K. The temperature dependent electrical resistivity of $\text{Eu}_2\text{Pd}_{14}\text{B}_5$ in external magnetic fields up to 12 T is shown in Fig. 7.6a. The application of external fields is responsible for the suppression of the minimum. In case of $\text{Eu}_2\text{Pd}_{14}\text{B}_5$ magnetic order appears at about 6 K, but is suppressed by magnetic fields above 12 T.

$\text{Gd}_2\text{Pd}_{14}\text{B}_5$ exhibits a negative slope of $\rho(T)$ below about 15 K, and a maximum at 6 K (see Fig. 7.6b). A rapid decrease of the resistivity below that maximum results from the onset of long range magnetic order, in fine agreement with magnetisation and heat capacity results (see below). The application of external fields causes an overall decrease of the electrical resistivity as well as a shift of the resistivity anomaly to higher temperatures.

7.5 Magnetoresistance

The magnetoresistance $\rho(B)/\rho(0)$ of $\text{Pr}_2\text{Pd}_{14}\text{B}_5$ and $\text{Nd}_2\text{Pd}_{14}\text{B}_5$ as function of external magnetic fields up to 12 T for various temperatures between 0.5 K and 25 K is shown in Fig. 7.7. $\rho(B)/\rho(0)$ of $\text{Pr}_2\text{Pd}_{14}\text{B}_5$ exhibits a negative magnetoresistance between 0.5 K and 25 K for fields from 4 T up to 12 T (compare inset of Fig. 7.7a). The temperature dependent electrical resistivity for various of external magnetic fields up to 12 T is displayed in the

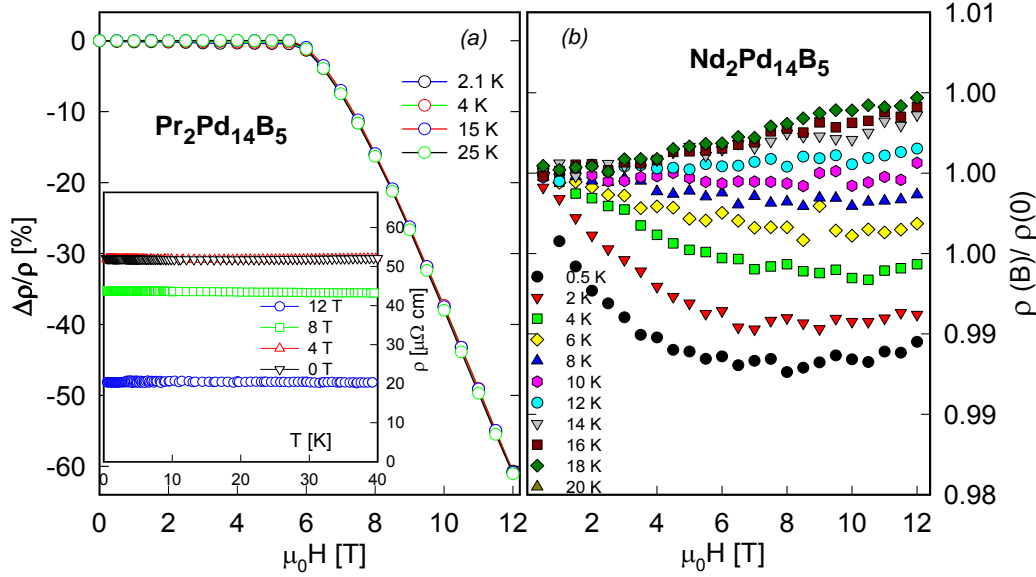


Figure 7.7: (a) Isothermal magnetoresistance $\Delta\rho/\rho$ of $\text{Pr}_2\text{Pd}_{14}\text{B}_5$. The inset shows the field dependence of $\rho(T)$. (b) reduced isothermal resistivities $\rho(B)/\rho(0)$ of $\text{Nd}_2\text{Pd}_{14}\text{B}_5$.

inset of Fig. 7.7a. In case of $\text{Nd}_2\text{Pd}_{14}\text{B}_5$, $\rho(B)/\rho(0)$ is mainly negative for temperatures below 8 K and for all fields up to 12 T, but above about 12 K $\rho(B)/\rho(0)$ is positive for all fields up to 12 T (see Fig. 7.7b).

The magnetoresistance $\rho(B)/\rho(0)$ of $\text{Sm}_2\text{Pd}_{14}\text{B}_5$ and $\text{Eu}_2\text{Pd}_{14}\text{B}_5$ are plotted in Fig. 7.8 as functions of the magnetic field $\mu_0 H$. $\text{Sm}_2\text{Pd}_{14}\text{B}_5$ (Fig. 7.8a) shows a negative magnetoresistance below 8 K, but changes sign above 8 K for fields up to 12 T. Figure 7.8b display the magnetoresistance $\rho(B)/\rho(0)$ of $\text{Eu}_2\text{Pd}_{14}\text{B}_5$. A negative magnetoresistance is found between 2 K and 25 K for all fields up to 12 T; its magnitude decreases with increasing temperature. Such a behaviour is reminiscent of a single impurity Kondo system.

7.6 Specific heat

The experimental specific heat data for $M_2\text{Pd}_{14}\text{B}_5$ are summarised in Figs. 7.9 and 7.10, where the measured heat capacities C_p are plotted up to 140 K. $\text{Lu}_2\text{Pd}_{14}\text{B}_5$ is used as reference compound. The solid line in inset of Fig. 7.10a denotes the results of a least-squares fit to the experimental data below 5 K, according to $C_p = \gamma T + \beta T^3$, yielding a Sommerfeld value $\gamma = 19 \text{ mJ/mol K}^2$ and $\beta = 0.00177 \text{ J/mol K}^4$ (inset in Fig. 7.10a), revealing $\theta_D^{LT} = 284 \text{ K}$.

A common procedure to approximate the overall heat capacity of metallic

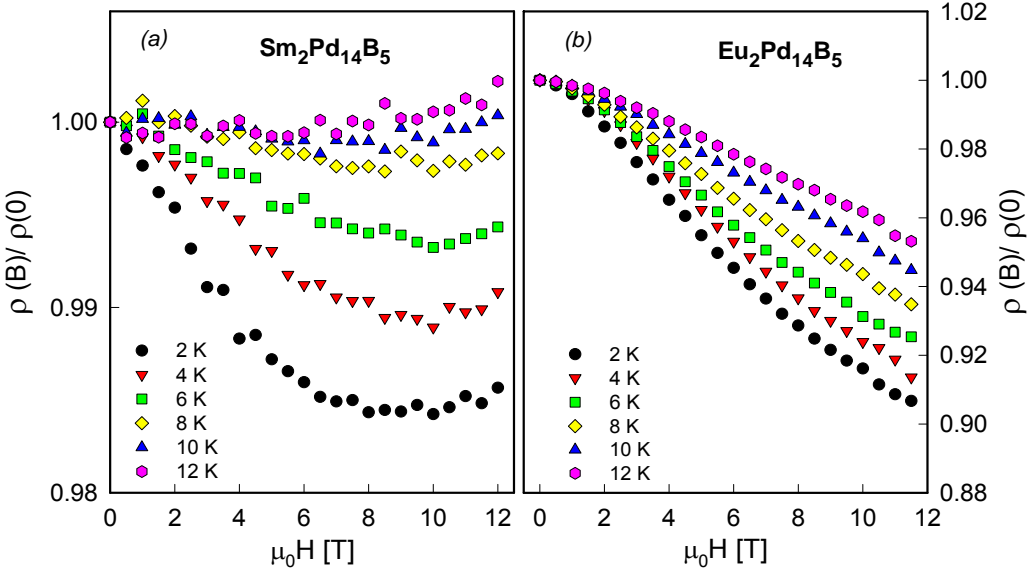


Figure 7.8: Isothermal magnetoresistance $\rho(B)/\rho(0)$ of (a) $Sm_2Pd_{14}B_5$, (b) $Eu_2Pd_{14}B_5$.

compounds usually assumes a Debye spectrum. In the present case, however, the simple Debye model did not yield convincing agreement with the experimental data, whereas adding three Einstein functions leads to accurate fitting results for the overall temperature range [93]. In order to explore the vibrational properties in more detail, we subtracted the electronic contribution from the specific heat and adopted a model consisting of a combination of one Debye- and three Einstein functions:

$$C_{ph}(T) = \frac{9R}{\omega_D^3} \int_0^{\omega_D} \frac{\omega^2 \left(\frac{\omega}{2T}\right)^2}{\sinh^2\left(\frac{\omega}{2T}\right)} d\omega + \sum_{i=1,2,3} c_i R \frac{\left(\frac{\theta_{Ei}}{2T}\right)^2}{\sinh^2\left(\frac{\theta_{Ei}}{2T}\right)}. \quad (7.1)$$

Here ω_D is the Debye temperature, $c_1 + c_2 + c_3 = 3n - 3$, the number of optical branches of the dispersion relation and θ_{Ei} are the respective Einstein temperatures. It should be noted that the Debye temperature ω_D according to Eqn. 7.1 is determined only by the acoustic modes, whereas θ_D^{LT} evaluated from low temperature specific heat data according to Eqn. 1.37 is some averaged value over acoustic and optical branches of the phonon dispersion, contributing in a particular manner to the low temperature specific heat. Considering 21 atoms per formula unit, the phonon dispersion relation of $\{Lu,Gd\}_2Pd_{14}B_5$ consists of 3 acoustic and 60 optical branches. The parameters c_i are then evaluated in the way that they weight the respective fractions of $\{Lu,Gd\}$, Pd and B to one formula unit. Thus $\sum c_i = 60$, since

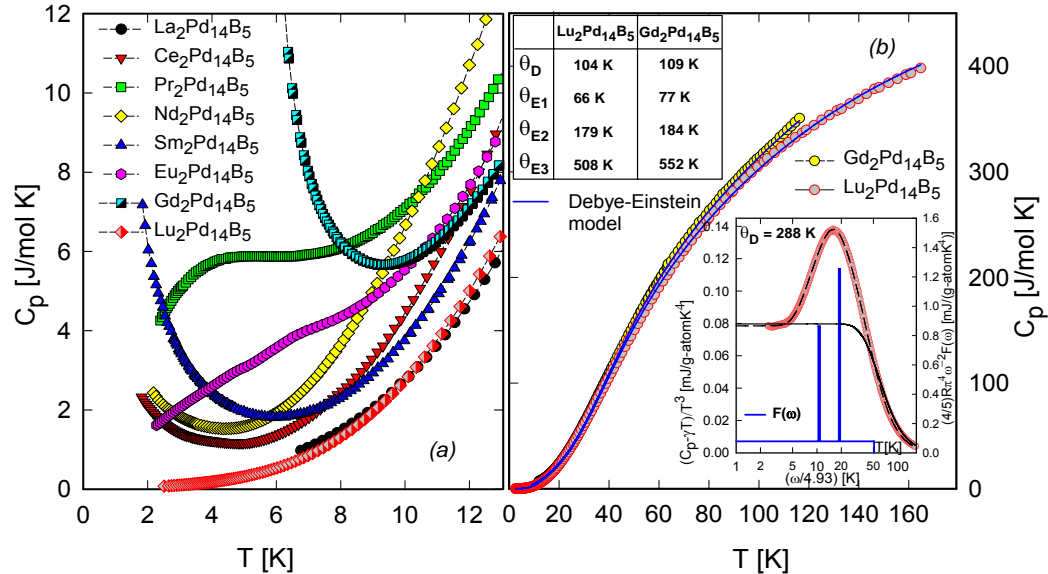


Figure 7.9: (a) Temperature dependent specific heat C_p of $\text{M}_2\text{Pd}_{14}\text{B}_5$ plotted as C_p vs. T . (b) Least-squares fit to C_p of $\text{Lu}_2\text{Pd}_{14}\text{B}_5$ and $\text{Gd}_2\text{Pd}_{14}\text{B}_5$ in terms of Eqn. 7.1. The solid line is a least squares fits of the experimental data using the model described in the text with three additional Einstein temperatures (Debye temperature $\theta_D = 107$ K for $\text{Lu}_2\text{Pd}_{14}\text{B}_5$ and $\theta_D = 109$ K for $\text{Gd}_2\text{Pd}_{14}\text{B}_5$.

the 3 acoustic modes are assumed to be accounted for by the Debye contribution. The first part of equation 7.1 represents the Debye contribution and the second part accounts for three additional Einstein temperatures with weights assumed to be $c_1 = 6$, $c_2 = 40$ and $c_3 = 14$. Using these weights (6:40:14 in accordance with the compositional ratio among {Lu,Gd}, Pd and B) for Einstein temperatures allows a reasonable parametrisation of the whole temperature range up to 150 K. Due to the presence of magnetic contribution in Gd compound phonon specific heat was cut off below 10 K. Only for the Lu compound phonon specific heat could be adjusted directly from 2 K, featuring no upturn originating from magnetic contributions. This procedure provides a satisfactory description of the temperature dependent specific heat data shown as solid lines in Fig. 7.9b. Least squares fit of the experimental data (solid line in Fig. 7.9b) for $\text{Lu}_2\text{Pd}_{14}\text{B}_5$ reveals excellent agreement with a Debye temperature $\theta_D = 107$ K, Einstein temperatures $\theta_{E1} = 66$ K, $\theta_{E2} = 178$ K and $\theta_{E3} = 507$ K. For $\text{Gd}_2\text{Pd}_{14}\text{B}_5$ a least squares fit of the experimental data reveals fine agreement with a Debye temperature $\theta_D = 109$ K and Einstein temperatures $\theta_{E1} = 77$ K, $\theta_{E2} = 184$ K and $\theta_{E3} = 552$ K (solid line in Fig. 7.9b). It should be noted that in order to compare the Debye

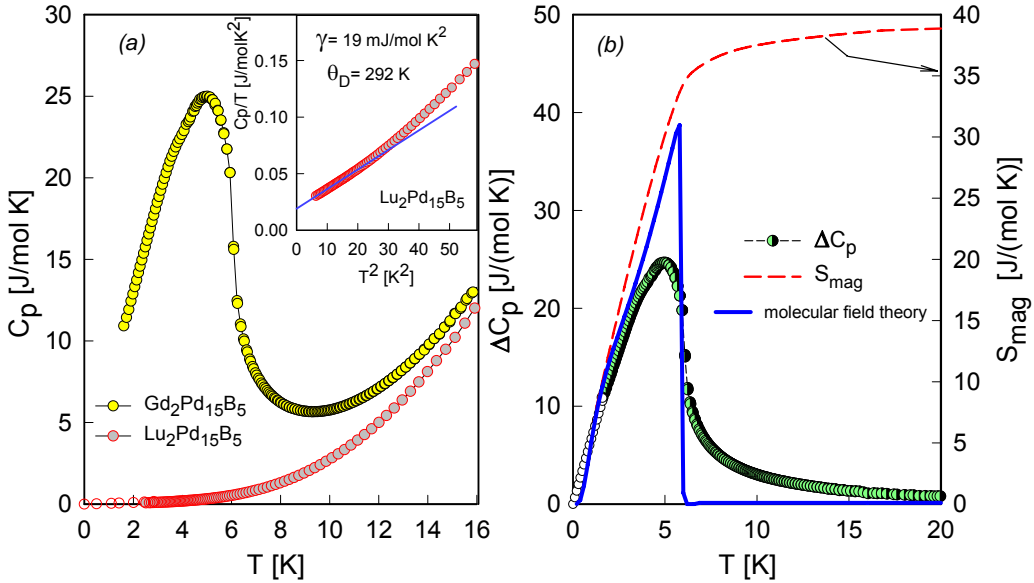


Figure 7.10: (a) Temperature dependent specific heat C_p of $Lu_2Pd_{14}B_5$ (the unfilled symbols represent an extrapolation to zero) and $Gd_2Pd_{14}B_5$ plotted as C_p vs. T . The inset shows the low temperature specific heat of $Lu_2Pd_{14}B_5$ plotted as C_p/T vs. T^2 . The solid line represents a fit according to the expression $C_p/T = \gamma + \beta T^2$ (see text).(b) Magnetic contribution for the specific heat $C_{mag}(T)$ of $Gd_2Pd_{14}B_5$ plotted as C_{mag} vs. T (filled circles) . The solid line denotes ΔC_{mag} in terms of the molecular field theory and the dashed line represents the magnetic entropy S_{mag} (right axis).

temperature from fit by Eqn. 7.1 with low temperature θ_D^{LT} , the former has to be multiplied with the factor $\sqrt[3]{n} = 2.75$, where n (the number of atoms per formula unit) is 21 in this case. This result is comparable with results derived from the model of Junod et. al. [91, 92] in case of $Lu_2Pd_{14}B_5$ ($\theta_D=288$ K, $\omega_{EL1} = 52.5$ K, width: 2.3 K, $\omega_{EL2} = 94$ K, width: 3.6 K). The low lying phonon branches are in good agreement with each other. The reconstruction of the phonon density of states of $Lu_2Pd_{14}B_5$ is shown in inset of Fig. 7.9b.

The difference in the total heat capacities of $Gd_2Pd_{14}B_5$ and $Lu_2Pd_{14}B_5$ results in the magnetic contributions. ΔC of $Gd_2Pd_{14}B_5$, shown in Fig. 7.10b. The entropy of a system is connected to the specific heat by

$$S_m = \int_0^T \frac{c_m(T')}{T'} dT', \quad (7.2)$$

allowing to derive $S_{mag}(T)$ of $Gd_2Pd_{14}B_5$ released at T_{ora} (Fig. 7.10b, solid line). The entropy saturates already at ~ 10 K, revealing 37.5 J/mol K. This value is slightly higher than the theoretical value expected for magnetic

Gd^{3+} with $J = 7/2$. Taking into account 2 Gd atoms, $S_{mag} = 2 \times R \ln(8) = 34.57 \text{ J/mol K}$. In the molecular-field approach the specific heat jump at the magnetic ordering temperature follows from [211]

$$\Delta C_{mag}(T_{mag}) = 5R \frac{J(J+1)}{2J^2 + 2J + 1}. \quad (7.3)$$

Within this model, the specific heat jump is of second-order and directly correlated to the total angular momentum. The jump of ΔC_p at about 6 K is approximately 21.5 J/mol K. In the scope of the molecular field model $\Delta C(T_{mag}) = 38.7 \text{ J/mol K}$ for $J = 7/2$ (compare Eqn. 7.3). Deviations from the theoretical value may be attributed to short range magnetic correlations above T_{mag} , which transfer a part of the entropy S_{mag} associated with magnetic ordering to higher temperatures as well as the broadening of the anomaly below T_{mag} .

Heat capacity measurements suggest that the compounds based on Ce, Nd and Sm order magnetically below 2 K, while both Pr and Eu seem not to exhibit a magnetically ordered ground state (see Fig. 7.9a). The total angular momentum $J = 4$ of the Pr ion in the context of crystalline electric field effects of the tetragonal crystal structure of $\text{Pr}_2\text{Pd}_{14}\text{B}_5$ can create a non-magnetic ground state due to singlet formation or due to the presence of a non-magnetic doublet.

The absence of long range magnetic order in the Eu based compound would be the result of a valency of the Eu ion which significantly deviates from the $2+$ state. Note that Eu in the $2+$ state would behave like Gd and as a consequence, ordering should occur around the value deduced for the isomorphous $\text{Gd}_2\text{Pd}_{14}\text{B}_5$. The intermediate electronic configuration of the Eu ion in $\text{Eu}_2\text{Pd}_{14}\text{B}_5$ results in a significantly enhanced electronic contribution to the specific heat, attaining about 0.8 J/mol K^2 for $T \rightarrow 0$. A hump-like structure in the heat capacity of $\text{Pr}_2\text{Pd}_{14}\text{B}_5$ around 4 K may refer to a low lying CEF level above the nonmagnetic ground state (see Fig. 7.9a).

7.7 Magnetic properties

Figure 7.11a displays the isothermal magnetisation M of $\text{RE}_2\text{Pd}_{14}\text{B}_5$ as a function of externally applied fields $\mu_0 H$ at 2 K. The isothermal magnetisation measurements were performed in fields ranging from 0.01 T to 6 T. The inverse of the temperature dependent magnetic susceptibility, $\chi(T)^{-1}$, of $\text{RE}_2\text{Pd}_{14}\text{B}_5$ is shown in Fig. 7.11b for an applied magnetic field of 1 T. With the exception of Sm and Eu, all compounds exhibit Curie–Weiss behaviour above 50 K. The susceptibility data can be accounted for applying the modified Curie–Weiss law,

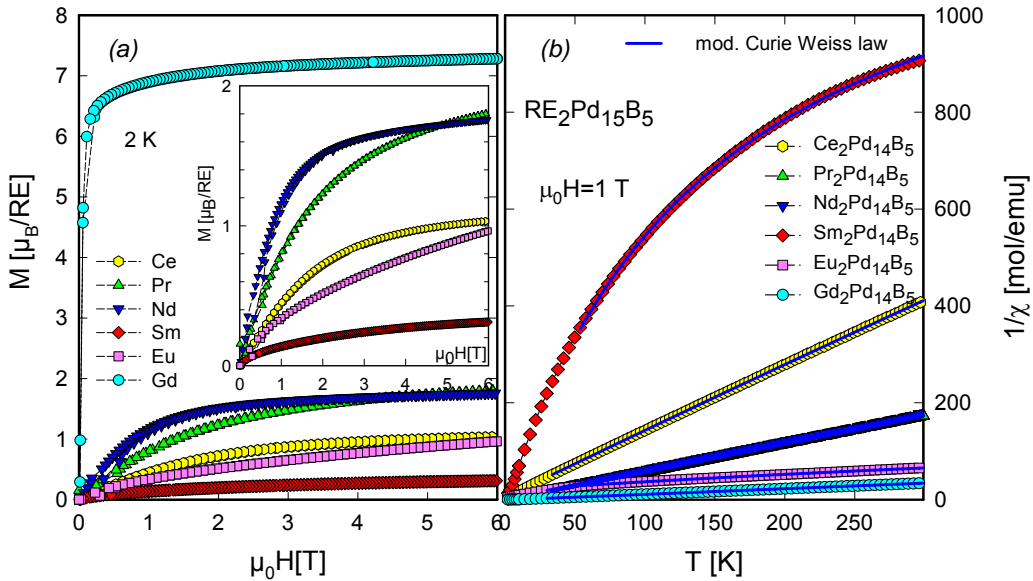


Figure 7.11: (a) Isothermal magnetisation M vs. magnetic field μ_0H of $RE_2Pd_{14}B_5$ at 2 K. (b) Temperature dependent inverse magnetic susceptibility $1/\chi$ of $RE_2Pd_{14}B_5$ in a magnetic field of 1 T.

$$\chi = \chi_0 + \frac{C}{T - \theta_p} \quad (7.4)$$

with the paramagnetic Curie temperature θ_p , the temperature-independent susceptibility χ_0 and the Curie constant C . Least squares fits according to Eqn. 7.4 were performed in the temperature range $50\text{ K} < T < 300\text{ K}$. Results of least squares fits are summarised in Table 7.2. The effective moments observed vary from $0.9\mu_B$ to $\sim 7.8\mu_B$ and the paramagnetic Curie temperature between -150 K for Eu to 12 K for the Sm compound. With the exception of Eu, the effective moments μ_{eff} are close to theoretical values associated with the 3+ state of a particular rare earth ion, thereby inferring stable magnetic moments as well as reasonably small crystal field splitting. The temperature independent susceptibility χ_0 for most of these compounds is found between 10^{-3} and 10^{-5} emu/mol, however Sm and Eu compounds reveal much larger χ_0 values.

For $Ce_2Pd_{14}B_5$ and $Pr_2Pd_{14}B_5$ the trends of χ^{-1} are linear and follow the Curie Weiss law above 50 K, indicating a simple paramagnetic state. The positive paramagnetic Curie temperature $\theta_p = 2.6\text{ K}$ of $Pr_2Pd_{14}B_5$ can be related to ferromagnetic interactions, while a negative value of θ_p refers to antiferromagnetic interactions.

The temperature dependence of $1/\chi$ of $Sm_2Pd_{14}B_5$ distinctly differs from

	lattice parameters a, c [nm]	T_{mag} [K]	μ_{eff}^{exp} [μ_B/RE]	μ_{eff}^{theo} [μ_B/RE^{3+}]	θ_p [K]
La ₂ Pd ₁₄ B ₅	0.8612(1); 1.6643(3)				
Ce ₂ Pd ₁₄ B ₅	0.8591(4); 1.6620(9)		2.38	2.54	-3.12
Pr ₂ Pd ₁₄ B ₅	0.8582(2); 1.6600(1)		3.7	3.58	2.6
Nd ₂ Pd ₁₄ B ₅	0.8577(1); 1.6628(1)		3.58	3.62	-0.9
Sm ₂ Pd ₁₄ B ₅	0.8516(1); 1.6589(4)		0.92	0.84	2.9
Eu ₂ Pd ₁₄ B ₅	0.8562(7); 1.6605(1)		5.86	7.94 for Eu^{2+}	-87
Gd ₂ Pd ₁₄ B ₅	0.8497(4); 1.6614(8)	6	7.8	7.94	8
Lu ₂ Pd ₁₄ B ₅	0.84237(1); 1.65824(4)				
Th ₂ Pd ₁₄ B ₅	0.86102(2); 1.66019(5)				

Table 7.2: Lattice parameters and magnetic transition temperatures T_{mag} , effective magnetic moments μ_{eff} and paramagnetic Curie temperatures θ_p of RE₂Pd₁₄B₅.

that of the other compounds is a characteristic of Sm intermetallics for two reasons. It arises from the rather small g -value ($\frac{2}{7}$) of Sm³⁺ as well as from ground state (⁶H_{5/2}) and the first excited multiplet (⁶H_{7/2}) being separated only by about 1500 K. In order to fully account for the experimentally observed temperature dependencies of Sm containing compounds, the first excited multiplet in combination with crystal electric field effects within both multiplets has to be considered [212, 213]. A review of magnetic properties of binary Sm compounds can be found in [214]. To quantitatively account for $T > 50$ K, a least squares fit according to the modified Eqn. 7.4 was applied, revealing $\chi_0 = 7.4 \times 10^{-4}$ emu/mol as a temperature independent Pauli-like susceptibility, the Curie constant $C = 0.079$ yields an effective moments $\mu_{eff} = 0.92 \mu_B/\text{Sm}$ and $\theta_p = 2.9$ K, respectively. The effective magnetic moment is close to the theoretical value associated with the Sm³⁺ state.

The inverse magnetic susceptibility of Eu₂Pd₁₄B₅ follows a Curie–Weiss law in the temperature region above 50 K. The effective magnetic moment $\mu_{eff}/\text{Eu-ion}$ was extracted from a least squares fit within the non-linear region ($T < 100$ K). The obtained value $\mu_{eff} = 5.86 \mu_B/\text{Eu}$ is significantly smaller than that of the free Eu²⁺ ground state ($\mu_{eff}^{theor} = 7.94 \mu_B$). The respective paramagnetic Curie temperature $\theta_p = -87$ K refers to antiferromagnetic correlations of the Eu²⁺ moments. This finding is furthermore corroborated by results ($\mu_{eff} = 6.67 \mu_B/\text{Eu}$ and $\theta_p = -125$ K derived from the least squares fits according to the modified Eqn. 7.4 from the high temperature region ($T > 100$ K). The inverse magnetic susceptibility $\chi^{-1}(T)$ at a magnetic field of $\mu_0 H = 1$ T for Gd₂Pd₁₄B₅ above about 50 K can be reasonably well described by the modified Curie–Weiss law. Least squares fits to the data of Gd₂Pd₁₄B₅ indicate that the effective magnetic moment, $\mu_{eff} = 7.8$ is slightly

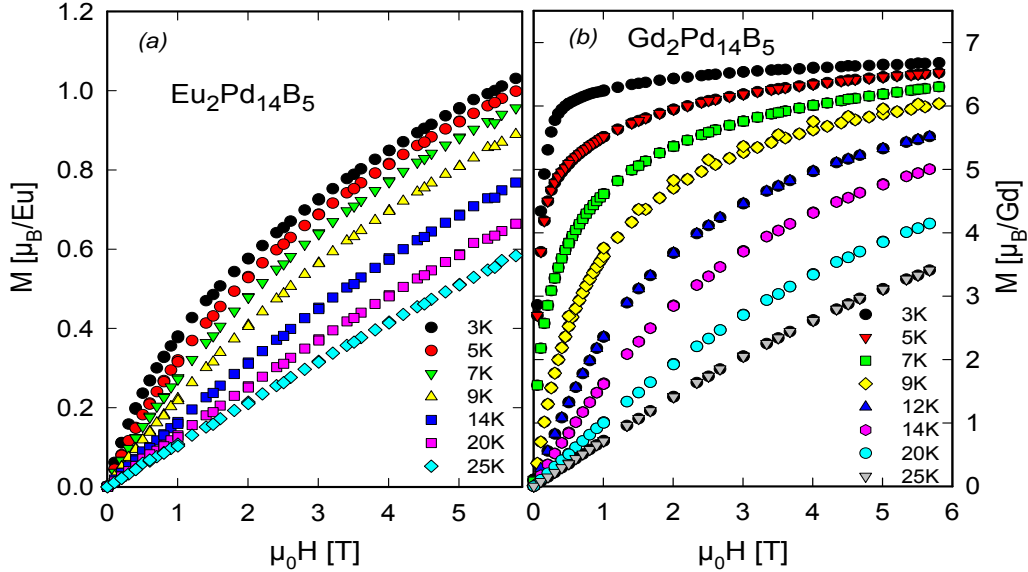


Figure 7.12: Isothermal magnetisation M as a function of the magnetic field $\mu_0 H$ of (a) $\text{Eu}_2\text{Pd}_{14}\text{B}_5$ and (b) $\text{Gd}_2\text{Pd}_{14}\text{B}_5$ at various temperatures.

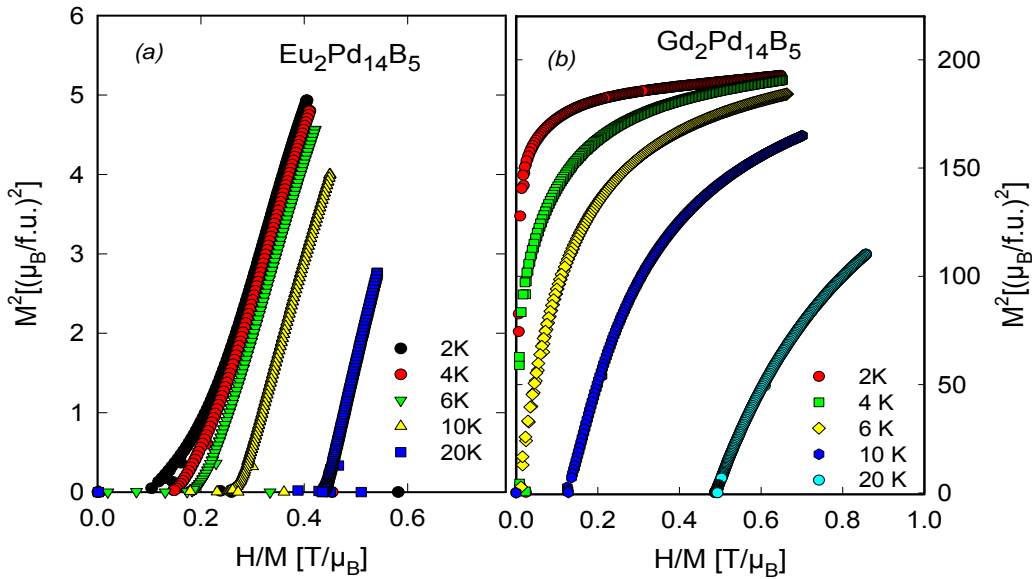


Figure 7.13: Arrott plots of (a) $\text{Eu}_2\text{Pd}_{14}\text{B}_5$ and (b) $\text{Gd}_2\text{Pd}_{14}\text{B}_5$.

below that of the free Gd^{3+} ion ($\mu_{\text{eff}} = 7.94 \mu_B$). Also, the saturation magnetisation is only slightly smaller than the theoretically expected value of $g_J J = 7 \mu_B/\text{Gd}$ (see figures 7.11a and 7.12b). Results of isothermal magnetisa-

tion measurements for $\text{Eu}_2\text{Pd}_{14}\text{B}_5$ and $\text{Gd}_2\text{Pd}_{14}\text{B}_5$ are displayed in Fig. 7.12 as a function of external field. A non-saturating magnetisation is observed in case of $\text{Eu}_2\text{Pd}_{14}\text{B}_5$ (Fig. 7.12a). The magnetisation reaches about $2.1 \mu_B/\text{f.u.}$ at the maximum field of 6 T. The experimentally deduced figure, $1.04 \mu_B$ per Eu^{2+} ion is far below the theoretical saturation magnetisation of $7 \mu_B$ arising from divalent Eu. The magnetisation of $\text{Gd}_2\text{Pd}_{14}\text{B}_5$ increases to larger values than those of the other compounds at 2 K, approaching a value of $M=6.7 \mu_B/\text{Gd}^{3+}$ at 6 Tesla (see Fig. 7.11a). The magnetisation of $\text{Sm}_2\text{Pd}_{14}\text{B}_5$ exhibits the lowest values at 2 K, increasing to $M=0.34 \mu_B/\text{Sm}^{3+}$ at 6 T (see Fig. 7.12b). Arrott plots of $\text{Eu}_2\text{Pd}_{14}\text{B}_5$ and $\text{Gd}_2\text{Pd}_{14}\text{B}_5$ are shown in Fig. 7.13. These plots indicate that $\text{Gd}_2\text{Pd}_{14}\text{B}_5$ orders magnetically below 7 K (Fig. 7.13b), whereas above 7 K a simple paramagnetic state occurs. $\text{Eu}_2\text{Pd}_{14}\text{B}_5$ does not shows typical signs of long range magnetic order (Fig. 7.13a).

Summary

The ternary Ce–Pt–Si system have been investigated and phase relations have been established for the isothermal section at 800°C based on X-ray powder diffraction, metallography, scanning electron microscopy (SEM) and electron probe microanalysis (EPMA) techniques. Results of XRD and EPMA analysis obtained from all measurements were used in the construction of the isothermal cross-section of the Ce-Pt-Si phase diagram at 800°C. The interaction of Ce, Pt and Si leads to the formation of at least 19 ternary stable phases. X-ray diffraction and electron probe methods lead to the speculation that ternary-phases with unknown crystal structures may exist in this area. Atom order in the crystal structures of τ_{18} -Ce₅(Pt,Si)₄ (space group Pnma), τ_3 - Ce₂Pt₇Si₄ (space group Pnma) and τ_{10} - CePtSi₂ (space group Cmcm) was determined by direct methods from X-ray single crystal studies and found to be isotypic with the Sm₅Ge₄-type, the Ce₂Pt₇Ge₄ - type and the CeNiSi₂-type, respectively. Rietveld refinements established atom arrangement in the structures of τ_{16} -Ce₃Pt₅Si (space group Imma) and τ_{17} - Ce₃PtSi₃ (space group Imm). Phase equilibria in Ce-Pt-Si are characterized by the absence of cerium solubility in the various platinum silicides. Mutual solubility among cerium silicides and cerium platinides, however, are significant whereby random substitution of the almost equally sized atom species platinum and silicon is also reflected in extended homogeneous regions at constant Ce-content such as for τ_{13} - Ce(Pt_xSi_{1-x})₂ or τ_6 - Ce₂Pt_{3+x}Si_{5-x}.

Superconducting {Sr, Ba, Th}Pt₄Ge₁₂ are the first skutterudites where the framework in the structure is entirely built by Ge-atoms. DFT calculations proved that X=(Ba,Sr) guest atoms strongly stabilize the compounds. Most strikingly, the calculated DOS around E_F is composed of hybridized Ge 4p-like and Pt 5d-like states, and it has a sharp peak with its maximum very close to E_F. The influence of the guest atoms (Ba or Sr) on superconductivity, however, may be ruled out due to the fact that (i) the Ba- or Sr-like DOS around E_F is negligible and (ii) the DOS around E_F for the *hypothetical* X-free Pt₄Ge₁₂ framework is very similar to the one of XPt₄Ge₁₂ (X = Sr, Ba and Th). Hence, superconductivity appears to be an intrinsic property of the Pt-Ge cage-forming structure. This conclusion is in line with the slightly smaller value of T_c observed in SrPt₄Ge₁₂, in marked contrast to

the isotope effect, where lighter masses would originate larger SC transition temperatures. Low temperature resistivity studies of EuPt₄Ge₁₂ evidence magnetic ordering at $T_m \approx 1.7$ K. Electropositive elements Ca (in part) or Eu (complete) stabilize the new compounds as well. A maximum filling grade of about 20 % of Ca is possible in Ba_{1-x}Ca_xPt₄Ge₁₂, yielding a superconducting ground state below $T_c = 5.2$ K. A comparison with BaPt₄Ge₁₂ shows that T_c is only weakly influenced by the Ba/Ca substitution. The unimportance of scattering on non-magnetic impurities clearly refers to a conventional type of superconductivity, in line with results from our specific heat studies.

{Th, U}Pt₄Ge₁₂ are further representatives of skutterudites with a [Pt₄Ge₁₂] sublattice. Resistivity, magnetic susceptibility and specific heat measurements indicate a phonon-mediated superconducting state in ThPt₄Ge₁₂ below $T_c = 4.75$ K. Superconducting properties of ThPt₄Ge₁₂ have been analyzed in detail ($\mu_0 H_{c2}(0) = 0.21$ T, $\xi_0 = 4 \times 10^{-8}$ m, $\lambda(0) = 1.2 \times 10^{-7}$ m), characterizing ThPt₄Ge₁₂ as a type II superconductor. UPt₄Ge₁₂ is dominated by spin fluctuations at low temperatures, preventing magnetic order and SC. DFT calculations proved the hybridization between Ge 4p-like and Pt 5d-like states in an energy region around the Fermi level, dominating the DOS at $E = E_F$. Consequently, SC arises primarily from the electronic [Pt₄Ge₁₂] sublattice states, while Th (and U) plays a key role to electronically stabilize these skutterudites.

Physical properties of Ba₈Pd_xGe_{46-x-y}□_y, such as charge carrier density and transport quantities were found to be heavily influenced by Ge/Pd-substitution in the clathrate framework: the system changes from a bad metal for lower Pd content to a clear activation-type behaviour for the largest Pd concentration. This gradual change is originated by the combined effect of both the substitution of Ge/Pd and by the vanishing of vacancies. Thermopower indicates that the majority charge carriers are electrons, but the density of these carriers decrease by almost one order of magnitude when proceeding from a Pd content $x = 2$ to $x = 3.8$. The observation that the sample with $x = 2$ has a larger overall resistivity than that with $x = 2.9$, although the charge carrier density is already reduced, is then associated with an improved mobility of the charge carriers in the latter case as a consequence of a reduced number of vacancies. The efficiency of scattering on such vacancies is evidenced also from the thermal conductivity study. The substitution of Ge by Cd in Ba₈Cd_xGe_{43-5x/8}□_{3-3x/8}, also allows a variation of the charge carrier density, hence of transport quantities. Particularly, such systems may be driven towards a metal to insulator transition, as obvious from the temperature dependent resistivity of Ba₈Cd_xGe_{43-5x/8}□_{3-3x/8} for $2.4 \leq x \leq 7.6$. We have developed a model density of states, characterized by a narrow gap of the DOS right above the Fermi energy, which allows to qualitatively tracing various details of the temperature dependent electrical resistivity.

$S(T)$ basically defines the figure of merit $ZT = S^2/(\rho\lambda)$, which represent the thermoelectric performance of a certain material. Using the compound with the highest Seebeck coefficient, i.e., $x = 3.8$ reveals $ZT(300 \text{ K}) = 0.045$ for $\text{Ba}_8\text{Pd}_{3.8}\text{Ge}_{42.3}$ and $ZT(300 \text{ K}) = 0.0042$ in case of $\text{Ba}_8\text{Cd}_{7.6}\text{Ge}_{38.4}$, respectively. Physical properties of $\text{Ba}_8\text{Zn}_x\text{Ge}_{46-x}$ compounds were found to be heavily influenced by Ge/Zn-substitution in the clathrate framework: the system is driven towards a metal to insulator transition, as found from temperature dependent resistivity measurement of $\text{Ba}_8\text{Zn}_x\text{Ge}_{46-x-y}\square_y$ for $2.1 \leq x \leq 7.7$. Besides the charge carrier density, also the carrier mobility likely changes throughout the series, being much higher for the nominal $x_{Zn} = 7.7$ system; consequently, the overall resistivity is even below that of the system with nominal $x_{Zn} = 5.7$. Such a behaviour can possibly be correlated to the vanishing of the voids in the crystal structure. For $\text{Ba}_8\text{Zn}_{7.7}\text{Ge}_{38.3}$ a figure of merit $ZT = S^2/(\rho\lambda) \approx 0.035$ is derived at room temperature from the present experimental data. Applications are possible, if the thermoelectric figure of merit surpasses a value of $ZT = 1$ as realized in Bi_2Te_3 with $ZT(300 \text{ K}) \approx 0.7$ [190, 215]. Fine-tuning of the charge carrier concentration is in progress to drive this class of materials to even more promising values of the thermoelectric efficiency.

Phase relations at 900°C , crystal chemistry, electrical and thermal transport measurements have also been studied for the clathrate systems $\text{Ba}_8\{\text{Pd}, \text{Pt}\}_x\text{Si}_{46-x}$. Structural investigations for both systems at 300, 200 and 100 K define cubic primitive symmetry with the space group type $\text{Pm}\bar{3}n$ consistent with clathrate type I. Studies of transport properties evidence electrons as the majority charge carriers except for $\text{Ba}_8\text{Pt}_{2.8}\text{Si}_{43.2}$. Owing to an enlarged density of these carriers, overall $S(T)$ values remain within some tens of $\mu\text{V/K}$. The smaller masses of $\text{Ba}_8\{\text{Pd}, \text{Pt}\}_x\text{Si}_{46-x}$ in comparison to $\text{Ba}_8\{\text{Pd}, \text{Pt}\}_x\text{Ge}_{46-x}$ are the cause for the larger thermal conductivity observed in both former series. Nevertheless, increasing point defect scattering due to the statistical Pd/Si substitution depletes λ_{ph} to values close-by the theoretical lower limit.

A novel compound, BaPtSi_3 , has been characterized from X-ray data and prompted a tetragonal unit cell, space group $\text{I}4mm$ (No. 107), isotropic with BaNiSn_3 -Type. BaPtSi_3 exhibits type-II superconductivity at low temperatures below 2.3 K. Based on magnetization, electrical resistivity and specific heat data the compound was characterized as a dirty-limit weak-coupling superconductor with $T_c=2.3$ K with an upper critical field at $T = 0$ below 0.2 Tesla, dominated for orbital pair breaking.

The crystal structure of novel ternary compounds, $\text{M}_2\text{Pd}_{14+x}\text{B}_{5-y}$ ($\text{M} = \text{Th, Ce, Pr, Nd, Sm, Eu, Gd}$), was determined from X-ray single crystal data for $\text{Nd}_2\text{Pd}_{14}\text{B}_5$ and $\text{Th}_2\text{Pd}_{14}\text{B}_5$ and found to be closely related to the structure type of $\text{Sc}_4\text{Ni}_{29}\text{Si}_{10}$ with tetragonal unit cell and space group type

I4₁/amd. All rare earth homologues were characterized by Rietveld analyses and found to be isotypic with the Nd₂Pd₁₄B₅ type. The electrical resistivity, ρ , of M₂Pd_{14+x}B_{5-y}, in general, is characterized by small RRR values originated by defects inherent to the present crystal structure. Low temperature $\rho(T)$ data of the compounds exhibit a minimum in the vicinity of 20 K followed by an increase towards lower temperatures. Although a nonmagnetic origin like variable range hopping is conceivable due to statistical disorder of the crystal structure, a magnetic origin is more likely, since magnetic fields of the order of several Tesla completely suppress the above indicated anomalies. A hump-like structure in the heat capacity of Pr₂Pd₁₄B₅ around 4 K may refer to a low lying CEF level above the nonmagnetic ground state. Heat capacity studies at low temperatures indicate clear long range magnetic order in Gd based compound below 6 K. Heat capacity measurements suggest that the compounds based on Ce, Nd and Sm order magnetically below 2 K, while Pr seem not to exhibit a magnetically ordered state. The absence of long range magnetic order in Eu₂Pd₁₄B₅ would be a result of a valency of the Eu ion which significantly deviates from the 2+ state.

Appendix A

User defined functions

The least squares fits to the data were carried out using the program *Table-Curve* distributed by SYSTAT. The user defined functions (*udf*'s) for electrical resistivity $\rho(T)$, specific heat $C_p(T)$ are listed.

A.1 Electrical resistivity

A.1.1 Woodard and Cody model

In order to analyses the electrical resistivity $\rho(T)$ measurements in temperature ranges between 4 K and room temperature were used the theoretical and empirical formulas as fit functions. Some materials are characterized by a metallic behaviour, however the overall features are different. Based on Debye Model, the resistivity of metals/compounds due to the electron-phonon scattering is scaled by a specific Debye temperature θ_D that effectively divides temperature range into different regions. The corresponding electron-phonon scattering resistivity is given by Eqn. 1.4 [75]. However good metals deviate from a metallic temperature dependence of resistivity. The significantly deviation from such a common shape of metallic resistivity curves described by the empirical formula of Woodard and Cody [155]

$$\rho(T) = \rho_0 + \rho_1 T + \rho_2 \exp(-T_0/T), \quad (\text{A.1})$$

where T_0 is the characteristic temperature. Equation A.1 yields a strong curvature at low temperatures and accounts for some tendency towards saturation in the high temperature limit.

User defined function:

```
#F1 = EXP(-#A3/X)
Y = #A0 + #A1*X + #A2*#F1
                                         'exponential (-T0/T) term
                                         '#A0; residual resistivity
                                         'ρ(T) = ρ0 + ρ1(T) + ρ2e^(T0/T)
```

A.1.2 parallel resistor model

The normal-state resistivity could be explained by a modified "parallel resistor" model [216, 217, 218, 219]. In the parallel resistor model the expression of $\rho(T)$ is given by

$$\rho(T) = \left(\frac{1}{\rho_0 + \rho_{ph}} + \frac{1}{\rho_{max}} \right)^{-1}. \quad (\text{A.2})$$

where ρ_0 is the residual resistivity, ρ_{ph} is the resistivity due to phonon-electron scattering similar to *s-d* scattering in transition metal alloys, and ρ_{max} is the saturation resistivity, which is independent of the temperature. The saturation resistivity is interpreted as a lower limit to the electron mean free path. When the mean free path is short, the momentum dependence of the scattering can be ignored, and the resistivity is simply proportional to a weighted integral over the phonon density. In this approximation, one can write simple expression for the weighted phonon distribution:

$$\rho_{ph}(T) = \alpha \left[\frac{E_1 - E_2}{k_B} + T \ln \frac{e^{E_2/k_B T} - 1}{e^{E_1/k_B T} - 1} \right], \quad (\text{A.3})$$

where α and k_B are the fitting coefficient and Boltzmann's constant, respectively. Equation A.3 is derived by assuming that a thermal phonon with a flat energy distribution between E_1 and E_2 contributes to the scattering of the conduction electrons and that the resistivity satisfies the Bose-Einstein statistics. Therefore, this formula allows us to estimate the energy distribution of the thermal phonon that gives rise to $\rho_{ph}(T)$. The experimentally obtained $\rho(T)$ values can be fitted with a curve by using Eqn. A.2 and A.3.

User defined function:

```
#F1=1.381*10^(-23)                                'Boltzmann's constant k_B
#F2=EXP((#D/X)-1)                                 'e^{E_1/k_B T} - 1
#F3=EXP((#E/X)-1)                                 'e^{E_2/k_B T} - 1
#F4=(#D-#E)                                       '(E_1-E_2)
#F5=LN(EXP(#E/X)-1)-LN(EXP(#D/X)-1)
#F6=#C*(#F4+X*#F5)                               'ρ_{ph}(T)
Y=(1/(#A+#F6)+(1/#B))^(−1)                      'ρ(T)
```

Here #A is the residual resistivity, #B , the saturation resistivity and #C is the fitting coefficient.

A.1.3 Ferromagnetic case

In general, the resistivity due to electron-magnon scattering from an arbitrary type of boson excitation (magnon or phonon) can be written as [220]

$$\rho_B(T) = \frac{m\pi N(0)}{ne^2} \int_0^{2k_F} \frac{k^3}{k_F^2} dk \int \frac{d\Omega_{\vec{k}}}{4\pi} |g_{\vec{k}}|^2 \frac{\frac{\hbar\omega_{\vec{k}}}{k_B T}}{4\sinh^2(\frac{\hbar\omega_{\vec{k}}}{2k_B T})}, \quad (\text{A.4})$$

where $n = k_F^2/3\pi^2$ is the number density of the charge carriers, $N(0) = mk_F/2\hbar^2\pi^2$ is the density of states per spin at the Fermi level, $2k_F$ represents the maximum wave-vector transfer, $g_{\vec{k}}$ is the electron-magnon coupling, k_B is the Boltzmann constant and $\hbar\omega_{\vec{k}}$ is the boson energy. In the case of an anisotropic ferromagnetic (FM) materials, there is a gap Δ in the magnon spectrum, and the energy dispersion relation of the magnon can be expressed by $\hbar\omega_{\vec{k}} = \Delta + C_0 k^2$, where C_0 is the spin-wave stiffness. It should be noted that electron-magnon coupling $|g_{\vec{k}}|^2$ for ferromagnetic system is independent of \vec{k} [221]. In the limit of $\hbar\omega_{\vec{k}}/2k_B T \gg 1$, the leading term of electron-magnon resistivity in the anisotropic ferromagnetic material ρ^{FM} [222] below the transition temperature can be written as

$$\rho^{FM}(T) = BT\Delta \left(1 + \frac{2T}{\Delta}\right) e^{-\Delta/T}. \quad (\text{A.5})$$

Here B is the constant related to the spin disorder.

User defined function:

```
#F1 = 2*(X/#C)                                '#A is residual resistivity rho0
Y = #A + #B*X*#C*(1+2*#F1)*EXP(-#C/X)      '#B spin disorder constant
                                                '#C is energy gap
                                                'Y; total resistivity rho^{FM}(T)
```

A.1.4 Antiferromagnetic case

In the case of an antiferromagnetic (AFM) system, the electron-magnon coupling $|g_{\vec{k}}|^2 \propto k$ and the energy dispersion relation [223] is $\hbar\omega_{\vec{k}} = \sqrt{\Delta^2 + Dk^2}$. By using this information the resistivity is derived as:

$$\rho^{AFM}(T) = \frac{C}{T} \int_0^\infty \frac{k^4 \sqrt{\Delta^2 + Dk^2}}{\sinh^2(\sqrt{\Delta^2 + Dk^2}/2T)} dk, \quad (\text{A.6})$$

where C is constant. Using the change of variable, $y = \sqrt{\Delta^2 + Dk^2}/2T$, one can approximate $\sinh^2 y \approx e^{2y}$ in the small temperature limit $T \ll \Delta$, and find

$$\rho^{AFM}(T) = CT^5 \int_y^x y^2 (y^2 - y_0^2)^{3/2} e^{-2y} dy, \quad (\text{A.7})$$

where $y_0 = \Delta/2T$. This integral can be calculated if it use another change of variable $y = y_0 \cosh(x)$. The limit of the integral then is from 0 to x_c , where x_c is the solution of $-2y_0 \cosh(x_c) + 2y_0 = -1$, and Eqn. A.8 becomes

$$\rho^{AFM}(T) \approx CT^5 y_0^5 e^{-2y_0} \int_0^{x_c} \cosh^2 x \cdot \sinh^2 x dx. \quad (\text{A.8})$$

Thus, the leading term of the resistivity in the antiferromagnetic case is given by

$$\rho^{AFM}(T) = C\Delta^5 e^{-\Delta/T} \left[\frac{1}{5} \left(\frac{T}{\Delta} \right)^5 + \left(\frac{T}{\Delta} \right)^4 + \frac{5}{3} \left(\frac{T}{\Delta} \right)^3 \right]. \quad (\text{A.9})$$

In the gapless limit $\Delta \rightarrow 0$, its obtains $\rho \sim T^2$ and $\sim T^5$ from Eqn.A.9 for the ferromagnetic (FM) case and the antiferromagnetic (AFM) case, respectively. Thus, the resistivity is given as

$$\rho = \rho_{FL} + \rho^{FM,AFM}. \quad (\text{A.10})$$

where $\rho_{FL} \approx \rho_0 + AT^2$ is simple Fermi-liquid behavior.

User defined function:

```
#F1 =(X/#C)                                '#A is residual resistivity rho_0
Y =#A + #B*#C^5*EXP(-#C/X)*[(1/5)*(#F1)^5  '#B spin disorder constant
+ (#F1)^4+(5/3)*(#F1)^3]                   '#C is energy gap
                                              'Y; total resistivity rho^{AFM}(T)
```

A.2 Phonon specific heat

As already discussed in the previous chapters, deviations from the simple Debye model indicate a rather complicated phonon spectrum. The spectrum is supposed to be composed of background vibrations originating from the cage-like structure represented by a Debye spectrum and, additionally, from the rattling modes of the loosely bound electropositive filler-atoms in case clathrate and skutterudite systems. In order to qualitatively and quantitatively describe the lattice dynamics, we have adapted a model which incorporates some fine-structure in the phonon density of states [91, 92]. The latter is represented by a spectral function $F(\omega)$, allowing to express the heat capacity as:

$$C_{ph}(T) = 3R \int_0^\infty F(\omega) \frac{\left(\frac{\omega}{2T}\right)^2}{\sinh^2\left(\frac{\omega}{2T}\right)} d\omega, \quad (\text{A.11})$$

with ω the phonon frequency and R the gas constant. The most common assumptions on $F(\omega)$ are: $F(\omega) = \delta(\omega)$ and $F(\omega) \sim \omega^2$ up to a cut-off

frequency ω_D , corresponding to the well known Einstein and Debye model, respectively. Junod et al. [91] demonstrated that certain functionals of the phonon specific heat take the form of convolutions of the phonon spectrum. In particular, $(5/4)R\pi^4C_{ph}T^3$ is an image of the spectrum $\omega^{-2}F(\omega)$ for $\omega = 4.93 \cdot T$, where ω is expressed in kelvin. Based on these considerations we have constructed an elementary phonon spectrum and have carried out least squares fits to the data.

User defined function:

```
#F1=3*X^3*$^4/sinh($)^2          'θ_D Debye temperature [K]
#F2=#A/(2*X)
#F5=#F/(2*X)
#F6=#G/(2*X)
#F7=#B/(2*X)
#F8=#C/(2*X)
G=8.314                           'gas constant R
#F9=3/(#D*#F^3+(#D+#H)*(#G^3-#F^3)+  'normalization factor N
+ #D* (#B^3-#G^3)+(#D+#E)*(#C^3-#B^3)+  'C_p(T)/T^3
+ #D* (#A^3-#C^3))
Y=#I*#F9*G*(#D*AI(1,0.0001,#F5)+      +
+ (#D+#H)*AI(1,#F5,#F6)+#D*AI(1,#F6,#F7)+  +
+ (#D+#E)*AI(1,#F7,#F8)+#D*AI(1,#F8,#F2))/X^3
```

A.2.1 spin fluctuation systems

If one system refers to distinct deviations from a Fermi liquid ground state due to strong spin fluctuations, which are evident also from a large value of the Sommerfeld constant γ (see 4.1.5 in UPt₄Ge₁₂ skutterudite case $\gamma = 156 \text{ mJ/molK}^2$). Moreover, classical spin fluctuation systems like YCo₂ exhibit at elevated temperatures a tendency towards saturation, which can also be conceived for UPt₄Ge₁₂. We attempted to fit the low temperature data of with the simple ansatz,

$$C_p(T) = \gamma T + \beta T^3 + \delta T^3 \ln(T/T^*), \quad (\text{A.12})$$

where the latter term accounts for spin fluctuations.

User defined function:

```

#A          '#A is Sommerfeld constant γ
#B          '#B is β
#C          '#C is δ
#D          '#D is characteristic temperature T*
Y =#A*X + #B*X3 + #C*X3*(ln(X/#D)   'Y; Cp(T)

```

A.3 Determination of some SC- and Normal-state parameters

Superconductivity in general only occurs in a phase space spanned by three key parameters, i.e, the critical temperature T_c , the critical current I_c and the critical magnetic field $H_c(T)$ which are specific for each material. As discussed in chapter 1 an from the critical field slopes near T_c several important superconducting and normal-state parameters can be estimated. In order to determination the superconducting and normal state parameters like penetration depth λ_{ep} in [nm], Maki parameter α , Fermi surface S_s , upper critical field $\mu_0 H_{c2}$ in [T], slope of upper critical field H'_{c2} in [T/K], Ginzburg-Landau parameter κ_{GL} , transformation of electronic specific heat coefficient γ from [J/mol K²] in [erg/cm³K²] and in [J/m³K²] are used the *MATHEMATICA* software in this work to perform different model calculations.

calculations and solutions:

Input: unit cell Volume; number of formula units per unit cell;

γ_{exp} ; ρ_0 ; T_c ; $H_{c2}(0)$; B'_{c2} ;

fields in green: specific sample properties;

calculates the Maki parameter α ; transforms specific heat from J/molK² to erg/(cm³K²), electron-phonon coupling constant λ_{ep} from *McMillan formula*.

phi0 = 2.07*10 ⁻¹⁵ ;	Fluxoid Φ_0
kb = 1.3806*10 ⁻¹⁶ ;	Boltzmann's constant k_B , in [erg/K]
hbar = 1.055*10 ⁻²⁷ ;	Planck's constant $\hbar /2\pi$, in [ergs]
m0 = 9.109*10 ⁻³⁴ ;	free electron mass m_0 in g
mu0 = 4*Pi*10 ⁻⁷ ;	permeability μ_0
echarge = 4.80*10 ⁻¹⁰ ;	electronic charge in [esu]
na = 6.022*10 ²³ ;	Avogadro constant
v = 6.34*10 ⁻²⁸ ;	volume of unit cell of a specific sample in m ³
num = 2;	number of formula units per unit cell
xx = 1/(v*na/num)	
gammaex = 0.035;	experimental Sommerfeld coefficient in [J/molK ²]
gamma = gammaex * xx	transformation of γ from J/molK ² \longrightarrow J/m ³ K ²
gammaerg = 10*gammaex * xx	transformation of γ from J/molK ² \longrightarrow erg/(cm ³ K ²)
rho0 = 3*10 ⁻⁶	residual resistivity input in Ω cm
tc = 4.76 ;	SC transition temperature in [K]
hc2' = -0.067 ;	slope of upper critical field in [T/K]
rl = 1.05;	I_{rl} between 1(dirty limit) and 1.18 (clean limit)
hc2 = 0.21;	upper critical field $H_{c2}(0)$ in Tesla
End Input	

Determination of slope of upper critical field B_{c2}' Eqn.1.66;

$$hc2' = rl((1.18*10^{-35}*\gamma*tc/ss^2 + 4490*\gamma*\rho_0))$$

hc2theo' = 4490 *gamma*rho0	in dirty case
ss = (rl*1.18*10 ³⁵ *gamma ² *tc/(hc2')) ^(1/2)	Fermi surface, clean case
ssfull = (1.18*10 ³⁵ *gamma ² *tc/(hc2'/rl -(4490*gamma*rho0))) ^(1/2)	Fermi surface, total case

Calculation of the Maki parameter α

$$\alpha = 3 * echarge^2 * hbar * gammaerg * rho0 / (2 * m0 * Pi^2 * kb)$$

Calculation of λ_{ep} based on McMillan Formula;

input: Debye temperature, Coulomb repulsion strength;
output: electron-phonon enhancement λ_{ep}

theta = 260;
mustar = 0.13;
tc = 4.76;

Debye temperature θ_D

μ^*

SC transition temperature in [K]

tc=theta/1.45*Exp[(-1.04*(1+lambda)/(lambda-mustar*(1+0.62*lambda))),lambda]

calculation of κ based on Gor'kov-Goodman relation;

input: residual resistivity, κ_0 ; $H_{c2}(0, \text{theo})$; $H_c(0)$;

output: $\kappa_{GL}(0)$

r0 = 3;
kappa0 = 1.9;
kappa = kappa0 + 0.0237*.Sqrt[gamma]*r0

residual resistivity input in Ωcm

κ_0

κ from Gor'kov-Goodman relation

r00 = 3*10⁻⁶;
kappa0 = 1.9;
kappa = kappa0 + 7.5*10³*Sqrt[gammaerg]*r00

residual resistivity input in $\mu\Omega\text{cm}$

κ_0

κ from Gor'kov-Goodman relation

Hc2= 0.21;
Hc = 0.050;
kappaGL = Hc2/(Sqrt[2]*Hc)

upper critical field in Tesla

thermodynamic critical field $H_c(0)$ in [T]

Ginzburg-Landau parameter $\kappa_{GL}(0)$

A.3.1 Determination of the upper critical field of dirty limit type II SC in term WHH model.

Input: lambdaso & Maki-parameter α ; T_c in [K]; dH_{c2}/dT in [T/K]

Output: Data are calculated and plotted in reduced units as Tesla vs. Kelvin.

Input of the experimental data:

Measurement = OpenRead["c:\\Mathematica \\temp \\hc2-cp.txt"];

```

q := Round[(t - n + in)/in];          Start temperature
n=0.0001;                            End temperature
m=0.9999;                            increment of t
in=0.01;                             superconducting transition temperature
tc=4.76;                             initial slope of the upper critical field
dhc2=-0.067;

lambdaso=15;                          lambdaso
alpha=0.016;                           Maki parameter

x := ((lambdaso/4)^2-4*h^2*alpha^2/Pi^4)^(1/2)
y := 2*h/Pi^2

magn=Re[h/.Table[FindRoot[Log[t]==PolyGamma[1/2]-0.5*(1+lambdaso/4/x)*PolyGamma
[1/2+(y+lambdaso/4-x)/t]-1/2*(1-lambdaso/4/x)*PolyGamma[1/2+(y+lambdaso/4+x)/t],h,0.5],
{t,n,m,in}]]]

Output: plotting as Tesla vs. Kelvin
habs=N[Table[t*tc,magn[[q]]*(-dhc2)*tc,t,n,m,in]];

save and export calculated data
result = OpenWrite["c:\\Mathematica\\temp\\test.txt", FormatType → OutputForm];
Write[result, TableForm[habs]];

```

Bibliography

- [1] F. Steglich, J. Aarts, C. D. Bredl, W. Lieke, D. Meschede, W. Franz and H. Schäfer, *J. Magn. Mater.* **15-18** (1980) 889.
- [2] G. R. Stewart, *Rev. Mod. Phys.* **56** (1984) 755; and references therein.
- [3] N. Grewe and F. Steglich, in *Handbook on the Physics and Chemistry of Rare Earths*, **Vol. 14** Ch. 97, edited by K. A. Gschneidner, Jr. and LeRoy Eyring, Elsevier Science Publishers B. V. North-Holland, Amsterdam (1991) 343.
- [4] S. H. Liu, in *Handbook on the Physics and Chemistry of Rare Earths*, **Vol. 17** Ch. 111, edited by K. A. Gschneidner, Jr., LeRoy Eyring, G. H. Lander and G. R. Chopin, Elsevier Science Publishers B. V. North-Holland, Amsterdam (1993) 87.
- [5] A. C. Hewson, *The Kondo Problem to Heavy Fermions*, (1993) Cambridge University Press.
- [6] N. Grewe and F. Steglich, in *Handbook on the Physics and Chemistry of Rare Earths*, **Vol. 11**, Ch. 97, edited by K. A. Gschneidner, Jr., LeRoy Eyring, (1991) Elsevier Science Publishers B. V. North-Holland, Amsterdam.
- [7] O. Zaharko, L. Keller and C. Ritter, *J. Magn. Magn. Mater.* **253** (2002) 130.
- [8] L. Durivault, F. Bourée, B. Chevalier, G. André and J. Etourneau, *J. Magn. Magn. Mater.* **246** (2002) 366.
- [9] F. Steglich, C. D. Bredl, W. Lieke, U. Rauchschwalbe and G. Sparn, *Physica B+C* **126** (1984) 82.
- [10] F. Steglich, U. Ahlheim, A. Böhm, C. D. Bredl, R. Caspary, C. Geibel, A. Grauel, R. Helfrich, R. Köhler, M. Lang, *Physica C: Superconductivity*, **185-189** (1991) 379.
- [11] E. Bauer, G. Hilscher, H. Michor, C. Paul, E.W. Scheidt, A. Grybanov, Yu. Seropgin, H. Noël, M. Sigrist and P. Rogl; *Phy. Rev. Lett.*, **92(2)**, 027003,1-4 (2004).
- [12] M. Yogi, K. Kitaoka, S. Hashimoto, T. Yasuda, R. Settai, T.D. Matsuda, Y. Haga, Y. Onuki, P. Rogl, E. Bauer; *Phy. Rev. Lett.*, **93**, 027003,1-4 (2004).
- [13] E. Bauer, R. Lackner, G. Hilscher, H. Michor, M. Sieberer, A. Eichler, A. Gribanov, Y. Seropgin, P. Rogl, *J. Phys.: Cond. Mat.* **17**, 1-12 (2005).
- [14] M. Yogi, H. Mukuda, Y. Kitaoka, S. Hashimoto, T. Yasuda, R. Settai, T.D. Matsuda, Y. Haga, Y. Onuki, P. Rogl and E. Bauer, *J. Phys. Soc. Jap.*, **75(1)**, 013709 (2006).
- [15] E. Bauer, H. Kalldarar, A. Prokofiev, E. Royanian, A. Amato, J. Seren, W. Brämer-Escamilla and I. Bonalde. *J. Phys. Soc. Jap.*, Volume **76**, Issue 5, pp. 051009 (2007).
- [16] R. Troc, A. M. Strydom, P. de V. du Plessis, V. H. Tran, A. Czopnik and J. K. Cockcroft, *Philosophical Magazine* **83** (2003) 1235.
- [17] S. Gabani, E. Bauer, M. Della Mea, K. Flachbart, Y. Paderno, V. Pavlik and N. Shitsevalova, *J. Magn. Magn. Mater.* **272-276** (2004) 397.
- [18] P. Estrela, A. de Visser, F. R. de Boer, G. J. Nieuwenhuys, L. C. J. Pereira and M. Almeida. *Physica B: Condens. Matter*, **295-261** (1999) 409.
- [19] E.W. Scheidt, T. Schreiner, K. Heuser and G. R. Stewart, *Physica B: Condens. Matter* **259-261** (1999) 388.
- [20] Lee W.H., Shelton R.N., "CePtSi: A new Heavy-Fermion Compound" *Phys. Rev. B* **35**, 5369-5371 (1987)

- [21] Lee W.H., Ku H.C., Shelton R.N., Phys. Rev. B **38**, 11562-5 (1988).
- [22] Lee W.H., Ku H.C., Shelton R.N., Chinese Journal Physics, **26**, 46-53 (1988).
- [23] Shelton R.N., Klavins P., Lee W.H., Ku H.C., Physica C, **155-155**, 447-448 (1988).
- [24] Köhler B., Strobel B., C. Kämmerer, Grauel A., Gottwick U., Göring E., Höhr A., Sparn G., Geibel C., Horn S., J. Magn. Magn. Mater., 90/91, 428-430 (1990).
- [25] Lee W.H., Kwan K.S., Klavins P., Shelton R.N., Phys. Rev. B **42**, 6542-6545 (1990).
- [26] Geibel C., Kämmerer C., Göring E., Moog R., Sparn G., Henseleit R., Cordier G., Horn S., Steglich F., J. Magn. Magn. Mater., 90/91, 435-437 (1990).
- [27] Geibel C., C. Kämmerer, Seidel B., Bredl C.D., Grauel A., Steglich F., J. Magn. Mater., **108**, 207-208 (1992).
- [28] Gignoux D., Schmitt, D., Zerguine M., Ayache C., Bonjour E., Phys. Lett., **117**, 145-149 (1986).
- [29] Hiebl, K.; Horvath, C.; Rogl, P., J. Less-Common Met., **117**, 375-383 (1986).
- [30] Palstra T.T.M., Menovsky A.A., Nieuwenhauys G.J., Mydosh, J.A., J. Magn. Mater., 54-57, 435-436 (1986).
- [31] Ayache C., Beille J., Bonjour E., Calemczuk R., Creuzet G., Gignoux D., Najib A., Schmitt, D., Voiron J., Zerguine M., J. Magn. Magn. Mater., 63-64, 329-331 (1987).
- [32] Grier B.H., Lawrence J.M., Horn S., Thompson J.D., J. Phys. C: Solid State Phys. **21**, 1099-1110 (1988).
- [33] N. Kimura, K. Ito, K. Saitoh, Y. Umeda, H. Aoki, T. Terashima, Phys. Rev. Lett. **24**, 247004/1-4 (2005).
- [34] J. M. Robinson, Phys. Rep. **51** (1979) 1.
- [35] J. M. Lawrence, P. S. Riseborough and R. D. Parks, Rep. Prog. Phys. **44** (1981) 1.
- [36] M. B. Maple, L. E. Delong and B. C. Sales, in *Handbook on the Physics and Chemistry of Rare Earths*, Vol. 1 Ch. 11, edited by K. A. Gschneidner, Jr., LeRoy Eyring, (1978) Elsevier Science Publishers.
- [37] N. B. Brandt and V. V. Moshchalkov, Adv. Phys. **33** (1984) 373.
- [38] K. Yosida, *Theory of Magnetism* (1996) Springer Berlin.
- [39] C. Kittel, Introduction to Solid State Physics, (1996) John Wiley & Sons, Inc.
- [40] I. Oftedal, Z. Kristallogr. A **66**, 517 (1928).
- [41] W. Jeitschko and D.J. Braun, Acta Crystallogr. B **33**, 3401 (1977).
- [42] G. Slack, V. G. Tsoukala, J. Appl. Phys. **76**, 1665 (1994).
- [43] C. Uher, *Skutterudites: Prospective Novel Thermoelectrics*, in Semiconductors and Semimetals, Academic Press, edited by T. M. Tritt, Vol. **69**, Chap. 5, Academic Press, San Diego, 139-253 (2001).
- [44] G.S. Nolas, D.T. Morelli, and T.M. Tritt, Annu. Rev. Mater. Sci **29**, 89 (1999).
- [45] B. C. Sales, B. C. Chakoumakos, D. Mandrus, Phys. Rev. B **61**, 2475 (2000).
- [46] M.D. Hornbostel, H. Sellinschegg, D.C. Johnson, *Thermoelectric Materials - New Directions and Approaches* Mater. Res. Soc. Symposium (Pittsburgh, PA, USA) 211 (1997).
- [47] M.D. Hornbostel, E.J. Hyer, J. Thiel D.C. Johnson, J.Am.Chem.Soc. **119(11)**, 2665 (1997).
- [48] H. Takizawa, K. Miura, M. Ito, T. Suzuki, T. Endo, J. of Alloys and Compounds **282**, 79 (1999).
- [49] I. Shirotani, Y. Shimaya, K. Kihou, C. Sekine, J. Solid State Chemistry, (2003).
- [50] B.C. Sales, B.C. Chakoumakos, D. Mandrus, J.W. Sharp, J. Solid State Chem. **146**, 528 (1999).
- [51] O. Gunnarson, Rev. Mod. Phys. **69**, 575 (1997).
- [52] A. San-Miguel and P. Toulemonde, High Pressure Res. **25**, 159 (2005).
- [53] M. Imai et al. Phys. Rev. B **75**, 184535 (2007).

- [54] E. Bauer, A. Grytsiv, N. Melnychenko-Koblyuk, X.A. Chen, G. Hilscher, H. Kaldarar, H. Michor, E. Royanian, M. Rotter, R. Podloucky, P. Rogl; Phys. Rev. Lett. **99**, 217001 (2007).
- [55] E. Bauer, A. Grytsiv, Xing-Qiu Chen, N. Melnychenko-Koblyuk, P. Rogl, G. Hilscher, H. Kaldarar, H. Michor, E. Royanian, M. Rotter, R. Podloucky, Martin Rotter & G. Giester. J. Phys. Soc. Jap. Vol. **77** pp. 121-127 (2008).
- [56] E. Bauer, A. Grytsiv, X.-Q. Chen, N. Melnychenko-Koblyuk, G. Hilscher, H. Kaldarar, H. Michor, E. Royanian, M. Rotter, R. Podloucky, P. Rogl, Adv. Mater. **20**, 1325 (2008).
- [57] V. Sechovsky and L. Havela, in Handbook of Magnetic Materials, Volume 11, edited by K. H. J. Buschow, Elsevier, Amsterdam, p. 1, 1998.
- [58] R. Gumenniuk, W. Schnelle, H. Rosner, M. Nicklas, A. Leithe-Jasper, and Yu. Grin; Phys. Rev. Lett. **100**, 017002 (2008).
- [59] E. Bauer, Xing-Qiu Chen, G. Hilscher, H. Michor, E. Royanian, G. Giester, R. Podloucky, O. Sologub, A.P. Gonçalves; Phys. Rev. B, **78**, 064516 (2008).
- [60] A.F. Wells, in Structural Inorganic Chemistry, 3rd Ed., Oxford Press (1962)
- [61] H. Davy, Ann. Chim. **79**, 326 (1811)
- [62] M. von Stackelberg, Naturwissenschaften **36**, 27 (1949)
- [63] W.F. Claussen, J. Chem. Phys. **19**, 259 (1951)
- [64] L. Pauling, R. Marsh, Proc. Nat. Acad. Sci. **38**, 112 (1952)
- [65] G. Jeffrey, in *Inclusion Compounds*, edited by J. Atwood et al., Academic Press, p. 135 (1984)
- [66] Rowe D M, Ed, *CRC Handbook of Thermoelectrics* (CRC Press, Boca Raton, FL, 1995).
- [67] Nolas G, Slack G, Morelli D T, Tritt T M, Ehrlich AC, 1996 *J. Appl. Phys.* **79** **4002**.
- [68] G. Cordier, P. Woll, J. Less Common Metals **169**(2), 291, (1991).
- [69] N. Melnychenko-Koblyuk, A. Grytsiv, St. Berger, H. Kaldarar, H. Michor, F. Röhrbacher, E. Royanian, E. Bauer, P. Rogl, H. Schmid, G. Giester, J. Phys. Condens. Mat. , **19**, 046203-26, (2007)
- [70] N. Melnychenko-Koblyuk, A. Grytsiv, F. Fornasari, H. Kaldarar, H. Michor, F. Röhrbacher, M. Koza, E. Royanian, E. Bauer, P. Rogl, M. Rotter, H. Schmid, F. Marabelli, A. Devishvili, M. Doerr, G. Giester. Journal of Physics-Condensed Matter**19** 216223, 2007.
- [71] W. Carrillo-Cabrera, J. Curda, K. Petters, M. Baenitz, Y. Grin, von H. G. Schnering, Z. Kristallogr. New Crystal Structures, **215**, 321, (2000)
- [72] W. Carrillo-Cabrera, H. Borrmann, S. Paschen, M. Baenitz, F. Steglich, Y. Grin, J. Solid State Chem., **178**, 715, (2005)
- [73] N.F. Mott, H. Jones, *The Theory of the Properties of Metals and Alloys*, Dover Publications, Inc. New York, (1958)
- [74] J. M. Ziman, Principles of the Theory of Solids, (1965) Cambridge University Press.
- [75] E. Grüneisen, Ann. Physik **16**, 530 (1933).
- [76] P. L. Rossiter, The Electrical Resistivity of Metals and Alloys, (1987) Cambridge University Press
- [77] N. W. Ashcroft and N. D. Mermin, Solid State Physics, (1981) Holt-Saunders
- [78] G. H. Meaden, Electrical Resistance of Metals, (1965) Plenum Press
- [79] G. Wiedemann, R. Franz, Ann. Physik **89**, 497 (1853).
- [80] A.H. Wilson, Proc. Cambridge, Phil. Soc. **33**, 371 (1937).
- [81] J. Callaway, H. C. von Baeyer, Phys. Rev. **120**, 1149 (1960).
- [82] J. Callaway, Phys. Rev. **113**, 1046 (1959).
- [83] J. Callaway, Phys. Rev. **122**, 787 (1961).
- [84] J.Yang, in *Thermal Conductivity, Theory, Properties and Applications*, p. 1. edited by T.M. Tritt, Springer, 2004.
- [85] T.J. Seebeck, Abh. K. Akad. Wiss. Berlin, 265 (1822-1823)

- [86] N.F. Mott, Proc. Royal Soc. **156**, 368 (1936).
- [87] G.S. Nolas, J. Sharp, H.J. Goldsmid, Thermoelectrics, Basic Principles and New Materials Developments, Springer Series in Material Sciences, vol 45., Berlin, Heidelberg 2001.
- [88] S. Paschen, V.H. Tran, M. Baenitz, W. Carrillo-Cabrera, Y. Grin, F. Steglich, 2002 *Phys. Rev. B* **65** 134435.
- [89] E. Bauer, The lecture on the Physics of *Highly Correlated Electron Systems, The Kondo Problem to Heavy Fermions*, Vienna University of Technology: TU Vienna, 2007.
- [90] G. Grimvall, Thermodynamical properties of materials (North-Holland 1986).
- [91] A. Junod, D. Bichsel, J. Muller, Helvetica Physica Acta **52**, 580 (1979).
- [92] A. Junod, T. Jarlborg, J. Muller, Phys. Rev. B **27**, 1568 (1983).
- [93] G. Hilscher, H. Michor, N.M Hong, W. Perthold, P. Rogl, Physica B **206-207**, 542 (1995).
- [94] L.N. Cooper, phys. Rev. **104**, 1189 (1956).
- [95] J. Bardeen, L.N. Cooper and J.R. Schrieffer, phys. Rev. **106**, 162 (1957).
- [96] M. Tinkham, G. Mackay - *Introduction to superconductivity* Textbook - 2th Ed., McGraw-Hill, (1996).
- [97] J. Bardeen, L.N. Cooper and J.R. Schrieffer, phys. Rev. **108**, 1175 (1958).
- [98] V.L. Ginzburg and L.D. Landau, Zh. Ekspерим. Teor. Fiz. **20**, 1064 (1950)
- [99] A.A. Abrikosov, Zh. Ekspерим. Teor. Fiz. **32**, 1442 (1957); [Soviet Phys. JETP **5**, 1174 (1957)]
- [100] L.P. Gor'kov, J.E.T.P. USSR **36**, 1918 (1959); [Soviet Phys. J.E.T.P. USSR **9**, 1364 (1959)] and Zh. Eksp. Teor. Fiz. **37**, 1407 (1959); [Soviet Phys. JETP **10**, 998 (1960)]
- [101] H.W. weber, O. Hittmair, *Handbook on the superconductivity, Band 64* 1979.
- [102] A.A. Abrikosov, Dokl. Akad. Nauk. U.S.S.R. **86**, 489 (1952).
- [103] V.L. Ginzburg and L.D. Landau, J. Exptl. Theoret. Phys. (U.S.S.R.) **20**, 1064 (1950).
- [104] V.L. Ginzburg, Nuovo Cimento (10) **2**, 1234 (1955).
- [105] B.B. Goodman, IBM Journal of Research and Development, 1962.
- [106] W. Meissner and R. ochsenfeld, Naturwissenschaften **21**,787 (1933).
- [107] R.A. Ferrel, Phys. Rev. Letters **3**, 262 (1959).
- [108] G. Grimvall, Phys. Scr. **14**, 63 (1976).
- [109] P.W. Anderson, Phys. Rev. Letters **3**, 325 (1959).
- [110] A.A. Abrikosov and L.P. Gor'kov, Zh. Ekspерим. i Theor. Fiz. **42**,1088 (1962).
- [111] T.P. Orlando, E.J. McNiff, Jr., S. Foner, M.R. Beasley, Phys. Rev. B **19**, 4545 (1979).
- [112] D. Rainer, G. Bergmann, J. Low Temp. Phys. **14**, 501 (1974).
- [113] D. Rainer, G. Bergmann and U. Eckhard, Phys. Rev. B **8**, 5324 (1973).
- [114] G. Eilenberg and V. Ambegaokar, Phys. Rev. **158** 322 (1967).
- [115] N.R. Werthamer, W.L. McMillian, Phys. Rev. **158** 415 (1967).
- [116] U. Rauchschwalbe, Physica **147** B, 1 (1987).
- [117] Nonius Kappa CCD Program Package COLLECT, DENZO, SCALEPACK, SORTAV, Nonius Delft, the Netherlands (1998).
- [118] G.M. Sheldrick SHELX-97, *Program for Crystal Structure Refinement*, (University of Göttingen, Germany); Windows version by McArdle, Natl. Univ. Ireland, Galway (1997).
- [119] J. Rodriguez-Carvajal, *FULLPROF: A Program for Rietveld Refinement and Pattern Matching Analysis*, Abstracts of the Satellite Meeting on Powder Diffraction of the XV Congr. Intl. Union of Crystallogr., Talence, France, p. 127 (1990).
- [120] T. Roisnel, J. Rodriguez-Carvajal, Materials-Science-Forum **378-381**(1), 118 (2001).

- [121] J.L. Pouchou, F. Pichoir, J. Microsc. Spectrosc. Electron. , **10**, 279 (1985).
- [122] St. Berger, Diploma thesis, TU Vienna (1998)
- [123] M. Liendl, Diploma thesis, TU Vienna (1995)
- [124] R. Resel, E. Gratz, A. T. Burkov, T. Nakama, M. Higa, K. Yagasaki, Rev. Sci. Instrum. **67**, 1970 (1996)
- [125] W. Nernst, Sitzungsbericht der K.Preuss. Akad. Wiss. **12**, 261 (1910)
- [126] G. Schaudy, Diploma thesis TU Vienna (1991)
- [127] G. Schaudy, Thesis TU Vienna (1995)
- [128] H. Michor, Diploma thesis TU Vienna (1993)
- [129] A.V. Gribanov, Y.D. Seropegin, A.I. Tursina, O.I. Bodak, P. Rogl, H. Noel; "Isothermal Section of the Phase Diagram of the Ce-Pt-Si Ternary System at 600°C", Journal of alloys and compounds (J. alloys compd.), Vol. 383 **16** ref., pp. 286-289, 517 (1928), 2004.
- [130] R. Kolb, A. Mielke, E.-W. Scheidt, G.R. Stewart, J. Alloys Compd. 239 (1996) **124**. edited by T. M. Tritt, Chap. 5, 139 (2001).
- [131] M. Kasaya, M. Ito, A. Ono, O. Sakai, Physica B 223–224 (1996) **336**.
- [132] K. Hiebl, P. Rogl, J. Magn. Magn. Mater. 50 (1985) **39**.
- [133] P. Villars, et al. (Eds.), Inorganic Materials Database and Design System, Pauling File-Binaries Edition, version 1.0, Vitznau, Switzerland, 2002.
- [134] A.V. Gribanov, Y.D. Seropegin, A. Grytsiv, E. Bauer, E. Royanian, P. Rogl and G. Giester; "On the System Ce-Pt-Si Ternary System at 800°C", Journal of Solid State Chemistry, Vol. 181, **Issue 11**, 2964-2975 (2008).
- [135] Massara R. and Feschotte P. "The Binary System Pt-Si" (in French), J. Alloys Compd. 201, 223-227 (1993).
- [136] A. Gribanov, Int. Centre for Diffraction Data, PDF-54-0563 (2003).
- [137] L.E. Tanner, H. Okamoto, J. Phase Equilib. 12 (1991) 571.
- [138] M.V. Bulanova, P.N. Zheltov, K.A. Meleshevich, P.A. Saltykov, G. Effenberg, "Cerium-silicon system", J. Alloys Comp. **345**, 110-115 (2002).
- [139] P. Schobinger-Papamantellos and K.H.J. Buschow, J. Alloys Comp. **198**, 47-50 (1993).
- [140] Binary Alloy Phase Diagrams, Second Edition, Ed. T.B. Massalski, ASM International, Materials Park, Ohio (1990).
- [141] R. Gohle, R. Schubert, "Zum Aufbau des Systems Platin-Silizium", Z. Metallkunde, **55**, 503-511 (1964).
- [142] W. Gold, K. Schubert, "The Crystal Structure of Pt₁₂Si₅", Z. Kristallographie, **128**, 406-413 (1969).
- [143] Ram R.P., Bhan S. "On the Constitution of Platinum-Silicon Alloys", Z. Metallkunde **69**, 524-529 (1978).
- [144] G. Majni, M.C ostano, F. Panini G. Celotti, J.Phys. Chem. Sol. **46** 631-641 (1985).
- [145] Gribanov, A.V., Seropegin, Y.D., Kubarev, O.L., Akselrud, L.G., Bodak O.I., J. Alloys Comp **317** 318, 324-326 (2001).
- [146] Gribanov A., Rogl P., "Cerium - Platinum - Silicon", in New Series - Landolt-Börnstein, Ed. W. Martienssen, Group IV Physical Chemistry, Volume 11 Ternary Alloy Systems, Phase Diagrams, Crystallographic and Thermodynamic Data critically evaluated by MSIT, Subvolume B Noble Metal Systems, Eds G. Effenberg & S. Ilyenko, Springer, Berlin, pp356-366, 2006.
- [147] Gribanov A.V, unpublished research, (2004).
- [148] D. Rossi, R. Marazza, R. Ferro, J. Less-Common Met., **66**(2), P17-P25 (1979).
- [149] K. Kleep, E. Parthé, Acta Crystallogr. B38 (1982) 1105.
- [150] A.I. Tursina, A.V. Gribanov, Y.D. Seropegin, K.V. Kuyukov, O.I. Bodak, J. Alloys Compd. 347 (2002) 121.

- [151] A.I. Tursina, A.V. Gribanov, H. Noel, P. Rogl, Y.D. Seropegin, O.I. Bodak, J. Alloys Compd. **383** (2004) 239-241.
- [152] E. Parthé, L. Gelato, B. Chabot, M. Penzo, K. Cenzual, R. Gladyshevskii, *TYPIX Standardized Data and Crystal Chemical Characterization of Inorganic Structure Types* Springer, Berlin, Heidelberg (1994).
- [153] L. D. Chen, T. Kawahara, X. F. Tang, T. Goto, T. Hirai, J. S. Dyck, W. Chen, and C. Uher, J. Appl. Phys. **90**, 1864-1868 (2001).
- [154] C. Uher, *Beyond Bismuth Telluride, in Chemistry, Physics and Materials Science of Thermoelectric Materials*, ed. M. G. Kanatzidis, S. D. Mahanti and T. P. Hogan (Kluwer Academic, Plenum Publishers, New York, 2003) P.121
- [155] D.W. Woodard and G.D. Cody, Phys. Rev. **136**, A166 (1964).
- [156] R. Caton and R. Viswanathan, Phys. Rev. B **25**, 179 (1982).
- [157] K. Ikeda, K.A. Gschneidner Jr, R.J. Stierman, T.-W.E Tsang, and O.D. McMasters, Phys. Rev. B **29**, 5039 - 5052 (1984)
- [158] F. Mayr, G.F. Blanckenhagen, G.R. Stewart, Phys. Rev. B **55**, 947 (1997).
- [159] R. G. Chambers, Proc. Phys. Soc. London **78**, 941 (1961)
- [160] W.L. McMillan, Phys. Rev. **167**, 331 (1968).
- [161] K.H. Bennemann and J.W. Garland, in *Superconductivity in d- and f-bands metals*, edited by D. H. Douglass, (American Institute of Physics, New York), P.103 (1971).
- [162] D.K. Finnemore and D.E. Mapother, Phys. Rev. **140**, A507 - A518 (1965)
- [163] H. Michor, R. Krendelsberger, G. Hilscher, E. Bauer, C. Dusek, R. Hauser, L. Naber, D. Werner and P.C Hohenberg, P. Rogl and H. W. Zandbergen, Phys. Rev. B **54**, 13, 9408 - 9420 (1996).
- [164] K. Maki, Phys. Rev. **148**, 362 (1966).
- [165] N.R. Werthamer, E. Hefland, and P.C Hohenberg, Phys. Rev. **147**, 295 (1966).
- [166] M. Wong, E. J. Cotts, and S. J. Poon, Phys. Rev. B **30**, 1253 (1984).
- [167] R.R. Hake, Phys. Rev. **158**, 356 (1967).
- [168] G. Venturini, I. Ijjaali, B. Malaman, J. Alloys Compds. **285** (1999) 194.
- [169] R. Troc, V.H. Tran, J. Magn. Magn. Mater. **73** (1988) 289.
- [170] M. Kuznietz, H. Pinto, H. Ettedgui, M. Melamud, Phys. Rev. B **40** (1989) 7328.
- [171] B. Chevalier, P. Gravereau, T. Berlureau, L. Fournes, J. Etourneau, J. Alloys Compds. **233** (1996) 174.
- [172] P. Boulet, M. Potel, G. Andre', P. Rogl, H. Noe' l, J. Alloys Compds. **283** (1999) 41.
- [173] G. Kresse and J. Furthmüller, Comput. Mater. Sci. **6**, 15 (1996).
- [174] G. Kresse and J. Furthmüller, Phys. Rev. B **54**, 11169 (1996).
- [175] P. E. Blöchl, Phys. Rev. B **50**, 17953 (1994).
- [176] G. Kresse and D. Joubert, Phys. Rev. B **59**, 1758 (1999).
- [177] B. Silvi and A. Savin, Nature, **371**, 683 (1994).
- [178] G. Henkelman, A. Arnaldsson, and H. Jónsson, Comput. Mater. Sci. **36**, 254 (2006).
- [179] J.P. Perdew, K. Burke, M. Ernzerhof, Phys. Rev. Lett. **77**, 3865 (1996).
- [180] V. V. Krishnamurthy, J. C. Lang, D. Haskel, D. J. Keavney, G. Srainer, J. L. Robertson, B. C. Sales, D. G. Mandrus, D. J. Singh, and D.I. Bilc, Phys. Rev. Lett. **98**, 126403 (2007).
- [181] S. L. Dudarev, G. A. Botton, S. Y. Sarasov, C. J. Humphreys, and A. P. Sutton, Phys. Rev. B **57**, 1505 (1998).
- [182] J. Kunes and W. E. Pickett, Phys. Rev. B **69**, 165111 (2004).

- [183] E. Bauer, St. Berger, A. Galatanu, M. Galli, H. Michor, G. Hilscher, Ch. Paul B. Ni, M. M. Abd-Elmeguid V. H. Tran, A. Grytsiv, and P. Rogl Phys. Rev. B 63, 224414 (2001).
- [184] B.C. Sales, *Handbook on the Physics and Chemistry of Rare Earths*, edited by K. A. Gschneidner Jr., J.C.G. Bünzli and V. K. Pecharsky(Elsevier Science Publisher, North-Holland, Amsterdam 2003) Vol. 33, Chap. 211. PP.134.
- [185] St. Berger, 2003 Ph.D thesis, Vienna University of Technology.
- [186] A. Einstein, Ann. Phys. (Leipzig) **35**, 679 (1911)
- [187] D. Cahill, R. Pohl, Solid State Commun. **70** 927 (1989).
- [188] K. Gianno, A. V. Sologubenko, M. A. Chernikov, H. R. Ott, I. R. Fisher, P. C. Canfield, Phys. Rev.B **62**, 292 (2000).
- [189] N. Melnychenko-Koblyuk, A. Grytsiv, L.Fornasari, H. Kaladarar, H. Michor, F. Röhrbacher, M. Koza, E. Royanian, E. Bauer, P. Rogl, M. Rotter, H. Schmid, F. Marabelli, A. Devishvili, M. Doerr, G, Giester; J. Phys.: Condens. Matter **19** 216223 (26pp) (2007).
- [190] T. Tritt, 1999, *Science*. **283** 804
- [191] Barron T, Collins J and White G, Adv. Phys.**29** 609 (1980).
- [192] J.L. Cohn, G.S. Nolas, V. Fessatidis, T.H. Metcalf, G.A. Slack, Phys. Rev. Lett.**82** 779, (1999).
- [193] Nolas G, Cohn J L, Slack G and Schujman S B, Appl. Phys. Lett. **73** 178 (1998).
- [194] W. Carrillo-Cabrera, S. Budnyk, Y. Prots, Y. Grin, Z. Anorg. Allg. Chem., **630**, 7226, (2004).
- [195] D.Saint-James and P.G. de Gennes, Phys. Lett. **7**, 306 (1963).
- [196] B. Mühlischlegel, Z. Phys. **155**, 313 (1959).
- [197] H. S. Lee, D.J. Jang, H.G. Lee, W. Kang, M. H. Cho and S.I. Lee, J. Phys.: Condens. Matter **20** 255222 (2008).
- [198] Z. Fisk and G. W. Webb, Phys. Rev. Lett. **36** 1084(1976).
- [199] O. Gunnarsson, M. Calandra and J.E. Han, Rev. Mod. Phys. **75** 1085 (2003).
- [200] S. Paschen, W. Cabrillo-Cabrera, A. Bentien, V.H. Tran, M. Baenitz, Yu. Grin, and F. Steglich, Phys. Rev. B **64** (2001).
- [201] B.C. Sales, B.C. Chakoumakos, R. Jin, J.R. Thompson, and D. Mandrus, Phys. Rev. B **63**, 245113 (2001).
- [202] N. Melnychenko-Koblyuk, A. Grytsiv, P. Rogl, M. Rotter, E. Bauer, G. Durand, H. Kaladarar, R. Lackner, H. Michor, E. Royanian, M. Koza, and G. Giester, Phys. Rev. B, in press (2007).
- [203] N. Melnychenko-Koblyuk, A. Grytsiv, P. Rogl, M. Rotter, R. Lackner, E. Bauer, L. Fornasari, F. Marabelli, and G. Giester, Phys. Rev. B, submitted (2007).
- [204] S.K. Malik; S.K. Dhar; R. Vijayaraghavan, Bull. Mater. Sci., **6(2)**, 263-72 (1984).
- [205] R. Lackner, E. Bauer, P. Rogl, Physica B **378-380**, 835-836 (2006).
- [206] P. Salamakha, A.P. Goncalves, O.L. Sologub, M. Almeida, Journal of Alloys and Compounds 360 (2003) **61-68**.
- [207] Y.B. Kuz'ma , O.M. Dub , V.A. Bruskov , N. Chaban , and L.V. Zavalii , Kristallografiya 33 **841-844** (July-August 1988).
- [208] O. Sologub, P. Rogl, A. Grytsiv, G. Giester, J. Phys. Conference Series (2009).
- [209] O. Sologub, P. Rogl, G. Giester, in preparation.
- [210] S.K. Sinha, Handbook on the Physics and Chemistry of Rare Earths,edited by K. A. Gschneidner ET AL. (North-Holland, Amsterdam) (1987).
- [211] W. Perthold , Ph.D thesis, TU Wien, (1995).
- [212] S. Ozeki, Y. Ohe, Y.S. Kwon, Y. Haga, O. Nakamura, T. Suzuki, T. Kasuya, Physica B **171**, 286 (1991).
- [213] S. Ozeki, Y.S. Kwon, Y. Haga, G. Kido, T. Suzuki, T. Kasuya, Physica B **169**, 499 (1991).

- [214] O. Vogt, K. Mattenberger, *Magn. Meas. on Rare Earth and Actinide Monopnictides and Monochalcogenides*, in Handbook on the Physics and Chemistry of Rare Earths, edited by K. A. Gschwendner, Jr., L. Eyring, G.H. Lander and G.R. Choppin, Elsevier Science Publishers B. V., Vol. **17**, 301 (1993).
- [215] Tritt T 1999 *Science* **283** 804.
- [216] H. Wiesmann, M. Gurvitch, H. Lutz, A. Ghosh, B. Schwarz, M. Strongin, P. B. Allen, and J. W. Halley: *Phys. Rev. Lett.* **38** (1977) 782.
- [217] E. S. Hellman and E. H. Hartford, Jr.: *Phys. Rev. B* **47** 11346 (1993).
- [218] S. Ramakrishnan, K. Ghosh, A. D. Chinchure, V. R. Marathe, and G. Chandra: *Phys. Rev. B* **52** 6784 (1995).
- [219] N. Kase, T. Muranaka, and J. Akimitsu, *J. Phys. Soc. Jpn.* **77** 054714 (2008).
- [220] N.H. Anderson and H. Smith; *Phys. Rev. B*, **19**, 384 (1979).
- [221] A. Sumiyama, Y. Oda, H. Nagano, Y. Onuki, K. Shibutani and T. Komatsubara; *J. Phys. Soc. Jpn.*, **55**, 1294 (1986).
- [222] E. Jobilong, J.S. Brooks, E.S. Choi, H. Lee and Z. Fisk; *Phys. Rev. B*, **72**, 104428 (2005).
- [223] M.B. Fontes, J.C Trochez, B. Giordanengo, S.L. Bud'ko, D.R. Sanchez, E.M. Baggio-Saitovich and M.A. Continentino; *Phys. Rev. B*, **60**, 6781 (1999).

List of Publications

1. E. Bauer, H. Kaldarar, A. Prokofiev, E. Royanian, A. Amato, J. Seren, W. Brämer-Escamilla and I. Bonalde. *J. Phys. Soc. Jap.*, Vol. **76**, 5, pp. 051009-1 - 051009-15 (2007).
Heavy Fermion Superconductivity and Antiferromagnetic Ordering in CePt₃Si without Inversion Symmetry
2. A. Gribanov, A. Tursina, E. Murashova, Y. Seropegin, E. Bauer, H. Kaldarar, R. Lackner, H. Michor, E. Royanian, M. Reissner and P. Rogl. *Journal of Physics: Condensed Matter* **18** 9593-9602 (2006)
New orthorhombic modification of equiatomic CePdAl
3. E. Bauer, A. Grytsiv, Xing-Qiu Chen, N. Melnychenko-Koblyuk, G. Hilscher, H. Kaldarar, H. Michor, E. Royanian, G. Giester, M. Rotter, R. Podloucky & P. Rogl. *Physical review letter* **99**, pp. 217001-1 (2007).
Superconductivity in novel Ge-based skutterudites: {Sr, Ba}Pt₄Ge₁₂.
4. E. Bauer, A. Grytsiv, X. Chen, N. Melnychenko-Koblyuk, G. Hilscher, H. Kaldarar, H. Michor, E. Royanian, M. Rotter, R. Podloucky, P. Rogl. *Advanced Materials*, **20**, pp. 1325 - 1328 (2008).
BaPt₄Ge₁₂: A Skutterudite Based Entirely on a Ge Framework.
5. N. Melnychenko-Koblyuk, A. Grytsiv, St. Berger, H. Kaldarar, H. Michor, F. Röhrbacher, E. Royanian, E. Bauer, P. Rogl, H. Schmid, G. Giester. *Journal of Physics: Condensed Matter* **19**, 046203 (2007).
Ternary clathrates Ba-Cd-Ge: phase equilibria, crystal chemistry and physical properties
6. N. Melnychenko-Koblyuk, A. Grytsiv, F. Fornasari, H. Kaldarar, H. Michor, F. Röhrbacher, M. Koza, E. Royanian, E. Bauer, P. Rogl, M. Rotter, H. Schmid, F. Marabelli, A. Devishvili, M. Doerr, G. Giester. *Journal of Physics: Condensed Matter* **19** (2007), 216223.
Ternary clathrates Ba-Zn-Ge: phase equilibria, crystal chemistry and physical properties
7. N. Melnychenko-Koblyuk, A. Grytsiv, P. Rogl, E. Bauer, G. Durand, H. Kaldarar, R. Lackner, H. Michor, E. Royanian, M. Koza, G. Giester. *Phys. Rev. B* **76**, 144118/1-11 (2007).
Clathrate Formation in the Ba-Pd-Ge System: Phase Equilibria, Crystal Structure and Physical Properties
8. E. Bauer, H. Kaldarar, H. Michor, M. Reissner, E. Royanian, E.W. Scheidt , P. Rogl, A. Gribanov, Y. Seropegin. *Physica B: Condensed Matter*, **403**, PP. 919 - 921 (2008).

- Low temperature transport and thermodynamic properties of $YbPd_2Si$*
9. N. Melnychenko-Koblyuk, A. Grytsiv, P. Rogl, M. Rotter, E. Bauer, R. Lackner, E. Royanian, Martin Rotter and G. Giester, J. Phys. Soc. Jap. Vol. **77** suppl. A, pp. 54-60 (2008).
- Structure and Physical Properties of Clathrate I Systems $Ba_8Pd_xSi_{46-x}$ and $Ba_8Pt_xSi_{46-x}$*
10. B. Popescu, E. Royanian, H. Michor, G. Hilscher, E. Bauer, A. Galatanu. Physica B, **403**, PP. 937 - 939 (2008).
- Low temperature magnetic and transport properties in $Ce(Ag,Ni)Sb_2$ compounds*
11. E. Bauer, A. Grytsiv, Xing-Qiu Chen, N. Melnychenko-Koblyuk, P. Rogl, G. Hilscher, H. Kaldarar, H. Michor, E. Royanian, M. Rotter, R. Podloucky, Martin Rotter & G. Giester. J. Phys. Soc. Jap. Vol. **77** suppl. A, pp. 121-127 (2008).
- Superconductivity and Magnetism in MPt₄Ge₁₂, M = Ca, Ba, Sr, Eu*
12. A.V Gribanov, Y.D Seropegin, P. Rogl, E. Bauer, E. Royanian and G. Giester, Journal of Solid State Chemistry, Vol. 181, Issue **11**, 2964-2975 (2008).
- On the System Ce-Pt-Si Ternary System at 800°C*
13. E. Bauer, Xing-Qiu Chen, P. Rogl, G. Hilscher, H. Michor, E. Royanian, R. Podloucky, G. Giester, O. Sologub, A. P. Gonçalves. Phy. Rev. B. **78**, 064516 (2008).
Superconductivity and spin fluctuations in {Th,U}Pt₄Ge₁₂ skutterudites.
14. E. Bauer, E. Royanian, H. Michor, G. Hilscher, H. Kaldarar, P. Rogl, A. Grytsiv, A.V Gribanov, D. Shtepa, Y.D Seropegin, S. Nesterenko. Phys. Rev. B., (2008) in press.
Thermal and electronic properties of CePd₃In₂.
15. P. Rogl, E. Bauer, E. Royanian, H. Kaldarar, E.-W. Scheidt, H. Michor, O. Sologub, G. Giester, A.P. Gonçalves. Phys. Rev. B., (2008) in press.
Structure and Physical Properties of Novel {Th,U}Pt₃B
16. E. Royanian, E. Bauer, H. Kaldarar, A. Galatanu, G. Hilscher, H. Michor, M. Reissner, P. Rogl, O. Sologub, G. Giester, A. Pereira-Goncalves, Journal of Physics, (2009) in press.
Formation, Structure and Physical Properties of $M_2Pd_{14+x}B_{5-y}$ Compounds, M=(Th, La, Ce, Pr, Nd, Sm, Eu, Gd)
17. N. Nasir, N. Melnychenko-Koblyuk, A. Grytsiv, P. Rogl, E. Bauer, H. Michor, G. Hilscher, E. Royanian, G. Giester. Intermetallics. Mater. Intermetallics (2009), doi:10.1016/j.intermet.2008.12.010, in press.
Crystal structure and physical properties of EPCo_{5-x}Ge₉ (EP= Sr, Ba, Eu)

List of Conference Contributions

- Workshop on "Quantum Complexities in Condensed Matter", An International Conference, 4th of July-7th of July, 2006, Cambridge, United Kingdom
Crystal chemistry and low temperature properties of novel $Yb_{18}Pt_{51.1}Si_{15.1}$ ($\sim YbPt_3Si$)
E. Bauer, R. Lackner, H. Kaladarar, E. Royanian, H. Michor, G. Hilscher, E.-W. Scheidt, W. Scherer, M. Sieberer, A. Gribanov, A. Tursina, Y. Seropegin, P. Rogl, G. Giester.
- 15th International Conference on Solid compounds of Transition Elements, Krakow, Poland; 15-20 July 2006
New orthorhombic modification of equiatomic CePdAl
A Gribanov, A Tursina, E Murashova, Y Seropegin, E Bauer, H Kaladarar, R Lackner, H Michor, E Royanian, M Reissner and P Rogl.
- The International Conference on Strongly correlated electron systems. Houston, Texas, USA May 13-18, 2007
1- "Low temperature transport and thermodynamic properties of YbT_2Si , ($T = Pd, Pt$)"
E. Bauer, H. Kaladarar, H. Michor, M. Reissner, E. Royanian, E.-W. Scheidt, P. Rogl, A. Gribanov.
2- "Low temperature magnetic and transport properties in $Ce(Ag,Ni)Sb_2$ compounds"
B. Popescu, E. Royanian, H. Michor, G. Hilscher, E. Bauer, A. Galatanu.
- 13th Czech and Slovak Conference on Magnetism - CSMAG'07, Kosice, Slovakia; 09.07.2007 - 12.07.2007
Tunneling Spectroscopy studies of $CePt_3Si$
M. Baťko, I. Baťková, E. Royanian, A. Prokofiev, E. Bauer.
- 13th Czech and Slovak Conference on Magnetism - CSMAG'07, Kosice, Slovakia; 09.07.2007 - 12.07.2007
Magnetic behaviour in $Ce(Ag,Ni)Sb_2$ system
A. Galatanu, B. Popescu, A. Birsan, E. Royanian, H. Kaladarar, R. Lackner, H. Michor, G. Hilscher, E. Bauer.
- 6th European Conference on Thermoelectrics, Paris, France July 2 - 4, 2008

Thermoelectric properties of MPt₄Ge₁₂ (M=Sr,Ba,Eu)

E. Royanian, A. Valade, E. Bauer, X. Chen, R. Podloucky, A. Grytsiv, N. Melnychenko-Koblyuk, P. Rogl.

- **International Conference on "New Quantum Phenomena in Skutterudite and Related Systems", Centennial Hall, Kobe University, Japan September 26-30, 2007**

Formation, Structure and Physical Properties of M₂Pd_{14+x}B_{5-y} Compounds, M=(Th, Ce, Pr, Nd, Sm, Eu, Gd)

E. Royanian, E. Bauer, H. Kaladarar, H. Michor, M. Reissner, P. Rogl, A. Pereira-Gonçalves, G. Giester.

- **12th Symposium: "Thermochemistry & Thermophysics of Nuclear Materials", Parkhotel Pörtschach, Aug.30th-Sept.3rd, 2008**

Superconductivity and Spin Fluctuations in {Th,U}Pt₃B

E. Royanian, P. Rogl, E. Bauer, H. Kaladarar, E.-W. Scheidt, H. Michor, O. Sologub, G. Giester, A.P. Gonçalves.

Ich danke...

... meinem Doktorvater Prof. Dr. Ernst Bauer, der mir mit Rat und Tat zu Seite stand. Er ermöglichte mir weitgehend freies Arbeiten in freundschaftlicher Atmosphäre und damit die Fertigstellung dieser Dissertation.

... Prof. Dr. Peter Rogl vom Institut für Physikalische Chemie der Universität Wien für die Hilfestellung bei den Strukturanalysen der untersuchten Verbindungen sowie für die vielen aufschlussreichen Gespräche.

... den Kollegen von der Arbeitsgruppe Magnetismus & Supraleitung Prof. Dr. Gerfried Hilscher und Prof. Dr. Herwig Michor für Messungen der Suszeptibilität und spezifischen Wärme aber vor allem für ihre ständige uneingeschränkte Bereitschaft zur Hilfestellung bei jeglichen Fragen und Problemen.

... Univ. Doz. Dr. Andrey Prokofiev für die Hilfestellung bei der Probenpräparation, die Strukturanalysen, sowie für die vielen aufschlussreichen Gespräche.

... den Mitgliedern des Instituts für Festkörperphysik für deren Unterstützung und das freundliche Arbeitsklima.

... vor allem meiner Mutter, dass sie mir diese Ausbildung ermöglicht hat und immer für mich da war.

... besonders meinem Onkel Herrn Dr. Zabilolla Mafi für die Ermöglichung des Studiums, Unterstützungen und für alle Hilfestellungen.

Ohne Ihre Hilfe hätte ich das Studium nicht erfolgreich abschließen können.

Diese Arbeit wurde vom Fonds zur Förderung der wissenschaftlichen Forschung FWF durch die Projekte P 18054 unterstützt.

Curriculum Vitae

Dipl.-Ing. Esmaeil Royanian
Friedrich-Engels-Pl. 9/6/18
1200 Wien

Persönliche Daten:

Geburtsdatum: 6.2.1971
Geburtsort: Noshahr, IRAN
Staatsbürgerschaft: Österreich
e-mail: Royanian@ifp.tuwien.ac.at

Schulbildung und Akademisches Studium:

1977 - 1982 Volksschule , Noshahr - IRAN
1983 - 1985 Hauptschule , Noshahr - IRAN
1985 - 1990 Gymnasium , Noshahr - IRAN
1990 Matura und Reifeprüfung
1990 - 1992 24 Monate Ableistung des ordentlichen Zivildienstes
1992 - 1997 B.Sc. in der Angewandte Physik ,
Mazandaran Universität - IRAN
2000 - 2003 Fortsetzung des Studiums Technische Physik an der
Technischen Universität Wien
2003 - 2004 Abfassung der Diplomarbeit "*TEM Kontrast von Stapelfehlern und Präzipitaten in Czochralski-Silizium*" am Institut für
Festkörperphysik, Technischen Universität Wien
15.06.2004 Ablegung der 2. Diplomprüfung
01.06.2005 Beginn der Beschäftigung als Dissertant am
Institut für Festkörperphysik der Technischen Universität Wien
ab Juni 2005 Beschäftigung als Projektassistent an der
Institut für Physikalische Chemie - Universität Wien

Praxis:

1.06.05 - 1.06.08 Projektassistent im Rahmen des FWF-Projektes (P 18054)
"Phaseninstabilität hochkorrelierter Materialien"
Betreuung: a.o. Prof. Dipl.Ing. Dr. Ernst Bauer
o. Prof. Univ. Dr. Peter Franz Rogl
Institut für Festkörperphysik, TU-Wien